UNIVERSITÉ DE STRASBOURG

ÉCOLE DOCTORALE de Physique et Chimie-Physique (ED182)

Observatoire Astronomique de Strasbourg (UMR 7550)

THÈSE présentée par :

Amandine DOLIVA-DOLINSKY

soutenue le : **15 septembre 2023**

pour obtenir le grade de : **Docteur de l'université de Strasbourg**

Discipline/ Spécialité : Astrophysique

Les galaxies naines du Groupe Local comme sondes cosmologiques

THÈSE dirigée par :

M. MARTIN Nicolas	Chargé de recherche, Observatoire Astronomique de Strasbourg

RAPPORTEURS :

Mme. BATTAGLIA Giuseppina	Tenured researcher, Instituto de Astrofìsica de Canarias
Mme. HILL Vanessa	Directrice de recherche, Observatoire de la Côte d'Azur

---

AUTRES MEMBRES DU JURY :

M. AUBERT Dominique	Professeur, Observatoire Astronomique de Strasbourg
Mme. COLLINS Michelle	Senior Lecturer, University of Surrey

Remerciement

Antoine de Saint-Exupéry, Le petit prince, 1943

Je voudrais tout d'abord remercier Dominique Aubert, Giuseppina Battaglia, Michelle Collins et Vanessa Hill d'avoir accepté d'être membre du jury de cette thèse. C'est un honneur et un plaisir que de vous présenter le travail effectué durant cette thèse.

Ces trois années de thèse ont été un véritable périple, dont la qualité a été grandement façonnée par celui que les livres d'aventures pourraient considérer comme un guide, Nicolas Martin. Je te remercie pour l'opportunité de cette thèse, ainsi que pour le soutien constant que tu m'as apporté. Je suis sincèrement ravie d'avoir pu parcourir l'Univers Local en ta compagnie.

Ce voyage ne peut être résumé uniquement par le travail scientifique, car il a été avant tout une expérience humaine, ponctuée de nouvelles rencontres et d'amitiés. Je pense bien sûr à l'accueil chaleureux du personnel de l'Observatoire et aux moments de convivialité partagés lors des repas du solstice ou des déjeuners du vendredi matin. Je souhaite particulièrement remercier les postdocs du groupe "galaxies archéologie" : Anke, Karina, Rapha et Zhen pour avoir été un véritable soutien. Zhen, je tiens également à te remercier pour avoir été à la fois une mentore et une amie tout au long de cette thèse. Merci pour ces discussions autour d'un bubble tea et surtout merci pour notre séjour d'observation à l'INT, un moment suspendu, si rare, hors du temps et de la réalité.

Je tiens à remercier mes compagnons de voyages, que ce soit dans les moments de fortune ou d'infortune, les doctorants de l'observatoire et plus particulièrement Emilie, Elisabeth, Jakub, Julien, Lucie, Pierre-Antoine, Thibaut et Wassim. Merci d'avoir été des partenaires de voyage, de tusmo, de pause thé/café, du schluck, de poke bowl... Merci d'avoir illuminé ces 3 années par votre joie, votre présence et votre amitié. C'était *cher* bien grâce à vous, et j'ai hâte qu'on vive de nouvelles aventures ensemble! Elisabeth, merci à toi et à toutes tes déclinaisons, particulièrement l'artiste des jeux de mots qui m'a fait rire tout au long de ces trois ans. Emilie, tu as été une collègue de bureau *incroyable*, et je te suis reconnaissante d'avoir fait de notre bureau un espace de vie où j'ai pris plaisir à travailler (et discuter). Merci à vous tous d'avoir fait de ma thèse une expérience si belle.

Je voudrais aussi remercier mes amis, strasbourgeois ou lyonnais : Claudine, Elsa, Gaetan, Guillaume, Julien, Justine, Mathis, Romain, Vincent. Vous partagez ma vie depuis le lycée, la prépa ou l'université, et je me considère extrêmement chanceuse de vous avoir à mes côtés.

Je tiens aussi à remercier mes grands-parents, mes oncles et tantes pour votre soutien sans faille et pour ces moments de joie et de bonheur que nous partageons. Un merci particulier, Mémé, car nous sommes toutes les deux de vraies barbèles. Merci Andréa et Maelle, respectivement ma grande soeur et ma petite soeur préférée. Finalement, je voudrais

remercier mes parents sans qui ce manuscrit n'existerait pas. J'ai mille et une raisons de vous remercier, donc je ne les détaillerai pas ici, mais sachez qu'elles sont toutes contenues dans ce merci.

List of Publications

First author publications

The PAndAS View of the Andromeda Satellite System. III. Dwarf Galaxy Detection Limits
2022, *The Astrophysical Journal*, 933, 135
A. Doliva-Dolinsky, N. Martin, G. Thomas, A. Ferguson, R. Ibata, G. Lewis, D. Mackey, A. McConnachie, Z. Yuan

The PAndAS View of the Andromeda Satellite System. IV. Global Properties
2023, *The Astrophysical Journal*, 952, 72
A. Doliva-Dolinsky, N. Martin, Z. Yuan, A. Savino, D. Weisz, A. Ferguson, R. Ibata, S. Kim, G. Lewis, A. McConnachie, G. Thomas

Is M31 at the center of its satellite system?
To be submitted
A. Doliva-Dolinsky, et al.

Co-author publications

The Complexity of the Cetus Stream Unveiled from the Fusion of STREAMFINDER and StarGO
2022, *The Astrophysical Journal*, 930, 103
Z. Yuan, K. Malhan, F. Sestito, R. Ibata, N. Martin, J. Chang, T. Li, E. Caffau, P. Bonifacio, M. Bellazzini, Y. Huang, K. Voggel, N. Longeard, A. Arentsen, **A. Doliva-Dolinsky**, J. Navarro, B. Famaey, E. Starkenburg, D. Aguado

The Pristine survey - XVII. The C-19 stream is dynamically hot and more extended than previously thought
2022, *The Astrophysical Journal*, 933, 135
Z. Yuan, N. Martin, R. Ibata, E. Caffau, P. Bonifacio, L. Mashonkina, R. Errani, **A. Doliva-Dolinsky**, E. Starkenburg, K. Venn, A. Arentsen, D. Aguado, M. Bellazzini, B. Famaey, M. Fouesneau, J. González Hernández, P. Jablonka, C. Lardo, K. Malhan, J. Navarro, R. Sánchez Janssen, F. Sestito, G. Thomas, A. Viswanathan, S. Vitali

Local Group Dwarf Galaxy Detection Limit in the CSST survey
2023, *MNRAS*, 523, 876-886
H. Qu, Z. Yuan, **A. Doliva-Dolinsky**, N. Martin, X. Kang, C. Wei, G Li, Y. Luo, J. Chang, C. Tsai, Z. Fan, R. Ibata

Contents

I Constraining cosmology and galaxy formation & evolution with the Milky Way satellite system **1**
I.1 The search for Milky Way dwarf galaxies 1
I.2 Satellite systems as cosmological and galaxy evolution probes 7

II The M31 satellite system: a secondary testbed for cosmology and galaxy formation & evolution **14**
II.1 The search for M31 satellites: from visual inspection to SDSS 14
II.2 Probing M31 halo through PAndAS 16
II.3 Towards a characterization of M31 satellite system 23

III PAndAS search algorithm **25**
III.1 Introduction 25
III.2 Dataset 26
III.3 A Bayesian search method 28
III.4 Results 34
III.5 A tailored search algorithm for detection limits 36

IV Detection Limits **42**
IV.1 Introduction 42
IV.2 Preliminaries 44
IV.3 Methods 44
IV.4 Results 57
IV.5 Discussion and conclusion 61

V Global Properties of M31 Satellite System **63**
V.1 Introduction 64
V.2 Sample 66
V.3 Model 68
V.4 Results 72
V.5 Discussion and conclusion 82

VI Is M31 at the center of its satellite system ? **86**
VI.1 Introduction 86
VI.2 Sample 87
VI.3 Method 89
VI.4 Results 92
VI.5 Discussion 94

VII Conclusion **96**
VII.1Summary 96
VII.2The MW and M31 satellite system : a comparative study 97
VII.3Future prospects 101

Appendices **103**

A Model parameters **104**

B Contraindre la cosmologie et la formation & l'évolution des galaxies grâce au système satellitaire de la Voie lactée **115**
B.1 La recherche de galaxies naines de la Voie lactée 115
B.2 Les systèmes satellitaires comme sondes cosmologiques et d'évolution des galaxies 121

C Le système satellitaire de M31: un second test pour la cosmologie et la formation et l'évolution des galaxies **129**
C.1 La recherche des satellites de M31 : de l'inspection visuelle à SDSS 129
C.2 Explorer le halo de M31 grâce à PAndAS 131
C.3 Vers une caractérisation du système satellitaire de M31 139

D Conclusion **141**
D.1 Résumé 141
D.2 Le système de satellites de la Voie Lactée et de M31 : une étude comparative 142
D.3 Perspectives 146

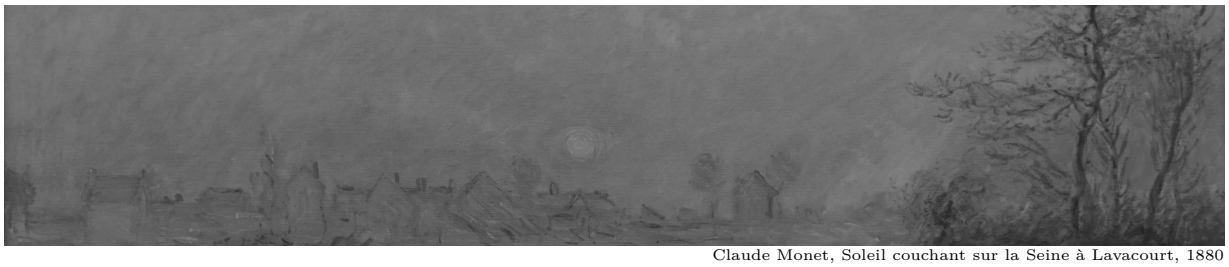

Claude Monet, Soleil couchant sur la Seine à Lavacourt, 1880

Chapter I

Constraining cosmology and galaxy formation & evolution with the Milky Way satellite system

I.1 The search for Milky Way dwarf galaxies

I.1.1 First discoveries

The earliest recorded observation of a dwarf galaxy can be traced back to the sighting of the two Magellanic clouds. These celestial objects were first documented by the renowned explorer Amerigo Vespucci during his voyages in 1503-1504. However, it was the expedition led by Ferdinand Magellan in 1519 that brought these celestial objects to wider attention. The Magellanic clouds, named after Magellan himself, are a pair of dwarf galaxies that can be seen from the Southern Hemisphere and are known as the Large Magellanic Cloud (LMC) and the Small Magellanic Cloud (SMC).

The next discovery of a Milky Way (MW) dwarf galaxy did not occur until 1938 when Shapley (1938a) made a groundbreaking observation of a "*large rich cluster with remarkable characteristics*" on the photographic plates from the Boyden Observatory. After the identification of the Sculptor dwarf galaxy, another major breakthrough came with the discovery of a second system in the constellation of Fornax (Shapley, 1938b). This discovery led the author to suggest the presence of other similar celestial objects. This hypothesis was confirmed about twenty years later with the identification of Leo I, Leo II (Harrington & Wilson, 1950), Draco and Ursa Minor (Wilson, 1955) thanks to the visual inspection of the photographic plates from the Palomar Sky Survey. Later, Carina was discovered thanks to plates from the UK Schmidt Telescope (Cannon et al., 1977). An example of an annotated Schmidt plate centered on the Draco dwarf galaxy is shown in Figure I.1, highlighting the difficulty to detect faint objects and to dig into the noise with visual methods.

While the visual inspection of existing photographic plates for further discoveries appeared challenging, the advent of fast measuring machines revolutionized the process by

enabling analysis at the catalogue level. This breakthrough serves as the foundation for automated search techniques, as shown by the pioneering discovery of Sextans (Irwin et al., 1990) in the UK Schmidt photographic plates.

The last discovery of the twentieth century, the Sagittarius dwarf galaxy emerged from the analysis of spectroscopic rather than photometric data. Indeed, the fortious detection of the Sagittarius dwarf galaxy relied on the discovery of a large and extended co-moving group of stars near the MW's bulge (Ibata et al., 1995). Moreover, subsequent studies have demonstrated that this satellite is undergoing tidal disruption and is consequently embedded within a stream (Ibata et al., 1997; Majewski et al., 2003). This detection is the first observation of a merger occurring between a satellite and its host, offering an exceptional opportunity to investigate and analyze these interactions. The importance of this discovery lies in its ability to shift the perspective regarding the state of our own Milky Way galaxy. Previously, the Milky Way was viewed as stable, static, and having already attained its final form. However, Sagittarius demonstrated that our galaxy is currently engaged in an ongoing merger, signifying that it is still undergoing changes.

I.1.2 Large photometric surveys

In total, 11 satellites of the MW were discovered during the twentieth century (Figure I.2); however, based on the favored cosmological model, a much larger number of dark matter subhaloes were anticipated to exist in the vicinity of the MW (Klypin et al., 1999; Moore et al., 1999). To find the potential other satellites, it was necessary to dig deeper into the noise. This was made possible thanks to the advent of large, homogeneous photometric surveys. The implementation of CCD sky surveys greatly facilitated the study of stellar catalogs and strengthened the utilization of automated methods for detecting faint dwarf galaxies. These technics rely on the identification of over-densities of stars in the color-magnitude diagram (CMD) and/or in the sky (Figure I.3). Automated algorithm are further discussed in the Chapter III.

The first such survey was the Sloan Digital Sky Survey (Abazajian et al., 2003). Its first data release included a comprehensive photometric catalog with five bands (u, g, r, i, z), covering over 2099 deg^2 and achieving a 50% completeness limit of $(u, g, r, i, z) = (22.5, 23.2, 22.6, 21.9, 20.8)$. This survey led to a fast and considerable increase in the number of known MW satellites, as 16 new satellites were discovered in the span of $\sim$ 7 years (Figure I.2; Willman, 2005; Willman et al., 2005; Zucker et al., 2006; Belokurov et al., 2006, 2007; Irwin et al., 2007; Walsh et al., 2007; Grillmair, 2009; Belokurov et al., 2009, 2010). The significance of these new discoveries extends beyond the mere expansion of the satellite sample size; it also introduces a new magnitude range, as nearly all the newly found dwarf galaxies exhibit $M_V > -8$ (Figure I.2) going as faint as M_V=−1.5 (Segue 1; Belokurov et al., 2006).

The distinction between dwarf galaxies and globular clusters became increasingly ambiguous with the advent of the SDSS survey, which enabled the discovery of fainter objects.

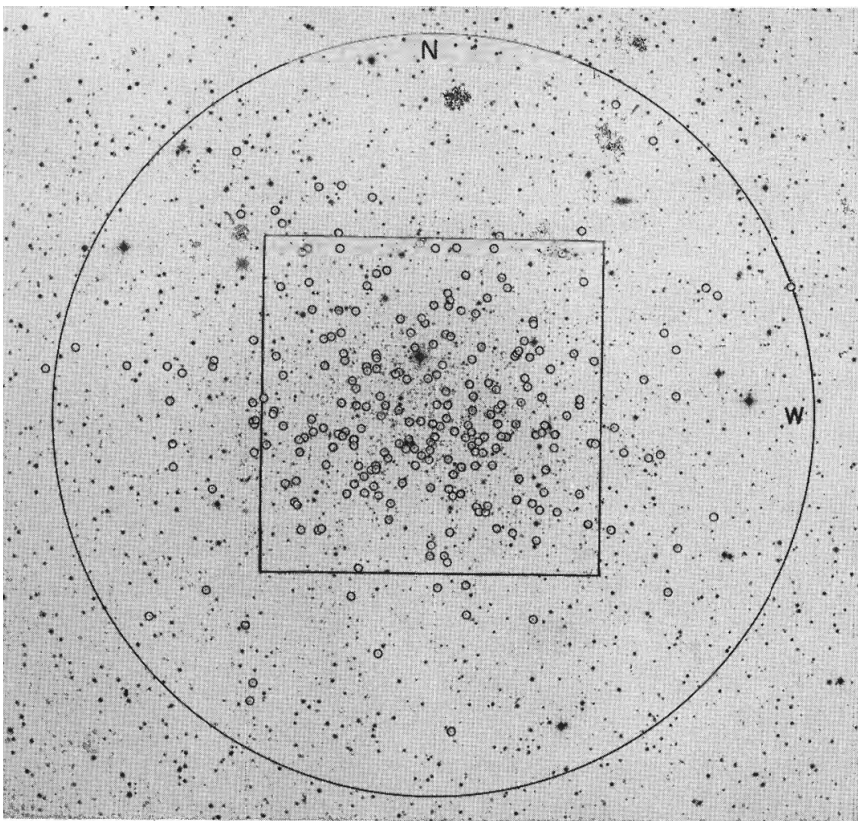

Figure I.1: Portion of a 48-inch Schmidt plate. The ring represent the extent of the Draco dwarf galaxy. Credit : Baade & Swope (1961).

Previously, it was believed that, for the same luminosity, dwarf galaxies possessed a larger radius, resulting in an apparent gap that served as a boundary between globular clusters and dwarf galaxies on the size-luminosity graph (Figure I.4). However, this perspective underwent a shift with the identification of satellites such as William 1, Segue 1, Segue 2, and Bootes II, which reside within the previously empty region on the size-luminosity graph, known as the "valley of ambiguity" (Gilmore et al., 2007).

In 2015, a notable increase in the count of Milky Way satellites occurred through the Dark Energy Survey (DES), which extensively observed an area of approximately 5000 deg^2 in the southern Galactic cap using the $grizY$ bands and reaching a median depth of (g, r, i, z, Y)=(23.4,23.2,22.4,22.1,20.7). This survey led to the discovery of 17 candidate dwarf galaxies (Drlica-Wagner et al., 2015; Koposov et al., 2015; Luque et al., 2016). Once again, a significant number of those candidates have an ambiguous nature and for some, the classification as a dwarf galaxies is still debated (Tucana V, Cetus II; Conn et al., 2018a,b). In the meantime, the Panoramic Survey Telescope And Rapid Response System (Pan-STARRS 1) probed three quarters of the sky with $grizy$ bands at a depth similar to SDSS and led

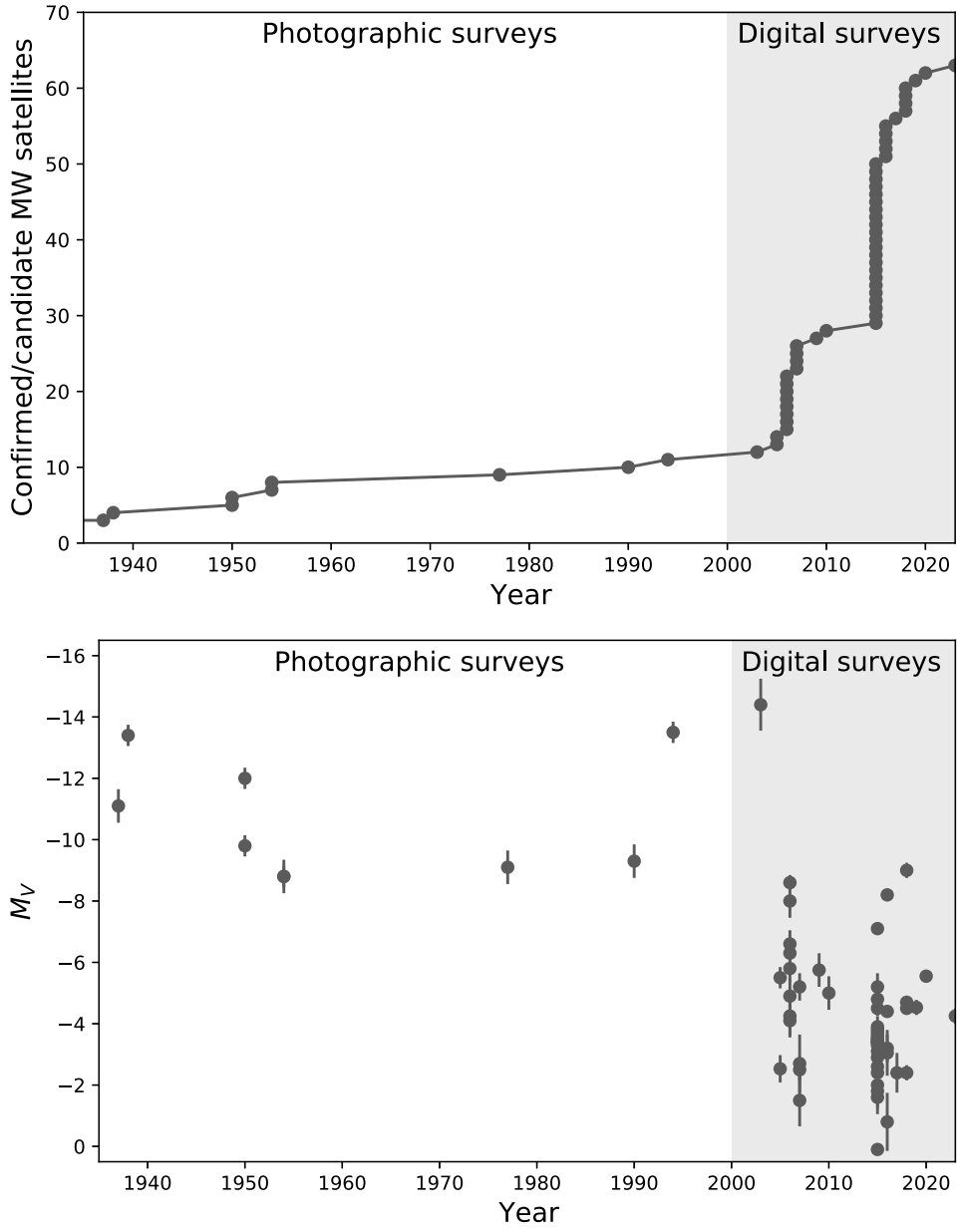

Figure I.2: *Top panel:* Number of confirmed/candidate MW dwarf galaxies as a function of time. The sample size considerably increase with the advent of large, homogenous photometric surveys going from 11 to ~ 60 as of 2023. *Bottom panel:* Absolute magnitudes in V-band of the confirmed/candidate MW dwarf galaxies as a function of time. The introduction of digital surveys in the twenty one century has enabled the detection of fainter objects by delving deeper into the noise.

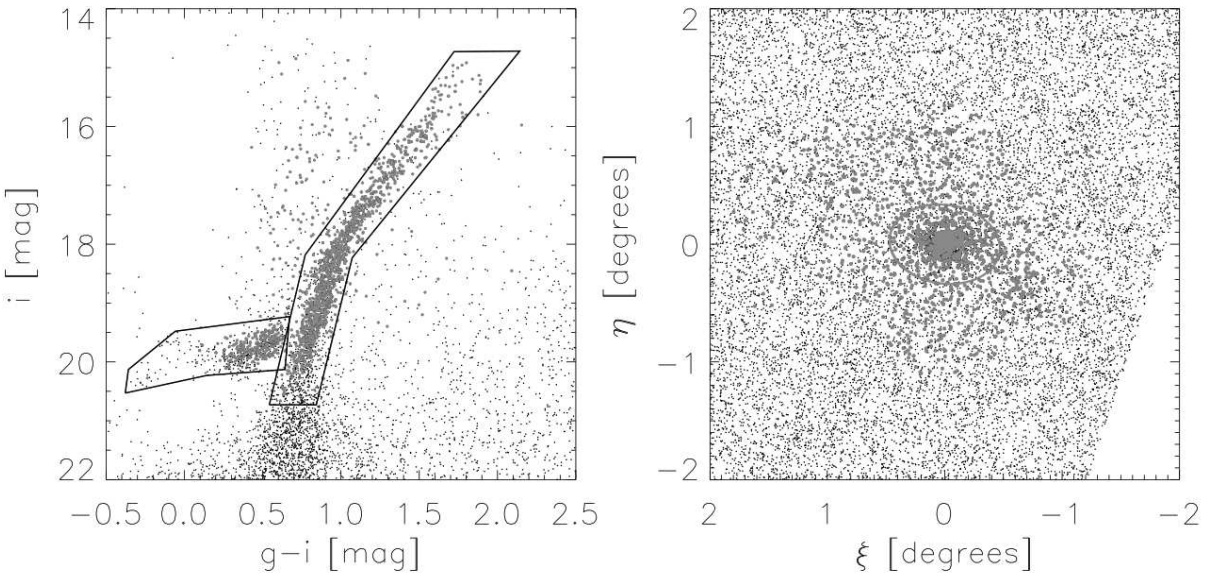

Figure I.3: *Left panel:* Color-magnitude diagram of stars from SDSS photometric catalogue, within $\sim 10'$ of Draco's center. *Right panel:* Spatial distribution of red giant and horizontal branch stars from SDSS photometric catalogue. Credit:Walker et al. (2015)

to the discovery of 3 new satellites (Laevens et al., 2015), while the VST ATLAS survey observed 4500 deg^2 of the Southern Sky with ugriz bands at a similar depth than the SDSS and uncovered 2 new dwarf galaxies (Torrealba et al., 2016a,b).

As it is expected that the LMC has its own dwarf galaxies, more localized efforts were made to search for faint object in its vicinity (e.g., SMASH, MagLites) which led to the discoveries of 5 more dwarf galaxies (Martin et al., 2015; Drlica-Wagner et al., 2016; Koposov et al., 2018). It is important to note that the true host of some of the satellite found within the MW halo is debated given that the LMC has its own satellite system (Battaglia et al., 2022).

Thanks to the Hyper Suprime-Cam (HSC) Subaru Strategic Program (SSP), three dwarf galaxies (Homma et al., 2018, 2019) were successfully identified. The HSC SSP is a deep photometric survey, achieving 5σ depth values of (g, r, i, z, y)= (26.5, 26.1, 25.9, 25.1, 24.4) and leading to the discovery of Virgo I, the faintest known dwarf galaxy to date, with a magnitude of $M_V = -0.33^{+0.75}_{-0.87}$. Recently, the DECam Local Volume Exploration Survey (DELVE) has successfully unveiled two dwarf galaxies (Mau et al., 2020). DELVE employs a comprehensive approach by combining archival DECam data (e.g., DES, DECals, DeROSITAS) with new observations utilizing the same instrument and encompassing the Milky Way, analogs of the Magellanic Clouds, and the Local Volume.

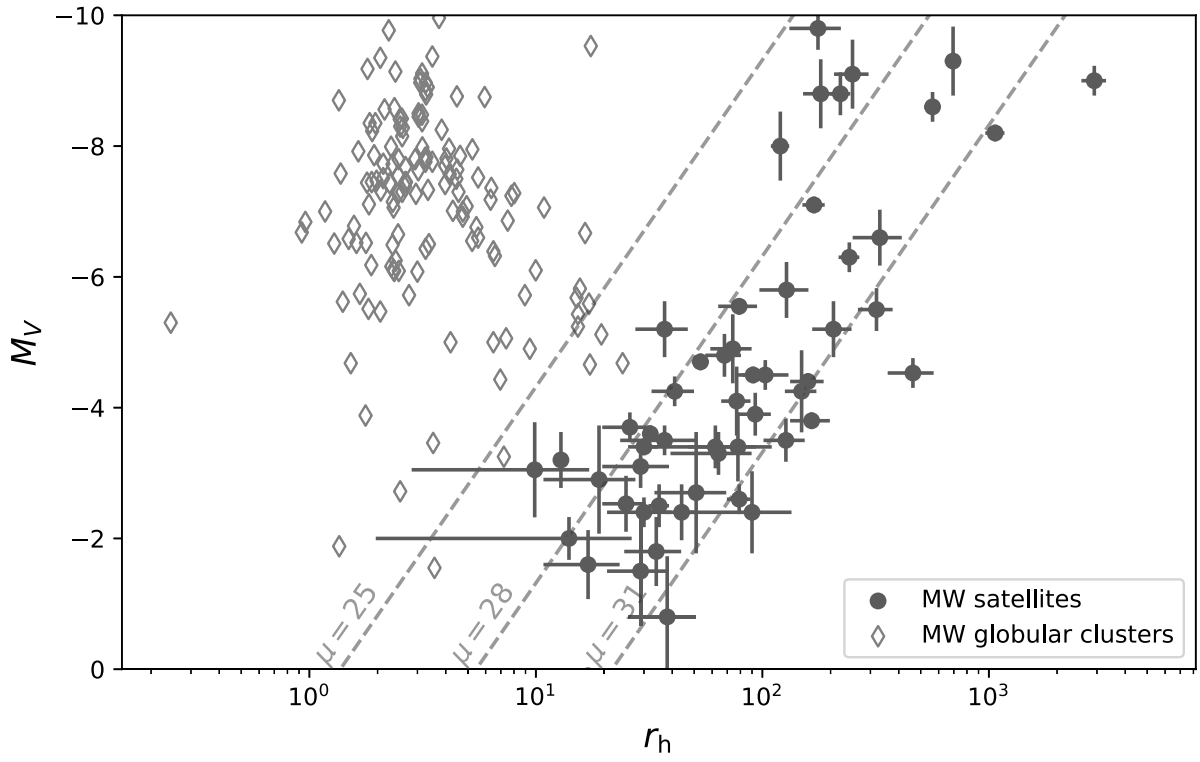

Figure I.4: Distribution of the MW and M31 dwarf galaxies in the size-luminosity space. As a comparison the MW GCs from Harris (1996) are represented by the grey diamond. Considering the magnitude range of the MW satellites, the distinction between GC and dwarf galaxy is ambiguous.

I.1.3 Detection limits and global properties

The advent of large, homogeneous photometric surveys has significantly expanded our knowledge of MW dwarf galaxies. The size of the sample of known dwarf galaxies enables comprehensive statistical analysis of the satellite system, allowing the derivation of global properties for comparison with cosmological and galaxy formation & evolution simulations. However, given that not all dwarf galaxies are detected, it is necessary to derive the completeness of the sample to robustly compare observations with prediction from models of galaxy formation & evolution. This tedious step is greatly facilitated thanks to the use of automatic detection tools. These tools offer quantifiable and consistently defined detection limits, surpassing the subjective nature of visual inspections. Nevertheless, the implementation of these tools necessitates extensive computational resources.

The first analysis of this kind focused on characterizing the detection limits of the SDSS survey (Koposov et al., 2008). This was accomplished by injecting simulated dwarf galaxies into the SDSS catalogue and subsequently identifying their detection using a match

filter algorithm. The completeness of the sample was then quantified as a function of the luminosity and size of the dwarf galaxies across various distance intervals, ranging from a heliocentric distance of 8 to 1024 kpc.

Since then, efforts have been made to characterize and publish the detection limits of the surveys leading to the discovery of new satellites (DES: Drlica-Wagner et al. 2020; Pan-STARRS: Laevens 2015), bringing the gap between observations and models and therefore enabling the use of satellite systems as cosmological and galaxy formation & evolution probes.

We now have a well populated and understand satellite system along with the detection limits associated. What can we learn from it ?

I.2 Satellite systems as cosmological and galaxy evolution probes

I.2.1 Galaxy formation in a ΛCDM context

The initial indication of "missing matter" was reported by Zwicky in 1933 (Zwicky, 1933). This discovery arose from the observation that the velocity dispersion of the Coma Cluster exceeded the threshold at which it could be gravitationally bound solely by accounting for baryonic matter. However, it wasn't until the 1970s that the concept of Dark Matter started to gain traction, following the discovery of missing mass required to explain the rotation curves of galaxies (Rubin et al., 1978). In the interim, the discovery of the Cosmic Microwave Background (CMB) (Penzias & Wilson, 1965) further solidified the view of a universe that was once hot and dense, and has since expanded over time. Consequently, in 1984, the ΛCDM theory emerged (Peebles, 1984; Turner et al., 1984), which was later reaffirmed by the measurement of the anisotropies in the Cosmic Microwave Background (CMB) (Smoot et al., 1991).

Currently, the ΛCDM model stands as the most widely accepted cosmological framework, composed primarily of two key components. Firstly, the cosmological constant from General Relativity (Λ) represents the presence of dark energy (Peebles, 1984; Turner et al., 1984), which is necessary to account for the accelerated expansion of the universe established by Riess et al. (1998) and Schmidt et al. (1998). Secondly, the Cold Dark Matter (CDM) which plays a pivotal role in galaxy formation, as galaxies are believed to form within haloes composed of dark matter (White & Rees, 1978). One consequence of the cold/massive nature of dark matter particles is the potential formation of extremely low-mass dark matter haloes (Loeb & Zaldarriaga, 2005; Bullock & Boylan-Kolchin, 2017). These haloes can not be formed if the dark matter particles were warmer/lighter. This highlights the significance of the cold dark matter hypothesis in explaining the observed structures and behavior of the universe at various scales.

In the ΛCDM model, the structures in the Universe are a consequence of primordial adiabatic fluctuations that occur prior to hydrogen recombination, when baryons and photons are in a state of quasi-equilibrium and are distributed nearly uniformly. Following

recombination ($\sim$ 380 000 years after the Big Bang), hydrogen atomes no longer experience radiation pressure, they gravitationally condense within the potential wells created by the dark matter halos (White & Rees, 1978) leading to the formation of molecular clouds. In turn, these processes lead to the rise of the first generation of stars and to the start of the Reionization era, which occurred approximately 100 million years after the Big Bang. Early stars are characterized by their high mass, low metallicity, and short lifetimes (Abel et al., 2002) and through the explosion of supernovae, they initiate the chemical enrichment of their immediate surroundings. The Reionization is a crucial stage in galaxy formation; as this era concludes, existing galaxies continue to evolve through star formation within dark matter halos and mergers, aligning with the concept of the hierarchical evolution of galaxies.

The ΛCDM model succeeded in describing the large scales structure of our Universe (Eisenstein et al., 2005), the CMB (Planck Collaboration et al., 2016), and the Big Bang nucleosynthesis (Planck Collaboration et al., 2016). However, apparent tensions arise when comparing expectation from the favored ΛCDM cosmological model and the observations of dwarf galaxies properties such as their numbers, their spatial distribution around their host, their sizes, their rotation curves, and the quenching of their star-formation (Bullock & Boylan-Kolchin, 2017; Sales et al., 2022). While cosmological predictions predominantly rely on dark matter simulations, comparisons with observations necessitate the incorporation of galaxy formation simulations. Consequently, such comparisons are challenging due to our limited understanding of the baryonic physics that governs the formation and evolution of galaxies. The process of star formation, for example, which directly impacts the properties of satellite systems, is influenced by various physical phenomena including reionization and stellar feedback (Bullock et al., 2000; Somerville, 2002; Mashchenko et al., 2008; Wheeler et al., 2015). Although the comparison of observational and simulation data for satellite systems is a complex endeavor, it serves as a perfect test to constrain and enhance our understanding of both cosmology and the physics of galaxy formation & evolution.

I.2.2 Comparing the MW satellite system with simulations

I.2.2.a Number of satellites

In 1999, the first comparisons between the observed number of satellites and the number of Dark Matter sub-haloes were conducted by Klypin et al. (1999) and Moore et al. (1999). Both studies highlighted a significant disparity between the hundreds of subhaloes found in Dark Matter simulations around hosts similar to the Milky Way and the mere $\sim$ 10 known MW satellites at that time (Figure I.5). Three type of solutions have been proposed:

- The first approach is observational in nature, as it is crucial to acknowledge the difficulties involved in detecting dwarf galaxies. Indeed, it is worth noting that a portion of the missing satellite galaxies is likely just undetected. Since 1999, approximately 40 new dwarf galaxies of the Milky Way have been discovered and more are still expected to be discovered (Koposov et al., 2008; Tollerud et al., 2008; Drlica-Wagner

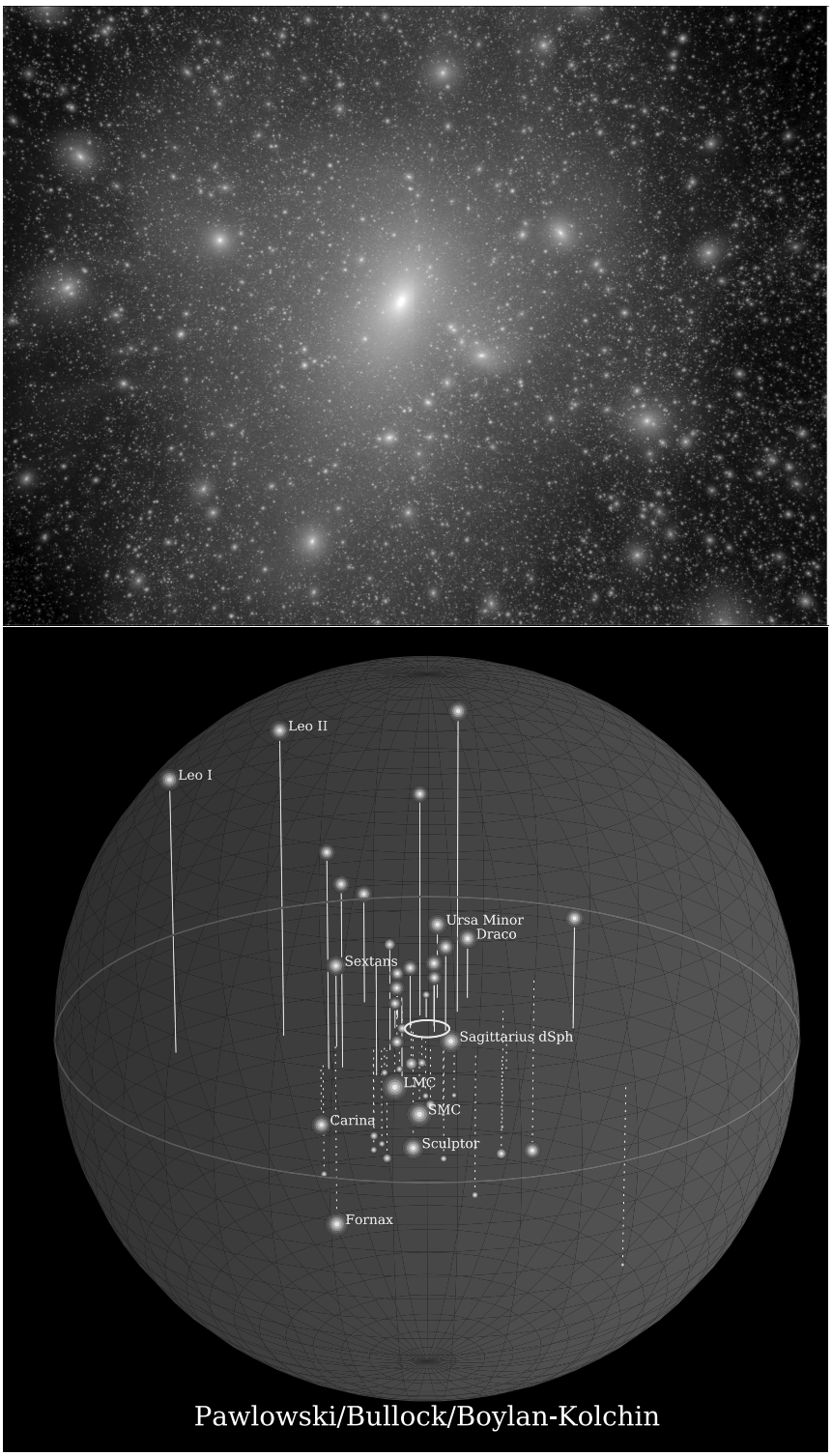

Figure I.5: *Top panel:* Dark Matter distribution in a MW-like halo from the Aquarius simulation at the present day (z=0). Each luminous dot represent a Dark Matter subhaloe. Credit : Springel et al. (2008). *Bottom panel:* Distribution of the $\sim$ 60 known satellites around the MW. Credit: Bullock & Boylan-Kolchin (2017).

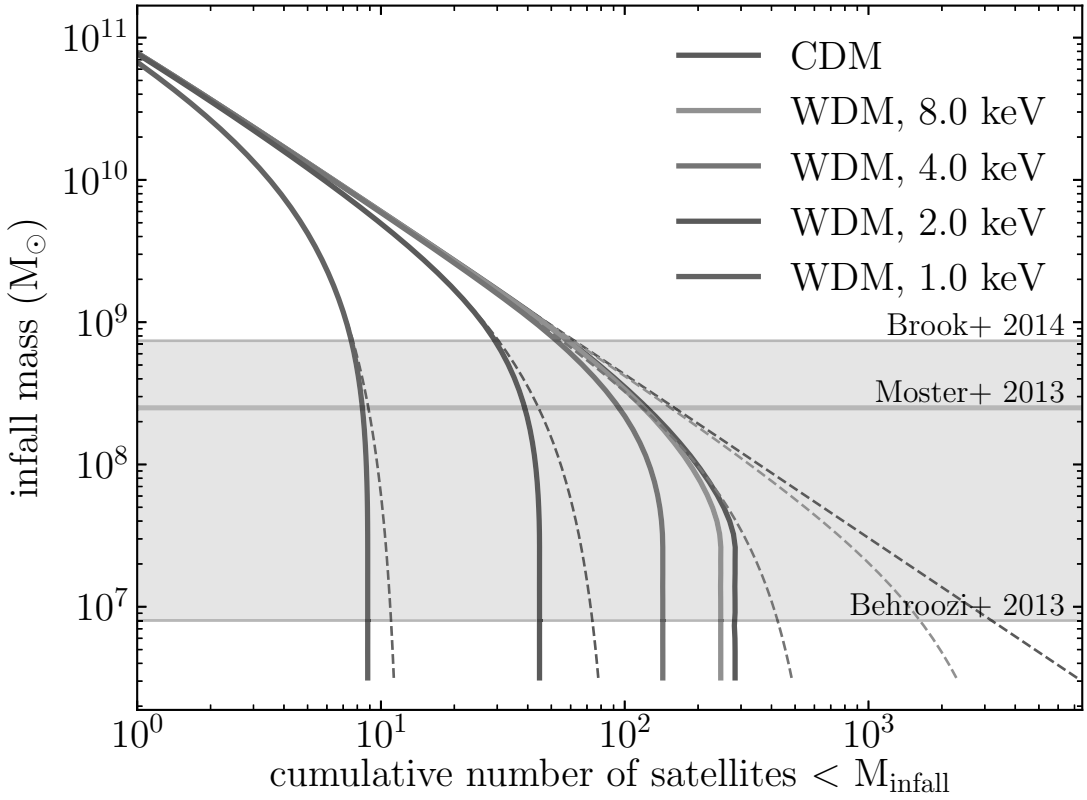

Figure I.6: The infall mass of luminous subhaloes (full lines) and total subhaloes (dashed lines) is presented as a function of their cumulative number. Different types of dark matter are distinguished by a color code, showing the impact of cosmology on the expected numbers of satellites. The same baryonic physics model is applied to all the simulations with different types of dark matter to derive the luminous fraction of subhaloes. The grey lines correspond to the various predicted infall masses for Segue I, highlighting the significance of baryonic physics on the properties of the satellites. Credit: Kim et al. (2018).

et al., 2020). Although this does not bridge the gap between the number of observed MW dwarf galaxies observations and the simulated number of dark matter subhaloes, it emphasizes the necessity of accounting for detection limits when making comparison.

- The second approach relies on baryonic physics to explain why a portion of subhaloes fails to "light up". The suppression of star formation is influenced by various phenomena, notably reionization and stellar feedback (Bullock et al., 2000; Somerville, 2002; Mashchenko et al., 2008; Wheeler et al., 2015). Since the magnitude of these processes

remains uncertain, it is possible to fine-tune the impact of these processes to enhance the suppression of star formation and, in turn, increase the number of Dark Matter subhaloes lacking a dwarf galaxy.

- The last approach arises from a cosmological perspective, as it involves altering the mass of Dark Matter particles, thereby influencing the projected number of Dark Matter subhaloes and, consequently, dwarf galaxies, as illustrated in Figure I.6.

Combining those approaches, studies have demonstrated that the observed count of dwarf galaxies can be compatible with the number of Dark Matter subhaloes identified in simulations (Koposov et al., 2009; Kim et al., 2018). Even with the lack of constraints on physical phenomena, the count of satellites remains a potent tool for investigating the mass of Dark Matter particles. This is achieved by considering diverse Stellar-Halo Mass Functions that incorporate varying degrees of stellar feedback processes and reionization. Through such approaches, constraints on the mass of the Warm Dark Matter (WDM) particule have been derived ($m_{WDM} > 4$ keV: Kim et al. 2018; $m_{WDM} > 6.5$ keV: Nadler et al. 2021). This is particularly promising with the advent of upcoming large surveys such as LSST and Euclid. These surveys hold great potential in uncovering a multitude of MW dwarf galaxies, thereby enhancing the constraints on cosmological models.

I.2.2.b Spatial Distribution

Dwarf galaxies, being born within the subhaloes of Dark Matter, offer valuable insights into the spatial distribution of Dark Matter. As a result, they serve as an important benchmark for cosmological and, galaxy formation & evolution simulations. Comparisons between the radial distribution of classical Milky Way satellites ($M_V \lesssim -8$) and Dark Matter Only (DMO) simulations have revealed a discrepancy: the brighter satellites display greater radial concentration compared to the larger subhaloes (Kravtsov et al., 2004; Lux et al., 2010; Yniguez et al., 2014; Carlsten et al., 2020). This observation is further reinforced by the overall radial concentration of the entire population of Milky Way satellites, which exceeds the predictions of simulations when assuming a reasonable Stellar-Halo Mass Function (Kim et al., 2018). This discrepancy may arise from the following causes:

- The incompleteness of the survey undoubtedly affects the observed radial distribution of satellites, however, it has been shown that detection limits alone cannot account for the disparities between observations and simulations (Kim et al., 2018; Carlsten et al., 2020).

- Reionization presents another potential solution, as it effectively halts star formation and, consequently, leads to the brightest haloes being formed earlier and located in closer proximity to the host (Font et al., 2011; Starkenburg et al., 2013). However, hydrodynamical simulations suggest that the influence of reionization on star formation

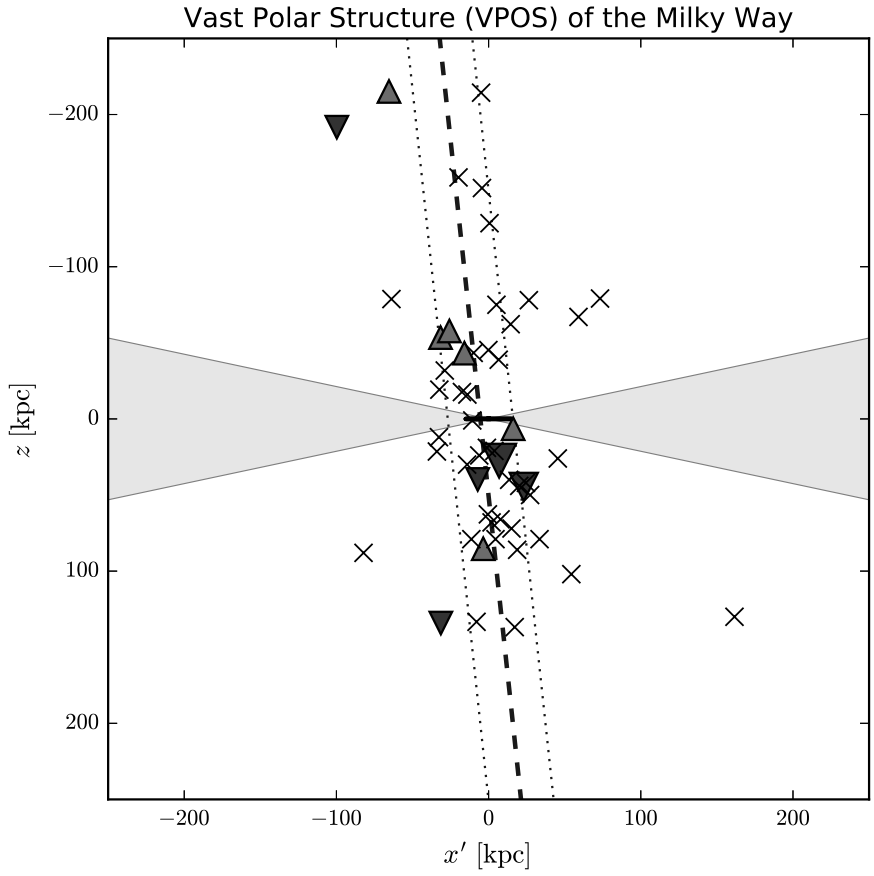

Figure I.7: The plane of satellites in the Milky Way (observed edge-on). The favored plane is represented by a dashed line indicating its orientation, while the dotted line denotes its width. Known satellites are marked by red triangles if they are approaching, blue triangles if they are receding, and crosses if their proper motions are unknown. The grey region highlights an area where the detection of dwarf galaxies is affected by the galactic foreground. Credit: Pawlowski (2018)

should not be significant within the mass range considered for classical dwarf galaxies (Ocvirk et al., 2016; Wheeler et al., 2019).

- The mechanism of tidal disruption of subhaloes by the host remains not entirely understood (Carlsten et al., 2020).

It is important to acknowledge that these comparisons may be influenced by an already peculiar spatial distribution of satellites. In fact, it is now widely recognized that a substantial portion of MW dwarf galaxies exhibit a thin planar co-rotating distribution (Figure I.7

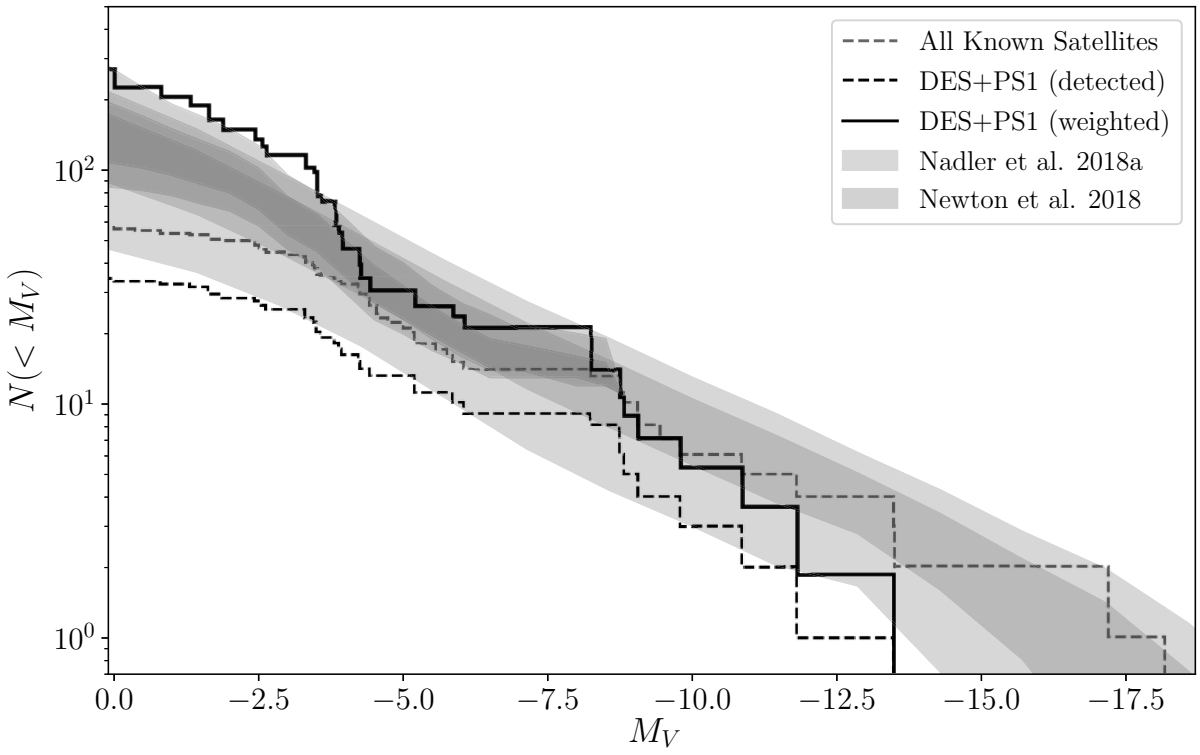

Figure I.8: Cumulative luminosity function of MW satellites. The known satellites are represented by the dashed grey line. Satellites detected in the DES survey are shown in the dashed black line. The luminosity function corrected for the observable volume is shown in the black full line. Credit: Drlica-Wagner et al. (2020)

Lynden-Bell, 1976; Kroupa et al., 2005; Metz et al., 2008; Pawlowski et al., 2012) even if the challenging nature of this feature to the ΛCDM framework is still debated (Pawlowski, 2021; Sales & Navarro, 2023; Sawala et al., 2023; Xu et al., 2023).

I.2.2.c Environmental impact

Most of the constraints on cosmology and the physics of galaxy formation & evolution have been derived through the study of Milky Way dwarf galaxy, given their accessibility. But, this satellite system may not be typical.

The MW satellite system might be merging with that of the LMC (Battaglia et al., 2022), a process that has a noteworthy influence on the properties of its satellite system. The presence of satellite galaxies brought by the merging galaxy indeed leads to an increase in the number of satellites for the host galaxy (Nadler et al., 2020; Joshi et al., 2023). This effect may provide an explanation for the bump observed at the faint end ($M_V > -5$) of the Milky Way luminosity function, as presented by the DES team (see Figure I.8; Drlica-Wagner et al.,

2020). Furthermore, this increase in satellites also impacts the observed radial distribution of satellites, as demonstrated by Carlsten et al. (2020), who showed that systems with an LMC-like dwarf galaxy exhibit a slightly more pronounced radial concentration.

Throughout this section, we have explored the significant impact of star formation suppression on the properties of a satellite population. When examining the quenching times of MW dwarf galaxies, Weisz et al. (2019) showed that all faint satellites were quenched 12 Gyr ago, while the more luminous ones experienced recent quenching events. In contrast, the quenching history of M31 dwarf galaxies exhibits a more extended star formation history (Savino et al., 2023). This difference in quenching patterns leads Weisz et al. (2019) to propose that the accretion history of the host galaxy plays a pivotal role in determining the properties of its dwarf galaxies.

Consequently, the properties of a satellite system are significantly shaped by the environment and merger history of its host galaxy. Considering that the Milky Way may not be representative of a typical system, it is crucial to explore diverse satellite systems. One of the most accessible systems for detailed study is our cosmic neighbor, M31, which lies within a distance of less than 800 kpc from the MW. This proximity enables us to resolve the dwarf galaxies of M31 into individual stars, providing a great second laboratory to test the cosmology and the physics of galaxy formation & evolution.

Tarsila do Amaral, A Lua, 1928

Chapter II

The M31 satellite system: a secondary testbed for cosmology and galaxy formation & evolution

II.1 The search for M31 satellites: from visual inspection to SDSS

The first recorded observation of a dwarf galaxy outside of the MW was made in 1654 by Hodierna. Hodierna (1654) report a cloud-like object near the Triangulum constellation, which was later rediscovered by Messier in 1764 (Messier, 1781). This object is now known as the Triangulum galaxy or M33 and is considered the brightest satellite of M31. In the 18th century, three other M31 satellites were also detected. NGC 221, initially discovered by Guillaume Le Gentil in 1749, was later classified as M32 in Messier's catalogue in 1781. Another satellite, NGC 205, was first discovered by Caroline Herschel and reported by William Herschel in 1785 (Herschel, 1785). Although Messier did not classify this dwarf galaxy initially, as it was present in his drawing of Andromeda's Nebula, it was later added to the list as M101. Lastly, NGC 185 was discovered by Herschel in 1787, followed in the 19th century by the discovery of NGC 147 by John Herschel and the discovery of IC10 by Lewis Swift.

The next discoveries of M31 dwarf galaxies did not occur until the late 20th century, thanks to the introduction of photographic plates. Although the search for M31 dwarf galaxies in the Palomar Sky Survey proved unsuccessful due to the distance and faintness of these objects, following the discoveries around the MW, new dwarf galaxies were expected to be present around M31. Therefore, new observations were conducted using a set of nine highly sensitive plates, leading to the detection of three new satellites: And I, And II, and And III (van den Bergh, 1972). Another significant finding was the identification of LGS 3, which was later recognized as the Pisces dwarf galaxy by Karachentseva (1976).

Following these discoveries, a span of 20 years elapsed before new dwarf galaxies were

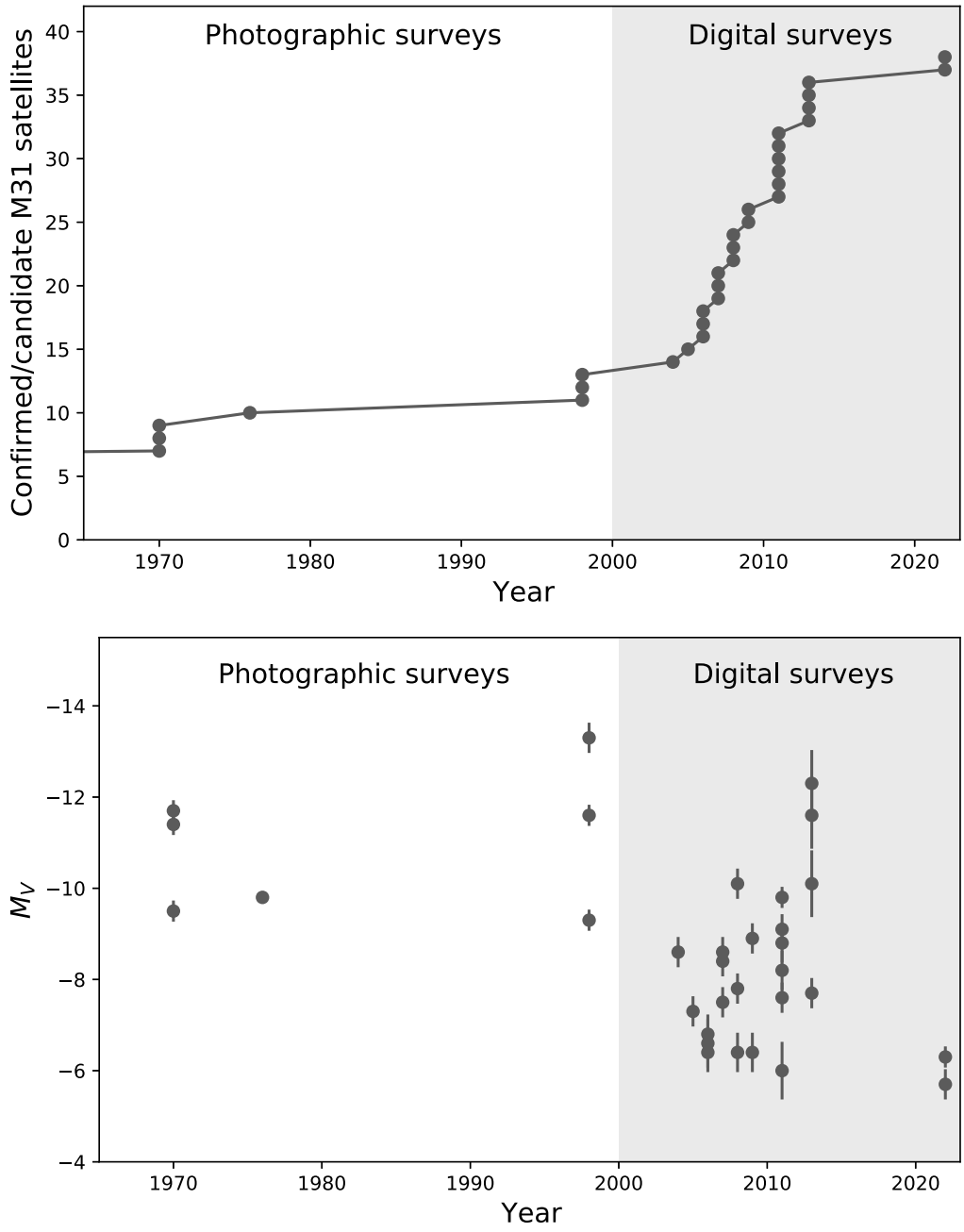

Figure II.1: *Top panel:* Number of confirmed/candidate M31 dwarf galaxies as a function of time. The sample size considerably increase with the advent of digital surveys going from 11 to $\sim$ 40 as of 2023. *Bottom panel:* Magnitude of the confirmed/candidate M31 dwarf galaxies as a function of time.

uncovered using the second version of the Palomar Observatory Sky Survey (POSS II). Utilizing the digitalized version of the survey and employing a match filter technique, Armandroff et al. (1999) successfully identified two previously unknown dwarf galaxies, namely And V and And VI. Meanwhile, Karachentsev & Karachentseva (1999) employed a morphological criteria on the POSS II, leading to the discovery of And VI and And VII. These significant findings increased the total count of M31 dwarf galaxies to 11, which is comparable to the number observed in the MW at that time. The first comparative analysis of the satellite systems of the MW and M31, conducted in Armandroff (1994) revealed similarities in the properties of their dwarf galaxies. Notably, these galaxies followed the same size-luminosity and luminosity-metallicity relations. Consequently, the author suggested that despite the different masses of the two hosts, they both offered a somewhat similar environment for the formation and evolution of satellites.

Similarly to the search for dwarf galaxies around the MW, the advent of large homogeneous photometric survey led to a significant increase of M31 known satellites (Figure II.1). Over the span of ~ 10 years, the SDSS survey led to the discovery of 4 new dwarf galaxies as faint as $M_V = -8.1 \pm 0.5$ (And IX, And X, And XXVIII, And XXIX; Zucker et al., 2004a, 2007; Bell et al., 2011; Slater et al., 2011). In the meantime, two more fortuitous discovery were made by Irwin et al. (2008) and Majewski et al. (2007). Nonetheless, the most substantial advancement in our understanding of the M31 satellite system, and more generally of the M31 halo, emerged through the Pan-Andromeda Archaeological Survey (PAndAS).

II.2 Probing M31 halo through PAndAS

II.2.1 A brief technical overview

In 2001, Ibata et al. (2001) conducted a survey using the 2.5 m Isaac Newton Telescope (INT) with the aim to investigate the region within approximately 55 kpc from M31. This survey resulted in the discovery of the Giant Stellar Stream (Ibata et al., 2001; Ferguson et al., 2002). Around the same time, significant progress was made in the study of gas and star streams in the Milky Way (Ibata et al., 1997), revealing an active evolution through mergers with satellite galaxies. The discovery of the Giant Stream in M31 confirmed this perspective on galaxy evolution and prompted a careful follow-up survey using the 3.6m Canada-France-Hawaii Telescop (CFHT) with MegaCam to map the whole stream (Ibata et al., 2007). Due to the abundance of substructure unveiled during this survey, it was ultimately transformed into the official PAndAS survey. New observations were made with the CFHT/MegaCam to map a region within ~ 150 kpc of M31 and ~ 50 kpc of M33. The footprint of the survey is represented in Figure II.2.

While a more in depth description of the survey can be found in Ibata et al. (2014) and McConnachie et al. (2018), I will give here a quick overview of its design. PAndAS observed over 400 fields of ~ 1 deg^2 in the g and i-band with the MegaCam instrument. The layout

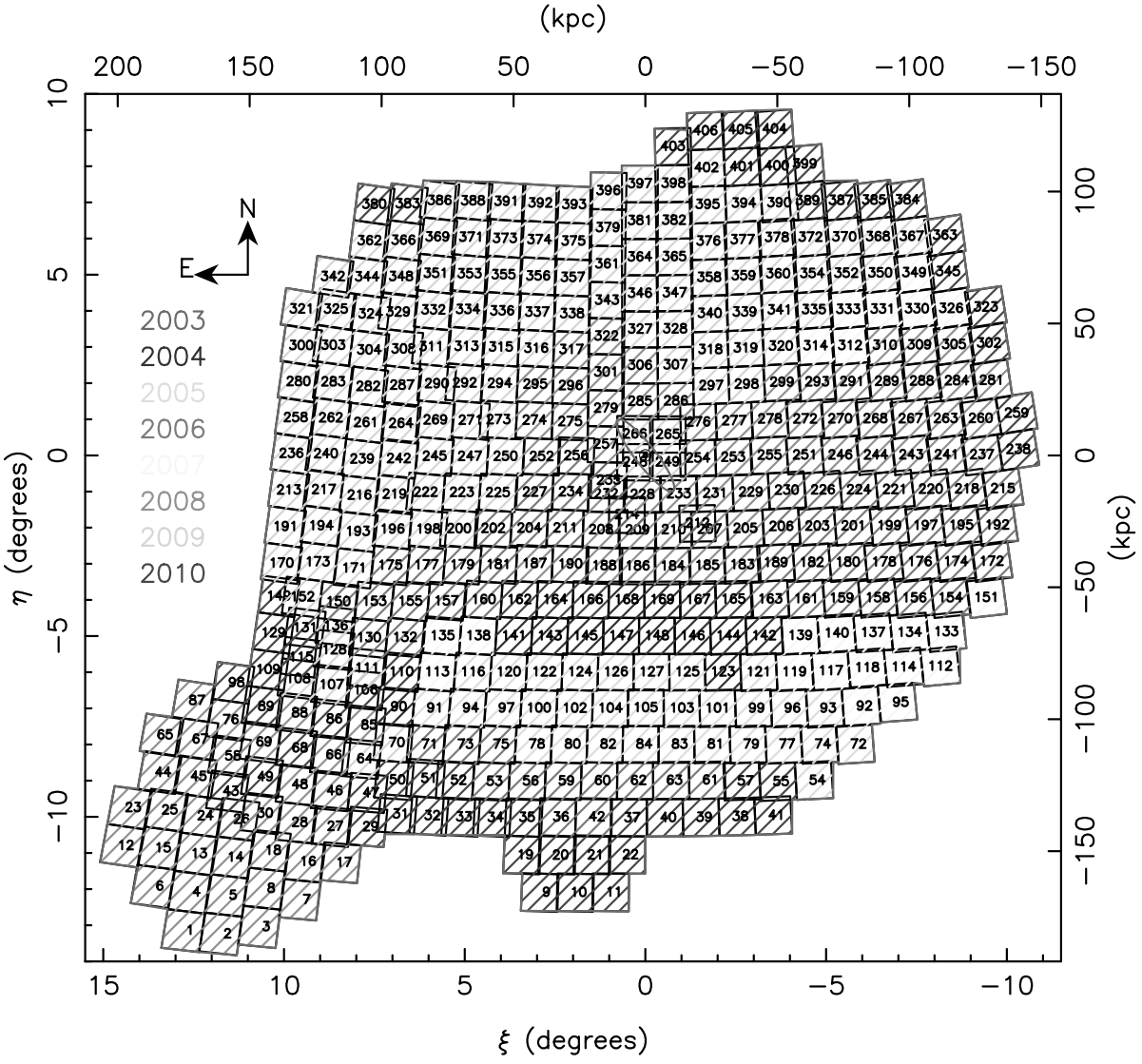

Figure II.2: Footprint of PAndAS as a function of time for the i-band imaging. Each 406 square is a field in the survey. The footprint and observation timeline for the g-band are nearly identical. The red ellipse is used to depict the M31 disk. The extensive coverage includes over 400 deg^2, strategically centered on M31 and its companion M33, allowing for a comprehensive exploration of their surroundings. Credit: Ibata et al. (2014).

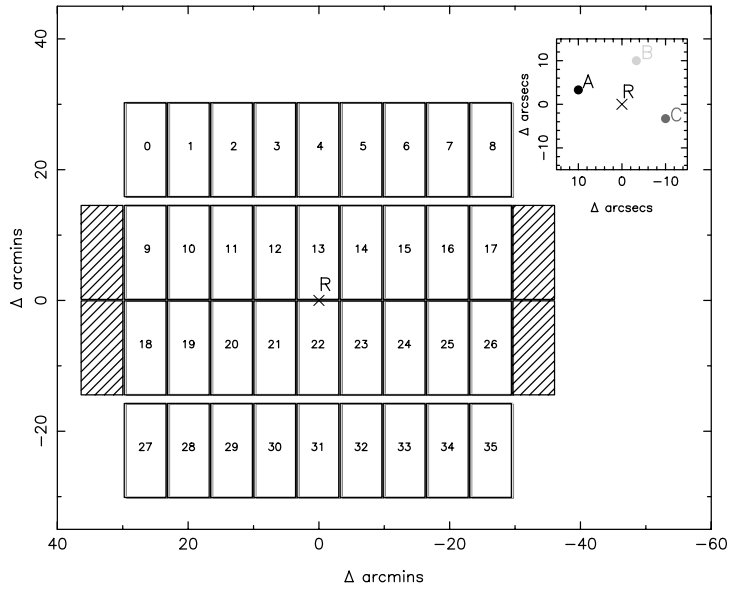

Figure II.3: Layout ouf the 36 CCDs of the CFHT/MegaCam instrument. Each field within the survey underwent three exposures, and the resulting footprints are represented with the colors associated with their centers (A, B, C) that are represented in the top right panel. While the small gap within a range of CCD are filled by the different exposures, the chip gap between two range of CCD are still present. Credit: McConnachie et al. (2018).

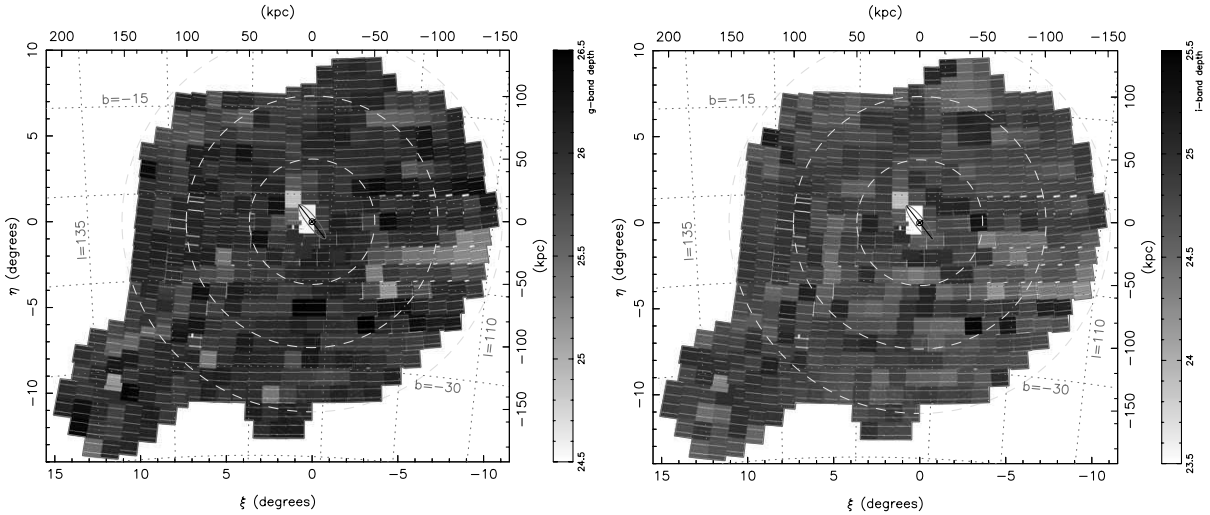

Figure II.4: *Left Panel*: Map of the 5σ photometric depth for the g-band. *Right Panel*: Map of the 5σ photometric depth for the i-band. In both panel, The red ellipse is used to depict the M31 disk and the dashed blue circle delimit the regions within 50, 100 and 150 kpc from M31. It is worth noting that the depth are quite homogeneous over the all survey despite small variation. Credit: Ibata et al. (2014).

of MegaCam and its 36 CCDs are shown in Figure II.3. Each field of the large program was observed through 3 exposures of 450s taken at 3 slightly different positions. As highlighted in Figure II.3, this shift in position is sufficient to cover the gaps within a chips gaps within a range of CCD but not between rows.

The photometry was corrected for extinction using the maps of by Schlegel et al. (1998) and refined by Schlafly & Finkbeiner (2011). PAndAS conducted a deep photometry in both the g and i-bands, benefiting from excellent conditions (median seeing of $0.67''$ for the g-band and $0.60''$ for the i-band). This resulted in a 5σ depth of 26.0 for the g-band and 24.7 for the i-band. Figure II.4 displays a map of the point source completeness, illustrating a consistent survey depth despite minor variations.

II.2.2 The current view of M31 halo structures

Figure II.5 presents a composite image comprising red, green, and blue maps of RGB stars, which individually correspond to stellar populations with [Fe/H] values of -0.7, -1.4 and -2.3, respectively. The numerous and various structures within the halo are visually enhanced by the image metallicity gradient. Consequently, distinct streams become apparent, with the most prominent being the Giant Stream (red color). Additionally, most of the known dwarf galaxies are also identifiable as green and blue dots.

The wealth of M31 halo structure is summarized in Figure II.6. A total of 13 stellar substructures have been identified in previous studies (Ibata et al., 2001; Ferguson et al., 2002; Zucker et al., 2004b; Ibata et al., 2007; McConnachie et al., 2009). Subsequent investigations from Ferguson et al. (2005), Richardson et al. (2008) and Bernard et al. (2015) have revealed that the Giant Stream, Western Shelf, and Eastern Shelf are potentially linked to the same accretion event, supported by their similar stellar populations to that of the Giant Stellar Stream. On the other hand, Andromeda Northeast and the G1 clump exhibit a disk-like stellar population, suggesting they may have formed due to disk heating or disruption resulting from the interaction between M31 and a satellite (McConnachie et al., 2018). Therefore, these five substructures likely originated from the same merger event. Notably, McConnachie et al. (2018) proposed that a minimum of five events, including the M33 and NGC147/185 interaction, the GSS, K1, and K2 event, are necessary to account for the observed PAndAS view of the M31 halo.

The PAndAS survey has also significantly contributed to expanding our knowledge of globular clusters (GC) within the M31 halo (Huxor et al., 2004, 2008, 2014). Indeed, in Mackey et al. (2019) the number of known clusters was reported to be as high as 92 and a significant portion, ranging from 35% to 60%, of these clusters exhibited spatial correlation with stellar substructures and thus appear to have been accreted through recent mergers. Furthermore, according to McConnachie et al. (2018), the abundance of globular clusters observed in the PAndAS survey implies two possibilities: either a series of multiple mergers involving more massive progenitors than what the luminosities of their remnants indicate, or

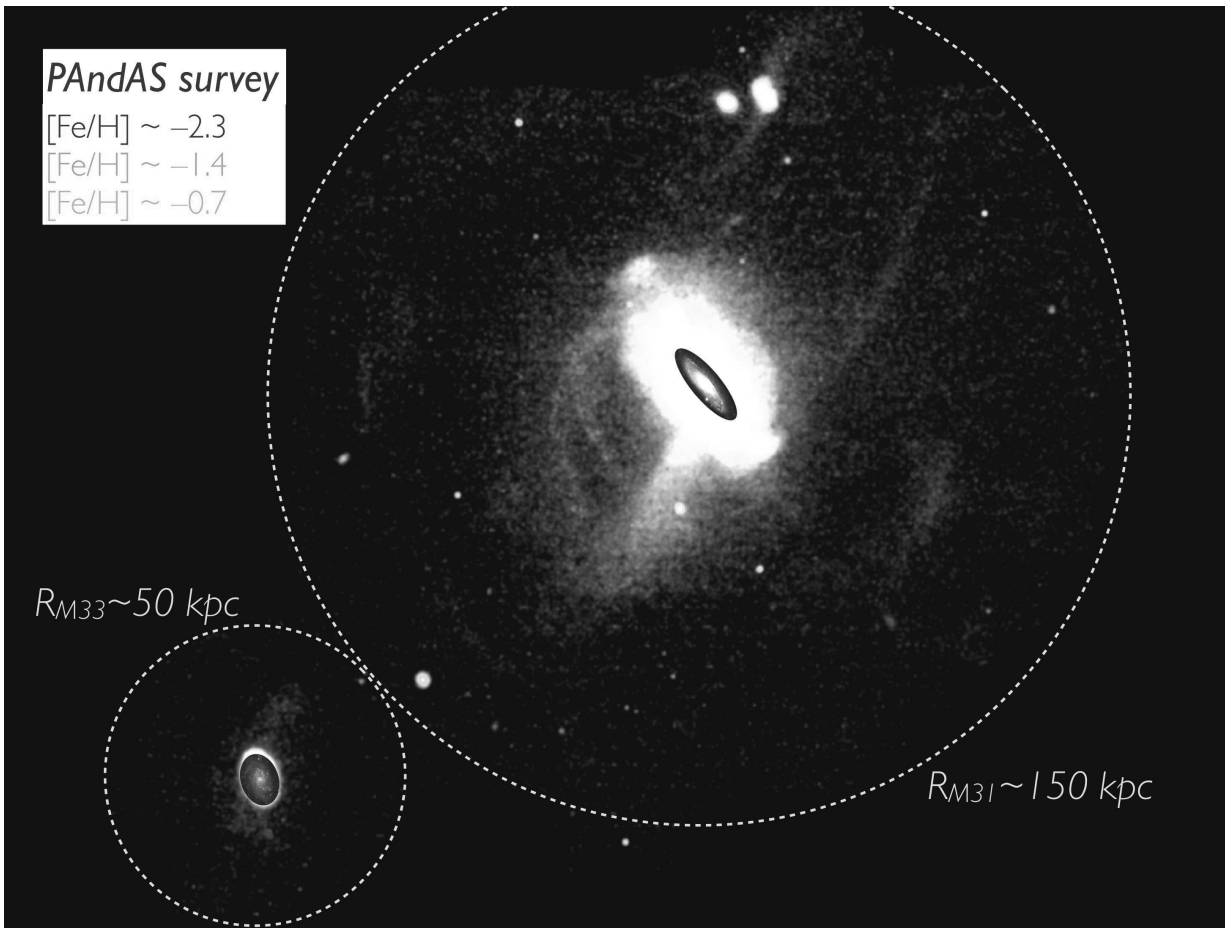

Figure II.5: Distribution of RGB stars in the PAndAS survey, color coded by the metallicity. Stellar populations with an [Fe/H] of -0.7, -1.4 and -2.3 are respectively in red, green and blue. The color intensity scale with the density. Credit: Martin et al. (2013a).

a merger with a single, large progenitor.

The PAndAS survey played a pivotal role in expanding our understanding of the M31 dwarf galaxy population, effectively doubling the number of known satellites by enabling the discovery of 19 previously unidentified companions through visual inspections and match filter technics (Martin et al., 2006; Ibata et al., 2007; McConnachie et al., 2008; Martin et al., 2009; Richardson et al., 2011). These discoveries have significantly expanded our understanding of M31 satellites as PAndAS has enabled the detection of fainter satellites, with the faintest one being And XXVI, with an absolute magnitude of $M_V = -6.0^{+0.7}_{-0.5}$ (Richardson et al., 2009; Martin et al., 2016; Savino et al., 2022). However, due to the distance of M31 and its satellite, it is difficult to detect satellites as faint as the low-luminosity one of the MW. Therefore, in the case of M31, there is still a clear distinction between dwarf galaxies and GCs as shown in the Figure I.4. To delve further into the noise, the PAndAS team developed

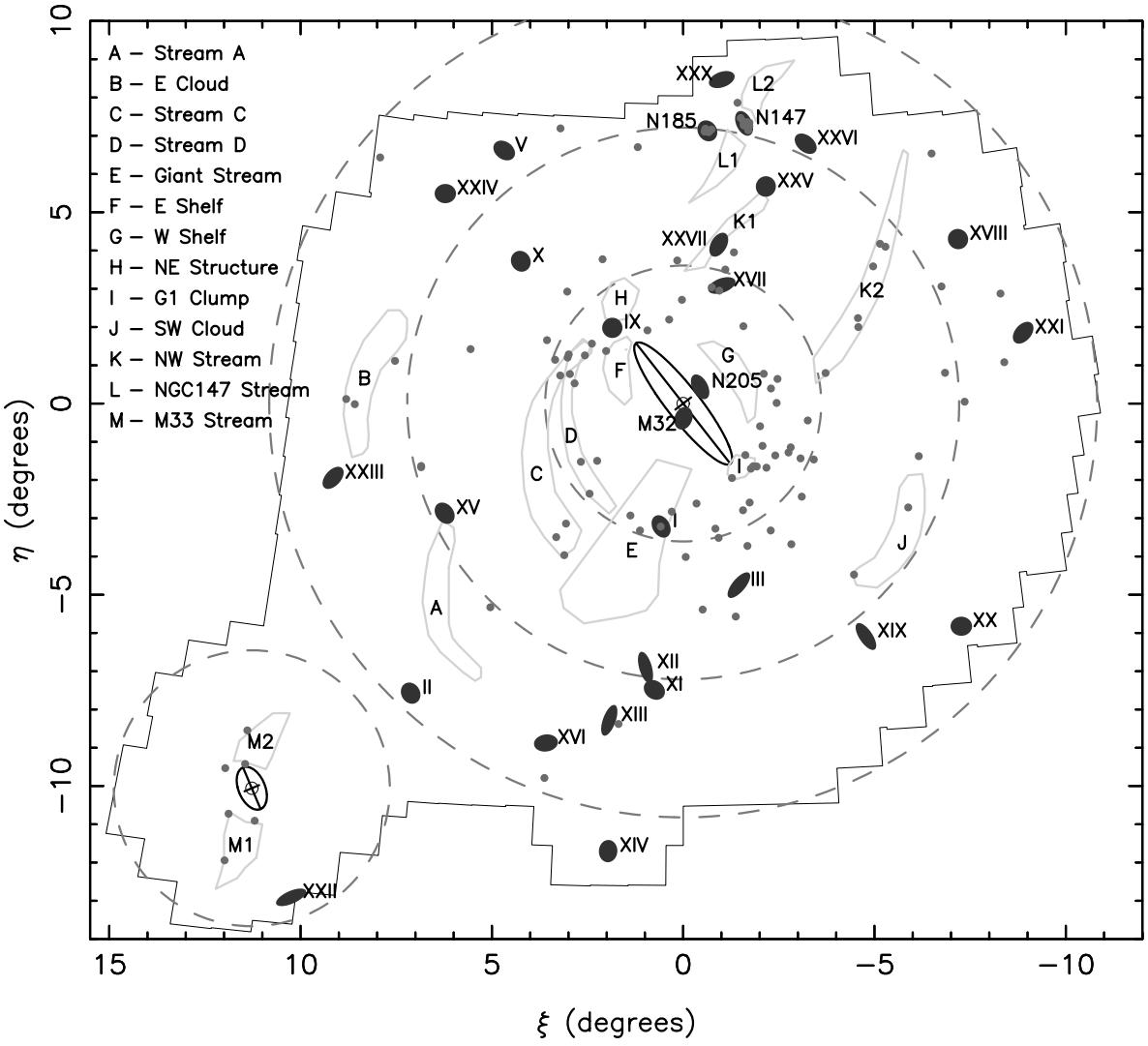

Figure II.6: Schema of the most prominent substructures in M31 halo as seen by PAndAS. The blue ellipses correspond to dwarf galaxies, the green polygons represent stellar substructures, and the red dots indicate globular clusters. The dotted pink circles delimits regions within 50, 100, and 150 kpc from M31 and 50 kpc from M33. Credit: McConnachie et al. (2018).

an automatic Bayesian search algorithm, which was introduced in Martin et al. (2013a) and is detailed in the Chapter III, together with the resulting candidates dwarf galaxies.

The spatial distribution of M31 dwarf galaxies as found in PAndAS unveiled some questions as the surface density of satellites on the sky appear to be flat (McConnachie et al., 2009). Furthermore, similarly to the MW, Ibata et al. (2013) revealed a plane-like distribu-

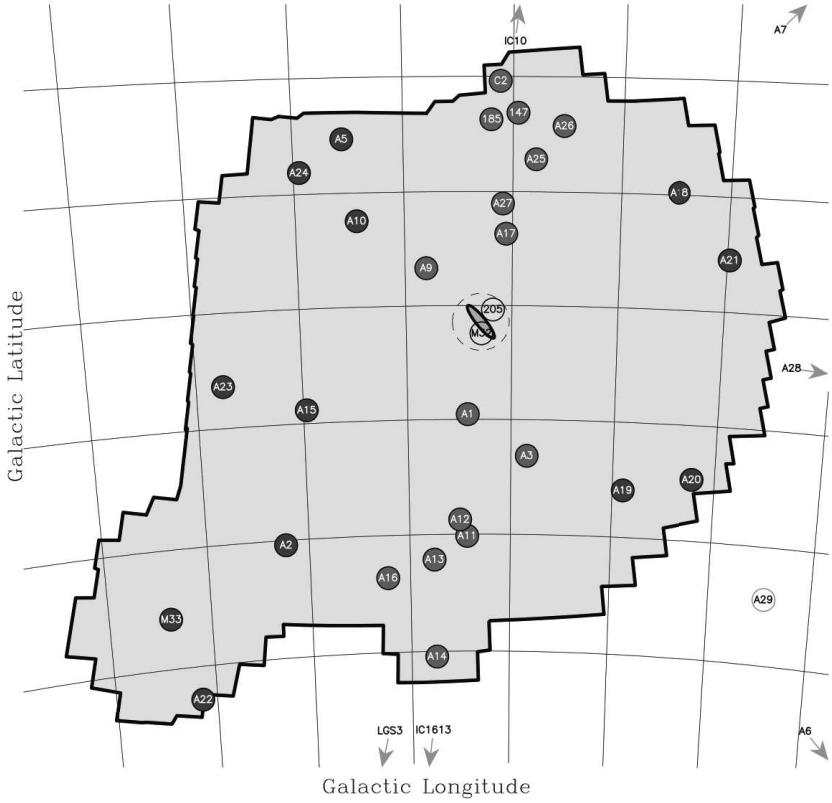

Figure II.7: Map of the M31 dwarf galaxies (full circle) position in the PAndAS survey. Satellites in red are found to be in a plane-like spatial distribution. Credit: Ibata et al. (2013).

tion for 15 dwarf galaxies around M31 (Figure II.7). Among this sample of satellites, 13 of them exhibit co-rotation. Pawlowski et al. (2013) also identified a comparable plane distribution, consisting of 19 dwarf galaxies, which he referred to as the Great Plane of Andromeda (GPoA). Furthermore, Santos-Santos et al. (2020) discovered a plane perpendicular to the GPoA, encompassing 18 satellites. However, analyzing the transient aspect of these distributions proves challenging due to the lack of proper motion measurements for most satellites. Nonetheless, Sohn et al. (2020) suggest that the system may exhibit dynamic coherence, as indicated by their determination of the proper motion of NGC 147 and NGC 185. In any case, the presence of these planes of satellites in Andromeda reinforces the notion that the distribution of dwarf galaxies around their host may not be isotropic.

An additional peculiar aspect of the distribution of M31 satellites is highlighted by McConnachie & Irwin (2006). Remarkably, the majority of M31 companions are situated between M31 and the MW. This anisotropic pattern was further confirmed by Conn et al. (2012) via the determination of the TRGB distances and Savino et al. (2022), who reassessed

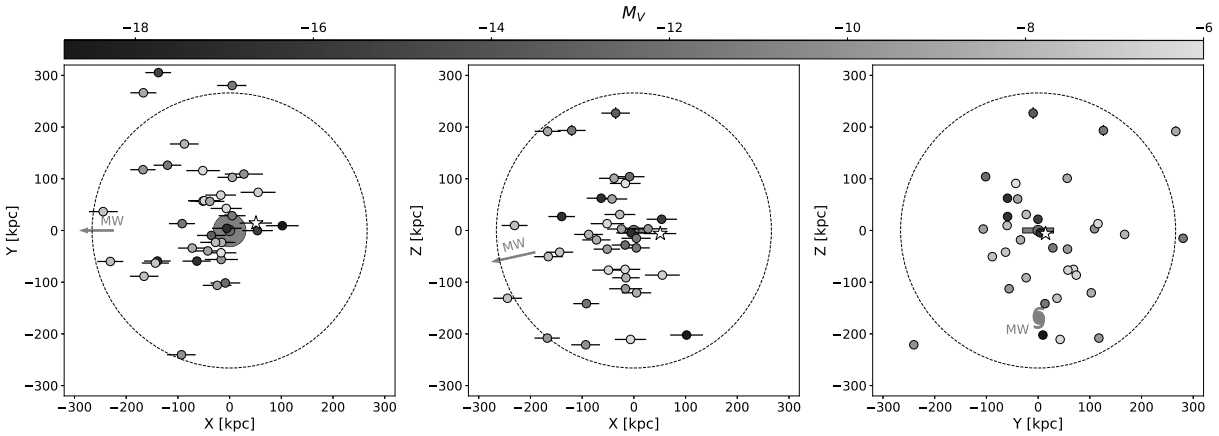

Figure II.8: Spatial Distribution of M31 dwarf galaxies in a cartesian coordinates system where the XY-plane corresponds to the M31 disk and the Z-axis points towards M31's north galactic pole. The color code the magnitude of the satellites. The dashed circle delimit a region within 266 kpc of M31. It is noteworthy that most of M31 dwarf galaxies are located in the hemisphere between the MW and M31. Credit: Savino et al. (2022).

the distances to the dwarf galaxies using RR-Lyrae stars, leveraging deep observations from the Hubble Space Telescope (HST). Figure II.8 display the anisotropic spatial distribution of M31 satellites as found with the new distances. The distinctive nature of this distribution raises questions not only about cosmology, as it deviates from the typical ΛCDM expectations, but also about the physics of galaxy formation & evolution. It could potentially indicate that M31 is not at the center of its satellite system, similar to the positional shift expected in the Milky Way due to the presence of the LMC or that a significant portion of M31's satellites have been recently accreted, resulting in them not being phase-mixted.

There was an expectation to discover numerous faint dwarf galaxies in the vicinity of M33, similarly to what is observed around the LMC. However, the sole satellite candidate found around M33 is And XXII. This observation aligns with a scenario involving a past encounter between M31 and M33, as most of M33's satellites may have been stripped away (Chapman et al., 2013). Nevertheless, the occurrence of such an interaction is subject to debate. On the one hand, some evidence suggests that a previous close interaction took place, leaving a distinct signature in the star and gas distribution of M33 (McConnachie et al., 2009; Putman et al., 2009; Semczuk et al., 2018). On the other hand, the kinematics of M33 and M31 seem to support a scenario in which M33 and M31 have not yet interacted or had an interaction approximately 6 billion years ago, with a minimum distance of 100 kpc (Patel et al., 2017; van der Marel et al., 2019). Nonetheless, research conducted by Patel et al. (2018) demonstrated that considering the coverage and detection limits of the PAndAS survey, the limited number of M33 satellites is not inconsistent with the expectations derived from ΛCDM.

The PAndAS survey has yielded a multitude of discoveries regarding the composition of the M31 halo, providing an exceptional opportunity to explore its formation history. Subsequent to these findings, various merger scenarios have been proposed to elucidate the observed features within the M31 halo. Hammer et al. (2018) report that the M31 disk is consistent with a 4:1 merger event occurring approximately 1.8-3 Gyr years ago. In parallele, D'Souza & Bell (2018) propose a predominant single merger event around 2 billion years ago involving a satellite with a stellar mass of approximately 2.5×10^{10} M$\odot$, with M32 being the remnant of the merging dwarf galaxy. This merger event provides an explanation for the M31 inner rotation, the presence of the Giant Stream, and the burst of star formation in M31 approximately 2 Gyr ago.

II.3 Towards a characterization of M31 satellite system

As previously stated, satellite systems serve as powerful tools to investigate both cosmology and the physics of galaxy formation & evolution. However, studying dwarf galaxy systems in detail around hosts with diverse environments and merger histories is challenging due to the difficulty in detecting these objects. Fortunately, the emergence of large, homogeneous photometric surveys like SDSS and particularly PAndAS has substantially increased the number of known dwarf galaxies around M31, enabling us to conduct a rigorous statistical study of this satellite system. Given the apparently active history of M31, such studies have the potential to enhance our understanding of the impact of host merger history on dwarf galaxies, but also to better constrain the impact of baryonic processes and the Dark Matter properties. The motivation behind my work stems from the necessity to determine the properties of the M31 satellite system while taking into account the incompleteness of the dwarf galaxy sample. This a crucial step to compare observed and simulated dwarf galaxies, as well as to enable comparisons among different satellite systems.

Chapter III describes the search algorithm developed by Martin et al. (2013a) to identify faint satellites in the PAndAS survey, as well as the modifications I implemented to determine the completeness of the PAndAS dwarf galaxy sample.

Chapter IV presents the determination of accurate detection limits for the search for dwarf galaxies in the PAndAS survey.

Chapter V provides a detailed account of the statistical framework designed to derive the global properties of the M31 satellite system, while effectively incorporating the detection limits. Furthermore, this analysis presents and discusses the various properties derived from the study, including the number of dwarf galaxies, their radial distribution, luminosity function, and their size-luminosity relation. Finally, I study the impact of detection limits on the observed anisotropy of M31 satellites.

In *Chapter VI*, given the possibility of a positional shift of M31 as a potential explanation for the peculiar distribution of its dwarf galaxies, I infer the position of the center of the satellite distribution to test its compatibility with the center of M31.

I provide a comprehensive summary of my work in *Chapter VII*. Subsequently, I present a comparative analysis of the satellite systems of M31 and the MW, highlighting their similarities and differences. Finally, I suggest potential direction for future research.

Van Gogh, De sterrennacht, 1889

Chapter III

PAndAS search algorithm

III.1 Introduction

In the last century, the search for dwarf galaxies was achieved by visual inspection of photographic plates, such as the Palomar Observatory Sky Survey or more localized observations probing the surrounding of M31. During 50 years, this tedious search led to the detection of $\sim$ 20 satellites in the Local Group (Shapley, 1938b; Wilson, 1955; van den Bergh, 1972). However, this approach has a clear limitation: the surface brightness of the dwarf galaxy must be sufficiently high to be observed (e.g., <25.5 mag.arcsec^2 for the second Palomar Observatory Sky Survey; Whiting et al., 2007). While the potential for further discoveries using existing photographic plates was thought to be rather limited, (Irwin et al., 1990) discovered Sextans through the pioneering use of an automated search algorithm. The images were processed by a fast measuring machine into a catalogue of resolved stars, which was then scanned in order to find spatial stellar overdensities.

Later, with the advent of large-scale, homogeneous, photometric surveys (e.g., SDSS, Pan-STARRS, DES, PAndAS; Abazajian et al., 2003; Chambers et al., 2016; Abbott et al., 2018; McConnachie et al., 2018), more complex automated search algorithms were developed to tackle the vast amount of data and the need to uncover fainter dwarf galaxies. Furthermore, the automation of the satellite search allows us to determine precise detection limits (Koposov et al., 2008; Drlica-Wagner et al., 2020; Doliva-Dolinsky et al., 2022), which are necessary for a robust comparison between observations of satellite systems and their counterparts in simulations.

The search for dwarf galaxies encompasses a variety of techniques, all of which revolve around the identification of local overdensities of old, metal-poor stars. Match filter algorithms have largely been used to discover dwarf galaxies in SDSS, Pan-STARRS and DES (Willman, 2005; Willman et al., 2005; Grillmair, 2006; Zucker et al., 2006; Belokurov et al., 2007; Walsh et al., 2009; Laevens et al., 2015; Bechtol et al., 2015; Kim & Jerjen, 2015; Koposov et al., 2015; Torrealba et al., 2016a). In its simplest form, a filtered stellar

catalog is obtained from the selection of stars thanks to a color-magnitude cut (i.e., ranging from a broad selection box to isochrones filters) that is then spatially binned or smoothed with a search kernel to find stellar overdensities (Koposov et al., 2008; Walsh et al., 2009). While the efficiency of such algorithm considerably improved the search for dwarf galaxies, maximum-likelihood-based matched-filter algorithms (Kepner et al., 1999; Rockosi et al., 2002) were needed to overcome the binary selection of stars imposed by a color-magnitude cut and to directly account for the contamination (Grillmair, 2006; Bechtol et al., 2015). This more complexe and model dependent version rely on the determination of the surface stellar density of an old and metal poor stellar population through the fit of a stellar distribution model.

At first, dwarf galaxies discovered in the PAndAS survey were spotted as overdensities of RGB stars (Martin et al., 2006; Ibata et al., 2007; McConnachie et al., 2008) or on matched-filter surface density maps of old, metal poor stars (Martin et al., 2009; Richardson et al., 2011). Later, to dig deeper into the noise and detect fainter satellites, the PAndAS team released a new search method that relies on the forward modeling of the distribution of sources in the color-magnitude diagram and in space to identify stellar overdensities (Martin et al., 2013a). One of the advantages of this algorithm is that it accounts for the contamination from MW stars, M31 stellar halo and red background galaxies. This automated tool is the basis for determining precise detection limits for M31 dwarf galaxies (further developed in Chapter IV), a necessary step in levelling the observed properties of a satellite system for subsequent comparison with simulations. In this Chapter, I propose to describe this tool, as designed by the PAndAS team (Martin et al., 2013a) and its updated version I implemented to obtain the recovery fraction of dwarf galaxies. This chapter is structured as follows: Section III.2 present the dataset used. Section III.3 details the method and model while Section III.4 present and discuss the results. Finally, Section III.5 presents the updated version of the search algorithm.

III.2 Dataset

The search algorithm was initially developed to dig for faint M31 satellites in the PAndAS survey (McConnachie et al., 2018). Although originally designed for this particular dataset, the method is applicable to other surveys and other satellite systems. A detailed description of the PAndAS survey can be found in Section II.2. However, it is important to emphasize that in this analysis, any holes resulting from CCD failures, saturation due to bright stars, CCD gaps, or misalignment between fields were filled using information obtained from neighboring regions. Additionally, in cases where there is an overlap between fields, the data acquired with the best seeing conditions are retained. Furthermore, the crowded areas surrounding M31, M33, NGC 147 and NGC185 are masked, as the stellar contamination from these galaxies would hinder the detection of a new satellite.

Only objects morphologically classified as stars in both the g and i bands are selected

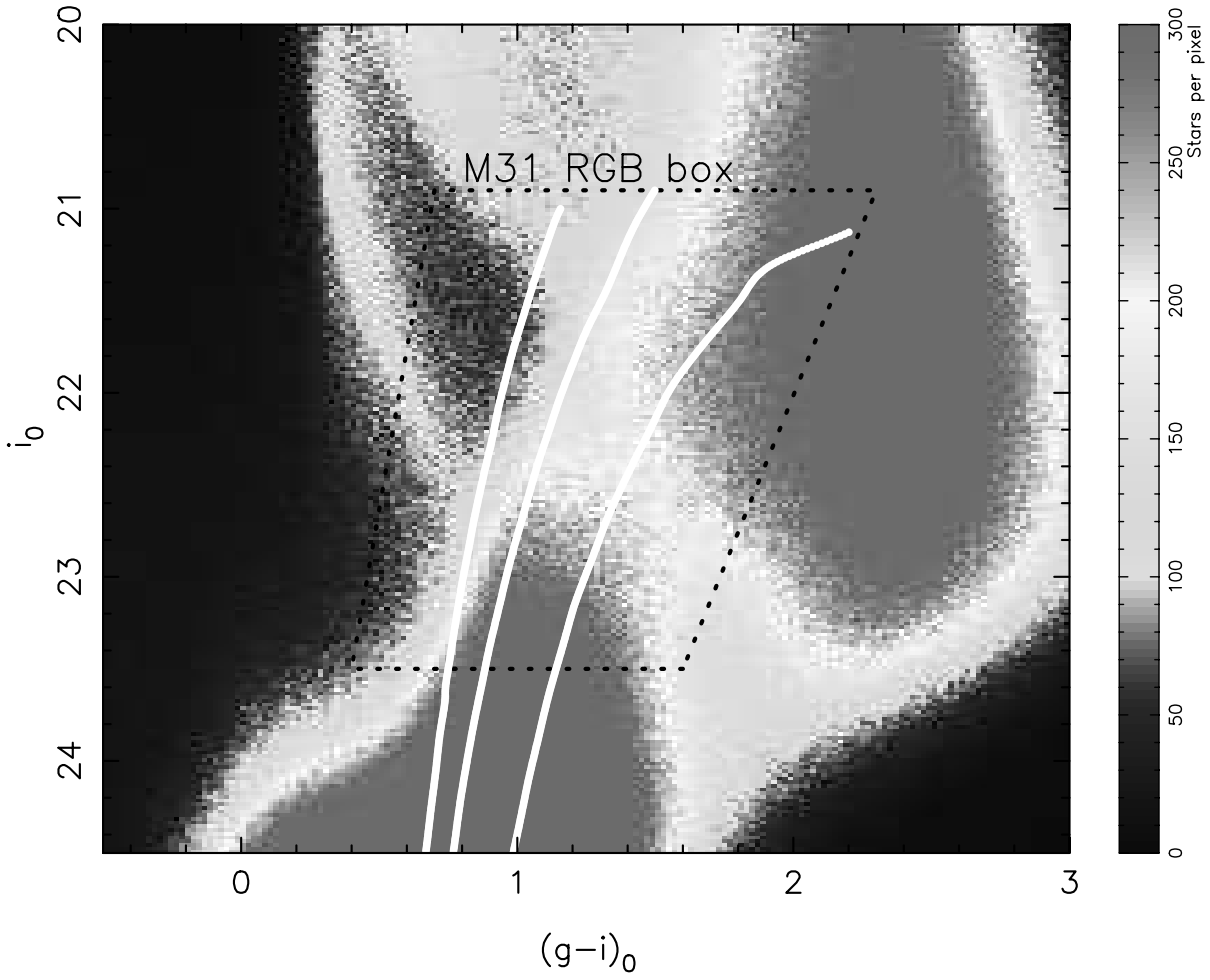

Figure III.1: CMD of all non-masked stellar sources in the PAndAS survey (i.e., located away from the crowded regions around M31 and its brightest satellites). The color gradient indicates the density of stars. Overlaid are the isochrones (Marigo et al., 2008) of stellar populations at the distance of M31, with ages of 13 Gyr and [Fe/H] of −2.3, −1.4 and −0.7 dex (from left to right). To target old, metal poor stars a selection box denoted by a black dotted line is used. Figure credit: Martin et al. (2013a).

from the PAndAS catalogue. Their apparent magnitude is then corrected for extinction using the E(B-V) maps from Schlegel et al. (1998) and the conversion coefficient from Schlafly & Finkbeiner (2011). As the search algorithm aims to find overdensities of old and metal-poor stars, the catalogue is filtered to retain only stars that are potential members of a dwarf galaxy via a selection box shown in Figure III.1. The box is designed so that the minimum luminosity in both bands is high enough that the survey is complete. To filter out as many non-M31 stars as possible, stars that are brighter than the TRBG at the distance of M31 are not selected.

Lastly, the equatorial coordinates of each star are projected onto the plane tangential to the centre of M31. In this chapter, we refer to these coordinates as (X, Y).

III.3 A Bayesian search method

Here, I present the methodology developed by Martin et al. (2013a) for the automated detection of dwarf galaxies in the PAndAS survey using the position and photometry of stellar sources. Through the application of forward modeling, this tool calculates the likelihood of the presence of a dwarf galaxy center at each position within the survey, or, in other words, it locates the center of stellar overdensities in the CMD and in the sky that are compatible with a dwarf galaxy stellar population (i.e., old and metal-poor stars with a defined density distribution).

III.3.1 Stellar density models

For each position in the survey and in a region $\mathcal{A}$, there is a sample of n neighboring stars, $\mathcal{D} = \left\{\overrightarrow{d_k}\right\}_{1\leq k\leq n}$ that are defined by their spatial coordinates, their magnitudes, and their colors, $\mathcal{D} = \{X_k, Y_k, i_k, (g-i)_k\}_{1\leq k\leq n}$. Therefore, the probability P for a position to be the center of a stellar surface density distribution ρ_{model} defined by a set of parameters $\mathcal{P}$ can be written

$$P\left(\mathcal{D}|\mathcal{P}\right) = \prod_{k=1}^{n} P_k\left(\overrightarrow{d_k}|\mathcal{P}\right), \tag{III.1}$$

$$= \prod_{k=1}^{n} \frac{\rho_{model}\left(\overrightarrow{d_k}|\mathcal{P}\right)}{\int_{\mathcal{A}} \rho_{model} d\mathcal{A}}. \tag{III.2}$$

The stellar surface density model is the combination of two contributions, one is from the dwarf galaxy, ρ_{dw}, and the other from the contamination, ρ_{cont}, which are respectively

defined by their parameters $\mathcal{P}^{dw}$ and $\mathcal{P}^{cont}$, such that

$$\begin{aligned} \rho_{model} &= \rho_{dw} + \rho_{cont}, \\ \text{and} \quad \mathcal{P} &= \mathcal{P}^{dw} \cup \mathcal{P}^{cont}. \end{aligned} \tag{III.3}$$

The density models used for the dwarf galaxy and the contamination are described in the following subsections.

III.3.1.a Dwarf galaxy density model

In this method, the stellar surface density of the satellite model at once the spatial and color-magnitude distribution of the stars.

The projected spatial distribution of stars is assumed to be spherically symmetric[1] and to follow an exponential law as a function of the radius $r = \sqrt{(X - X_0)^2 + (Y - Y_0)^2}$, where (X_0, Y_0) are the center coordinates in the plane tangent to the currently tested centroid. Let's define the scale radius $r_\mathrm{e} = r_\mathrm{h}/1.68$, where r_h is the half-light radius of the dwarf galaxy. The probability P_{dw}^{sp} for a member star to be at a given radius r is

$$P_{dw}^{sp}(r|X_0, Y_0, r_\mathrm{h}) = \frac{1.68^2}{2\pi r_\mathrm{h}^2} \exp\left(-1.68\frac{r}{r_\mathrm{h}}\right). \tag{III.4}$$

In this method, the dwarf galaxy is assumed to have a single stellar population that can therefore be defined by its age, t, metallicity, $[\mathrm{Fe/H}]_{dw}$ and distance modulus, $m - M$. The stars are distributed along a theoretical isochrone $\mathcal{I}(i', g' - i'|t, [\mathrm{Fe/H}]_{dw}, m - M)$ weighted by the corresponding luminosity function $\phi(i'|t, [\mathrm{Fe/H}]_{dw}, m - M)$ (Marigo et al., 2008). Both $\mathcal{I}(i', g' - i'|t, [\mathrm{Fe/H}]_{dw}, m - M)$ and $\phi(i'|t, [\mathrm{Fe/H}]_{dw}, m - M)$ depend on the properties of the stellar population. However, due to the age-metallicity-distance degeneracy for RGB stars, certain simplifications can be made. First, the age is fixed at 13 Gyr (Weisz et al., 2019). Additionally, a change in the modeled distance can be compensated by a change in the modeled metallicity.

To account for the observed photometric uncertainties, but also to relax the assumption of a single stellar population, the theoretical stellar distribution in the CM space is convolved by two Gaussians, $G(i|i', \delta_{i'})$ and $G(g - i|g' - i', \delta(g' - i'))$ defined as $G(x|\mu, \delta) = (1/\sqrt{2\pi\delta^2}) \exp(-1/2((x - \mu)^2/\delta^2))$. The dispersion δ is the joint contribution of the observed

[1] While this may not be exact (Martin et al., 2016), additional parameters, such as ellipticity and position angle, would be loosely constrained given the small number of data points. However, this would significantly increase the computation time.

uncertainty δ' and of an artificial dispersion σ, yielding

$$\delta_{i'} = \sqrt{{\delta'_{i'}}^2 + \sigma^2}, \tag{III.5}$$

$$\delta_{g'-i'} = \sqrt{{\delta'_{g'-i'}}^2 + \sigma^2}, \tag{III.6}$$

with $\sigma = 0.05$ so that the distribution of RGB stars is similar to the one of known dwarf galaxies in PAndAS. The dwarf galaxy PDF for the CM space can therefore be written

$$P_{dw}^{CM}(i, g-i|[\mathrm{Fe/H}]_{dw}) = A \int_{\mathcal{I}} \phi(i'|[\mathrm{Fe/H}]_{dw}) G(i|i', \delta_{i'}) \tag{III.7}$$

$$\times\ G(g-i|g'-i', \delta g'-i') d\mathcal{I}(i', g'-i'|[\mathrm{Fe/H}]_{dw}), \tag{III.8}$$

with A a normalization constant so that $\int_i \int_{g-i} P_{dw}^{CM}(i, g-i|[\mathrm{Fe/H}]_{dw}) = 1$.

Under the assumption that the position and the photometric properties are independent and if we consider a dwarf galaxy containing N^* stars, the total density function for the dwarf galaxy is

$$\rho_{dw}(X, Y, i, g-i|X_0, Y_0, , r_\mathrm{h}, [\mathrm{Fe/H}]_{dw}) = N^* P_{dw}^{sp}(X, Y|X_0, Y_0, r_\mathrm{h}) P_{dw}^{CM}(i, g-i|[\mathrm{Fe/H}]_{dw}). \tag{III.9}$$

III.3.1.b Contamination density model

The search for dwarf galaxies is limited by contamination from foreground stars of the MW, the M31 stellar halo, but also from background compact galaxies misidentified as stars. One of the strengths of this search algorithm is the spatial and photometric modeling of such contamination.

The sky-projected density of contamination is assumed to be uniformly distributed locally (i.e., it remains constant within the scale of a dwarf galaxy). To compute the local star density surrounding coordinates (X_0, Y_0), an annulus with an inner radius of $15'$ and an outer radius of $20'$ is divided into 36 parts. The density of the contamination sources, $\rho_{cont}^{sp}(X_0, Y_0)$, is the median of the density values of each wedge. The annulus radii are chosen to be small enough that the contamination is similar to that at (X_0, Y_0), but large enough to avoid stellar members of a dwarf galaxy centered on (X_0, Y_0).

Modeling the contamination in the CM space is challenging due to its spatial dependence. In particular, the influence of Milky Way stars, which mainly occupy the redder part of the CMD, becomes more pronounced towards the northern region of the survey at lower Galactic latitude. In addition, the faint M31 halo stars are concentrated near the main galaxy, while background compact galaxies appear sporadically throughout the entire survey area. Therefore, the contamination is assumed to be composed of two contribution, one from the MW, $P_{cont,MW}^{CM}$, and one related to M31, $P_{cont,M31}^{CM}$.

It is expected that the presence of the MW leads to an exponential increase of sources

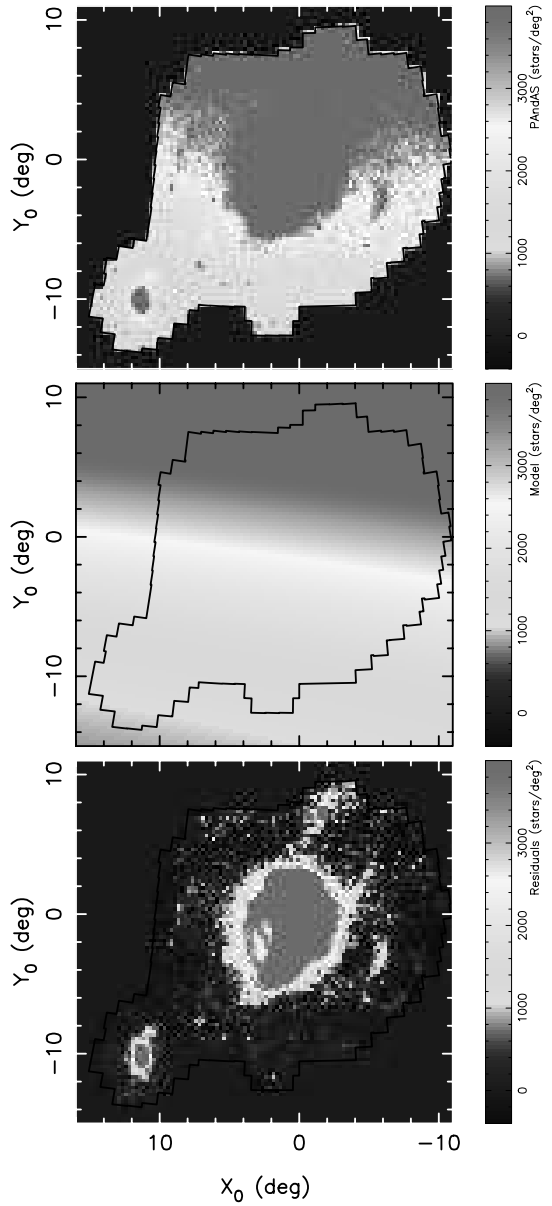

Figure III.2: *Top panel*: Density map of the PAndAS stars within the selection box. There are two prominent components, the M31 stellar halo with its stellar streams overlaid over the foreground contamination from the MW that increase toward the north. *Middle panel*: Model of the density map of the CM contamination for the MW, integrated over the RGB selection box. *Bottom panel*: Residuals from subtracting the contamination model from the PAndAS density map, indicating that the model replicate the overall behavior of the MW contamination. Figure credit: Martin et al. (2013a).

towards the north of the survey yielding variations depending on the selection of blue or red stars. Therefore the model for the density of contaminants at position (X_0, Y_0) and at CM $(g-i, i)$ can be modeled

$$\Sigma_{(g-i,i)}(X_0, Y_0) = \exp\Big(\alpha_{(g-i,i)} X_0 + \beta_{(g-i,i)} Y_0 + \gamma_{(g-i,i)}\Big). \tag{III.10}$$

To calculate the values of $\alpha_{(g-i,i)}$, $\beta_{(g-i,i)}$, and $\gamma_{(g-i,i)}$ for each bin in a 0.2×0.2 magnitude CM grid, a weighted χ^2 method is employed. This is performed over a specific region that lies at least 9° away from M31, and in which any potential streams and dwarf galaxies are masked and excluded from the analysis. The weight map used is derived from the map counts under the assumption of Poisson uncertainties. Figure III.2 shows the PAndAS density maps, the contamination model, and the residuals from subtracting the contamination model from the PAndAS density map. The residual map displays a low and uniform background density while known stellar streams and dwarf galaxies are highlighted, validating the modeling of the MW contamination.

Regarding the contamination from M31, the CM density model for M31, denoted as $P^{CM}_{cont,M31}(i, g-i|[\mathrm{Fe/H}]_{halo})$, is similar to the model constructed for the dwarf galaxy, $P^{CM}_{dw}(i, g-i|[\mathrm{Fe/H}]_{dw})$. However, it includes a broader RGB star locus to accommodate multiple stellar populations, therefore, the value of σ is chosen to be 0.15, which is the minimum value that avoids the detection of most M31 streams as dwarf galaxies. Indeed, streams have similar properties to dwarf galaxies without the compactness, which can make the modeling tricky.

The total contamination density model can therefore be written

$$\begin{aligned}\rho_{cont}(g-i, i|X_0, Y_0, \eta, [\mathrm{Fe/H}]_{halo}) = \; & \rho^{sp}_{cont}(X_0, Y_0)(\eta P^{CM}_{cont,MW}(g-i, i|X_0, Y_0) \\ & +(1-\eta) P^{CM}_{cont,M31}(g-i, i|[\mathrm{Fe/H}]_{halo})),\end{aligned} \tag{III.11}$$

with η the fraction of MW contamination and $(1-\eta)$ the fraction of M31 contamination. Finally, it means that $\mathcal{P}_{cont} = \{X_0, Y_0, \eta, [\mathrm{Fe/H}]_{halo}\}$.

III.3.2 Implementation

The search algorithm is tailored to discover faint dwarf galaxies (i.e., $M_V > -8$). The total density model for PAndAS stars in the RGB selection box ρ_{model}, is obtained by combining Equations III.3, III.9, and III.11. The density is thus fully expressed as a function of the model's parameters $\mathcal{P} = \{X_0, Y_0, r_{\mathrm{h}}, [\mathrm{Fe/H}]_{dw}, N^*, \eta, [\mathrm{Fe/H}]_{halo}\}$. In order to derive the probability for a position to be the center of the density distribution ρ_{model}, as defined by Equation III.2, the size of the region $\mathcal{A}$ that delimits the sample of neighboring stars must be fixed. $\mathcal{A}$ is chosen to encompass the area within $4r_{\mathrm{h,max}}$ from the location (X_0, Y_0), where $r_{\mathrm{h,max}}$ is the largest half-light radius that is explored for the possible dwarf galaxy (see Subsubsection III.3.2.b). Within this radius, $\mathcal{A}$ contains most of stars from the possible

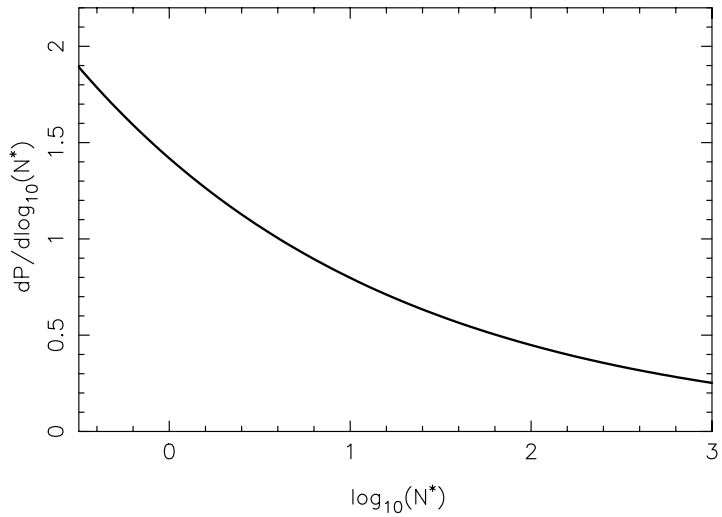

Figure III.3: PDF as a function of $\log_{10}(N^*)$ derived from the luminosity function from Koposov et al. (2008) that was obtained mainly from MW dwarf galaxies. This PDF is used as a prior on $\log_{10}(N^*)$. Figure credit: Martin et al. (2013a).

dwarf galaxy centered at (X_0, Y_0), but it remains sufficiently small to maintain the validity of the uniform contamination hypothesis and to avoid unnecessary computation time on non-member stars of the dwarf galaxy.

To determine the likelihood, $P(\mathcal{D}|\mathcal{P})$, of the presence of a dwarf galaxy at the coordinates (X_0, Y_0) across the PAndAS footprint, its value is computed over a finely spaced spatial grid as it is essential for the center of a potential dwarf galaxy to be in close proximity to one of the grid centers. Considering that a faint dwarf galaxy typically has a size of $\sim 1'$ (i.e., $M_V = -6$; Brasseur et al., 2011), the grid is designed with a center-to-center distance of $0.5'$.

For each position (X_0, Y_0) in the spatial grid, the PAndAS stars within region $\mathcal{A}$ are filtered via to the CM selection box (Figure III.1) to keep only RBG stars that are potential members of a dwarf galaxies. Thereafter, the probability for the sample of N star, as defined in Equation III.1, is calculated over the 5-dimensional grid of parameters (i.e., $r_{\rm h}, [{\rm Fe/H}]_{dw}, N^*, \eta, [{\rm Fe/H}]_{halo}$) given in Subsubsection III.3.2.b.

III.3.2.a Priors

Until now, only likelihoods were considered (i.e., $P(\mathcal{D}|\mathcal{P})$), but the aim is to obtain the probability of the model given the data $P(\mathcal{P}|\mathcal{D})$. Following the theory initiated by Bayes & Price (1763) and further developed by Marquis de Laplace (1812), $P(\mathcal{D}|\mathcal{P})$ and $P(\mathcal{P}|\mathcal{D})$ are

linked via the prior $P(\mathcal{P})$. The priors are detailed in Martin et al. (2013a) such that

$$P(\mathcal{P}|\mathcal{D}) \propto P\left(\mathcal{D}|\mathcal{P}\right) P(\mathcal{P}). \tag{III.12}$$

One has to note that the search algorithm calculates in reality the logarithm of such probability. For each of the 5 parameters the priors are defined as follows:

- A flat prior is applied on η.
- A flat prior is applied on $[\mathrm{Fe/H}]_{dw}$ and $[\mathrm{Fe/H}]_{cont}$.
- The prior on the size of the dwarf galaxies is extracted from Brasseur et al. (2011). For M31 satellites, the resulting size probability distribution function $P_{\log_{10}(r_{\mathrm{h}}(pc))}$ follows a normal distribution such as $P_{\log_{10}(r_{\mathrm{h}}(pc))} \propto \mathcal{N}(2.34, 0.23)$. The size distribution is shifted from physical to an angular size, by assuming a distance modulus of 24.46.
- The prior on $\log_{10}(N^*)$ is derived from the luminosity function obtained by Koposov et al. (2008) mostly for MW satellites (see Figure III.3).

III.3.2.b Parameter Grid

To efficiently evaluate the model for all positions in the spatial grid and to robustly track the variation in $P(\mathcal{P}|\mathcal{D})$, $P\left(\mathcal{D}|\mathcal{P}\right)$ is determined over a fixed grid of parameters detailed in Martin et al. (2013a):

- The range of η values is from 0 to 1, with an interval of 0.1.
- $[\mathrm{Fe/H}]_{halo}$ is evaluated at various values $(-1.7, -1.3, -1.1, -1.0, -0.9, -0.8, -0.7, -0.6)$ dex to cover the range of metallicities of the M31 streams.
- The tested values for r_{h} range from $0.5'$ to $4'$ with a step of $0.7'$. Those values encompasses the size of the faint dwarf galaxies targeted by the search algorithm (i.e., $M_V > -8$; Brasseur et al., 2011).
- The tested values for $\log_{10}(N^*)$ range from -0.5 to 3 with a step of 0.5 dex, once again targeting faint dwarf galaxies.

III.3.2.c Significance of detection

For each position (X_0, Y_0) in the spatial grid and for all set of parameters, the probability of the model as a function of the PAndAS stellar spatial and CM density maps are calculated. Although it is straightforward to obtain the best set of parameters by maximizing $P(\mathcal{P}|\mathcal{D})$, the added value of this tool and the motivation for such complex modeling is to derive a reliable significance, S, for potential detections of dwarf galaxies. To obtain this value,

$P(\mathcal{P}|\mathcal{D})$ is marginalized over all parameters but $\log_{10}(N^*)$ to obtain $P(\log_{10}(N^*)|\mathcal{D})$. The significance is defined by comparing the favored model to the model with no dwarf galaxy[2], assuming that $P(N^*|\mathcal{D})$ follows a Gaussian distribution, yielding

$$S^2 = 2\ln\left(\frac{\max(P(N^*))}{P(N^*=0)}\right). \tag{III.13}$$

III.4 Results

The significance map resulting from the run of the search algorithm over the PAndAS stellar catalogue is displayed in Figure III.4. Notably, all of the previously known dwarf galaxies (represented by white squares) are detected with a high significance level, confirming that the search algorithm easily detects previous discoveries. Additionally, several globular clusters (GCs) are detected with reasonable significance. The significance map also reveals localized and isolated regions of high significance in the outer halo that do not overlap with known structures, suggesting the presence of potential dwarf galaxy candidates. While some of these detections show promise, it is important to note that the high significance region located between $5° < X_0 < 9°$ and $-7° < Y_0 < -9°$ is attributed to the GCs of the NGC 507 group of background galaxies. These GCs appear as point sources in the PAndAS catalogue and share similar photometric properties with member RGB stars from an M31 satellite.

Another feature of the significance map is the low number of high significance regions along the numerous M31 streams, suggesting that the modeling of the M31 stellar contamination has effectively mitigated the influence of the structured M31 stellar halo (as shown in Figure II.6). Nevertheless, in regions closer to M31, where the streams are more complex or overlapping, a number of false detections persist. This issue resurfaces when determining the detection limits, and a similar approach to the proposed solution below is adopted.

To address the false detection of these intricate structures near M31, a distance-dependent detection significance threshold is enforced. The threshold value is derived from the significance distributions within a circular annuli at various distances from M31, as displayed in Figure III.5. The width of the annuli is narrower for the problematic region around M31 and increases gradually towards regions farther away from M31. Notably, the significance distribution of regions close to M31 exhibits a more extended distribution compared to the histograms obtained at larger radii, until a radius of 12°, where the histograms encompass the stellar debris from M33. The significance detection threshold is selected at the break between the Poisson-like portion of the distribution and the flat tail produced by the significance of potential dwarf galaxy candidates. This criterion ensures a more robust differentiation between true detections and potential false positives.

[2]As the search algorithm explores in reality the parameter $\log_{10}(N^*)$, a model with no dwarf galaxy can not be tested, but it is replaced by the model with the lowest number of stars.

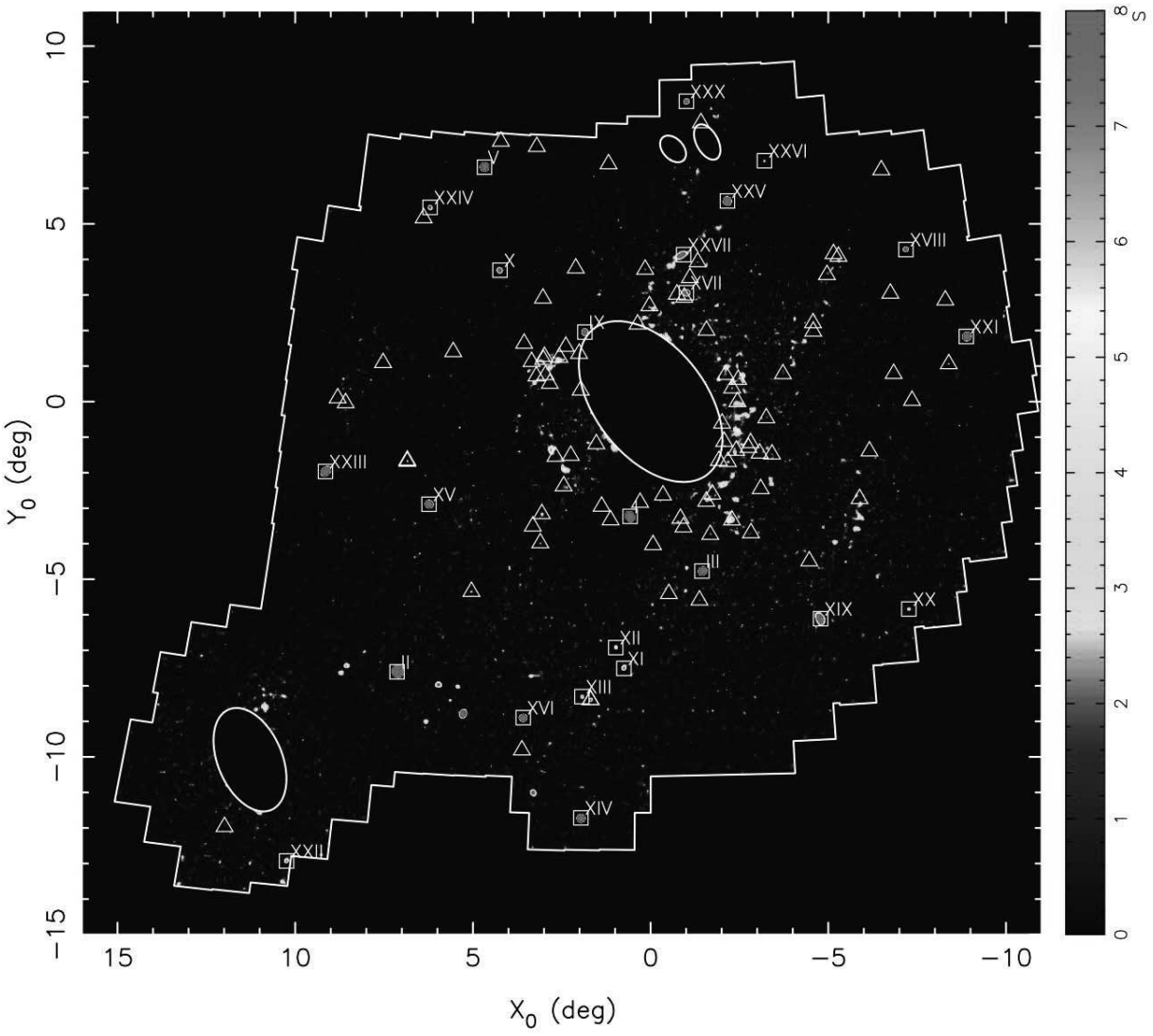

Figure III.4: Map of the significance of detection throughout the PAndAS footprint (*white polygone*). The masked regions surrounding M31, M33, NGC147, and NGC185 are represented by ellipses. Known dwarf galaxies and known globular clusters are represented respectively by squares and triangles. The results obtained from the search algorithm align with previous discoveries, as all known satellites are detected with high significances. Moreover, the search algorithm demonstrates a limited sensitivity to the complex structure of M31 stellar halo, suggesting an effective modeling of the M31 contamination. Figure credit: Martin et al. (2013a).

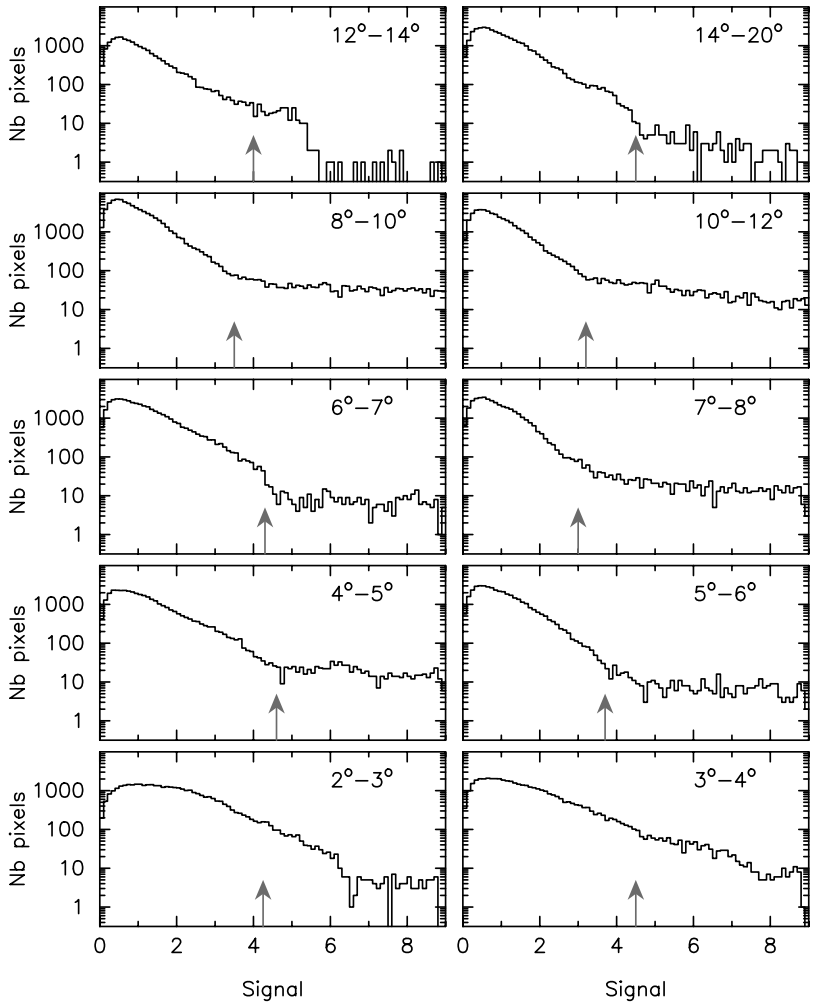

Figure III.5: Histograms of the significance within circular annuli at different distance from M31. The significance threshold for each annuli are highlighted by the red arrows. Figure credit: Martin et al. (2013a).

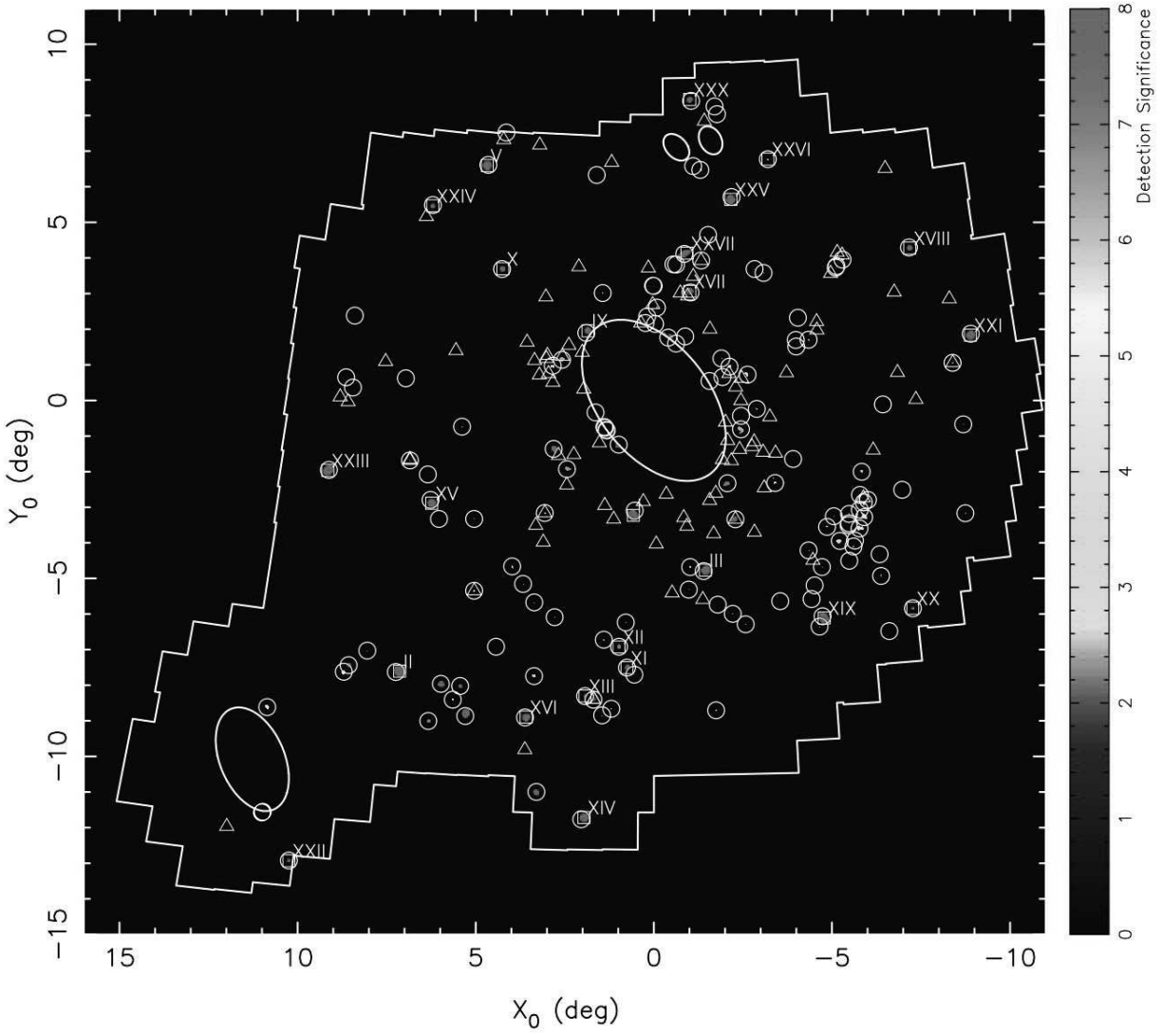

Figure III.6: Map of the significance of detection throughout the PAndAS footprint (*white polygone*). The masked regions surrounding M31, M33, NGC147, and NGC185 are represented by ellipses. Known dwarf galaxies and known globular clusters are represented respectively by squares and triangles. All detections are circle. Figure credit: Martin et al. (2013a).

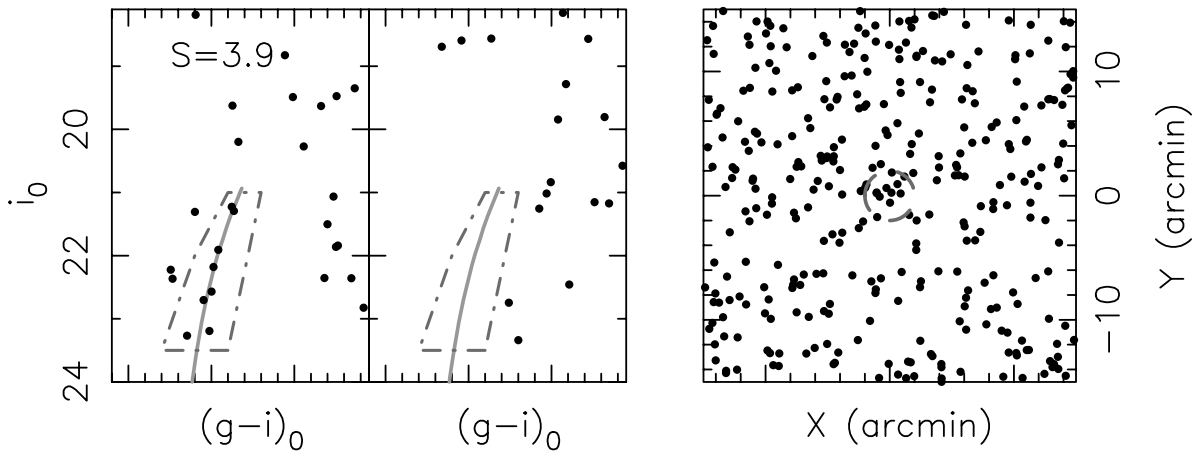

Figure III.7: *Left panels:* CMD of stars from a detection (S=3.9) in the region near And XI−XIII. To provide a comparison, the CMD derived from a field annulus at 15′ with equivalent coverage is shown as the adjoint panel. The overlaid grey line is the isochrone for a population with an age of 13 Gyr, at the distance of M31 with [Fe/H] = −1.7. *Right panel:* Spatial distribution of the stars falling within the box defined by the red dashed line, centered on the detection. An overdensity of stars with properties similar to members of a dwarf galaxy is visible both in the CMD and in the sky. Figure credit: Martin et al. (2013a).

Figure III.6 present a map of the resulting detections after applying the previously defined significance detection threshold. A table containing the 143 detections, along with their respective locations and potential nature (such as dwarf galaxies, streams, GCs, etc.), when applicable, is provided in Martin et al. (2013a). Among these detections, known dwarf galaxies exhibit the highest level of significance, with the least significant detection belonging to And XXVI, with a significance value of 5.9.

Once again, there are multiple detections beyond the stellar halo that do not overlap with known objects, indicating the possibility of them being dwarf galaxies. Figure III.7 presents CMD and spatial distribution of stars from one such detection, with a significance of 3.9. This example serves as a representative case of the most significant detections, a spatial and photometric overdensity of stars consistent with an old stellar population is observed. However, to confirm whether this detection is indeed a satellite of M31, further investigation through a deeper photometric follow-up is required.

III.5 A tailored search algorithm for detection limits

Detecting new satellites is a crucial step towards understanding the M31 satellite system. However, to gain comprehensive insights into its global properties, understanding the completeness of the search for dwarf galaxies is essential. The method involves injecting

artificial dwarf galaxies into the PAndAS catalogue, after which the search algorithm is executed to determine whether each injected object is detected or not. The first part of my PhD was dedicated to this task (Doliva-Dolinsky et al., 2022), and I will outline the process in Section IV. In this section, I will explain the modifications made to the search algorithm and the overall setup used to calculate the detection limits.

III.5.1 Modification to determine the completeness of the survey

A significant modification made to the search algorithm involved the introduction of artificial dwarf galaxies into the existing stellar catalogue of PAndAS. It was crucial to ensure that the injection process did not compromise the determination of the local contamination, as this could potentially introduce biases in the modeling of the contamination. Therefore, for each iteration, I only inject 1 dwarf per field of the survey (i.e., $\sim$1 dwarf per square degree).

The determination of detection limits is a time-consuming process, especially since we aim to obtain them as a function of the luminosity, size, and position of dwarf galaxies. I therefore adapted the search algorithm by leveraging the known properties of the injected galaxies, thus avoiding unnecessary calculations. As a first step, I limit the search algorithm to only pixels located within a $1.5'$ from the center of each ingested artificial dwarf galaxy, therefore focusing the computational resources on the most relevant regions. Then, I optimize the explored range of parameters to fit with the known properties of the artificial satellites:

- For the metallicity of halo stars, $[\mathrm{Fe/H}]_{halo}$, the values explored range from -1.3 to -0.6 with a step size of 0.1. We have verified that this adjustment does not have a substantial impact on the significance of detection for the artificial dwarf galaxies.

- The injected artificial dwarf galaxies are characterized by a maximum half-light radius of $3.5'$. Consequently, we limit our exploration of this parameter up to this specific value.

- Considering that several of our brightest dwarf galaxies contain a substantial number of stars exceeding 1000, we extend our exploration of parameter N^* up to 10^4.

Furthermore, the availability of the High Performance Computing (HPC) infrastructure of the University of Strasbourg played a crucial role in accelerating our calculations, ensuring that I could complete the analysis within an acceptable timeline. Figure III.8 illustrates the setup plan to determine the detection limits. The process presented is for a given set of dwarf galaxy properties and is therefore repeated $\sim$ 1000 times. The initial stage involves generating artificial dwarf galaxies for a given [Fe/H], size, distance, and to ensure efficiency, I draw photometry from a previously created main dwarf galaxy that contains millions of stars. Given that Python's parallelization is not fully optimized, to prevent unnecessary memory duplication for each CPU, I had to devise a buffer memory system. This solution

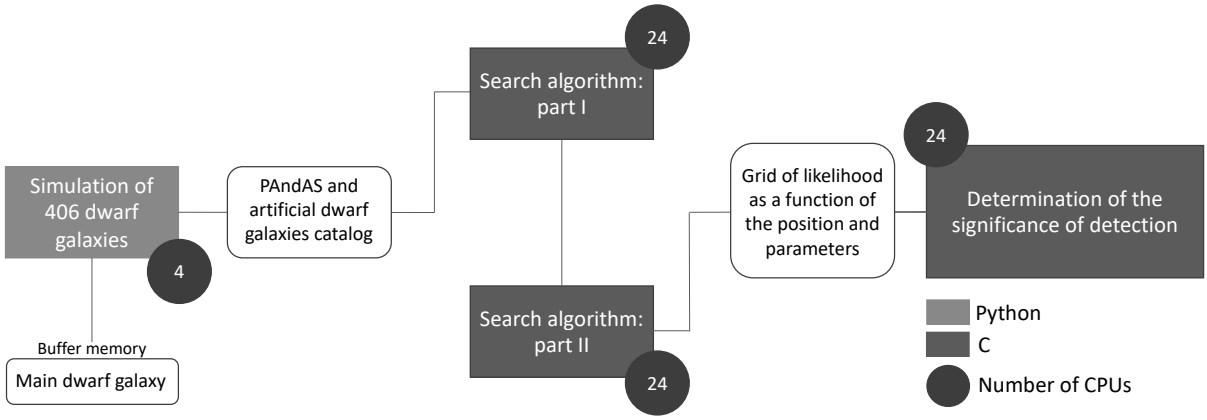

Figure III.8: Schematic graph of the algorithm set up to determine the detection limits. The use of an HPC allowed to improve considerable the computation time.

allowed to avoid redundant memory copies that would overload the RAM and improved the overall performance of the process. Subsequently, the search algorithm is run on the combined PAndAS and artificial dwarf galaxies catalogues. To prevent RAM overload, this procedure is carried out separately and consecutively on each half of the survey. Finally, the resulting grid of likelihood is marginalized over all parameters but the number of star N^* for each position in order to obtain the significance of detection. The parallelization of each stage of the process was a crucial and indispensable step in attaining accurate detection limits in a timely manner.

III.5.2 Conclusion

The search algorithm, developed by the PAndAS team (Martin et al., 2013a), relies on the identification of overdensity of old, metal-poor stars both in the CMD and in the sky. This achievement is made possible through forward modeling, which encompasses not only the dwarf galaxy but also the contamination. This comprehensive approach enhances our understanding of the resulting significance of detection.

The search algorithm demonstrated its efficiency by detecting all known dwarf galaxies with a high level of significance ($S > 5.9$). Furthermore, the detection of new sources with high significance holds promise, indicating potential discoveries of previously unknown dwarf galaxies. However, further in-depth follow-up investigations are essential to confirm their classification as genuine dwarf galaxies definitively. Consequently, I submitted proposals in order to obtain deep photometry observations of those potential satellites.

Finally, this search algorithm represents a crucial initial step in analyzing the global properties of the M31 satellite system, as it enables the determination of precise detection limits for the PAndAS survey, as detailed in the next chapter.

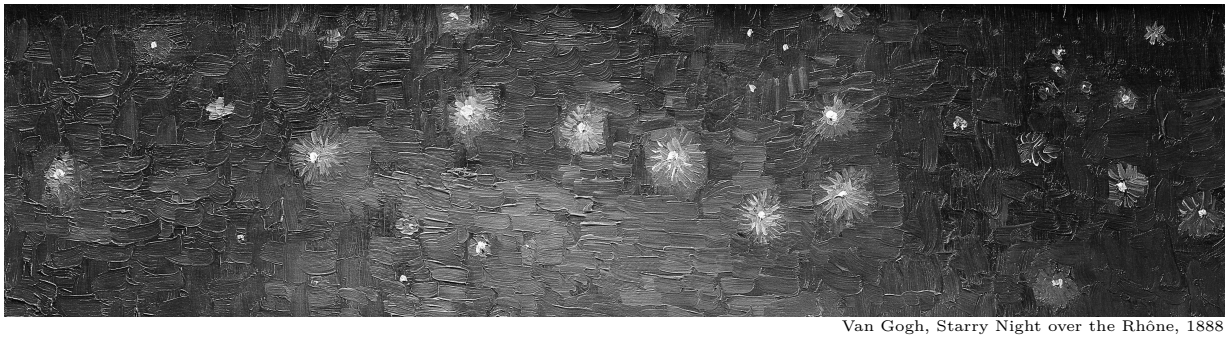

Van Gogh, Starry Night over the Rhône, 1888

Chapter IV

Detection Limits

The PAndAS View of the Andromeda Satellite System. III. Dwarf galaxy detection limits

Amandine Doliva-Dolinsky, Nicolas F. Martin, Guillaume F. Thomas, Annette M. N. Ferguson, Rodrigo A. Ibata, Geraint F. Lewis, Dougal Mackey, Alan W. McConnachie, Zhen Yuan

Astrophysical Journal, 2022, 933,135

Abstract

We determine the detection limits of the search for dwarf galaxies in the Pan-Andromeda Archaeological Survey (PAndAS) using the algorithm developed by the PAndAS team (Martin et al. 2013a). The recovery fractions of artificial dwarf galaxies are, as expected, a strong function of physical size and luminosity and, to a lesser extent, distance. We show that these recovery fractions vary strongly with location in the surveyed area because of varying levels of contamination from both the Milky Way foreground stars and the stellar halo of Andromeda. We therefore provide recovery fractions that are a function of size, luminosity, and location within the survey on a scale of $\sim 1 \times 1\,\mathrm{deg}^2$ (or $\sim 14 \times 14\,\mathrm{kpc}^2$). Overall, the effective surface brightness for a 50-percent detection rate range between 28 and 30 $\mathrm{mag\,arcsec}^{-2}$. This is in line with expectations for a search that relies on photometric data that are as deep as the PAndAS survey. The derived detection limits are an essential ingredient on the path to constraining the global properties of Andromeda's system of satellite dwarf galaxies and, more broadly, to provide constraints on dwarf galaxy formation and evolution in a cosmological context.

IV.1 Introduction

In cosmological models that include dark matter, hundreds of sub-halos of dark matter are orbiting around a central halo (Klypin et al., 1999; Moore et al., 1999). These sub-haloes are the place of birth of dwarf galaxies, but not all will "light up". The expected number of dwarf galaxies is highly sensitive to the cosmology (Spergel & Steinhardt, 2000; Bode et al., 2001) but also to diverse physical phenomena that can stop star formation, such as stellar feedback or the reionization (Bullock et al., 2000; Somerville, 2002; Mashchenko et al., 2008; Wheeler et al., 2015). Dark matter simulations with adding baryon physics are compared to dwarf galaxies observations in order to constrain those parameters (Koposov et al., 2009; Kim et al., 2018; Nadler et al., 2019).

The search for dwarf galaxies was revolutionized by large, homogeneous photometric surveys such as the Sloan Digital Sky Survey (SDSS; Abazajian et al. 2003), the Panoramic System Telescope and Rapid Response System 1 3π survey (Pan-STARRS1; Chambers et al. 2016) or the Dark Energy Survey (DES; Abbott et al. 2018). Those new datasets are searched for dwarf galaxies thanks to detection algorithms that look for over densities of stars compatible with an old stellar population (Belokurov et al., 2007; Martin et al., 2013a; Laevens et al., 2015). Thanks to these improvements, numerous new dwarf galaxies were detected. Indeed, before those surveys, there was a dozen known dwarf galaxies around the Milky Way (MW) with an absolute magnitude $M_V < -8.8 \pm 0.2$ (Draco; Mateo 1998). By now, the number of known MW satellites is 59, with $M_V < -0.8 \pm 0.9$ (Virgo I, Homma et al. 2016). Even if the nature of those objects is sometimes debated (Conn et al., 2018a; Jerjen et al., 2018; Mutlu-Pakdil et al., 2018), the increase in the number of known dwarf galaxies allows us to determine the dwarf galaxy detection limits of each survey, and so, to obtain more precise statistical estimations of the real number of dwarf galaxies around the MW. This was already done for SDSS, Pan-STARRS1 and DES searches (Koposov et al., 2008; Drlica-Wagner et al., 2020), and used to derived an estimate of the luminosity function for the MW.

The Local Group hosts another large galaxy that provides us with a different test sample for cosmological and galaxy formation models. Large photometric surveys also changed our knowledge on M31 and its satellites. Searches focused on the SDSS led to the discovery of 3 new dwarf galaxies around M31, as faint as $M_V = -8.1 \pm 0.5$ with And X (Zucker et al., 2004a, 2007; Bell et al., 2011). The INT/WFC imaging of the surrounding of M31 led to the discovery of And XVII (Irwin et al., 2008). But the main survey leading to the discovery of numerous new M31 dwarf galaxies is the Pan-Andromeda Archaeological Survey (PAndAS), a dedicated survey of the halo of the Andromeda galaxy. Searches within this survey led to the discovery of 19 satellite dwarf galaxies of M31 with $M_V < -5.9 \pm 0.7$ (Richardson et al., 2011; McConnachie et al., 2008; Ibata et al., 2007; Martin et al., 2006). For this survey, an algorithm was created by the PAndAS team to search for stellar populations of dwarf galaxies in the full survey by looking for overdensities of stars both spatially and in the color-magnitude diagram (CMD; Martin et al., 2013a, M13 hereafter). Thanks to the

algorithm, we can now determine the survey completeness limit.

In this paper, we determine the detection limits of Andromeda's dwarf galaxies using the PAndAS survey. In parallel to similar studies already conducted on the Milky Way, this will provide a second independent test for cosmological or galaxy formation simulations, using a different satellite system. Recovery fractions of dwarf galaxies are obtained by adding artificial galaxies to the PAndAS photometric catalogue and by determining whether they are detected by blindly running the search algorithm developed by the PAndAS team (M13).

This paper is structured as follows: Section IV.2, briefly describes PAndAS and its data. Section IV.3, details the generation of artificial dwarf galaxies and how we determine their recovery fractions. Section V.4 presents the modeled dwarf galaxy completeness for each field of the PAndAS survey. The impact of the galaxy's distance and metallicity is also investigated. Finally, we discuss our results in Section IV.5.

IV.2 Preliminaries

The Pan-Andromeda Archaeological Survey (PAndAS) was a Large Program conducted from 2008 to 2011 at the Canada-France-Hawai Telescope (CFHT), using the wide-field imager MegaCam to map the surroundings of the Andromeda galaxy (McConnachie et al., 2009, 2018). Combined with previous observations obtained through PI time, it includes over 400 fields of $\sim$1 deg^2 each and probes a region within $\sim$ 150 kpc of M31 and $\sim$ 50 kpc of its companion galaxy M33. Each field was observed in both the g and i band for photometry that includes the brightest three magnitudes of the red giant branch (RGB) at the distance of M31. The survey is presented in detail in McConnachie et al. (2018), along with the data reduction and catalogue creation steps, and we refer the reader to this publication for the full description of the catalogues that we use here. In a nutshell, these reach median, 5σ g and i depths of 26.0 and 24.8, respectively (Ibata et al., 2014).

The algorithm to generate dwarf galaxies, described and used below, requires two field-specific ingredients: a model of the photometric uncertainties and a model of the completeness. Thomas et al. (2021) presents models for these two components which are determined carefully for a small set of fields and propagated to the full survey by scaling these initial models with an anchor magnitude that corresponds to the magnitude at which the uncertainties are equal to 0.1 magnitude.

For the model of the photometric uncertainties, we model them with an exponential model as a function of magnitude (see Ibata et al. 2007 for more detail). The photometric uncertainties in the i and g bands are shown in Figure IV.1 for 3 different fields of the survey with the corresponding models. The exponential fits describe the photometric uncertainties reasonably well, despite small differences that arise between fields.

For the completeness, we use the work of Thomas et al. (2021) who determined, independently, the i- and g-band completeness of the PAndAS data by comparison with regions of deep photometry observed with the Hubble Space Telescope (HST) data. This process is

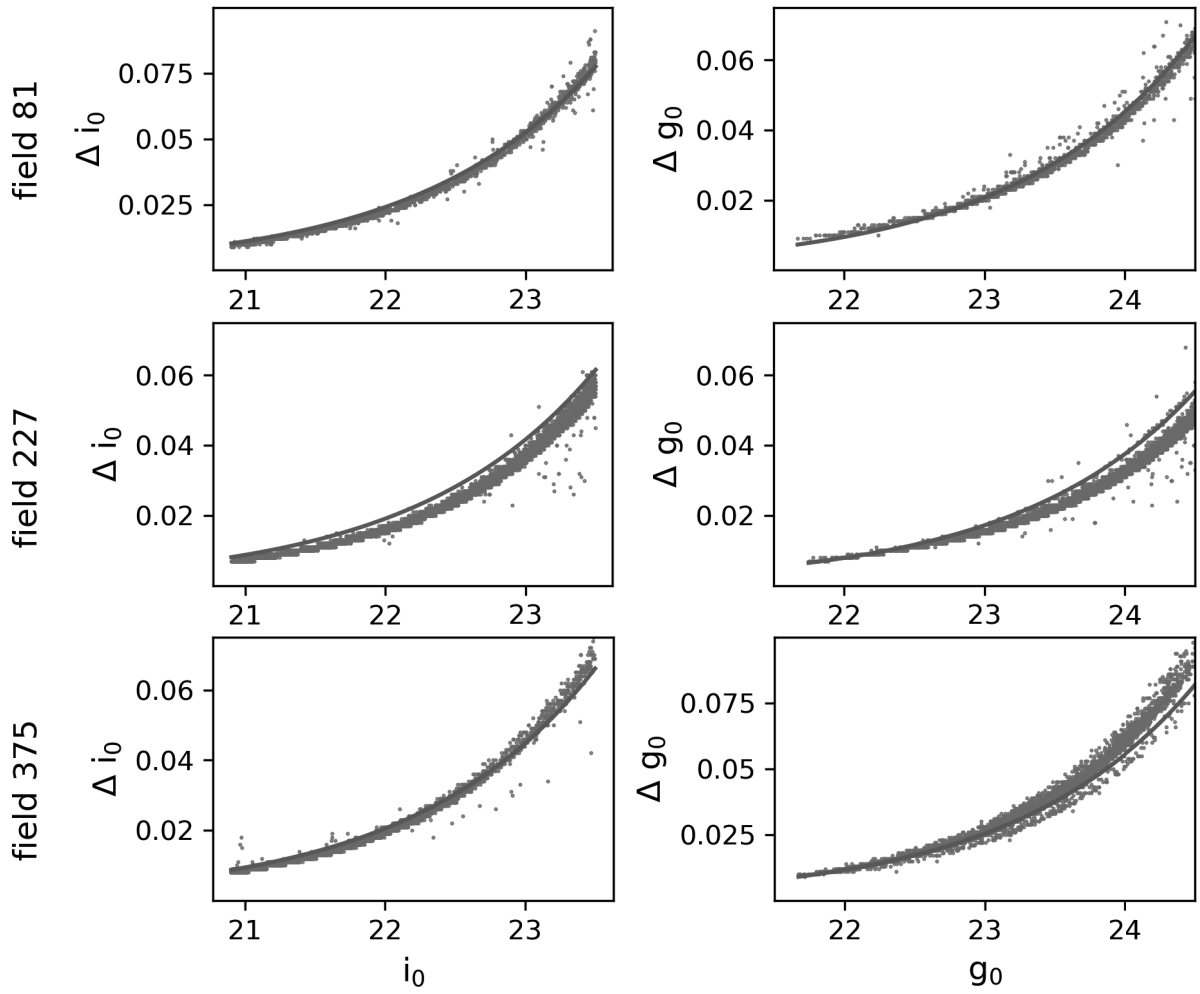

Figure IV.1: Uncertainties in the i (left) and g (right) magnitudes for 3 typical fields of the survey. The exponential fits (green lines), reasonably follow the photometric uncertainty distributions of each field.

based on 14 HST fields that are ∼2.5-3 magnitudes deeper than PAndAS and propagated to the full survey via changes in the anchoring magnitude, as described above.

IV.3 Methods

IV.3.1 Generating artificial dwarf galaxies

To determine the dwarf-galaxy detection limits of the PAndAS survey we need to generate artificial dwarf galaxies that can be added to the PAndAS photometric catalogue to measure their probability of being detected. For any artificial dwarf galaxy, we aim to generate a

catalogue of fake positions and g and i magnitudes that, combined, create a system of known properties (total magnitude, metallicity, radius, distance, and/or age).

The first step to generate an artificial dwarf galaxy is to determine the photometry of its individual stars. For simplicity, we assume that the artificial dwarf galaxy can be parametrized by a single age and metallicity. While this is clearly not accurate, the different stellar populations of the faint dwarf galaxies that will be simulated here are not clearly separated in the PAndAS photometry (Martin et al., 2016). For every artificial dwarf galaxy, we go through the following steps:

1. For a given choice of metallicity, age, distance, and total magnitude in the V band (M_V), we randomly draw stars from the corresponding luminosity function taken from the PARSEC library (Marigo et al., 2017), using the pre-2014 MegaCam photometric system and a Kroupa initial mass function (Kroupa, 2001). The corresponding isochrone from the same library provides the color that the randomly drawn stars must follow. Artificial stars are drawn with an absolute magnitude $-5 < M_i < 20$ until the total flux of the system reaches the target total magnitude M_V[1]. We then keep only bright stars as the selection box of the search algorithm will only use upper Red Giant Branch (RGB) stars with $i_0 < 23.5$. The exact shape of the horizontal branch is not modeled in detail as its stars are fainter than the magnitude limit used by the algorithm but their flux is properly taken into account to determine the total luminosity of the artificial dwarf galaxy.

2. To best represent the PAndAS observations, we randomize the perfect magnitudes drawn from the isochrone and luminosity function by adding noise to the magnitudes, following the photometric uncertainties models of the field in which the artificial galaxy will be placed. The added observed photometric uncertainties broaden the locus of stars in the CMD.

3. Finally, we use the (in)completeness model determined by Thomas et al. (2021) to test for the observability of any star drawn in the artificial galaxy. Every star generated in the previous step is tested against the completeness model. For every star drawn from the isochrone and luminosity function, we draw random deviates between 0 and 1 and independently test those against the completeness at the star's g- and i-band magnitudes.

The CMD of an artificial dwarf galaxy with $M_V = -8.5$, [Fe/H] $= -1.7$, an age of 10 Gyr (and $r_\mathrm{h} = 265\,\mathrm{pc}$) is shown in Figure IV.2 as it is pushed through the different steps of the process. We can see that the resulting CMD in the fourth panel, which is the one of an artificial dwarf galaxy added on a random location of the PandAS survey without any known

[1]MegaCam magnitudes are transformed into V-band magnitudes using the color equations presented in Ibata et al. (2014).

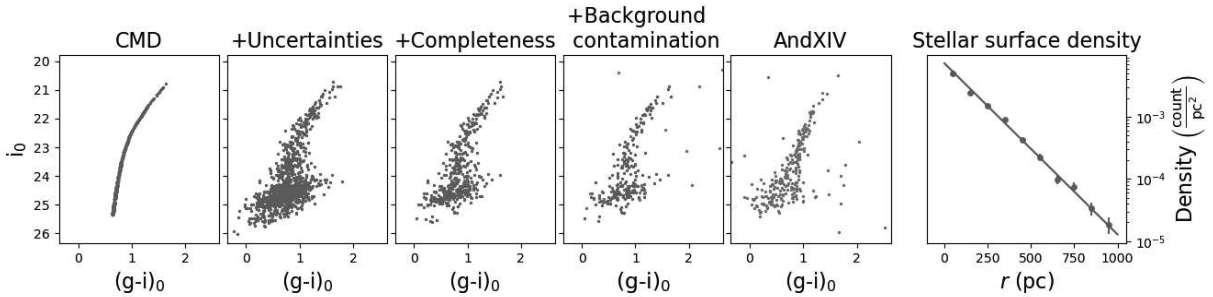

Figure IV.2: CMD of the stars of an artificial dwarf galaxy with $M_V = -8.5$, [Fe/H] $= -1.7$, an age of 10 Gyr, and $r_{\rm h}$=265 pc, as it is pushed through the different steps of the generation process. The first panel corresponds to the CMD of stars drawn from the chosen luminosity function and corresponding isochrone. As the search algorithm is only looking at RGB stars we only represent the bright stars that are of interest here. The second panel shows the CMD after taking the PAndAS photometric uncertainties into account. The CMD of the third panel folds in the incompleteness of the PAndAS data. Finally, the fourth panel shows the CMD of this artificial system within $2r_h$ overlaid on top of the typical field contamination from PAndAS (grey points). A direct comparison with the CMD within $2r_h$ of And XIV (fifth panel) that has similar parameters shows the similarities between the two CMDs. The sixth panel displays the perfect agreement between the radial surface density of stars in the artificial dwarf galaxy (blue points) and the chosen radial density model (green line).

satellite or stellar stream, is very similar to the CMD of the real dwarf galaxy And XIV that has a similar total luminosity ($M_V = -8.5$; Martin et al. 2016) and is shown in the fifth panel.

Now that the number of stars in the galaxy and their photometry is known, the next step is to determine their position with respect to the center of the galaxy. The radial stellar density is assumed to follow an exponential law with scale radius $r_{\rm e} = r_{\rm h}/1.68$, where $r_{\rm h}$ is the half-light radius of the system in pc. The probability density function of stars, $P(r)$, at radius r given in pc, is

$$P\left(r\right) = \frac{1.68^2 r}{2\pi r_{\rm h}^2} \exp\left(-1.68\frac{r}{r_{\rm h}}\right). \tag{IV.1}$$

For every star in the artificial dwarf galaxy that was assigned a color and a magnitude in the previous step and passed the completeness test, we draw its radius from this probability distribution function and assign it a random angle between 0 and 2π. These polar coordinates are then transformed into sky coordinates using the center of the artificial dwarf galaxy. The right-hand panel of Figure IV.2 shows the perfect agreement between the radial density profile of stars in this test artificial dwarf galaxy and the chosen model density profile.

IV.3.2 Determining the recovery rate of artificial galaxies

There are clear differences in the properties of observed stars throughout the PAndAS survey as, for instance, the contamination from MW foreground stars increases significantly towards the north (M13) or the density of M31 stellar halo stars changes with the density of stellar stream stars (Ibata et al., 2014). We therefore aim to determine the recovery fractions of artificial dwarf galaxies (and therefore the detection limits of dwarf galaxies in the survey) as a function of the location in the survey. A degree, at the distance of M31, corresponds to $\sim 14\,\mathrm{kpc}$. This means that the $1^\circ \times 1^\circ$ MegaCam field is a natural areal subdivision to consider since it corresponds to a sizable area of the M31 halo without being too large. The fact that there are subtle field-to-field differences in the photometry depth and completeness, despite the survey being very homogeneous, further comforts us in our choice to determine the artificial dwarf-galaxy recovery fractions on a field-to-field basis.

IV.3.2.a Choice of parameters for the artificial dwarf galaxies

We first need to carefully decide which parameters have the most significant impact on the detection limits so as to limit as much as possible the significant amount of computation required to determine the dwarf galaxy recovery fractions.

We know that the parameters with the most impact on the detection of a dwarf galaxy (or absence therefore) are the size and the total luminosity of a system because these are directly related to the surface brightness of a dwarf galaxy (e.g. Koposov et al., 2009; Walsh et al., 2009; Drlica-Wagner et al., 2020). The distance to the system is very important for searches of MW dwarf galaxies but is not so important for distant systems. At the distance of M31, a change in distance of $\pm 300\,\mathrm{kpc}$ only leads to a change to the location of stars in the CMD by $-1.1/+0.5$ magnitudes, respectively. While this is not subtle, the fact that PAndAS only observes red-giant branches that are sparsely populated, and so very noisy, means that a shift in distance is similar to a shift in metallicity and so the distance does not have a very significant impact on the recovery rate of a dwarf galaxy (M13).

To limit the required calculations, we therefore consider the distance to an artificial system as a secondary parameter and, for the moment, assume all artificial dwarf galaxies are located at the distance of M31, with a distance modulus of 24.47 (McConnachie et al., 2005).

The range of interest for a dwarf galaxy's total magnitude is $-4.5 \lesssim M_V \lesssim -8.5$ (Martin et al., 2016) and straddles the total magnitude of the faintest dwarf galaxy detections. In this regime, all known dwarf galaxies are invariably metal-poor with a metallicity contained between -1.5 and -2.3 (Tollerud et al., 2012; Collins et al., 2013). In addition, the PAndAS photometry is not very sensitive to metallicity variations in this range as the tracks followed by RGB stars in this metallicity range almost overlap in the $(g-i, i)$ CMD. To save on unnecessary computing time, we therefore assume a fixed metallicity for all dwarf galaxies, with $[\mathrm{Fe/H}] = -1.7$.

Finally, we know that the age of the stellar populations in a dwarf galaxy have little

impact on the color and magnitude of its RGB stars as long as they are at least moderately old ($\gtrsim$ 2 Gyr). Consequently, we assume an age of 10 Gyr for all artificial dwarf galaxies (Weisz et al., 2019).

We check the impact of these three assumptions on the distance, the metallicity, and the age in § V.4 below and confirm that it is indeed minimal, or can easily be modeled in the case of the distance.

In summary, for each field in the PAndAS footprint, we generate artificial galaxies with a metallicity [Fe/H] = −1.7, an age of 10Gyr, at a distance modulus of M31 ($m - M = 24.47$). To test the impact of the total magnitude (M_V) and the size (parametrized by the half-light radius r_h given in pc) of the system, we bin the M_V–$\log_{10}(r_\mathrm{h})$ plane over the generous range $-8.5 < M_V < -4.5$ and $1.8 < \log_{10}(r_\mathrm{h}) < 3$, with bin sizes of 0.25 and 0.1, respectively. From known M31 dwarf galaxies, we know that the transition from detected to undetected systems is within this range (Martin et al., 2016). For each of these bins, we generate an artificial galaxy with a random size and magnitude within the limits of this bin and ingest the photometry and position of its stars in the PAndAS catalogue at a random location within the considered field. Stars that fall in neighboring fields are kept but we remove any star of the artificial galaxy that falls in a CCD gap, in a hole between 2 fields or outside of the PAndAS footprint and we then test for the detection significance of this system (see below). This step is usually repeated 5 times so we can determine a recovery fraction for the studied magnitude-size bin and field. Ideally, we would like to ingest more than 5 artificial galaxies but, given the $\sim$ 400 fields and the number of bins in the magnitude-size plane, this already corresponds to about half a million ingested artificial galaxies and running the search algorithm 1000 times since ingesting all the artificial dwarf galaxies at once would lead to overlapping systems, change the properties of the survey, and bias the recovery rates. However, we will confirm below from a small subset of representative fields that ingesting only 5 artificial dwarf galaxies per M_V–$\log_{10}(r_\mathrm{h})$ bin and per field still yields reliable results.

Finally, we remove regions near known dwarf galaxies where the search algorithm would invariably return a detection, irrespective of the ingested system, and the regions close to M31 and M33, for which the search algorithm does not work well because of the complex mix of stellar populations (M13). We therefore mask regions within $4r_h$ of all known dwarf galaxies, as well as within $\sim$ 2 and $\sim$ 1 degrees of M31 and M33, respectively. In the south of the survey, a group of background nearby elliptical galaxies with globular clusters that masquerade as M31 RGB stars also needs to be masked out. We choose not to mask M31's globular clusters as they are rarely recovered by the search algorithm and only one of these is detected in M13 with a significance above 6. The resulting mask is shown in Figure IV.3. The detection limits of fields that are entirely within the masked regions are not determined and, for partially masked fields, we make sure to insert artificial dwarf galaxies in the non-masked part of the field.

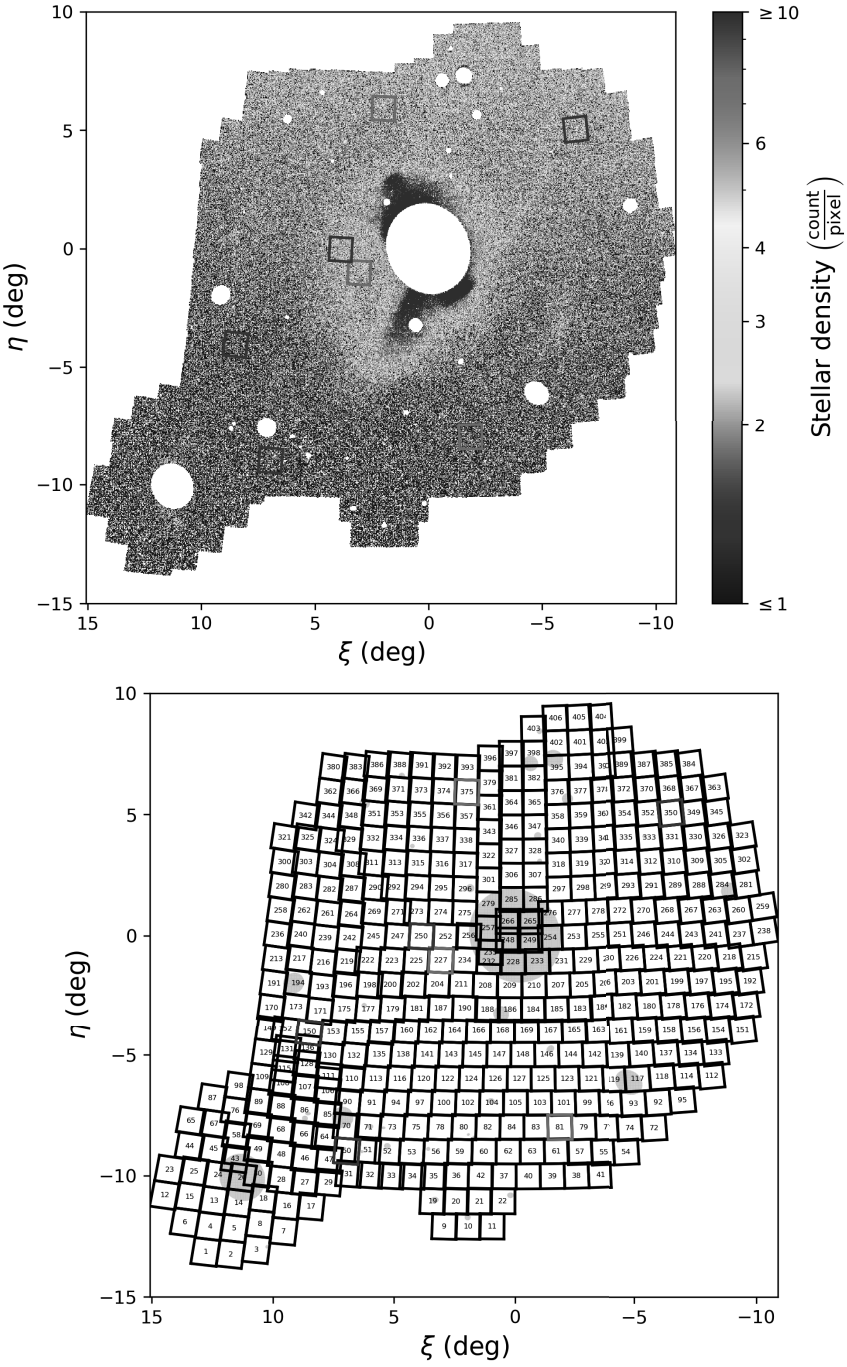

Figure IV.3: Local density of PAndAS stars in the CMD selection box (top panel). The white ellipses correspond to the regions we mask because of known stellar systems and the three fields chosen to be representative of the various regions of the survey are highlighted in red. The additional 4 fields used to test the effect of the distance on the recovery fractions are represented in purple. The bottom panel shows the distribution of PAndAS fields, following the numbering scheme of Ibata et al. (2014) and McConnachie et al. (2018). Masked regions are here shown in cyan.

Parameter	Minimal value	Maximal value	Step
$[\mathrm{Fe/H}]_{\mathrm{halo}}$	-1.3	-0.6	0.1
$[\mathrm{Fe/H}]_{\mathrm{dw}}$	-2.3	-1.1	0.3
r_{h}	$0.5'$	$3.5'$	$1'$
$\log_{10}(N)$	-0.5	4	0.5
η	0	1	0.1

Table IV.1: Ranges of parameters used to run the search algorithm

IV.3.2.b Set up of the search algorithm

To test for the recovery of an artificial galaxy, we use the algorithm developed by M13 to search for dwarf galaxies in the PAndAS survey. The algorithm is computationally costly to run as it determines the likelihood of there being a dwarf galaxy at all locations of PAndAS on a $0.5'$ grid (115 pc at the distance of M31), given the distribution of local RGB stars on the sky and in the color-magnitude space. The assumption is that this distribution can be well reproduced by three different components: one that simulates a metal-poor, compact dwarf galaxy, one that simulates the locally constant contamination of M31's halo stars, and a third part that represents the contamination from MW stars, following an empirically built model. We refer the reader to M13 for the full description of the search algorithm and its parametrization but we mention here our choices for the model parameter grid that we let the algorithm explore. Ideally, it would be best to explore a broad range of choices for all parameters of the model but, as mentioned in M13, this can be quite costly and we restrict the exploration to likely model parameters.

The five model parameters we focus on are:

- the metallicity of the dwarf galaxy, $[\mathrm{Fe/H}]_{\mathrm{dw}}$;
- the half-light radius of the dwarf galaxy r_{h};
- the number of stars in the dwarf galaxy component of the model, N;
- the metallicity of the M31 halo contamination, $[\mathrm{Fe/H}]_{\mathrm{halo}}$;
- the fractional contribution of MW stars to the total local contamination, η.

The 5-dimensional grid of parameters for which the algorithm determines a likelihood value are listed in Table IV.1. Similarly to M13, the favored model is the one that maximizes the likelihood and we use the comparison of this maximal likelihood with the likelihood of the best model with $N \simeq 0$ to determine the significance S of a detection.

Since we know the location of the artificial dwarf galaxies ingested in the survey catalogue, we can significantly save on computing time by only running the search algorithm near these locations. Therefore, we only test for the significance of a dwarf galaxy detection within

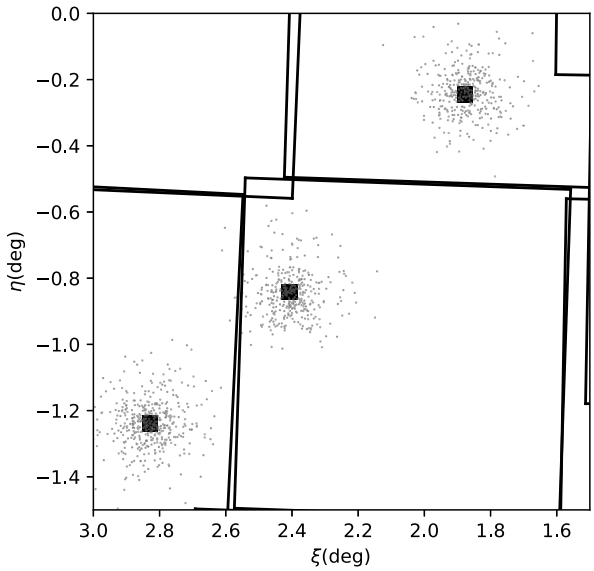

Figure IV.4: Example of the distribution of artificial dwarf galaxies stars in the survey (red points). The large polygons corresponds to the limits of the PAndAS fields in this region. The dark squares each correspond to the 7×7 test locations for the search algorithm, and are chosen to be around the known location of an artificial galaxy's center.

$\pm 1.5'$ of the known centers of ingested dwarf galaxies in both the ξ and η directions (or ± 3 steps on the spatial grid over which the algorithm is run)[2]. The corresponding locations are highlighted in Figure IV.4 for a run with artificial galaxies that have $r_{\rm h} = 1\,{\rm kpc}$.

IV.3.2.c Choice of the detection threshold

The search algorithm outputs the significance S of there being a dwarf galaxy at all tested locations but we still need to determine what constitutes a detection. If the threshold we consider for a detection is too low, it will lead to the detection of systems that would be too faint to be reliably classified as dwarf galaxies in PAndAS and it will not be possible to use the resulting detection limits to understand the M31 satellite system as seen by PAndAS. The threshold is derived from the distribution of significances determined by M13 for an area with low M31 and MW contamination near And XI-XIII (see their Figure 9). To determine expectations of detections stemming from noise in the data, we linearly fit the low significance tail of the significance distribution and choose as the significance threshold $S_{\rm th}$ the value of S that corresponds to less than one detection in this area of $\sim 9\,{\rm deg}^2$. This yields $S_{\rm th} = 6$. It is coherent with the significance from the dwarf galaxy with the lowest value of S that is

[2]We tested on the field 81 that the recovery fractions are similar when the significance calculations are made within a distance of $\pm 2.5'$ and $\pm 1.5'$ of the artificial galaxy center.

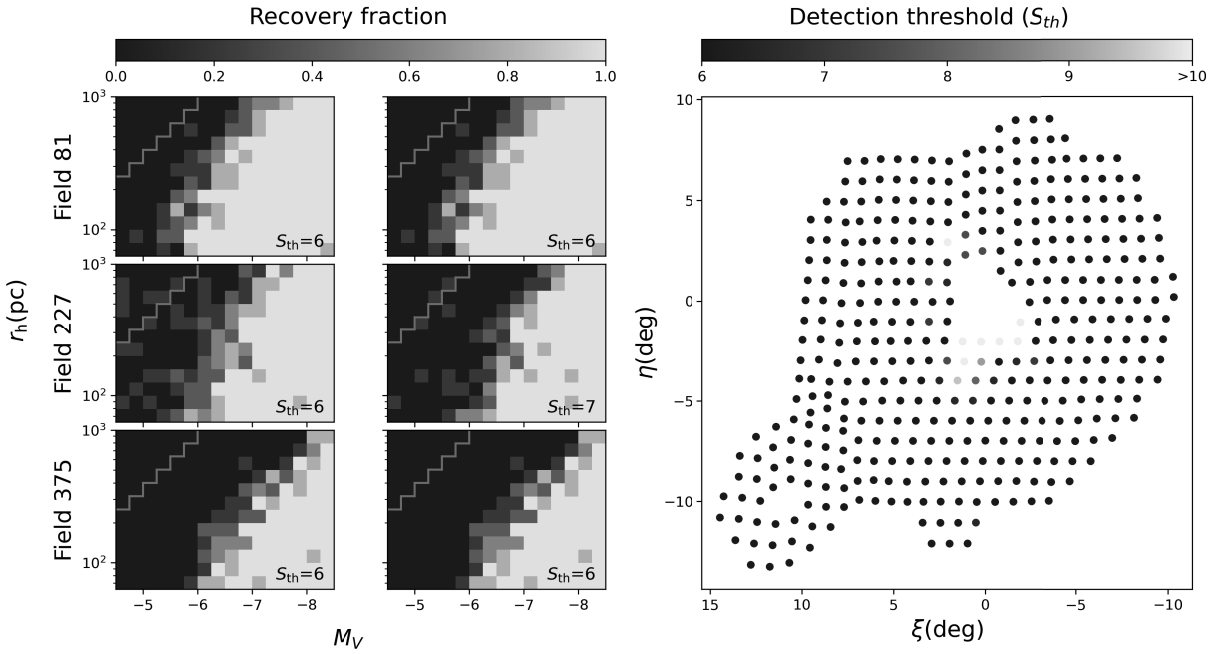

Figure IV.5: *Left:* Recovery fractions for 3 fields of the PAndAS survey, both with the common detection threshold value, $S_{\rm th}$=6, and with the updated threshold value determined to minimize the number of false positive in the region of large and faint dwarf galaxies that is highlighted in red. *Right:* Detection thresholds that are used for all considered PAndAS fields. Only fields with a high level of M31 stellar halo contamination have a higher $S_{\rm th}$ as the search algorithm struggles to always distinguish the structures of M31 and dwarf galaxies.

unambiguously detected, And XXVI, for which the algorithm determines $S_{\rm th} = 5.9$ (M13).

The dwarf galaxy recovery fractions for 3 representative fields are shown in Figure IV.5 for this threshold. These three fields are representative of an outer M31 halo region (field 81), a region contaminated by dense M31 stellar streams (field 227), and a region heavily impacted by the MW foreground contamination (field 375), as highlighted in Figure IV.3. We will discuss the recovery fractions in more detail in the next sub-section, but, at this stage, we wish to focus on the fact that, overall, they behave as expected with faint/compact dwarf galaxies recovered at a high fraction and larger and/or fainter systems showing lower detection rates. However, we note that for field 227 the recovery fractions are non-zero for systems that the search algorithm has no hope of detecting in PAndAS as they are too faint and too extended (region highlighted in red in the figure). This behavior is typical of fields that are heavily contaminated by M31 stellar structures. In these fields, the M31 streams have a color-magnitude distribution that is similar to what the algorithm searches for in a dwarf galaxy, which biases upwards the values of S. This was already shown by M13 and it forces us to increase the detection threshold for those fields to avoid false detections and unrealistically high recovery fractions. In practice, we increase $S_{\rm th}$ by steps of 0.5 until there are only at most 2 galaxies detected in the region of faint and extended dwarf galaxies highlighted in red in the top-left corner of the recovery-fraction panels of Figure IV.5. Our aim is to ensure a detection threshold that leads to only a very small number of false-positives, but to not have a threshold that is so conservative that only bright dwarf galaxies are recovered. The resulting recovery rate for field 227 is shown in the second column of panels of the figure, along with the map of final values of $S_{\rm th}$ throughout the survey in the right-hand panel. As expected, the nominal detection threshold value, $S_{\rm th} = 6$, is used for most fields and only fields close to M31 and significantly affected by M31 stellar halo structures require higher detection threshold values.

IV.3.3 The recovery-fraction model

The large amount of computing time required to determine the recovery fractions of artificial dwarf galaxies limits our calculations to only 5 simulated dwarf galaxies per field and per magnitude-size pixel, which leads to somewhat noisy recovery fractions. In this sub-section, we aim to build an analytical recovery-fraction model for each field to bypass these limitations.

The left-most column of panels in Figure IV.6 shows the outcome of the algorithm for the same three fields 81, 227, and 375 already discussed above. In this case, we run the algorithm with 20 galaxies per $(M_V, \log_{10}(r_{\rm h}))$ pixel and per field, to validate that the model we build on the regular simulations with only 5 dwarf galaxies per pixel are representative. In these panels, we also show the properties of known M31 dwarf galaxies located in the PAndAS survey (Martin et al. 2016). As expected, these known galaxies are located in the area of high recovery fractions but also cover the area of transition, in agreement with the

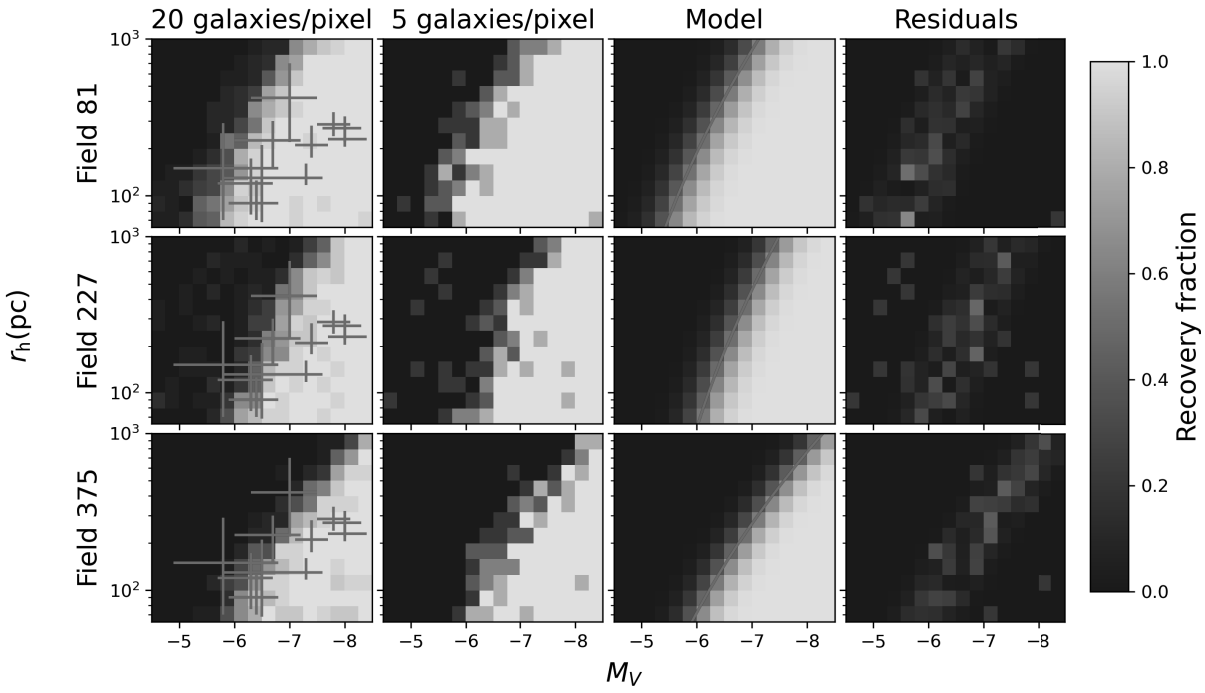

Figure IV.6: Recovery fractions for fields 81, 227, and 375. The first column of panels presents the recovery fractions when simulating 20 galaxies per field and per $(M_V, \log_{10}(r_h))$ pixel. The red dots correspond to known dwarf galaxies around M31. These straddle the transition region between no recovery and full recovery, as expected. The second column of panels presents the recovery fractions for only 5 galaxies per field and per $(M_V, \log_{10}(r_h))$ pixel. The third column shows the modeled recovery fractions. In these panels, the red line represents the 50-percent detection threshold. The fourth column displays the residuals that remain small, confirming that our model reproduces the recovery fractions well.

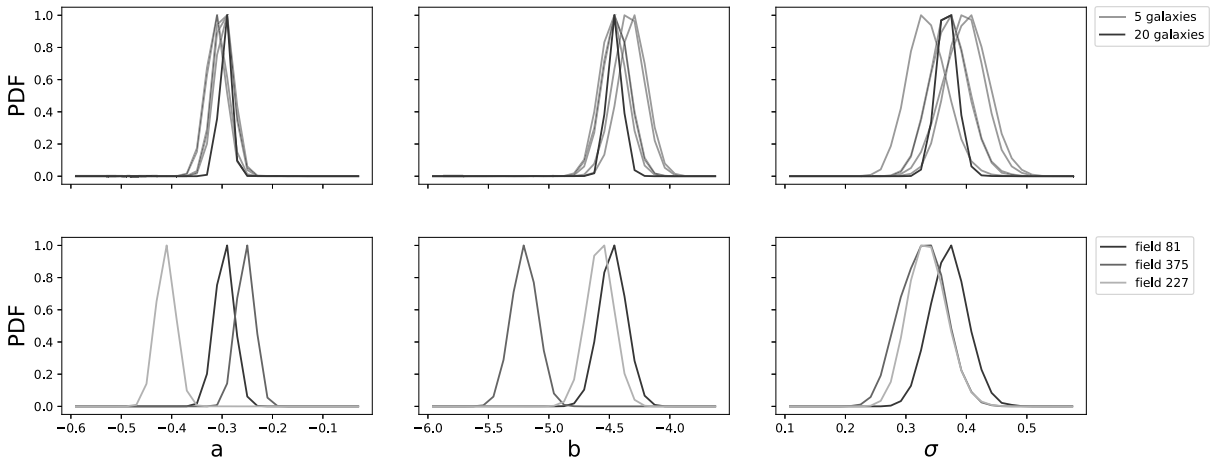

Figure IV.7: The top panels show the probability distribution functions for each parameter of the model for the case with 20 and 5 artificial dwarf galaxies per field and per $(M_V, \log_{10}(r_\mathrm{h}))$ pixel for the field 81. The bottom panels show the probability distribution functions for the case of 5 galaxies and for different fields. While using only 5 galaxies per pixel produces wider PDFs, as expected, these show no systematic bias compared to the PDFs resulting from the 20-galaxy case.

results of the search algorithm (M13) and our choice for the detection threshold values. For comparison, the second column of panels displays the recovery fractions of dwarf galaxies with our regular set up of 5 dwarf galaxies per pixel. It is reassuring that, even though the recovery fractions are here more noisy, as expected with fewer artificial galaxies, they do look similar to the more accurate results with 20 galaxies per pixel. We will provide a quantitative comparison below.

The recovery fractions behave as expected: high surface-brightness systems, i.e. compact and/or bright dwarf galaxies in the bottom-right half of the plots, are recovered at high efficiency while more extended and/or fainter systems are progressively missed by the search algorithm. The field contamination (mainly from the M31 stellar halo in field 227 or the MW in field 375) has an impact on the recovery fractions and, in general, degrades them. We note that, in the case of a high level of contamination from M31 stellar halo structures, the algorithm recovers a small number of large and faint dwarf galaxies below the transition region. As mentioned above, these are false detections and an artifact of the search algorithm that is sometimes struggling to discriminate contaminating M31 stream stars from the dwarf galaxy stars at the same location of the CMD because they all follow similar RGB tracks. However, this effect remains small since, as mentioned above, we adapt the threshold limit to minimize the presence of these false detections. This effect is not present for fields heavily contaminated by foreground MW stars (field 375 in Figure IV.6) since these contaminating stars have a color-magnitude distribution that is quite different from that of the M31 (artifi-

cial) dwarf galaxies (M13). In this case, the added contamination leads to recovery fractions that are shifted towards brighter and/or more compact systems.

We fit an analytical model to the recovery fractions to overcome the noise and the false detections. Given the shape of the recovery-fraction distributions, our analytical model is built around a quadratic transition region in the M_V–$\log_{10}(r_\mathrm{h})$ plane. We allow for the parameters of this quadratic transition to vary from field to field and we parametrize the width of the smooth transition between regions of full to no recovery.

We define the model for the recovery fraction of artificial dwarf galaxies as

$$\begin{aligned} f(M_V, \log_{10}(r_\mathrm{h})) &= F\left(\frac{M_V - M_{V,\mathrm{lim}}}{\sigma}\right), \\ \text{with } M_{V,\mathrm{lim}} &= a\log_{10}(r_\mathrm{h})^2 + b. \end{aligned} \tag{IV.2}$$

Here, a and b do not carry any significant physical meaning and are just used to parametrize the space, σ is the width of the transition, and F is the complementary error function, defined as

$$F(x) = \frac{1}{2}\,\mathrm{erfc}\left(\frac{x}{\sqrt{2}}\right). \tag{IV.3}$$

For each field, we fit the model to the recovery-fraction distribution in the M_V–$\log_{10}(r_\mathrm{h})$ plane by determining the likelihood of the data given the model thanks to a MetropolisHastings method. The variables a, b and σ are only used to parametrize the model, the important result is the threshold in surface brightness (which we will use for further analyses). Then, the best set of parameters is obtained by calculating the binomial likelihood of the number of recovered dwarf galaxies compared to the model. For the three representative fields and the case with 5 artificial galaxies per pixel, the resulting best fit models are displayed in the third column of panels in Figure IV.6, with the residuals shown in the fourth column. The models provide a good representation of the recovery fractions and the residuals remain small.

To confirm that we do not introduce any bias by simulating only 5 galaxies per $(M_V, \log_{10}(r_\mathrm{h}))$ pixel, in Figure IV.7, we compare the marginalized probability distribution functions (PDFs) obtained for the three parameters in the fields 81 when using 20 (dashed lines) and subsamples of 5 (full lines) simulated galaxies per pixel. Even though they are, as expected wider, we find no systematic bias in the PDFs obtained when using only 5 dwarf galaxies per pixel. Therefore, we go ahead and determine the recovery fractions with 5 artificial galaxies per pixel and per field as it already represents more than 90 000 CPU hours on the Strasbourg University High Performance Computing center for the simulations over the $\sim$ 400 PAndAS fields.

IV.4 Results

IV.4.1 Dwarf galaxy recovery fractions over the PAndAS survey

Figure IV.8 summarizes the recovery fractions of all studied PAndAS fields after ingesting more than 350,000 artificial dwarf galaxies in the stellar catalogue. The top three panels of the figure show, for each field, the values of the three model parameters over the survey. There are some clear changes to the values of parameters a and b that can be tracked to changes in the properties of the survey: the north-south gradient is linked to the increased MW foreground contamination towards the north and the presence of the Giant Stream south of M31 ($0 \lesssim \xi \lesssim 5°$ and $-5 \lesssim \eta \lesssim 0°$) clearly impacts the values of a. On the other hand, the speed of the transition, parametrized by σ, remains fairly constant over the survey.

The slope of the transition region in the $\log_{10}(r_{\rm h})$–M_V plane does not map lines of constant surface brightness. While this is common (e.g. Koposov et al., 2008; Walsh et al., 2009; Drlica-Wagner et al., 2020) and is likely related to the complex nature of the data and of the search algorithm, it can make it difficult to interpret our results in term of surface brightness limits. We therefore show, in the bottom panel of Figure IV.8, the corresponding surface brightness, μ_{250}, within the half-light radius of a system for a fixed $r_{\rm h} = 250\,{\rm pc}$. Most fields show $29 < \mu_{250} < 30$ mag/arcsec^2, with a clear impact from the MW contamination that is significantly more important on the northern side of the survey that reaches Galactic latitude $b\ -12°$. One can also note the impact of the M31 stellar halo contamination in the regions nearest M31. The necessity to increase the detection threshold $S_{\rm th}$ to avoid false-positives is partly responsible (Figure IV.6) but the lower surface brightness limit is also linked to a lower contrast because of a higher density of contaminating M31 stars. The model parameters for all fields are listed in Table A.

IV.4.2 Impact of fixed artificial dwarf galaxy parameters

As mentioned in Section IV.3, we fixed some of the supposedly less impactful parameters of the artificial dwarf galaxies to save on the computing time that is already quite large. Here, we test the impact of these parameters on the recovery fraction model parameters for seven representative fields of the survey. Those are chosen to be dispersed throughout the survey to represent different types of contamination.

To determine the impact of the distance to the artificial dwarf galaxies, we conduct a set of simulations with 5 galaxies/pixel and distances that vary between $\pm 300\,{\rm kpc}$ of the distance to M31 that is assumed for the main run. The resulting variations in the recovery model parameters are shown in the Figure IV.9 for steps of 150 kpc. One can expect that for a closer/further distance, the recovery fractions shown in Figure IV.6 would simply shift to the top-left/bottom-right. This is indeed the main effect that we seen in the left-hand panel of Figure IV.9, with b typically shifting by the distance modulus change that corresponds to the distance change. We note, however that changes in the distance to the artificial dwarf galaxies also have some impact on a of the recovery fraction model (middle panel). While the reason for this correlation is not readily evident, it may be related to the algorithm needing a

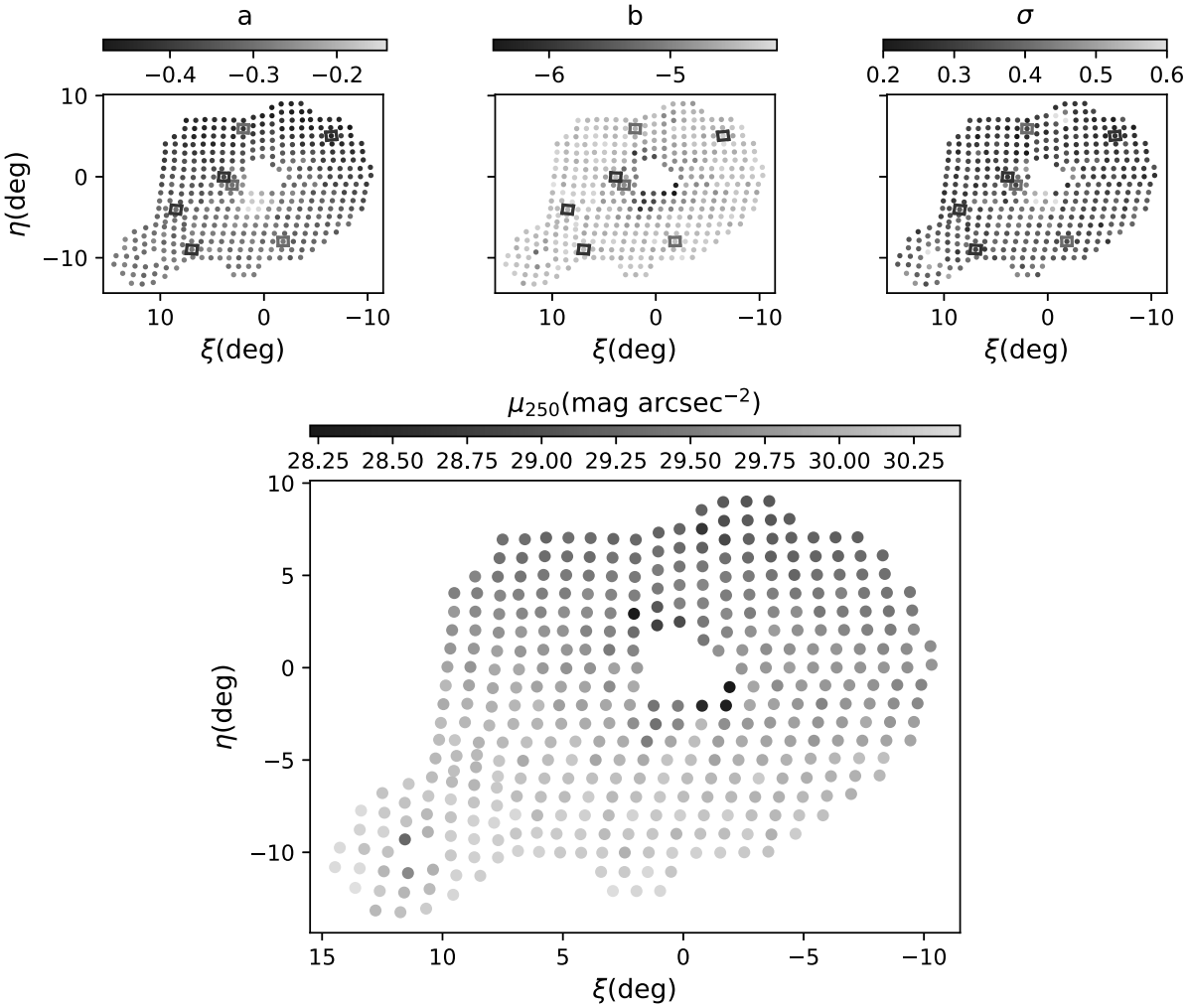

Figure IV.8: Values of the favored model parameters, a, b and σ, for each field in the PAndAS survey (top three panels). The bottom panel translates those into the surface brightness within the half-light radius 50% detection limit for a dwarf galaxy with $r_{\rm h} = 250\,{\rm pc}$ (see text for more details). The fields highlighted in red are those chosen to be representative of the different regions of the survey while those represented in purple are the additional fields use to test the impact of the distance on the recovery fractions. The surface brightness thresholds varie depending on the position: in regions with low contamination fainter galaxies can be detected compared to regions with significant M31 or MW contamination.

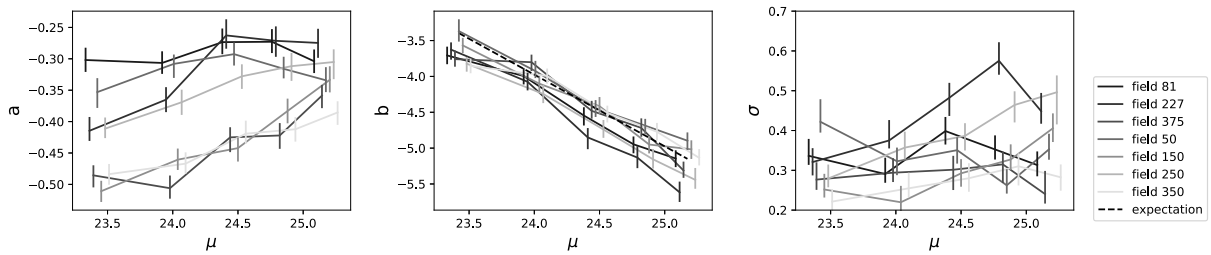

Figure IV.9: Changes to the best parameters of the recovery fraction model as a function of the distance modulus to the dwarf galaxy. Each point is slightly shifted in distance, in order to make the graph more legible. The black dashed line represents the theoretical change of M_V in function of the distance modulus for the field 50. Parameters a and b smoothly change with distance, which allows us to easily model the influence of the distance on the recovery fractions.

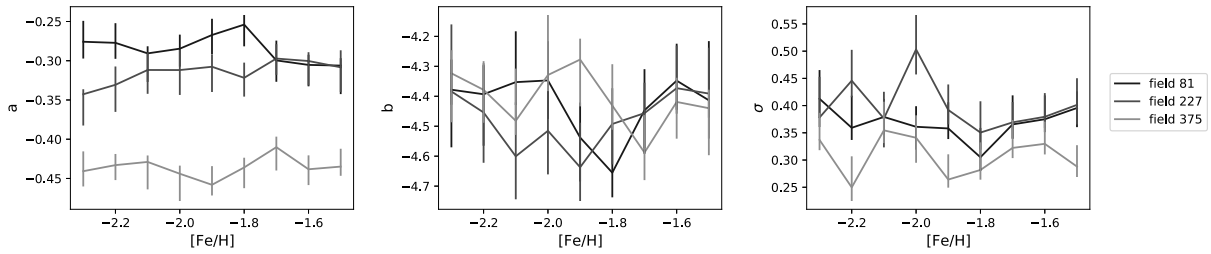

Figure IV.10: Changes to the best parameters of the recovery fraction model as a function of a dwarf galaxy's metallicity. Variation to the metallicity within this metal-poor range do not significantly change the parameters of the model.

minimum number of stars in the M31 CMD box to yield a reliable detection, with a smaller impact from the size of the system in this regime. Such an effect would tend to make the slope of the transition region of the recovery fractions steeper as the number of stars in the CMD box becomes smaller. It could explain why more distant artificial galaxies, which have fewer stars in the magnitude-limited CMD box, yield higher values of a.

Irrespective of the reason for the changes of a and b with distance, these anticorrelations are regular and can easily be modeled. This has the benefit of preventing numerous additional simulations while still taking into account that dwarf galaxies significantly in front or behind M31 have somewhat different recovery fractions. We therefore fit a linear model to the values of a and b shown in Figure IV.9, using the data from all fields together, but allowing for different intercepts for each field. We define as a_0 and b_0 the intercepts (their values are accessible in the appendix) and μ the distance modulus. The resulting fits yield

$$\begin{aligned} a &= 0.06\mu + a_0, \text{and} \\ b &= -0.89\mu + b_0. \end{aligned} \tag{IV.4}$$

The third parameter of the model, σ, which represents the width of the transition region of the recovery fractions in the $\log_{10}(r_\mathrm{h})$–M_V space, shows no significant changes with distance. We therefore assume that it is not impacted by changes in the distance to the dwarf galaxies.

In Section IV.3, we also fixed the metallicity of the metal-poor artificial dwarf galaxies to [Fe/H] $= -1.7$ as the color of the RGB only shifts slightly in color in this metal-poor regime. The impact of this choice of metallicity is explored by determining the recovery fraction for artificial galaxies in the range $-2.3 <$ [Fe/H] < -1.5, with steps of 0.1 dex, for fields 81, 227, and 375. The results are statistically similar over the metallicity range, as shown in Figure IV.10. We conclude that the impact of [Fe/H] on the recovery fraction is negligible and that our assumption of [Fe/H] $= -1.7$ does not affect our results.

IV.4.3 Using the recovery fractions

To facilitate the use of the previous results and, for instance, easily apply the PAndAS recovery fraction to sets of simulated dwarf galaxy satellite system, we make public a python module that is accessible at `https://github.com/dolivadolinsky/Recovery_dwarf_galaxy_M31`. Given the cartesian coordinates of a dwarf galaxy around its host, its half-light radius, and its V-band magnitude, this module returns the probability that such a dwarf galaxy would have been discovered in PAndAS. The module first determines the fields in which the tested dwarf galaxy would be located or if it is outside the PAndAS footprint. If there is an overlap of fields, the parameters values for the galaxy are the ones of the deepest photometry. Then, the relations described in Section IV.4.2 are used to determine the values of a and b at the galaxy's distance in order to retrieve the recovery fractions.

IV.5 Discussion and conclusion

In this paper, we determined the recovery fraction of Andromeda's dwarf galaxy based on the algorithm of M13 applied to the photometric data from the PAndAS survey. We repeatedly simulated artificial dwarf galaxies, blindly added them to the PAndAS photometric catalogue, and checked the significant of their recovery by running the search algorithm. We determined and modeled the recovery fractions of satellites on a field-to-field basis for the 390 $1^\circ \times 1^\circ$ fields of the survey and as a function of a dwarf galaxy's magnitude, half-light radius, and heliocentric distance. We publish the resulting recovery fraction as a python module that provides the probability of observing a dwarf galaxy of a given magnitude, half-light radius, and distance in the PAndAS survey.

As expected, we found that the recovery fractions are highly sensitive to the size and luminosity of a dwarf galaxy but also to its position due to the significant changes in the level of MW and M31 stellar halo contamination throughout the PAndAS footprint. Constant recovery fractions do not map constant surface brightness levels, likely because of the complex nature of the data and of the search algorithm. For galaxies with $r_{\rm h} = 250\,{\rm pc}$, the surface brightness threshold that corresponds to a 50-percent detection rate mainly varies between $\sim 29.0\,{\rm mag\ arcsec^{-2}}$ and $30.0\,{\rm mag\ arcsec^{-2}}$, with a median value of 29.8. These results are in good agreement with the surface brightness of genuine dwarf galaxies discovered in PAndAS (Martin et al., 2016). Depending on the field of the survey these limits can be as low as $28.0\,{\rm mag\ arcsec^{-2}}$ or as high and $30.5\,{\rm mag\ arcsec^{-2}}$. The completeness of the survey also depends on the distance to a dwarf galaxy but this variation of the surface brightness threshold roughly maps expectations from changes to the distance modulus.

Our results bear similarities with studies based on other data sets but using the same methodology of inserting stars from artificial dwarf galaxies at the photometric catalogue level. Even if the given surface brightness threshold values are not always comparable, we can calculate the μ_{250} values based on the results from other studies. Koposov et al. (2008) and Walsh et al. (2009) derive $\mu_{250} \sim 28$ mag arcsec^{-2} at the distance of M31, but for the significantly shallower SDSS data and without considering the specific of the region around M31 that becomes significantly contaminated by foreground MW stars. Recently, Drlica-Wagner et al. (2020) determined dwarf galaxy recovery fractions for a large part of the sky from both the Pan-STARRS1 and DES photometric data. The surface brightness thresholds obtained for the two surveys in this study are 28 and 30 mag arcsec^{-2}, respectively. It may seem surprising that these results based on the DES are similar to those we obtain for the deeper PAndAS data. First, we note that the PAndAS footprint (latitude $|{\rm b}| \sim 22^\circ$) is more contaminated by MW and M31 stars than a typical DES field (latitude $|{\rm b}| \geq 30^\circ$). In addition, the surface brightness limits are sensitive to the distance and the depth of surveys as well as the algorithm use to search for dwarf galaxies, those can be an explanation for the similarity between the DES thresholds and the ones obtained in this work. Finally, the detection threshold ($S_{\rm th}$ in our work) used by Drlica-Wagner et al. (2020) to determine if an

artificial dwarf galaxy is recovered is particularly low ($S_{\rm th} = 4.9$). In fact, it is lower than the value $S_{\rm th} = 6.0$ used by (Drlica-Wagner et al., 2015) to detect candidate satellite like Tucana V or Cetus II that were not confirmed as well-defined, localized stellar overdensities from deeper photometry (Conn et al., 2018a,b). A particularly aggressive detection threshold would naturally lead to deeper detection limits, but these would be over-estimated compared to the detection limits of genuine dwarf galaxies as the low threshold would lead to false positives in the list of candidate detections.

It is also interesting to compare our results with those of Garling et al. (2021) for the more distant galaxies NGC 3077 and NGC 4214, located more than 3 Mpc away. While the data of the LBT-SONG survey used by these authors are comparable or deeper than the PAndAS data, the larger distance forces them to ingest artificial dwarf-galaxy stars directly in the images to properly account for crowding that becomes an issue because of the smaller angular size of the systems. Their analysis yields $\mu_{250} \sim 28$ mag arcsec^{-2}, towards the brighter end of the detection limits we determined from M31 and shows one of the limitations of ground-based surveys beyond the Local Group.

Finally, we compare our results with the ones of Huxor et al. (2014), who determined the globular cluster completeness of the PAndAS survey. They found a 50% detection surface brightness inside the half-light radius threshold of $\sim 26\,{\rm mag/arcsec^2}$. Compared to our results, the brighter limit can be explain by the fact that they looked for more compact object and that the search for globular cluster was performed through visual inspection of the images.

The work presented here complements our build up of a thorough understanding of the dwarf galaxy satellite system of M31 (Martin et al., 2013a, 2016) by clearly expressing the limits to our dwarf galaxy searches within the PAndAS survey. Our results can be seen as an intermediate step towards the dwarf galaxy searches that will be possible within $\sim 1\,{\rm Mpc}$ with the next generation of ground-based photometric surveys like the Legacy Survey of Space and Time (LSST; Ivezić et al., 2019). More immediately, we aim to use these recovery fractions to infer the underlying properties of the M31 dwarf galaxy satellite system (number of dwarf galaxies, distribution, size-luminosity relation, etc.) to provide constraints on dwarf galaxy formation and evolution in a cosmological context (Doliva-Dolinsky et al., in preparation).

Edward Potthast, Starry Night, 1918

Chapter V

Global Properties of M31 Satellite System

The PAndAS View of the Andromeda Satellite System. IV Global properties

Amandine Doliva-Dolinsky, Nicolas F. Martin, Zhen Yuan, Alessandro Savino, Daniel R. Weisz, Annette M. N. Ferguson, Rodrigo A. Ibata, Stacy Y. Kim, Geraint F. Lewis, Alan W. McConnachie, Guillaume F. Thomas

Astrophysical Journal, 2023, 952, 72

Abstract

We build a statistical framework to infer the global properties of the satellite system of the Andromeda galaxy (M31) from the properties of individual dwarf galaxies located in the Pan-Andromeda Archaeological Survey (PAndAS) and the previously determined completeness of the survey. Using forward modeling, we infer the slope of the luminosity function of the satellite system, the slope of its spatial density distribution, and the size-luminosity relation followed by the dwarf galaxies. We find that the slope of the luminosity function is $\beta = -1.5 \pm 0.1$. Combined with the spatial density profile, it implies that, when accounting for survey incompleteness, M31 hosts 92^{+19}_{-26} dwarf galaxies with $M_V < -5.5$ and a sky-projected distance from M31 between 30 and 300 kpc. We conclude that many faint or distant dwarf galaxies remain to be discovered around Andromeda, especially outside the PAndAS footprint. Finally, we use our model to test if the higher number of satellites situated in the hemisphere facing the Milky Way could be explained simply by the detection limits of dwarf galaxy searches. We rule this out at $> 99.9\%$ confidence and conclude that this anisotropy is an intrinsic feature of the M31 satellite system. The statistical framework we present here is a powerful tool to robustly constrain the properties of a satellite system and compare those across hosts, especially considering the upcoming start of the Euclid or Rubin large

photometric surveys that are expected to uncover a large number of dwarf galaxies in the Local Volume.

V.1 Introduction

During the last decades, faint dwarf galaxies ($L < 10^6\,L_\odot$) have proven to be powerful testbeds for cosmological and galaxy formation models. The majority of these constraints are obtained from the dwarf galaxy satellite system of the Milky Way (MW) (e.g., Koposov et al., 2009; Kim et al., 2018; Nadler et al., 2021) because of the difficulty to detect those faint objects beyond our immediate surroundings with current panoptic photometric surveys (e.g., Koposov et al., 2008; Drlica-Wagner et al., 2020). However, as the Milky Way satellites and past satellite accretion may not be typical (e.g., Martin et al., 2017; Weisz et al., 2019; Evans et al., 2020), it is important to explore the satellite systems of other similar hosts, the most accessible of which is the Andromeda galaxy (M31).

M31 and the cohort of dwarf galaxies that inhabit its halo are close enough ($\sim 800\,$kpc; Savino et al., 2022) to be resolvable into stars with modern observing capabilities. At the turn of the century, systematic efforts were undertaken to survey the surroundings of our cosmic neighbor, with the Sloan Digital Sky Survey (SDSS Abazajian et al., 2003) and, more particularly, with the Pan-Andromeda Archaeological Survey (PAndAS McConnachie et al., 2018), the sample of known dwarf galaxies near M31 has increased significantly. From about 10 dwarf galaxies known at the end of the twentieth century (Herschel, 1789; van den Bergh, 1972; Karachentsev & Karachentseva, 1999), we now know of ~ 40 dwarf galaxies that are likely satellites of Andromeda. Four of those were discovered from SDSS photometry (Zucker et al., 2004a, 2007; Bell et al., 2011; Slater et al., 2011), four from more fortuitous efforts (Majewski et al., 2004; Irwin et al., 2008; Collins et al., 2022; Martínez-Delgado et al., 2022), three from searches based on the Pan-STARRS1 survey (Martin et al., 2013c,b), and, mainly, 19 from the exploration of the deeper PAndAS data (Martin et al., 2006; Ibata et al., 2007; McConnachie et al., 2008; Martin et al., 2009; Richardson et al., 2011). Because they are significantly more distant than their MW counterparts, these newly discovered dwarf galaxies are also somewhat brighter than the faintest MW dwarf galaxy satellites but they nevertheless reach total luminosities as faint as $10^{4.2\pm0.4}\,L_\odot$ ($M_V = -6.0^{+0.7}_{-0.5}$ for And XXVI; Savino et al. 2022).

Beyond the mere discovery of satellites, it is essential to also quantify the completeness of those large surveys (Koposov et al., 2008; Drlica-Wagner et al., 2020) as these are key ingredients to properly fold in observational biases when comparing the known dwarf galaxies (or dwarf galaxy systems) between themselves or with simulations of the faint-end of galaxy formation in a given cosmological model. This step in turn requires building well-understood search algorithms that can be run on artificial dwarf galaxies injected in the survey data. In the case of the PAndAS survey, Martin et al. (2013a) developed a likelihood-based algorithm that runs on the survey's photometric catalogue and determines the probability of there

being a dwarf galaxy at any location of the survey based on the distribution of local stars on the sky and in the color-magnitude space. Doliva-Dolinsky et al. (2022) then used this algorithm to characterize the detection limits of the survey, injecting half a million artificial dwarf galaxies with varying sizes, luminosities, and positions. The resulting detection limits show significant variations that are driven, as expected, by the size and luminosity of the systems (i.e., their surface brightness), but also by the location in the survey. With PAndAS spanning more than 20° on the sky and M31 being located fairly close to the Milky Way plane ($b = -22°$), the strongly varying MW foreground contamination between the southern edge of the survey ($b \sim -35°$) and its northern edge ($b \sim -11°$) leads to significant variations of the surface brightness limits (from $\sim$30.5 mag/arcsec^2 far from the MW plane to $\sim$29 mag/arcsec^2 closest to the plane, respectively). As shown in Doliva-Dolinsky et al. (2022), variations in the foreground contamination are at least as important as changes to the heliocentric distance of a satellite. Both lead to variations of ~ 1.5 mag/arcsec^2 in the surface brightness detection limit over the M31 halo.

With this knowledge in mind, it is possible to reliably infer the global properties of the dwarf galaxy satellite system of M31, taking detection limit biases into account. Among those global properties, the shape of its luminosity function is an important observational probe as it is sensitive to cosmology, to feedback processes and to reionization. Indeed, the normalization, shape and/or the existence of a break in the faint-end of the luminosity function is an imprint of the properties of dark matter (Spergel & Steinhardt, 2000; Bode et al., 2001) and of the suppression of star formation from stellar outflows and reionization (Bullock et al., 2000; Somerville, 2002; Mashchenko et al., 2008; Koposov et al., 2009; Wheeler et al., 2015; Boylan-Kolchin et al., 2015; Weisz & Boylan-Kolchin, 2017). The radial distribution of dwarf galaxy satellites around their host can also be shaped by the physics of reionization (Ocvirk & Aubert, 2011; Dooley et al., 2017) and the disruption of subhaloes by the central disk (D'Onghia et al., 2010; Kelley et al., 2019; Samuel et al., 2020).

Another challenge comes from the distribution of satellites that does not appear as isotropic as expected from ΛCDM (Pawlowski, 2018). Disk-like distributions of satellite dwarf galaxies have been found around the MW, M31 and Centaurus A (Lynden-Bell, 1976; Kroupa et al., 2005; Metz et al., 2007; Conn et al., 2013; Ibata et al., 2013; Müller et al., 2018). In addition, when looking at the position of M31 dwarf galaxies, most of them appear to lie closer to the MW than on the opposite hemisphere (McConnachie & Irwin, 2006; Conn et al., 2012; Wan et al., 2020). With updated RRLyrae-based distances, Savino et al. (2022) reenforces those conclusions, further highlighting the anisotropy in the M31 satellite distribution. The detection limits of dwarf galaxy searches could lead to an anisotropy between the close and far hemispheres of M31 as the farther the dwarf galaxy the harder it is to detect. It is therefore essential to fold in these detection limits when inferring the global properties of the M31 satellite system to check if this anisotropy could simply be the results of observational biases.

Faced with the issue of comparing biased, incomplete observations with models, it may

seem more convenient and straightforward to simply correct observed properties, for instance a binned luminosity function, with correction factors calculated from the detection limits. This technique is however plagued by noise in the case of small samples, as is the case for dwarf galaxy systems. Therefore, while it is computationally more expensive, it is much more reliable to forward model the limitations of the data (detection limits, irregular shape of the survey) directly into the model; this is the approach that we follow here.

We use a forward-modeling approach to infer the combined properties of the luminosity function, the radial distribution, and the size-luminosity relation of the dwarf galaxy system of M31. In Section V.2, we detail the sample of observed satellites and the dwarf galaxy completeness of PAndAS. Section V.3.1 and V.3.2, describes the framework and the model used to obtain the results presented in Section V.4. Finally, we summarize and discuss the main properties of the dwarf galaxy satellite system of M31 in Section V.5.

V.2 Sample

PAndAS (McConnachie et al., 2009, 2018) was conducted from 2008 - 2011 with the 1 square degree MegaCam wide field image at the Canada-France-Hawaii Telescope (CFHT). Combined with previous observations (Ibata et al., 2007; McConnachie et al., 2008), this Large Program resulted in a survey of over 400 square degrees surrounding M31 and M33, reaching out to ~ 150 kpc and ~ 50 kpc in projected distance from these galaxies, respectively. For the details of the survey and the creation of the catalogues, we refer the reader to McConnachie et al. (2018), but it is worth mentioning that the g and i band photometry is obtained for all fields with a median depth of 26.0 and 24.8 for 5σ detections, respectively (Ibata et al., 2014).

The 24 dwarf galaxies known within this footprint are listed in Table V.1. As the search algorithm struggles to separate dwarf galaxies from stellar structures near M31 (Martin et al., 2013a) and as the completeness in this region is not well constrained, we choose to mask the inner 30 kpc. The luminosity and size of each dwarf galaxy are taken from Martin et al. (2016) and Savino et al. (2022). Where needed, distance-related properties (physical half-light radii, absolute magnitudes) are updated using the distances from Savino et al. (2022). Given the uncertain nature of And XXVII that may well be a disrupted system (Preston et al., 2019) and has large uncertainties in its structural properties (Richardson et al., 2011; Martin et al., 2016), we choose not to add it to our sample.

The search for dwarf galaxies suffers from spatial and photometric incompleteness. The former arises from the complex PAndAS coverage on the sky and its correction is quite straightforward, while the latter stems from the complex detection process and is very sensitive to the characteristics of a given dwarf galaxy but also to its location within the survey, mainly because of the varying MW and M31 stellar contamination. The detection limits were derived by Doliva-Dolinsky et al. (2022) via the injection of nearly half a million artificial dwarf galaxies in the PAndAS catalogue to obtain the recovery fraction for each MegaCam

Table V.1: Sample of the dwarf galaxies present in the PAndAS survey.

Name	α(J2000)	δ(J2000)	rh($'$)	m_V	$D_{\rm MW}(kpc)$	M_V	rh(pc)	$D_{\rm M31}$(kpc)	Recovery fraction
And I	$00^{\rm h}45^{\rm m}39.7^{\rm s}$	$+38°02'15''$	$3.9^{+0.1}_{-0.1}$	$13.1^{+0.2}_{-0.2}$	775^{+19}_{-17}	-11.4±0.2	880^{+31}_{-30}	$48.0^{+10}_{-3.2}$	1.00
And II	$01^{\rm h}16^{\rm m}26.8^{\rm s}$	$+33°26'07''$	$5.3^{+0.1}_{-0.1}$	$12.4^{+0.2}_{-0.2}$	667^{+16}_{-15}	-11.7±0.2	1028^{+31}_{-30}	168.9^{+19}_{-16}	1.00
And III	$00^{\rm h}35^{\rm m}30.9^{\rm s}$	$+36°29'56''$	$2.0^{+0.2}_{-0.2}$	$14.8^{+0.2}_{-0.2}$	721^{+17}_{-16}	-9.5±0.2	420±43	84.9^{+19}_{-14}	1.00
And V	$01^{\rm h}10^{\rm m}17.5^{\rm s}$	$+47°37'42''$	$1.6^{+0.2}_{-0.1}$	$15.1^{+0.2}_{-0.2}$	759^{+21}_{-20}	-9.3±0.2	353^{+35}_{-24}	$110.5^{+7}_{-3.5}$	1.00
And IX	$00^{\rm h}52^{\rm m}53.4^{\rm s}$	$+43°11'57''$	$2.0^{+0.2}_{-0.2}$	$15.6^{+0.3}_{-0.3}$	702^{+19}_{-20}	-8.6±0.3	408^{+62}_{-42}	82.0^{+26}_{-24}	1.00
And X	$01^{\rm h}06^{\rm m}35.4^{\rm s}$	$+44°48'27''$	$1.1^{+0.4}_{-0.2}$	$16.7^{+0.3}_{-0.3}$	630^{+18}_{-18}	-7.3±0.3	202^{+74}_{-37}	162.2^{+25}_{-24}	1.00
And XI	$00^{\rm h}46^{\rm m}19.7^{\rm s}$	$+33°48'10''$	$0.6^{+0.2}_{-0.2}$	$18.0^{+0.4}_{-0.4}$	751^{+23}_{-22}	-6.4±0.4	131±44	$104.2^{+11}_{-4.2}$	0.97
And XII	$00^{\rm h}47^{\rm m}28.3^{\rm s}$	$+34°22'38''$	$1.8^{+0.2}_{-0.7}$	$17.7^{+0.5}_{-0.5}$	718^{+25}_{-26}	-6.6±0.5	376^{+251}_{-147}	107.7^{+20}_{-13}	0.80
And XIII	$00^{\rm h}51^{\rm m}51.0^{\rm s}$	$+33°00'16''$	$0.8^{+0.4}_{-0.3}$	$17.8^{+0.4}_{-0.4}$	821^{+28}_{-26}	-6.8±0.4	191^{+96}_{-72}	$126.4^{+16}_{-8.0}$	0.99
And XIV	$00^{\rm h}51^{\rm m}35.0^{\rm s}$	$+29°41'23''$	$1.5^{+0.2}_{-0.2}$	$15.8^{+0.3}_{-0.3}$	773^{+21}_{-21}	-8.6±0.3	337±46	$160.8^{+3.8}_{-4.2}$	1.00
And XV	$01^{\rm h}14^{\rm m}18.3^{\rm s}$	$+38°07'11''$	$1.3^{+0.1}_{-0.1}$	$16.0^{+0.3}_{-0.3}$	746^{+17}_{-18}	-8.4±0.3	283±23	$95.8^{+12}_{-4.8}$	1.00
And XVI	$00^{\rm h}59^{\rm m}30.3^{\rm s}$	$+32°22'34''$	$1.0^{+0.1}_{-0.1}$	$16.1^{+0.3}_{-0.3}$	517^{+18}_{-19}	-7.5±0.3	239±25	280.0^{+26}_{-27}	1.00
And XVII	$00^{\rm h}37^{\rm m}06.3^{\rm s}$	$+44°19'23''$	$1.4^{+0.3}_{-0.3}$	$16.6^{+0.3}_{-0.3}$	757^{+24}_{-23}	-7.8±0.3	315±68	$49.9^{+17}_{-5.8}$	1.00
And XIX	$00^{\rm h}19^{\rm m}34.5^{\rm s}$	$+35°02'41''$	$14.2^{+3.4}_{-1.9}$	$14.5^{+0.3}_{-0.3}$	813^{+31}_{-31}	-10.1±0.3	3357^{+816}_{-465}	$113.3^{+18}_{-6.9}$	1.00
And XX	$00^{\rm h}07^{\rm m}30.6^{\rm s}$	$+35°07'37''$	$0.4^{+0.2}_{-0.1}$	$18.0^{+0.4}_{-0.4}$	741^{+27}_{-27}	-6.4±0.4	86^{+43}_{-22}	$128.4^{+12}_{-5.5}$	0.98
And XXI	$23^{\rm h}54^{\rm m}47.9^{\rm s}$	$+42°28'14''$	$4.1^{+0.8}_{-0.4}$	$15.5^{+0.3}_{-0.3}$	770^{+23}_{-22}	-8.9±0.3	922^{+182}_{-95}	$124.4^{+5.1}_{-3.8}$	1.00
And XXII	$01^{\rm h}27^{\rm m}40.4^{\rm s}$	$+28°05'25''$	$0.9^{+0.3}_{-0.2}$	$18.0^{+0.4}_{-0.4}$	754^{+24}_{-23}	-6.4±0.4	$198\ ^{+66}_{-44}$	$216.8^{+5.7}_{-5.6}$	0.90
And XXIII	$01^{\rm h}29^{\rm m}21.0^{\rm s}$	$+38°43'26''$	$5.4^{+0.4}_{-0.4}$	$14.6^{+0.2}_{-0.2}$	745^{+24}_{-25}	-9.8±0.2	1170^{95}_{94}	$128.1^{10}_{-4.9}$	1.00
And XXIV	$01^{\rm h}18^{\rm m}32.7^{\rm s}$	$+46°22'13''$	$2.6^{+1}_{-0.5}$	$16.3^{+0.3}_{-0.3}$	609^{+19}_{-20}	-7.6±0.3	460^{+178}_{-90}	194.5^{+25}_{-24}	0.92
And XXV	$00^{\rm h}30^{\rm m}09.9^{\rm s}$	$+46°51'41''$	$2.7^{+0.4}_{-0.2}$	$15.3^{+0.3}_{-0.2}$	752^{+23}_{-23}	$-9.1^{+0.3}_{-0.2}$	590^{+90}_{-47}	$85.2^{+12}_{-4.4}$	1.00
And XXVI	$00^{\rm h}23^{\rm m}46.3^{\rm s}$	$+47°54'43''$	$1.0^{+0.6}_{-0.5}$	$18.5^{+0.7}_{-0.5}$	786^{+24}_{-23}	$-6.0^{+0.7}_{-0.5}$	229^{+138}_{-115}	$104.6^{+6.8}_{-3.5}$	7.00×10^{-5}
And XXX	$00^{\rm h}36^{\rm m}34.6^{\rm s}$	$+49°38'49''$	$1.5^{+0.2}_{-0.2}$	$16.0^{+0.3}_{-0.2}$	558^{+17}_{-16}	$-7.7^{+0.3}_{-0.2}$	245±33	238.6^{+24}_{-24}	1.00
NGC 147	$00^{\rm h}47^{\rm m}27.0^{\rm s}$	$+34°22'29''$	$6.70^{+0.09}_{-0.09}$	$7.76^{+0.06}_{-0.06}$	773^{+21}_{-20}	-16.6±0.07	1431^{+44}_{-43}	107.0^{+15}_{-8}	1.00
NGC 185	$00^{\rm h}38^{\rm m}58.0^{\rm s}$	$+48°20'15''$	$2.94^{+0.04}_{-0.04}$	$8.46^{+0.06}_{-0.06}$	650^{+18}_{-18}	-15.6±0.07	555±17	154.1^{+23}_{-21}	1.00

Notes: The apparent magnitude and apparent size values are taken from Martin et al. (2016), except for those of NGC 147 and NGC 185 that are taken from Crnojević et al. (2014). All absolute magnitudes, physical sizes and distances are from Savino et al. (2022). While being in the PAndAS footprint, some galaxies are not part of this sample because they are in a region where the completeness was not determined (M32, NGC205; Doliva-Dolinsky et al. 2022), because their structural parameters are too uncertain (And XXVII; Richardson et al. 2011), or because their distances from M31 is beyond 300 kpc (And XVIII; Savino et al. 2022).

field on a M_V and $\log\left(r_{\mathrm{h(pc)}}\right)$ grid defined by $-8.5 \leq M_V \leq -4.5$ and $1.8 \leq \log\left(r_{\mathrm{h(pc)}}\right) \leq 3.0$, with a step size of 0.25 and 0.10, respectively. The recovery (or lack thereof) of a dwarf galaxy is performed with the search algorithm developed by Martin et al. (2013a) and that looks for overdensities of stars both spatially and along a red-giant-branch feature in the color-magnitude diagram. An analytical model is fitted to the resulting M_V–$\log\left(r_{\mathrm{h(pc)}}\right)$ recovery fraction grid so that the recovery fraction of any galaxy at a given location, with a given magnitude and size, can easily be calculated. We have also built an analytical model to account for the impact of the heliocentric distance to a dwarf galaxy on recovery fractions. Although the impact of distance to a dwarf galaxy is less important than other parameters, the effect is still not negligible and needs to be taken into account (Doliva-Dolinsky et al., 2022). From these, the resulting efficiency of detection for all 24 dwarf galaxies in the sample are listed in Table V.1. For the recovery fraction of dwarf galaxies with $M_V < -8.5$ and/or $\log\left(r_{\mathrm{h(pc)}}\right) > 3$, we extrapolate the analytical model for larger/brighter dwarf galaxies.

V.3 Model

Here, we discuss our methodology to infer the global properties of the M31 dwarf galaxy system from the observed properties of the individual M31 dwarf galaxies. Accounting for the PAndAS survey detection limits, we infer the underlying M31 luminosity function, size-luminosity relation, and spatial distribution via forward modelling.

V.3.1 Dwarf galaxy probabilistic model

Consider a dwarf galaxy whose observed properties, listed in Table V.1, are: its coordinates on the sky, (α, δ), its apparent magnitudes in both the g and i PAndAS bands, m_{g} and m_{i}, its angular half-light radius, $r_{\mathrm{h}}^{\mathrm{ang}}$, and its heliocentric distance, D_{MW}. As detailed in McConnachie et al. (2018), the apparent magnitude are corrected for extinction following Schlegel et al. (1998) and Schlafly & Finkbeiner (2011) and m_{V} is obtained from m_{g} and m_{i} using the transformation equations derived in Ibata et al. (2014). Then, using D_{MW}, it is straightforward to transform these observed properties into the intrinsic properties of the systems: the absolute magnitude, M_{V}, and the physical half-light radius, r_{h}. We also use the observed properties of the dwarf galaxy D_{MW} and (α, δ) to calculate the spherical coordinates of a dwarf galaxy in the M31-centric referential $(r_{\mathrm{M31}}, \theta, \phi)$. The dwarf galaxy properties considered here are therefore $\mathcal{D} = \{M_{\mathrm{V}}, \log r_{\mathrm{h}}, r_{\mathrm{M31}}, \theta, \phi\}$.

We chose to define the dwarf galaxy probabilistic model that depends on a set of parameters $\mathcal{P}$ as the combination of three independent components: the probability of a dwarf galaxy to have a given absolute magnitude, i.e., the shape of the luminosity function of the satellite system, $P_{\mathrm{LF}}(M_{\mathrm{V}}|\mathcal{P})$; the probability for a dwarf galaxy to have a given size knowing its magnitude, i.e., the size-luminosity relation of the satellite system, $P_{\log r_{\mathrm{h}}|M_{\mathrm{V}}}(\log r_{\mathrm{h}}|M_{\mathrm{V}}, \mathcal{P})$; and the probability of a dwarf galaxy to be at a given (sky-projected or 3-dimensional) location

around M31, $P_{\rm sp}(r_{\rm M31}, \theta, \phi|\mathcal{P})$. We assume that those components are independent of each other (see discussion in Section V.4.3.a), which allows us to simply write the probabilistic model as

$$P(\mathcal{D}|\mathcal{P}) \propto P_{\rm LF}(M_{\rm V}|\mathcal{P})\, P_{\log r_{\rm h}|M_{\rm V}}(\log r_{\rm h}|M_{\rm V}, \mathcal{P}) P_{\rm sp}(r_{\rm M31}|\mathcal{P}). \tag{V.1}$$

Following Tollerud et al. (2008), we model the shape of the luminosity function of the satellite system as a power law with exponent β over the magnitude range that we consider here for M31 dwarf galaxies ($M_V < -5.5$; this choice is discussed further in Section V.4.3.a).

$$P_{LF}(M_{\rm V}|\beta) \propto \frac{\log 10}{2.5} 10^{-(\beta+1)(M_{\rm V}-4.83)/2.5}. \tag{V.2}$$

Following Shen et al. (2003) and Brasseur et al. (2011), we assume a linear relation between $M_{\rm V}$ and the mean $\log(r_{\rm h})$, $\langle \log r_{\rm h} \rangle$, such that

$$\langle \log r_{\rm h} \rangle = z_p + s(M_{\rm V} + 6.0), \tag{V.3}$$

with s the slope and z_p the value of the relation for $M_V = -6.0$. The intrinsic dispersion, σ, around the relation is modeled as a Gaussian distribution along the $\log r_{\rm h}$ direction and yields

$$P_{\log r_{\rm h}|M_{\rm V}}(\log r_{\rm h}|M_{\rm V}, z_p, s, \sigma) = \frac{1}{\sqrt{2\pi}\sigma} \exp\left(-\frac{1}{2}\left(\frac{\log r_{\rm h} - \langle \log r_{\rm h} \rangle}{\sigma}\right)^2\right). \tag{V.4}$$

Finally, as the distribution of M31 satellite dwarf galaxies appears to be circularly but not spherically isotropic (Savino et al., 2022), we consider two cases for the spatial distribution part of the model: a sky-projected (2D) and a volumetric (3D) distribution model. In both cases, we choose a simple and agnostic shape for the radial density distribution function, a power law, with parameters $\alpha_{\rm 2D}$ and $\alpha_{\rm 3D}$, respectively[1]. At this stage, we introduce the assumption of an isotropic distribution of the dwarf galaxies around M31 (an assumption we will revisit later) to simplify the problem at hand. This allows us to remove the impact of

[1]It may be tempting to assume models informed by the distribution of dark matter sub-halos in simulations, such as, for example, an NFW profile (Navarro et al., 1996). However, considering that the region with $r_{\rm M31} < 30$ kpc is masked in our study, the concentration of the profile would be difficult to constrain. We will further explore a more complex modeling of the radial density distribution function in a future contribution.

the spherical coordinate angles on any model we define and, for the 3D case, we have

$$\begin{aligned} P_{\rm sp}(r_{M31},\theta,\phi|\alpha_{3D}) &= P_{\rm sp}(r_{M31}|\alpha_{3D}) \\ &\propto \int_0^{2\pi}\int_0^{\pi} r^2 r^{\alpha_{3D}}\sin(\theta)d\theta d\phi \\ &\propto 4\pi r^{2+\alpha_{3D}}. \end{aligned} \tag{V.5}$$

Similarly, for the sky-projected model,

$$P_{\rm sp}(r_{\rm M31}|\alpha_{\rm 2D}) \propto 2\pi r^{1+\alpha_{\rm 2D}}. \tag{V.6}$$

In summary, the probabilistic model has 5 parameters $\mathcal{P} = \{\beta, z_p, s, \sigma, \alpha\}$, with $\alpha = \alpha_{\rm 2D}$ or $\alpha = \alpha_{\rm 3D}$ in the 2D and 3D cases, respectively. Folding everything together and introducing the normalization constant $A(\mathcal{P})$ to ensure that $P(\mathcal{D}|\mathcal{P})$ integrates to unity over the full space (i.e., $-17 < M_{\rm V} < -5.5$, $1.8 < \log r_{\rm h} < 4$ and $30 < r_{\rm M31} < 300\,{\rm kpc}$), Equation V.1 becomes

$$P(\mathcal{D}|\mathcal{P}) = A(\mathcal{P})\, P_{\rm sp}(r_{\rm M31}|\alpha_{\rm 3D})\, P_{\log r_{\rm h}|M_{\rm V}}(\log r_{\rm h}|M_{\rm V}, z_p, s, \sigma) P_{LF}(M_{\rm V}|\beta), \tag{V.7}$$

with $A(\mathcal{P})$ such that

$$\iiint P(\mathcal{D}|\mathcal{P}) dr_{\rm M31} d\log r_{\rm h} dM_{\rm V} = 1. \tag{V.8}$$

V.3.2 Final likelihood function

The probabilistic model presented above describes the distribution of dwarf galaxies in the data space but does not provide any constraint on the theoretical number of dwarf galaxies that inhabit the M31 satellite system, $N_{\rm true}$, over the chosen ranges of observed properties[2]. At this stage we also introduce the data variable $N_{\rm obs}$ that is the number of observed dwarf galaxies in the considered magnitude range and volume[3]. For simplicity, we define $\mathcal{D}' = \mathcal{D} \cup \{N_{\rm obs}\}$ and $\mathcal{P}' = \mathcal{P} \cup \{N_{\rm true}\}$.

To constrain $N_{\rm true}$ using, in particular, $N_{\rm obs}$, we add another layer to the statistical frame-

[2]In all that follows, we choose the magnitude range $-17 < M_{\rm V} < -5.5$ that, at the bright end, includes the brightest M31 dwarf that is in the survey footprint (NGC 147) and, at the faint end, is fainter than the faintest dwarf galaxy known around M31 (And XXVI; $M_V = -6^{+0.7}_{-0.5}$). The volume we consider is delimited by $30\,{\rm kpc} < r_{\rm M31} < 300\,{\rm kpc}$, bound by a rough estimate of the virial radius of M31 and an inner boundary that corresponds to a region in which the search for dwarf galaxy is made extremely difficult by the presence of the galaxy's disk (Doliva-Dolinsky et al., 2022). We also choose to explore a size range of $1.8 < \log r_{\rm h} < 4$ which encompass the size of all known M31 dwarf galaxies (Table V.1).

[3]While we consider a sample constructed for the 24 dwarf galaxies listed in Table V.1, $N_{\rm obs}$ may not always be 24 as our drawing from the uncertainties on the parameters of the dwarf galaxies and, in particular, their distance may, in a small number of cases, push a sample dwarf galaxy outside of the studied volume.

work and now consider the theoretical density function, unaffected by the survey footprint and detection limits, $\rho_{\rm true}(\mathcal{D}|\mathcal{P}') = N_{\rm true} P(\mathcal{D}|\mathcal{P})$. Folding in the detections limits yields the observed version of this function, $\rho_{\rm obs,th}$, simply defined as

$$\begin{aligned} \rho_{\rm obs,th}(\mathcal{D}|\mathcal{P}') &= \tau(\mathcal{D})\, \rho_{\rm true}(\mathcal{D}|\mathcal{P}') \\ &= \tau(\mathcal{D})\, N_{\rm true}\, P(\mathcal{D}|\mathcal{P}), \end{aligned} \tag{V.9}$$

with $\tau(\mathcal{D})$ the probability of detecting a dwarf galaxy depending on its properties $\mathcal{D}$ (Doliva-Dolinsky et al., 2022).

Using the formalism of Kepner et al. (1999), Rykoff et al. (2012) and Drlica-Wagner et al. (2020), $N_{\rm true}$ can be constrained by first virtually binning the data space. In any bin i, the likelihood $\ell_i(\mathcal{D}'|\mathcal{P}')$ of generating a sample of $N_{\rm obs,i}$ dwarf galaxy in bin i can be described by the Poisson likelihood $\mathfrak{P}(N_{\rm obs,i}|N_{\rm obs,th,i})$. Here, the expectation $N_{\rm obs,th,i}$ is the theoretically observed number of dwarf galaxies in bin i, or

$$N_{\rm obs,th,i} = \tau(\mathcal{D}_i)\, N_{\rm true}\, P(\mathcal{D}_i|\mathcal{P})\, d\mathcal{D}. \tag{V.10}$$

The total likelihood of the dwarf galaxy system can therefore be expressed as

$$\begin{aligned} \mathcal{L}(\mathcal{D}'|\mathcal{P}') &= \prod_{i\in\text{bins}} \ell_i(\mathcal{D}'|\mathcal{P}') \\ &= \prod_{i\in\text{bins}} \mathfrak{P}(N_{\rm obs,i}|N_{\rm obs,th,i}) \\ &= \prod_{i\in\text{bins}} (N_{\rm obs,th,i})^{N_{\rm obs,i}} \exp(-N_{\rm obs,th,i})/N_{\rm obs,i}!, \end{aligned} \tag{V.11}$$

which further translates into

$$\log(\mathcal{L}(\mathcal{D}'|\mathcal{P}')) = -\sum_{i\in\text{bins}} N_{\rm obs,th,i} + \sum_{i\in\text{bins}} N_{\rm obs,i} \log\big(N_{\rm obs,th,i}\big) + \text{const.} \tag{V.12}$$

The first term of this equation is simply the integral of $\rho_{\rm obs,th}$ over the data space (i.e., the number of observable satellites predicted by the model). In addition, if we consider bins that are small enough to contain either one or no galaxy, the second part of the equation then becomes a sum over the $N_{\rm obs}$ bins that contain a galaxy. Equation V.12 therefore becomes

$$\begin{aligned} \log(\mathcal{L}(\mathcal{D}'|\mathcal{P}')) &= -\int_{\mathcal{D}} \rho_{\rm obs,th} d\mathcal{D} + \sum_{i=1}^{N_{\rm obs}} \log(N_{\rm obs,th,i}) + \text{const} \\ &= -\int_{\mathcal{D}} \tau(\mathcal{D}) N_{\rm true} P(\mathcal{D}|\mathcal{P}) d\mathcal{D} \\ &\quad + \sum_{i=1}^{N_{\rm obs}} \log(\tau(\mathcal{D}_i) N_{\rm true} P(\mathcal{D}_i|\mathcal{P})) + \text{const.} \end{aligned} \tag{V.13}$$

Here, $\mathcal{D}_i$ are the data values of dwarf galaxy i.

With the assumed isotropic distribution of the satellites, the integral of equation V.13 can be marginalized over θ (in the 2D case) or θ and ϕ (in the 3D case), which introduces the mean fraction of detected dwarf galaxies at radius $r_{\rm M31}$, $\langle\tau(M_V, \log r_{\rm h}, r_{\rm M31})\rangle$. This allows us to drop the dependence on θ and ϕ and the likelihood finally becomes

$$\begin{aligned}\log(\mathcal{L}(\mathcal{D}'|\mathcal{P}')) &= -\int_{M_V}\int_{\log r_{\rm h}}\int_{r_{\rm M31}}\langle\tau(M_V, \log r_{\rm h}, r_{\rm M31})\rangle \\ &\quad N_{\rm true}P(\mathcal{D}|\mathcal{P})dr_{\rm M31}d\log r_{\rm h}dM_V \\ &\quad +\sum_{i=1}^{N_{\rm obs}}\log(\tau(\mathcal{D}_i)N_{\rm true}P(\mathcal{D}_i|\mathcal{P})) + \text{const.}\end{aligned} \tag{V.14}$$

V.3.3 Implementation

We sample the likelihood with our own Metropolis-Hastings algorithm (Metropolis et al., 1953; Hastings, 1970). In order to obtain the probability distribution function (PDF) for each parameter while taking into account the uncertainties on the observed properties of the dwarf galaxies, we fold in the PDFs on the observed parameters instead of using a single value for each property. Following Conn et al. (2012), the likelihood becomes the convolution of the likelihood for a single value (Eq V.14) with the PDF of each observed property of the satellite system. With Ω the sample of all possible sets of values $\mathcal{D}'$ and $g(\mathcal{D}')$ being the probability of a given set, the likelihood function becomes

$$\mathcal{L}(\mathcal{D}'_\Omega|\mathcal{P}') = \int_\Omega \mathcal{L}(\mathcal{D}'|\mathcal{P}')g(\mathcal{D}')d\mathcal{D}'. \tag{V.15}$$

This integral is calculated numerically via a Monte-Carlo method and the random drawing of 50 satellite systems generated from the PDFs of $m_{\rm V}$, $r_{\rm h}$, D_{MW} and D_{M31} for all galaxies in the sample. The final distribution is the sum of the resulting chains.

Finally, we have only considered likelihoods to this point, but we seek to determine the probability of the model given the data $P(\mathcal{P}'|\mathcal{D}'_\Omega)$. It is linked to the probability of the data given the model $\mathcal{L}(\mathcal{D}'_\Omega|\mathcal{P}')$ via the prior $P(\mathcal{P}')$ such that

$$P(\mathcal{P}'|\mathcal{D}'_\Omega) \propto \mathcal{L}(\mathcal{D}'_\Omega|\mathcal{P}')P(\mathcal{P}'). \tag{V.16}$$

For simplicity, we choose uniform priors on all parameters and we impose that $0 < \beta < -4$, $1 < s < -1$,$1 < \alpha < -4$,$0 < N_{\rm true} < 1000$, $0 < \sigma < 1$, and $0 < z_p < 3$.

V.4 Results

V.4.1 Inferred global properties of the M31 dwarf galaxy system

The contraints on the global dwarf galaxy satellite system of M31 are listed in Table V.2 for both models with a sky-projected (2D, $\alpha = \alpha_{2D}$) and a volumetric (3D, $\alpha = \alpha_{3D}$) radial distribution component. The marginalized, posterior probability distribution function (PDF) of the different parameters of $\mathcal{P}'$ are presented in Figure V.2 for the case of the 3D radial distribution model. The favored parameters listed in Table V.2 correspond to the peak of a parameter's marginalized one-dimensional PDF and the associated credible intervals are bound by the parameter values that have a PDF values of 0.61 of the maximum (equivalent to a $\pm 1\sigma$ confidence interval in the case of a Gaussian PDF and that we prefer over the 68% central confidence interval in the case of skewed PDFs). In order to provide an extensive view of our results, we also provide in Table V.2 the median and 68% credible interval for each of the parameters. In any case, the MCMC chains are available at `https://github.com/dolivadolinsky`.

We first note that all six parameters of the model are well constrained and that the posterior PDFs are rarely perfect Gaussians or Poisson distribution in the case of $N_{\rm true}$. This is likely a consequence of the complexity of the model and the non-trivial impact of the detection limits on the model. In addition to constraints on the individual parameters, the statistical framework we have developed makes it very easy to study the correlations (or lack thereof) between different parameters. For instance, we note the strong correlation between β, the slope of the luminosity function, and $N_{\rm true}$, the number of M31 dwarf galaxies in the considered volume and magnitude range. This correlation is expected as changes to the slope of the luminosity function will directly lead to a change in the number of dwarf galaxies predicted by the model. The correlation between the slope of the size-luminosity relation, s, and the value of the slope at $M_V = -6.0$, z_p, is expect as there is a tradeoff between making the relation flatter and higher to ensure it goes through the cloud of data points. Similarly, a relation with a higher zero point will result in a larger scatter. However, it is interesting to note the weak correlation between the slope and the scatter that might results from the symmetry assumption on σ. This choice is further discussed in Section V.4.3.a.

Focusing on this part of the model, the size-luminosity relation for the M31 dwarf galaxies is shown in Figure V.3, overlayed on the data of the 24 dwarf galaxies of the sample (teal points with error bars) and the average detection limits determined by Doliva-Dolinsky et al. (2022) in this space (gray-scale background). From the marginalized one-dimensional posterior PDFs, we derive $z_p = 2.5^{+0.2}_{-0.1}$, $s = -0.05^{+0.03}_{-0.02}$ and $\sigma = 0.33 \pm 0.06$. This relation is compatible with the one obtained by Manwadkar & Kravtsov (2022) for the Milky Way satellites, even if theirs is slightly steeper. It is also similar to but shallower than the one determined by (Brasseur et al., 2011, the light orange model in the figure; $z_p = 2.34 \pm 0.1$, $s = -0.09 \pm 0.02$ and $\sigma = 0.23^{+0.02}_{-0.07}$), also determined through forward modeling, but with binary detection limits (recovery fractions of 0 or 1) that follow the dotted line in Figure V.3. The differences between the two favored models likely stems from these distinct detection

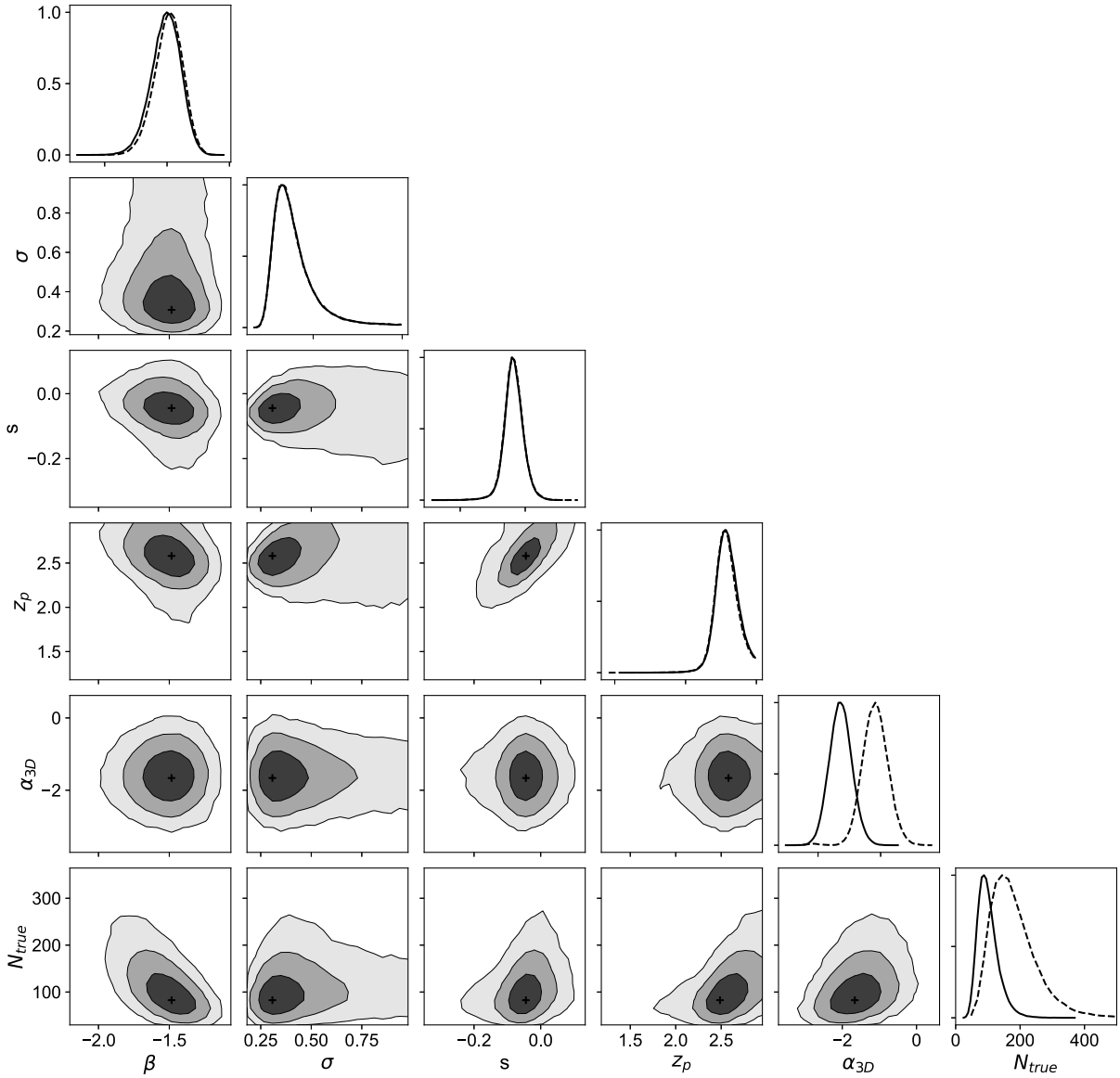

Figure V.1: Resulting correlation graphs and marginalized PDFs (full line) for each parameter of the 3D model. Black crosses represent the highest likelihood value for each couple of parameters. The marginalized PDFs for the 2D model are represented by the dashed lines.

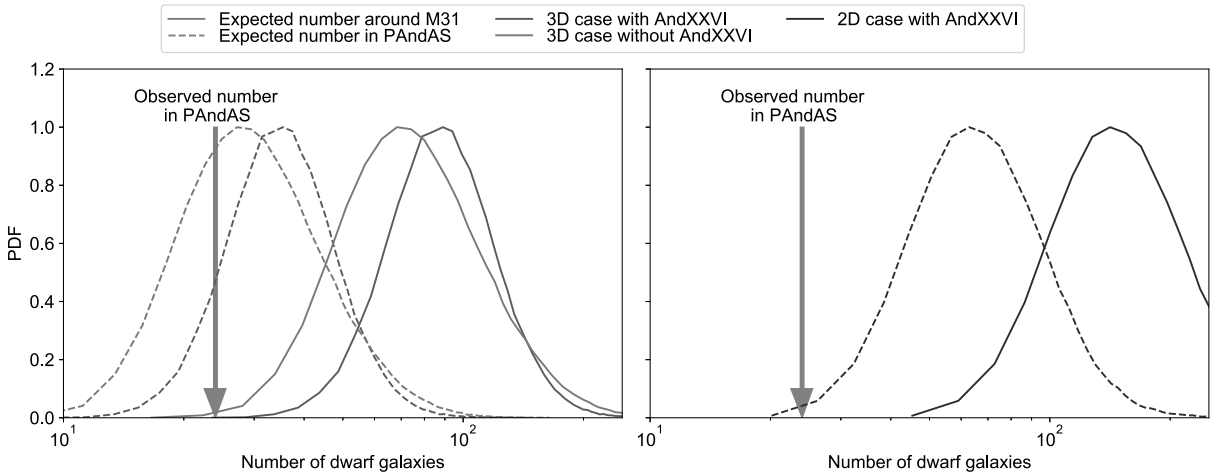

Figure V.2: PDFs of the inferred number of satellites with $M_V < -5.5$ within 300 kpc of M31 and within the PAndAS footprint for the 3D and 2D cases, with and without AndXXVI. We can note that the 3D models predict ~ 10 more satellites to be found in PAndAS with $M_V < -5.5$, while the 2D model predicts ~ 50.

Table V.2: Values for the model parameters in the case of a 2D and 3D spatial distribution of dwarf galaxies

	β	z_p	s	σ	α	$N_{\rm true}$
2D	-1.5 ± 0.1	$2.5^{+0.2}_{-0.1}$	$-0.05^{+0.03}_{-0.02}$	$0.32^{+0.07}_{-0.05}$	$-0.1^{+0.3}_{-0.5}$	136^{+65}_{-35}
3D	-1.5 ± 0.1	$2.5^{+0.2}_{-0.1}$	$-0.05^{+0.03}_{-0.02}$	0.33 ± 0.06	$-1.7^{+0.4}_{-0.3}$	92^{+19}_{-26}
$2D_{\rm med.-68\%}$	-1.5 ± 0.1	$2.6^{+0.2}_{-0.1}$	-0.05 ± 0.03	$0.36^{+0.1}_{-0.07}$	-0.2 ± 0.5	172^{+90}_{-55}
$3D_{\rm med.-68\%}$	-1.5 ± 0.1	$2.6^{+0.2}_{-0.1}$	-0.05 ± 0.03	$0.36^{+0.1}_{-0.07}$	-1.6 ± 0.4	95^{+35}_{-25}

Notes: This table presents the inferred global properties of the M31 satellites system in the case of a 2D and 3D spatial distribution. As defined in Section V.3, β is the slope of the luminosity function, z_p is the zero point, s is the slope, and σ is the dispersion of the linear relation between the size and the luminosity of dwarf galaxies, α is the slope of the spatial distribution and $N_{\rm true}$ is the expected number of M31 satellites. $2D_{\rm med.-68\%}$ and $3D_{\rm med.-68\%}$ are the results obtained if we use the median and quantiles.

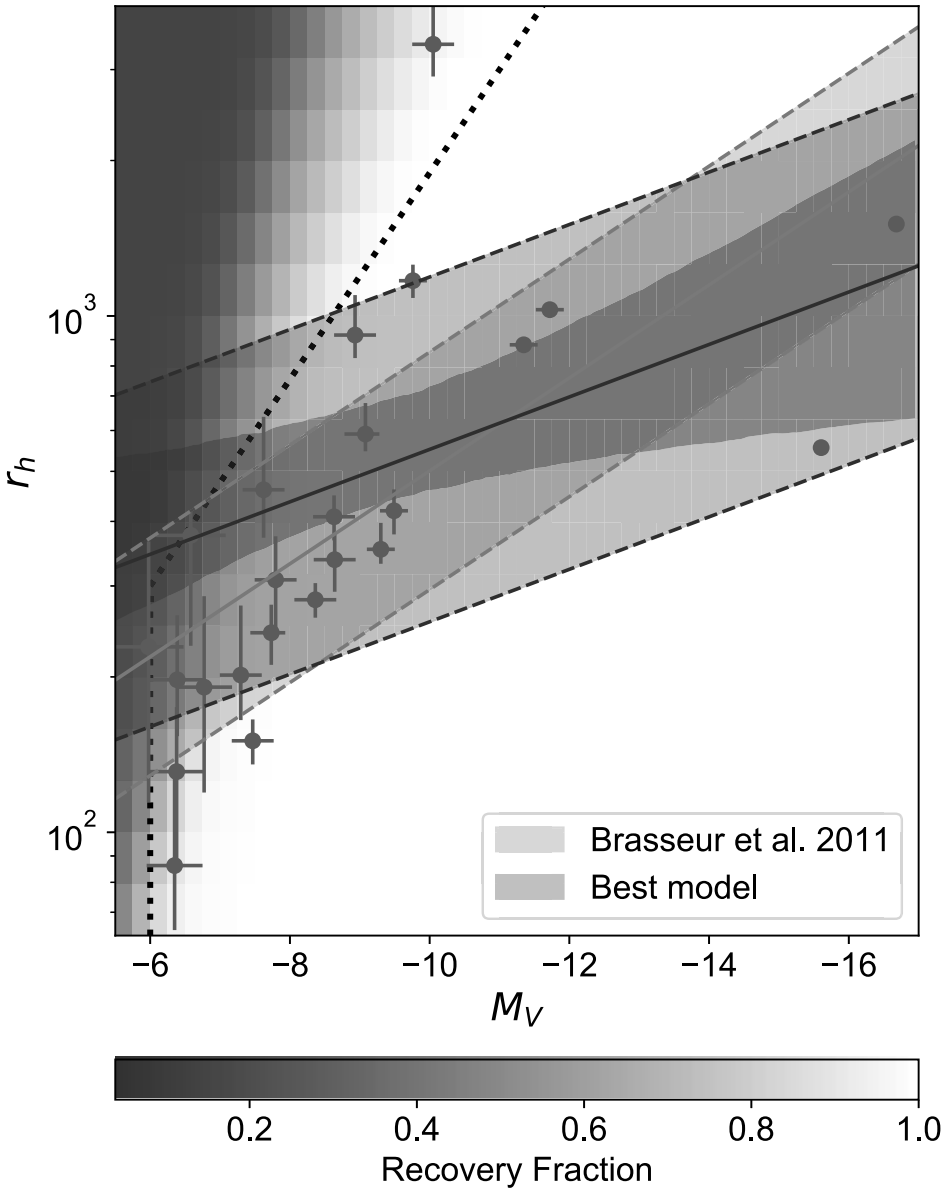

Figure V.3: Relation between the size and the luminosity of M31's dwarf galaxies as inferred through our modeling. The best relation and corresponding width are represented by the purple full line and dashed lines, with the uncertainties on the mean model shown as the high opacity purple band. The best model derived by Brasseur et al. (2011) is represented by the orange lines, and the binary completeness limits they used by the dotted black line. The average detection limits folded in our analysis are represented by the grey background scale (100% recovery in white and 0% recovery in dark gray). Given those, the inferred model compensates for the undiscovered large and faint dwarf galaxies and therefore is slightly shifted from what we would naïvely expect from the cloud of known dwarf galaxies (teal dots).

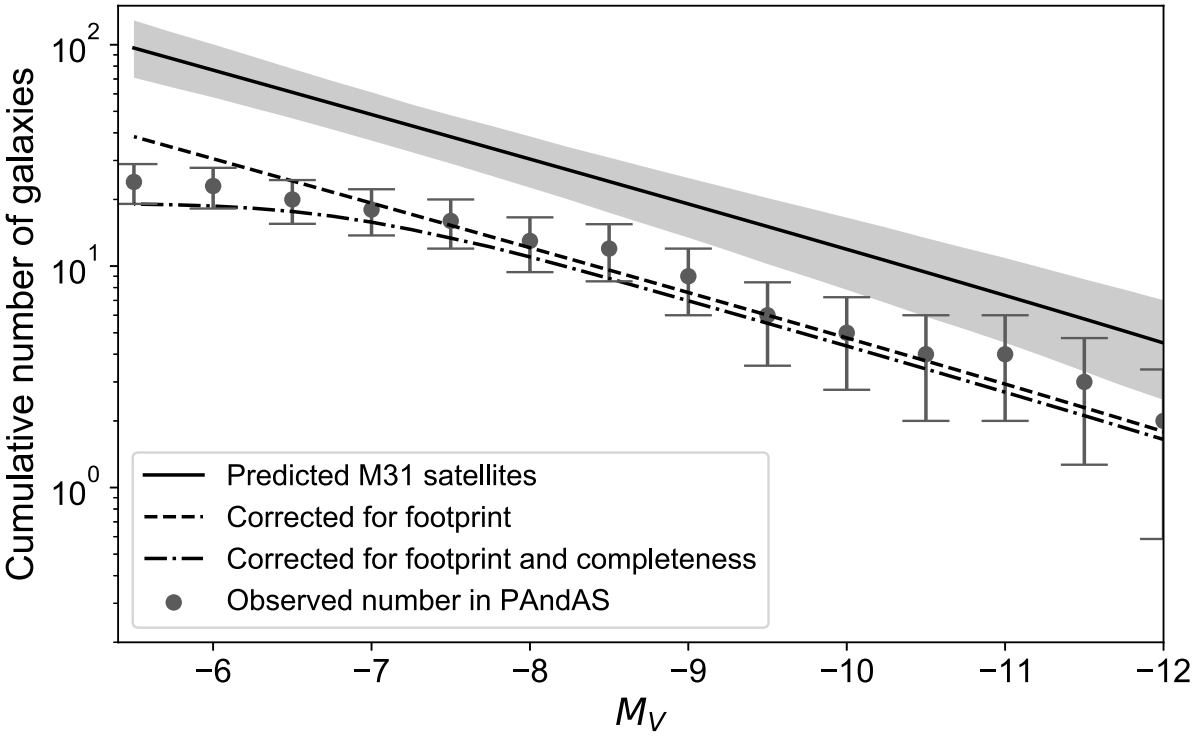

Figure V.4: Cumulative number of dwarf galaxies as a function of their magnitude. The inferred model is represented by the black line and gray band. The dashed line shows the inference for the PAndAS footprint and the dot-dashed line the favored model once the average detection limits are applied. This line is directly comparable to, and shows good agreement with, the cumulative distribution of known dwarf galaxies (teal points).

limits and our model infers higher overall values for r_h at the fainter end as it compensates for the large and faint dwarf galaxies that are yet undiscovered because of their low surface brightness limits. Even with this slight difference, the discussion of Brasseur et al. (2011) is still relevant as our result is compatible with the relation found for late type galaxies by Shen et al. (2003). This similarity may hint that the relations found for dwarf spheroidal galaxies are a continuation of the one obtained for more massive low-concentration galaxies that includes dwarf ellipticals.

The radial distribution of the assumed isotropic distribution of dwarf galaxies around M31 is well-constrained with $\alpha_{2D} = -0.1^{+0.3}_{-0.5}$ for the 2D case. It implies an almost flat surface density of dwarf galaxies on the sky and confirms previous hints that this is the case (McConnachie et al., 2009). For the 3D case, we determine a slope $\alpha_{3D} = -1.7^{+0.4}_{-0.3}$. A previous constraint on the slope of the 3D radial distribution function was provided by Conn et al. (2012), who determined $\alpha_{3D} = -1.52^{+0.32}_{-0.35}$ from the forward modeling of a very

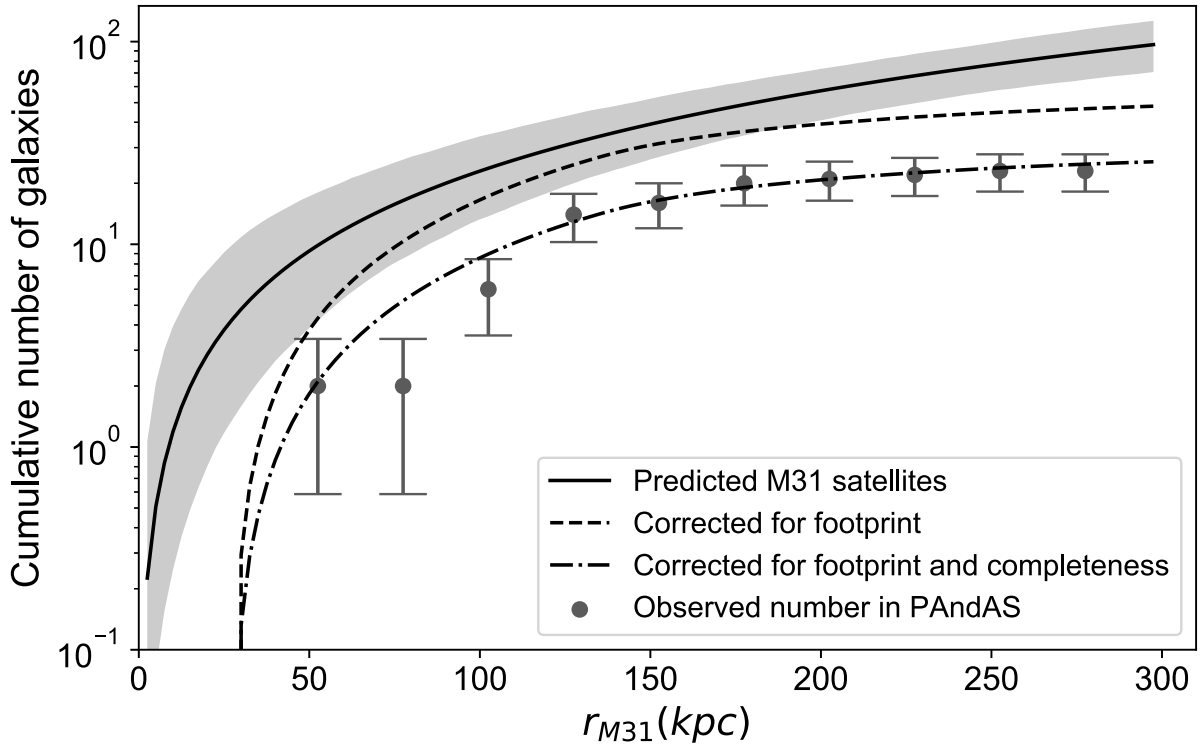

Figure V.5: Same as Figure V.4, but for the cumulative number of dwarf galaxies as a function of their distance to M31. The favored model, once the spatial and detection limits are accounted for, is compatible with the cumulative distribution of known dwarf galaxies.

similar sample of dwarf galaxies but different distance values for the dwarf galaxies[4] and also without taking the detection limits into account. The two constraints are nevertheless compatible within their uncertainties and yield a fairly steep density profile, even though it is not as steep as the NFW profile in the external part of the halo ($\alpha \sim -3$; Navarro et al., 1996).

One of the parameters that is most affected by the detection limits is certainly the slope of the luminosity function as dwarf galaxies that are missed because they are too faint to be discovered in PAndAS will cause the observed luminosity function to drop significantly at faint magnitude. Our analysis yields a strong constraint on this slope and we infer that the intrinsic luminosity function of M31 dwarf galaxies has a slope $\beta = -1.5 \pm 0.1$ (in the 3D case, similar in the 2D case). It is steeper than the one derived by Crnojević et al. (2019, $\beta = -1.22^{+0.11}_{-0.10}$), who did not model the impact of the detection limits. This difference arises from the consideration of the detection limits of the survey and therefore highlights their

[4]We now use the updated RRLyrae distances determined by Savino et al. (2022) instead of the tip of the red giant branch distances determined by Conn et al. (2012).

importance in deriving the faint end luminosity function.

Finally, we infer the total number of M31 dwarf galaxies within the considered magnitude range ($-17.0 < M_V < -5.5$) and volume ($30 < r_{\mathrm{M31/\,kpc}} < 300$), $N_{\mathrm{true}} = 136^{+65}_{-35}$ in the 2D case, or $N_{\mathrm{true}} = 92^{+19}_{-26}$ in the 3D case. Combined with our framework that only considers galaxies brighter than $M_V = -5.5$ ($\sim 10^4\,\mathrm{L}_\odot$), and even though the realm of dwarf galaxies extends to much fainter systems (e.g., around the MW; McConnachie, 2012) that are not detectable in PAndAS (Martin et al., 2013a), these values are in line with the expectation that a galaxy like M31 is surrounded by hundreds of dwarf galaxies, most of them faint (e.g., Garrison-Kimmel et al., 2019).

To check the quality of the model inference, a comparison of the favored model with the cumulative distribution of observed dwarf galaxies is shown in Figure V.4 for the luminosity function and in Figure V.5 for the 3D radial distribution. The inferred model is shown in black, with the gray band tracking the corresponding uncertainties, while the dashed lines represent the model, corrected to include only the PAndAS footprint, and the dash-dotted line further adds the impact of the detection limits. This final line is directly comparable with the observations (teal points) and shows a good agreement for both cumulative distributions. This is the sign that, despite its complexity, the favored model is a good representation of the known population of M31 dwarf galaxies. These figures also make it evident that the majority of still undiscovered M31 dwarf galaxies brighter than $M_V = -5.5$ are located outside of the PAndAS footprint, mainly beyond 150 kpc (the difference between the full and dashed line) but that about half of the dwarf galaxies in the magnitude range $-5.5 > M_V > -7.0$ remain to be discovered in the PAndAS footprint (difference between the dashed and dash-dotted line). Some of these are likely to be among the list of candidate satellites already published (Martin et al., 2013a; Mackey et al., 2019).

V.4.2 Anisotropy in the satellite distribution

With the inferred properties of the isotropic model we have constructed to represent the M31 dwarf galaxy system, we can now explore the perceived anisotropy of the satellite system and, in particular, whether it could be an artefact produced by the detection limits of the PAndAS survey. Looking at the RR Lyrae distances obtained by Savino et al. (2022), overlaid on the average detection limits in Figure V.6, it is clear that the distribution of Andromeda's dwarf galaxies is not isotropic. Among the 24 dwarf galaxies present in the PAndAS footprint and that contribute to our sample, 21 systems are located on the MW side of M31 and produce a strong anisotropy. The (in)completeness impacts the distribution of known satellites in two different ways: it is easier to detect a dwarf galaxy that has a smaller heliocentric distance but, because of the increasing foreground contamination, it is harder to detect a dwarf galaxy closer to the MW plane. Therefore, we aim to test if the favored inferred model, observed through the detection limits (the contours in Figure V.6) could naturally produce this observed anisotropy.

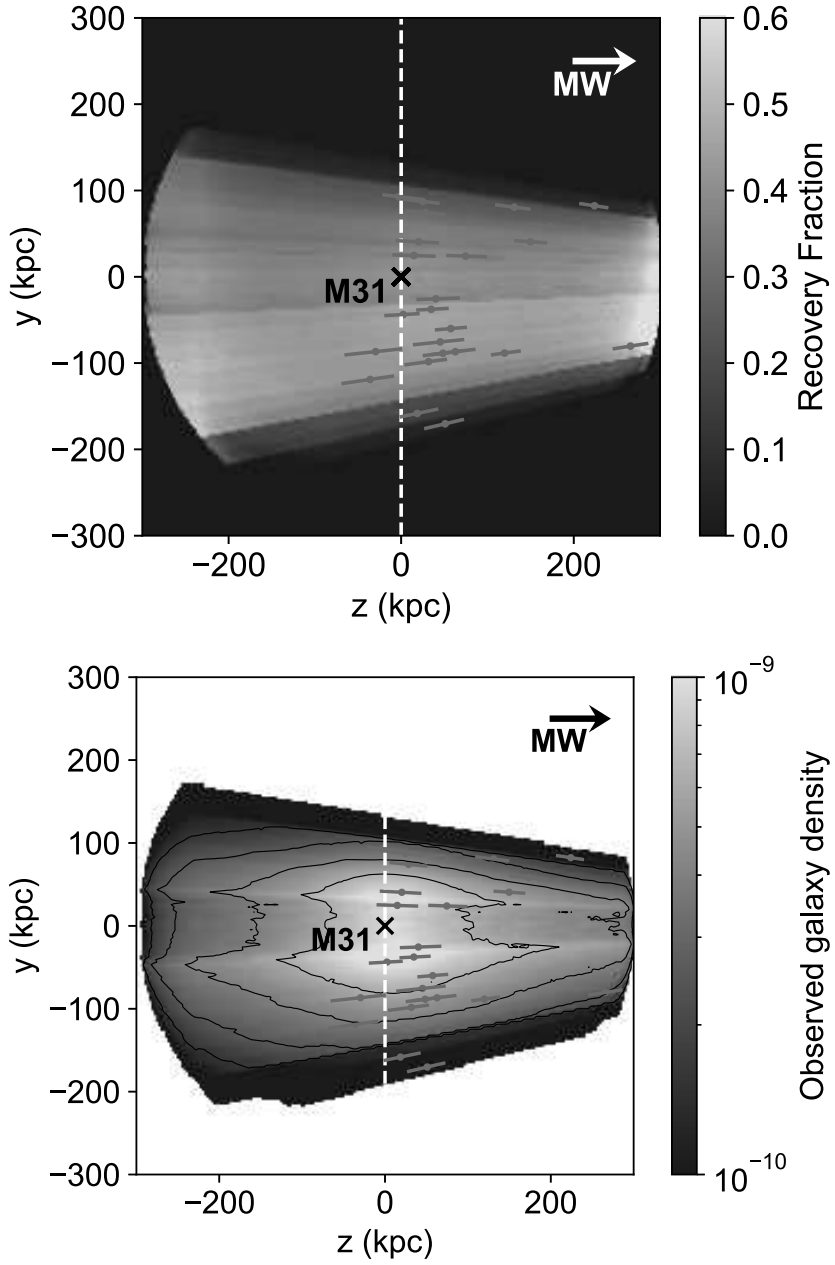

Figure V.6: *Top panel*: Map of the completeness in the y-z plane where z is the distance to M31 along the line of sight to the MW. The contamination due to MW and M31 stars lead to the variation of the completeness along the y-axis, while the impact of the distance is visible along the z-axis. *Bottom panel*: Map of the observable satellite density predicted by the best-fit (isotropic) model in the y-z plane. The color scale includes the masked region within 30 kpc of M31. The red dots represent the known dwarf galaxies. The model predicts a slightly higher density of observed satellites on the side closer to the MW (+z) but this impact is compensated by the increase of the observed space on the negative end.

To quantify the significance of the anisotropy, we use a simple Monte Carlo procedure to generate 10,000 satellite systems drawn from the favored isotropic model, folding in the PAndAS recovery fractions. In practice, we start by drawing the distance to M31 from the PDF obtained by Savino et al. (2022). Then, we randomly locate this satellite around M31 using the favored density model and, finally, we test them against the detection limits of Doliva-Dolinsky et al. (2022). We reject dwarf galaxies that do not pass this test and repeat this procedure until the sample of 'observed' dwarf galaxies contains 24 satellites.

Of these 10,000 systems drawn from the favored isotropic model, we find that only 7 systems have a distribution that is at least as anisotropic as M31's (at least 21 dwarf galaxies on the MW side of M31). Therefore, we conclude that the asymmetric dwarf galaxy completeness limits of the survey are very unlikely to explain, on their own, the observed anisotropy of the M31 dwarf galaxy satellite system.

V.4.3 Caveats

V.4.3.a Limit of the model

Given the small number of data points (i.e. the 24 known dwarf galaxies is our sample) and our decision to design an agnostic and empirical framework, we chose to restrict the different components of the model to rather simple functional forms in order to avoid an increase in the number of parameters that would only be poorly constrained. Here, we propose to review the limitations of those choices and the different biases that they may potentially produce.

First, reionization is expected to affect galaxies as bright as $M_{\rm V}$=-7.0 (Brown et al., 2014; Weisz et al., 2014; Koposov et al., 2009). As we choose to model the luminosity function as a simple power-law and we extrapolate our model until $M_{\rm V} = -5.5$, it might result in a slightly over-estimation of the number of dwarf galaxies expected around M31.

Then, simulations predict a change in the slope of the radial density profile between the most central regions, where it is shallower, and the outer parts of the halo, where it is steeper (Springel et al., 2008; D'Onghia et al., 2010; Garrison-Kimmel et al., 2017; Sawala et al., 2017; Samuel et al., 2020). This change is driven by the stronger impact of tides closer to the host. For the model, we used a simple, single power-law throughout the considered range between 30 and 300 kpc from M31. By masking the inner 30 kpc, we should not be biased by the strongest tidal effects but the simplicity of our model could be responsible for the small overprediction of dwarf galaxies in the region within 100 kpc displayed in Figure V.5 (although we note that this apparent discrepancy is not very significant). Including the impact of tidal effects is, at this stage, very difficult as the full orbital information is not available for the vast majority of M31 satellites and tidal stripping is related to both the orbit and the mass/density of the satellites (Springel et al., 2008). In the outer parts of the halo, while imposing a hard cutoff at 300 kpc could lead to an overestimation of the number of satellites between 200 and 300 kpc, it may be compensated for by the exclusion of dwarf

galaxies that are slightly further away.

Finally, we could design a model where the dispersion of the size-luminosity relation changes as a function of the magnitude but, given the small number of known dwarf galaxies, it would be difficult to constrain such a parameter without adding strong priors build, for instance, from simulations. We have decided to be keep our analysis data-driven so our results can be more appropriately and independently compared with the results of simulations.

Although the simplicity of our model doesn't muster all the subtleties of the reality for the faint end of dwarf galaxies, we do not anticipate our choices will have a major effect on our results given the small sample of known M31 dwarf galaxies. However, searching for and discovering the expected 92^{+19}_{-26} satellites would open the possibility to complexify the model and take into account the effects mentioned above.

V.4.3.b AndXXVI

While AndXXVI is part of our sample, its significance of detection is just below the threshold used to obtain the recovery fraction (i.e., it has a significance of 5.9 with a threshold of 6). Considering that a threshold of 5.9 or 6 shouldn't lead to a significant change in the detection limits, given the uncertainties of the recovery fraction, we decide to include AndXXVI in our sample. However, retrospectively, it may have been preferable to derive the detection limits with a threshold ≤ 5.9. Nevertheless, it is important to note that its low significance of detection is reflected in $\tau(\mathcal{D})$, the probability of detecting a dwarf galaxy with properties $\mathcal{D}$. To quantify the impact of its inclusion on our results, we also inferred the parameters when excluding this satellite for the 3D case. We find $\beta = -1.5 \pm 0.1$, $z_p = 2.5^{+0.3}_{-0.2}$, $s = -0.1^{+0.07}_{-0.06}$, $\sigma = 0.34 \pm 0.08$, $\alpha = -1.8^{+0.5}_{-0.4}$ and $N_{\rm true} = 75^{+23}_{-26}$. Although there are some variations in the parameter values, they are statistically compatible with the parameters obtained by including AndXXVI.

V.4.3.c Impact of the anisotropy

It is interesting to note that $\alpha_{\rm 3D}$ is not quite $\alpha_{\rm 2D} - 1$, suggesting that the surface density model, according to our definitions of these two parameters, is not simply the integration of the 3D density model, and therefore the chosen models are not a perfect representation of the data. A plausible cause could be that the assumption of isotropy may not be entirely valid in the 3D case. Indeed, as seen in Section V.4.2, the asymmetry in the spatial distribution of M31 satellites is a real feature, as it is unlikely to be explained by detection limits alone. Therefore, imposing the 3D spatial distribution to be symmetric could introduce a bias in the determination of $\alpha_{\rm 3D}$.

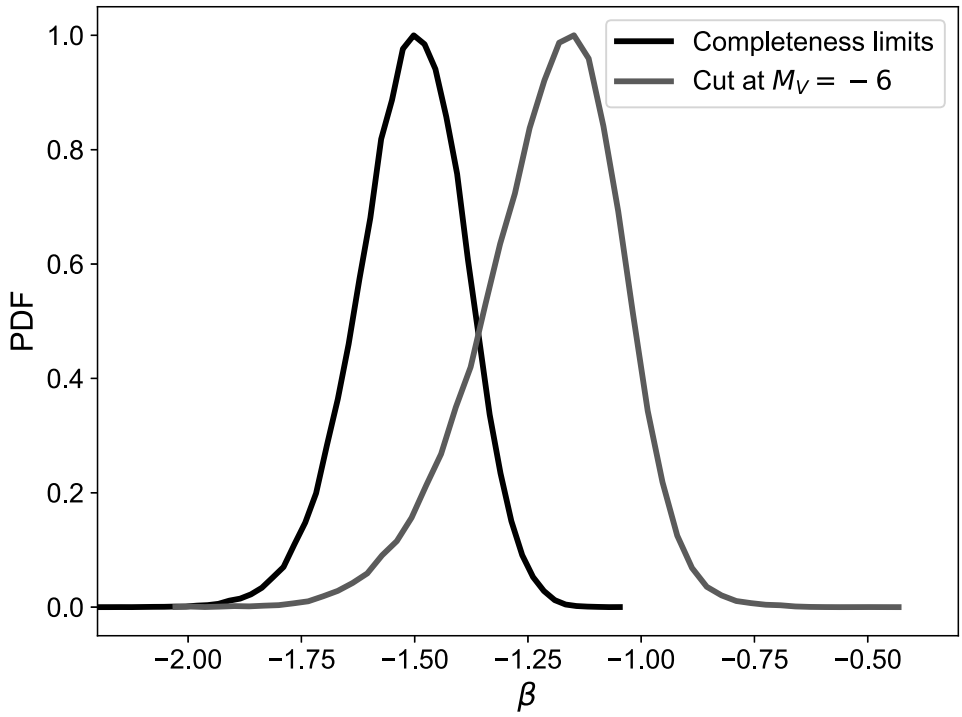

Figure V.7: Marginalized probability distribution function of the parameter β, the slope of the luminosity function, in a case where the dwarf galaxy detection limits are taken into account (black PDF) or they are approximated by a simple magnitude cut (teal PDF).

V.5 Discussion and conclusion

In this paper we inferred the global properties of the M31 dwarf galaxy satellite system within the PAndAS survey through forward modeling, carefully folding in the detection limits of dwarf galaxies in this survey. We conclude that M31 hosts 92^{+19}_{-26} or 136^{+65}_{-35} satellites, depending on whether the spatial distribution of satellites is modelled in 2D or 3D, over the magnitude range $-17 < M_{\rm V} < -5.5$ and $30 < r_{\rm M31/\,kpc} < 300\,$kpc, even though only 24 are known within the footprint and 33 overall. Both results would be slightly overestimated if the true luminosity function of M31 satellite dwarf galaxies were to differ from a power law at fainter magnitudes than $M_{\rm V} = -7$, for instance because of reionization (Brown et al., 2014; Weisz et al., 2014). In order to better constrain the luminosity function at the faint end and to model the possible turn over, it is essential to increase the size of the faint dwarf galaxy sample. As shown in Figure V.4, about half of the dwarf galaxies remain undiscovered in the PAndAS footprint and for the chosen magnitude limit. Yet, the most promising regions to search for these still fairly bright but elusive galaxies is to search for them outside the survey footprint: about half of the expected tally of dwarf galaxies brighter than $M_V = -5.5$

reside beyond the edges of the survey, out to the projected virial radius of M31. This also shows the importance of probing a wider area of the M31 surroundings to better constrain its global satellite properties. For the MW, model predictions range from ~ 20 to ~ 40 satellites with M_V >-5.5 and $r_{\rm MW}$ <300 kpc (Newton et al., 2018; Jethwa et al., 2018; Nadler et al., 2020; Manwadkar & Kravtsov, 2022) and Drlica-Wagner et al. (2020) derived an empirical estimates of ~ 30 satellites. For M31 we found 92^{+19}_{-26} , which means that it host $\sim 2-3$ times more satellites than the MW for the same luminosity range. Those results are in agreement with the larger number of M31 globular clusters compared to the MW (Huxor et al., 2014) and could easily be explained if M31 is significantly more massive than the MW.

Assuming a linear relation between $\log r_{\rm h}$ and M_V, we infer a slope $s = -0.05^{+0.03}_{-0.02}$, a zero point $z_p = 2.5^{+0.2}_{-0.1}$ at magnitude $M_V = -6.0$, and a scatter $\sigma = 0.33 \pm 0.06$. These are consistent with the values derived by Brasseur et al. (2011, $z_p = 2.38^{+0.16}_{-0.13}$, $s = -0.03 \pm 0.03$ and $\sigma = 0.2^{+0.08}_{-0.02}$,) for a similar model for the dwarf galaxies of M31 and, also of the MW. We therefore conclude that the satellite population of M31 and the MW do not show any significant difference in their size-luminosity relation.

We assumed that the slope of the luminosity function could be represented by a power law, which we constrained to be $\beta = -1.5 \pm 0.1$. This result is compatible with previous studies and for other satellite systems. It is, for instance, coherent with the results based on the Galaxy and Mass Assembly (GAMA) survey: Loveday et al. (2012) derive a slope of -1.50 ± 0.03 for the faint-end of the luminosity function of blue galaxies. For the MW, Tollerud et al. (2008) found $\beta = -1.9 \pm 0.2$ while Koposov et al. (2008) derived $\beta \sim -1.25$ and, for M81, Chiboucas et al. (2013) derived a $\beta = -1.27 \pm 0.04$. While some of those differences may be due to the merger history of the host galaxy (about 10 Gyr for the MW [5], 2–4 Gyr for M31, and ongoing for M81; e.g., Helmi et al., 2018, D'Souza & Bell, 2018, Okamoto et al., 2019), it is important to note that these constraints on β were obtained from very different sample sizes and techniques and without always taking a survey's detection limits into account. In the case of M81, for instance, Chiboucas et al. 2013, were limited to only 5 galaxies with $M_V > -10$, among which only one was fainter than $M_V = -8.0$. The same authors also derived $\beta = -1.13 \pm 0.06$ for M31 Chiboucas et al. 2009, which is significantly different from our inference, albeit from an earlier sample of known M31 dwarf galaxies and without taking the survey footprint and the detection limits into account.

This comparison underlines the importance of the impact of the detection limits on constraining the global properties of a satellite system. Determining these limits can admittedly be quite a tedious and computationally taxing task (Koposov et al., 2008; Drlica-Wagner et al., 2020; Doliva-Dolinsky et al., 2022) but it is absolutely essential to fold them into the analysis. The simplicity of using binary detection limits with magnitude cuts (e.g., Brasseur et al., 2011; Bennet et al., 2019; Crnojević et al., 2019) can be appealing but requires a very

[5]While a merger with the LMC satellites and the MW is ongoing (Battaglia et al., 2022), those dwarf galaxies were note taken into account by Tollerud et al. (2008) who studied the satellites in the northern hemisphere.

conservative approach (and throwing away some of the data) to not induce a bias on the slope of the luminosity function. We explore this effect in Figure V.7 as we simplify the Doliva-Dolinsky et al. (2022) detection limits to binary limits with a magnitude cut at $M_V = -6.0$. This leads to a clear bias on the slope of the luminosity function as undetected galaxies at the faint end are not compensated for. In fact, the value of β inferred in this case is similar to those determined by Chiboucas et al. (2009) and Crnojević et al. (2019) without taking the detection limits into account. The importance of determining accurate detection limits is complementary to the use of bayesian inference. Forward modeling has been used to go from the luminosity function to the stellar-halo mass relation and *vice versa* (Danieli et al., 2022), but the most common method to derive the luminosity function from observations is through their noisy correction from the incompleteness and, in some case, the unadvised fitting of the cumulative function (Chiboucas et al., 2009; Geha et al., 2017; Crnojević et al., 2019; Bennet et al., 2019). While this avoids the complex work of forward modeling, biases may arise from the loss of information implied by the use of a correction factor(e.g., an average of the detection limits, a magnitude cut). And, while fitting the cumulative function may seem like a straight forward process, those data points are intrinsically correlated, which makes it difficult to properly handle statistics and, consequently, uncertainties. The possible correlation between the slope of the luminosity function and the age of the last merger suffered by the host should therefore be consolidated by redetermining the slopes in a homogeneous analysis that would take the completeness of the different surveys into, for example by following the path traced in this paper.

Finally, we show that the radial distribution of the satellites can be modeled by a power law of exponent $\alpha_{2D} = -0.1^{+0.3}_{-0.5}$ and $\alpha_{3D} = -1.7^{+0.4}_{-0.3}$ in the sky-projected and 3D radial distribution, respectively. However, we determined that the observed anisotropy of the satellite dwarf galaxies (McConnachie & Irwin, 2006; Savino et al., 2022) is unlikely to be the consequence of the detection limits that make it more difficult to detect dwarf galaxies on the more distant side of M31. The observed anisotropy is rarely reproduced by drawing random satellite systems from the favored satellite system model that fold in the limits: only 0.07% of these have an anisotropy that is at least as strong as the observations. Since the incompleteness of the sample is ruled out as a major factor responsible for the observed anisotropy, another observational effect could be a bias in the distances. However, the fact that the anisotropy manifests using both RR Lyrae and TRGB distances disfavor such biases (Conn et al., 2012; Savino et al., 2022). In other words, we have, by using robust distances, combined with our detailed modeling of the (in)completeness of the data, built a strong case for the anisotropy to be a real physical configuration. Different solutions are proposed to explain such a distribution (Pawlowski et al., 2017; Thomas et al., 2018; Wan et al., 2020) and complexity could be added to the model presented here to explore these possibilities.

More generically, the statistical framework developed here is very flexible and can easily be expanded. One can, for instance, imagine replacing the current isotropic spatial distribution component of the model to make it more intricate and parametrize the observed anisotropy

of the system. It would also be straightforward to add more components to Equation V.1, for instance to use the M31 dwarf galaxies to place constraints on the dark matter particle (e.g., Kim et al., 2018) or the faint-end of galaxy formation Koposov et al. (e.g., 2009). Considering that, according to our inference, two thirds of dwarf galaxies with $M_V < -5.5$ are still undiscovered around M31, applying this framework to a wider and deeper M31 satellite sample (e.g., thanks to the surveys that will be conducted with the Euclid, Rubin, or Roman telescopes), would yield important and tighter constraints on the global properties of this system and, possibly, on the dark matter properties. Finally, the method we describe could similarly be applied to other galaxies, either the MW itself (Drlica-Wagner et al., 2020), or galaxies outside the Local Group (Mao et al., 2021; Mutlu-Pakdil et al., 2021; Carlsten et al., 2022; Nashimoto et al., 2022). Reproducing the current analysis on the dwarf galaxy systems of other hosts will be essential to place robust constraints on cosmological and galaxy formation physics and to continue refining the use of dwarf galaxies as cosmological probes. This framework will be particularly useful considering the future arrival of the LSST and Euclid that are going to revolutionize the study of satellite systems beyond the Local Group.

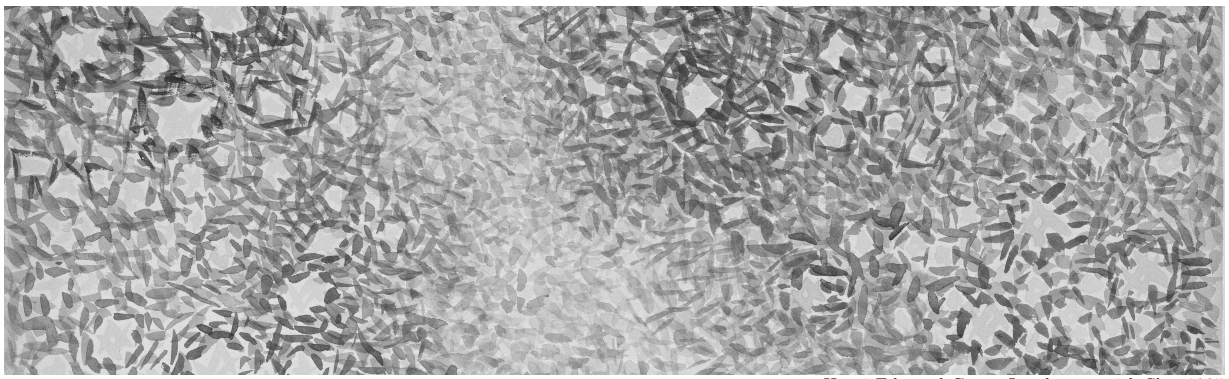

Henri-Edmond Cross, Landscape with Sky, 1905

Chapter VI

Is M31 at the center of its satellite system ?

Abstract

We use forward modeling to infer the center of M31's satellite 3D spatial distribution, folding in the completeness of the search for dwarf galaxies. The arrangement of M31's dwarf galaxies exhibits a strong anisotropy, with the majority located in the hemisphere between the Milky Way and the host galaxy. This study aims to investigate whether M31 occupies the central position in the distribution of dwarf galaxies. We observe a displacement of approximately 10-50 kpc towards the Milky Way in the center of the satellite distribution relative to the center of M31. Nonetheless, the center of M31 remains compatible with the center of the dwarf galaxy distribution given the lenient constraints on its position. Hence, expanding the number of known dwarf galaxies is crucial to deepen our understanding of the distribution of M31 satellites, thereby enabling a more comprehensive view of the formation and evolution of M31.

VI.1 Introduction

The distribution of M31 dwarf galaxies has been reported to be highly anisotropic with a majority of the satellites situated closer to the MW rather than on the opposite hemisphere (McConnachie & Irwin, 2006; Conn et al., 2012; Wan et al., 2020). This peculiar feature has been reenforced by the updated satellite distances derived from RR-Lyrae in Savino et al. (2022). Although the detection of dwarf galaxies located farther away from the Milky Way poses a greater challenge, our previous work convincingly dismisses detection limits as the only explanation for this distribution, with a confidence level exceeding 99% (Doliva-Dolinsky

et al., 2023). Consequently, the observed anisotropy in the M31 satellite system is indeed a genuine feature.

While the implications of this distribution on cosmology, as well as the formation and evolution of M31, remain uncertain, one proposed explanation by McConnachie et al. (2005) suggests that it could be attributed to the recent accretion of satellites, preventing them from being phase mix. Another plausible explanation arises from the anticipated displacement of approximately 15-25 kpc of the Milky Way from the center of its dark matter halo (Garavito-Camargo et al., 2021), which can be attributed to the presence of the Large Magellanic Cloud (LMC). Considering the presence of the Giant Stream in the M31 halo (Ibata et al., 2001, 2014) and given that most M31 models predict a significant merger event occurring roughly 2 Gyr ago (Hammer et al., 2018; D'Souza & Bell, 2018), this raises the question of whether M31 could be sloshing in its halo. We propose to constrain the significance of this potential shift and we use forward modeling to infer the center of the satellite distribution.

In Section VI.2, we describe the satellite sample and its completeness. Section VI.3 details the model and its implementation to obtain the results presented in Section VI.4 and discussed in Section VI.5.

VI.2 Sample

Our study is based on dwarf galaxies found within a projected radial distance of 30 kpc to a 3D radial distance of 300 kpc from M31. This range is determined based on an approximate estimate of M31's virial radius, with the inclusion of an inner boundary that considers the difficulties associated with detecting dwarf galaxies near M31's disk (Doliva-Dolinsky et al., 2022). Given the importance of the MW stellar contamination at higher latitude, north of M31, and its impact on the recovery of dwarf galaxies, we also impose a limiting $b > -9.5°$. The resulting list of dwarf galaxies is presented in Table VI.1. Considering the uncertain nature of And XXVII (Preston et al., 2019), as well as the significant uncertainties in its structural properties (Richardson et al., 2011; Martin et al., 2016), we have decided to exclude it from our sample. The distances are derived from the RR Lyrae measurements and are taken from (Savino et al., 2022).

The sample of dwarf galaxies is split into two categories: those detectable within the PAndAS footprint and those located outside of it. The search for dwarf galaxy inside of the PAndAS survey suffers from spatial and detection incompleteness, which was quantified in Doliva-Dolinsky et al. (2022) through the injection of the stars of approximately half a million artificial dwarf galaxies into the PAndAS catalogue. The search algorithm developed by Martin et al. (2013a) was used to locate spatial and photometric overdensities of old metal poor stars, determining the recovery (or lack thereof) of a dwarf galaxy. Specifically, for each MegaCam field, the recovery fraction was assessed for dwarf galaxies with $-8.5 < M_V < -4.5$ and $1.8 < \log(r_{\rm h}(\,{\rm pc})) < 3.0$. To facilitate the calculation of the recovery fraction for any galaxy at a given location, magnitude, and size, an analytical model is fitted to the resulting

Table VI.1: Sample of the dwarf galaxies present in the PAndAS survey.

Name	α(J2000)	δ(J2000)	$D_{\rm MW}(kpc)$
Within the PAndAS footprint			
And I	$00^{\rm h}45^{\rm m}39.7^{\rm s}$	$+38°02'15''$	775^{+19}_{-17}
And II	$01^{\rm h}16^{\rm m}26.8^{\rm s}$	$+33°26'07''$	667^{+16}_{-15}
And III	$00^{\rm h}35^{\rm m}30.9^{\rm s}$	$+36°29'56''$	721^{+17}_{-16}
And V	$01^{\rm h}10^{\rm m}17.5^{\rm s}$	$+47°37'42''$	759^{+21}_{-20}
And IX	$00^{\rm h}52^{\rm m}53.4^{\rm s}$	$+43°11'57''$	702^{+19}_{-20}
And X	$01^{\rm h}06^{\rm m}35.4^{\rm s}$	$+44°48'27''$	630^{+18}_{-18}
And XI	$00^{\rm h}46^{\rm m}19.7^{\rm s}$	$+33°48'10''$	751^{+23}_{-22}
And XII	$00^{\rm h}47^{\rm m}28.3^{\rm s}$	$+34°22'38''$	718^{+25}_{-26}
And XIII	$00^{\rm h}51^{\rm m}51.0^{\rm s}$	$+33°00'16''$	821^{+28}_{-26}
And XIV	$00^{\rm h}51^{\rm m}35.0^{\rm s}$	$+29°41'23''$	773^{+21}_{-21}
And XV	$01^{\rm h}14^{\rm m}18.3^{\rm s}$	$+38°07'11''$	746^{+17}_{-18}
And XVI	$00^{\rm h}59^{\rm m}30.3^{\rm s}$	$+32°22'34''$	517^{+18}_{-19}
And XVII	$00^{\rm h}37^{\rm m}06.3^{\rm s}$	$+44°19'23''$	757^{+24}_{-23}
And XIX	$00^{\rm h}19^{\rm m}34.5^{\rm s}$	$+35°02'41''$	813^{+31}_{-31}
And XX	$00^{\rm h}07^{\rm m}30.6^{\rm s}$	$+35°07'37''$	741^{+27}_{-27}
And XXI	$23^{\rm h}54^{\rm m}47.9^{\rm s}$	$+42°28'14''$	770^{+23}_{-22}
And XXII	$01^{\rm h}27^{\rm m}40.4^{\rm s}$	$+28°05'25''$	754^{+24}_{-23}
And XXIII	$01^{\rm h}29^{\rm m}21.0^{\rm s}$	$+38°43'26''$	745^{+24}_{-25}
And XXIV	$01^{\rm h}18^{\rm m}32.7^{\rm s}$	$+46°22'13''$	609^{+19}_{-20}
And XXV	$00^{\rm h}30^{\rm m}09.9^{\rm s}$	$+46°51'41''$	752^{+23}_{-23}
And XXVI	$00^{\rm h}23^{\rm m}46.3^{\rm s}$	$+47°54'43''$	786^{+24}_{-23}
And XXX	$00^{\rm h}36^{\rm m}34.6^{\rm s}$	$+49°38'49''$	558^{+17}_{-16}
NGC 147	$00^{\rm h}47^{\rm m}27.0^{\rm s}$	$+34°22'29''$	773^{+21}_{-20}
NGC 185	$00^{\rm h}38^{\rm m}58.0^{\rm s}$	$+48°20'15''$	650^{+18}_{-18}
Outside the PAndAS footprint			
LGS 3/Pisces	$01^{\rm h}03^{\rm m}55.0^{\rm s}$	$+21°53'06''$	605.3 ± 14
And VI	$23^{\rm h}51^{\rm m}46.4^{\rm s}$	$+24°35'11''$	831.8 ± 23
And VII	$23^{\rm h}26^{\rm m}31.7^{\rm s}$	$+50°40'33''$	824.1 ± 23
And XXIX	$23^{\rm h}58^{\rm m}55.6^{\rm s}$	$+30°45'20''$	711.2^{+20}_{-19}
And XXXI	$22^{\rm h}58\ ^{\rm m}6.3^{\rm s}$	$+41°17'28''$	744.7 ± 17
And XXXII	$00^{\rm h}35^{\rm m}59.4^{\rm s}$	$+51°33'35''$	801.7^{+23}_{-22}
And XXXIII	$03^{\rm h}01^{\rm m}23.6^{\rm s}$	$+40°59'18''$	704.7^{+20}_{-19}

Notes: All distances are from Savino et al. (2022). Some dwarf galaxies, although in the considered footprint, are not part of this sample because the detection limits for their survey and/or at their location are not quantified (M21, NGC205, Pisces VII, Pegasus V), because of significant uncertainties in their structural parameters (And XXVII; Richardson et al. 2011), or because their distances from M31 exceed 300 kpc (And XVIII; And XXVIII; Savino et al. 2022).

Table VI.2: Values for the models parameters depending on the dwarf galaxy sample and the position prior

Model	Prior on the center position	Sample	Δx (kpc)	Δy (kpc)	ΔD (kpc)	γ
Power law	Uniform	PAndAS	3^{+10}_{-11}	8±12	-46^{+35}_{-30}	-2.0 ± 0.10
Power law	Gaussian	PAndAS	3^{+8}_{-9}	5±10	-14^{+21}_{-24}	-2.0 ± 0.10
Power law	Gaussian	PAndAS + SDSS	2^{+7}_{-8}	4.5±10	-18^{+22}_{-27}	-2.0 ± 0.10
NFW	Gaussian	PAndAS	4^{+3}_{-3}	1±4	-27±14	

$M_V - \log(r_{\rm h}(\,{\rm pc}))$ recovery fraction grid. Furthermore, an additional analytical model has been developed to account for the influence of heliocentric distance on recovery fractions. While the impact of distance on the recovery fraction of a dwarf galaxy is less prominent compared to other parameters, it is still a factor that cannot be disregarded (Doliva-Dolinsky et al., 2022).

For dwarf galaxies outside of the PAndAS footprint, given the necessity to have an assessment of the search incompleteness, our selection is limited to dwarf galaxies that have been detected either in SDSS or in Pan-STARRS. As a result, the recently discovered dwarf galaxies Pisces VII and Pegasus V (Collins et al., 2022, 2023), are not considered in this study. Given the comparable depth of the SDSS (Abazajian et al., 2003) and Pan-STARR1 (Chambers et al., 2016) surveys, the recovery fractions for dwarf galaxies located outside the PAndAS footprint, within a radial distance of up to 300 kpc and with a galactic latitude $b < -9.5°$, are based on the detection limit derived by Koposov et al. (2008) using SDSS data. In this study, they evaluate the survey's completeness across a range of $-11 \leq M_V \leq 0$, $0 \leq \log(r_{\rm h}(\,{\rm pc})) \leq 3.0$, and different distance range but, given the distance of M31, we exclusively use the results obtained for distances between 512 and 1024 kpc. To assess the detectability, Koposov et al. (2008) inject artificial dwarf galaxies into the SDSS catalogue, and their detection or non-detection is determined using a match filter algorithm. The resulting recovery fraction is then fitted with an analytical model. We extrapolate both PAndAS and SDSS analytical model for detection limits to cover a range of $-17 < M_V < -5.5$ and $1.8 < \log(r_{\rm h}(\,{\rm pc})) < 4.0$.

VI.3 Method

VI.3.1 Basics of the model

We aim to infer the center of the spatial distribution of M31 satellites while accounting for the dwarf galaxy search completeness. We consider a sample of N dwarf galaxy, listed in Table VI.1, defined by the set of properties properties $\mathcal{D} = \{\overrightarrow{d_k}\}_{1 \leq k \leq N}$. The probability, P_{sp},

that those satellites follow a 3D spatial density distribution model, ρ_{sp}, defined by the set of parameters $\mathcal{P}$ over a region $\mathcal{A}$ is therefore

$$\begin{aligned} P_{sp}\left(\mathcal{D}|\mathcal{P}\right) &= \prod_k P_{sp,k}\left(\overrightarrow{d_k}|\mathcal{P}\right), \\ &= \frac{\rho_{sp}\left(\overrightarrow{d_k}|\mathcal{P}\right)}{\int_{\mathcal{A}} \rho_{sp}\left(\overrightarrow{d_k}|\mathcal{P}\right)\tau\left(\overrightarrow{d_k}\right)d\overrightarrow{d_k}}, \end{aligned} \tag{VI.1}$$

with $\tau\left(\overrightarrow{d_k}\right)$ a completeness coefficient taking into account the footprint of the survey and the surface brightness detection limits. This factor is obtained by marginalizing the recovery fraction calculated in Doliva-Dolinsky et al. (2022) within the PAndAS survey footprint and in Koposov et al. (2008) for the rest of the sky, over the magnitude and size of the dwarf galaxies using the luminosity function and the size-luminosity relation inferred in Doliva-Dolinsky et al. (2023).

Following the principle of Bayesian inference, first described by Bayes & Price (1763) and further developed by Marquis de Laplace (1812), the likelihood we aim to determine, $P\left(\mathcal{P}|\mathcal{D}\right)$, is link to $P\left(\mathcal{D}|\mathcal{P}\right)$ via the prior $P(\mathcal{P})$ such that

$$P(\mathcal{P}|\mathcal{D}) \propto P\left(\mathcal{D}|\mathcal{P}\right)P(\mathcal{P}). \tag{VI.2}$$

VI.3.2 Volumetric Spatial Distribution

Throughout this article, we assume an isotropic distribution of satellites and we choose to infer the center of the distribution for two models. We note r_c the distance of an object to the center of the distribution. The dwarf galaxies are defined by their sky coordinates (α_{gal}, δ_{gal}) and their heliocentric distance $D_{MW,gal}$, therefore $\overrightarrow{d_k} = \{\alpha_{gal,k}, \delta_{gal,k}, D_{MW,gal,k}\}_{1\leq k\leq N}$. As all model tested are isotropic, a simplification can be made by defining dwarf galaxies by r_c their distance to the center of the distribution, yielding $\overrightarrow{d_k'} = \{r_{c,k}\}_{1\leq k\leq N}$. This value is obtain through simple algebra while using the coordinates of the center of the dwarf galaxy (i.e, its sky coordinates (α_c, δ_c) and its heliocentric distance $D_{MW,c}$).

First, we choose to test an agnostic and simple spatial distribution function. The density is assumed to follow a power law as a function of the radius r_c. As the distribution is isotropic, we have

$$\begin{aligned} \rho(r_c|\gamma_{pow}) &= \int_0^{2\pi}\int_0^{\pi} r_c^2 r_c^{\gamma_{pow}}\sin(\theta)d\theta d\phi. \\ &= 4\pi r_c^{2+\gamma_{pow}} \end{aligned} \tag{VI.3}$$

Secondly, we choose to test an NFW distribution function (Navarro et al., 1996) as it is expected that satellites follow the NFW profil of the DM (Guo et al., 2013; McDonough &

Brainerd, 2022). The virial radius R_{vir} is roughly estimated at 300 kpc and the mass of M31, M_{M31}, is chosen to be $1.33 \times 10^{12} M_{\odot}$ (Peñarrubia et al., 2016), yielding a concentration c= 7.9 following the relation presented in Diemer & Joyce (2019). The density can be written

$$\begin{aligned} \rho(r_c) &= \frac{\rho_0}{\frac{r_c}{R_s}\left(1+\frac{r_c}{R_s}\right)^2}, \\ \text{with } \rho_0 &= \frac{M_{M31}}{4\pi R_s^3 \left(\ln(1+c) - \frac{c}{1+c}\right)} \text{ and } R_s = \frac{R_{vir}}{c}. \end{aligned} \tag{VI.4}$$

yielding,

$$\mathcal{P}_{pow} = \{\gamma_{pow}, \alpha_c, \delta_c, D_{MW,c}\}, \tag{VI.5}$$

$$\mathcal{P}_{NFW} = \{\alpha_c, \delta_c, D_{MW,c}\}. \tag{VI.6}$$

VI.3.3 Priors

Following Equation VI.2, we set a prior for each parameter to determine $P(\mathcal{P}|\mathcal{D})$.

- We impose $\gamma_{pow} \leq -2$ as it is expected that the density of dwarf galaxy decrease as a function of the distance to the main host. We therefore choose to impose a uniform prior on γ_{pow} such that $-10 \leq \gamma_{pow} \leq -2$.

- Salomon et al. (2023) present a prediction regarding the maximum/average distance between the center of mass of the disk and the center of mass of the DM halo/satellite distribution, estimating it to be 30 kpc. Based on this, we choose to impose Gaussian priors on the physical coordinates of the center in the tangential plane to M31, denoted as x_c and y_c. These Gaussian priors have a mean of 0 and a dispersion, σ_{offset}, equal to $\frac{30}{\sqrt{3}}$ kpc. These priors can be easily converted into priors on α_c and δ_c via the distance of M31.

- For the distance of the distribution center to the MW, $D_{MW,c}$, we choose to account for the possible offset with the center of M31 along with the uncertainty on M31's distance. We therefore choose a Gaussian prior with a mean of 0 and a dispersion σ such that $\sigma = \sqrt{\sigma_{offset}^2 + \sigma_{D_{M31}}^2}$. As determined by Savino et al. (2022), $\sigma_{D_{M31}}$=22 kpc and as detailed above $\sigma_{offset} = \frac{30}{\sqrt{3}}$.

VI.3.4 Implementation

The likelihood is sampled using our own Metropolis-Hasting algorithm (Metropolis et al., 1953; Hastings, 1970). To accurately account for the uncertainties associated with the observed properties of the dwarf galaxies, we incorporate the probability distribution functions (PDFs) for each parameter instead of relying on single values. Following Conn

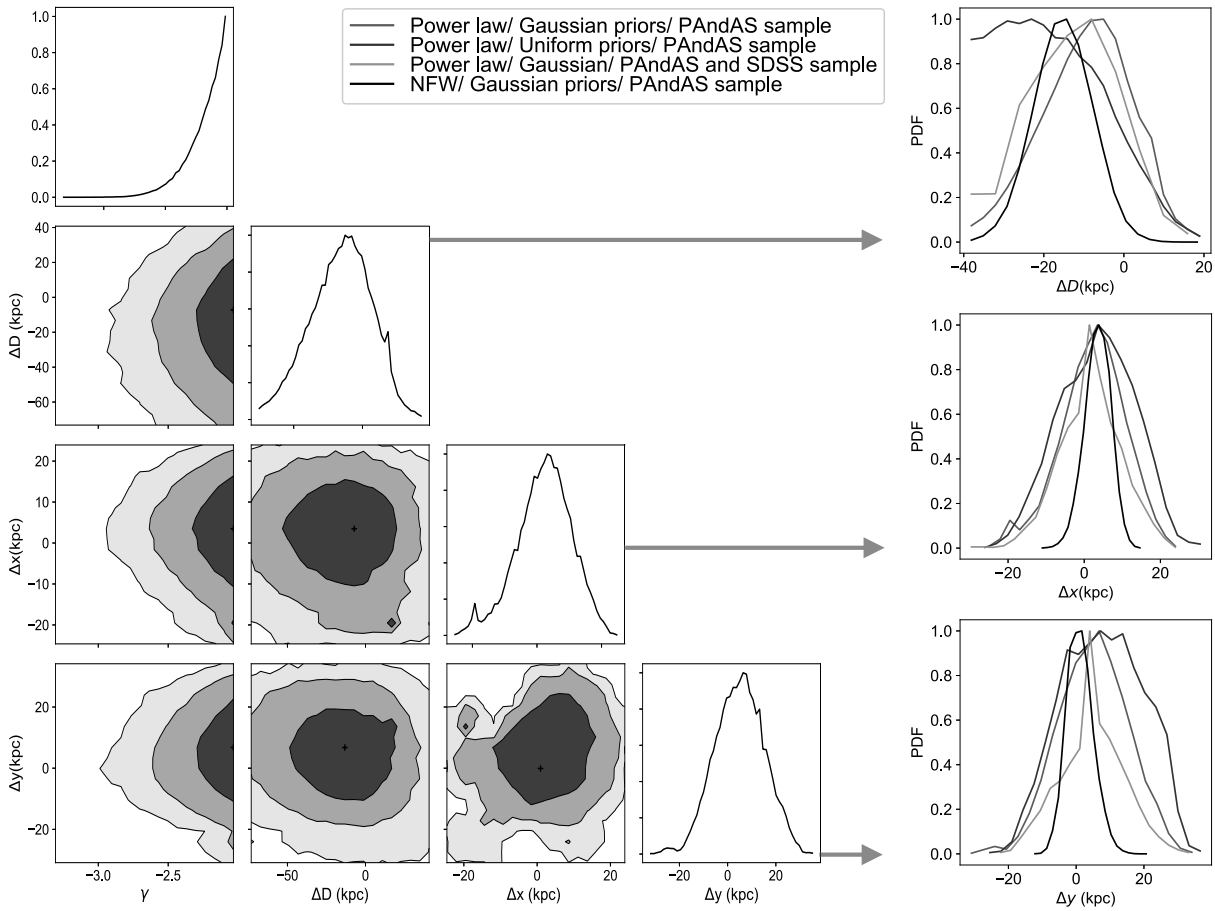

Figure VI.1: *Left panels*: Marginalized PDFs and correlation graphs for each parameters of the model composed by a power-law spatial distribution when enforcing a Gaussian prior on the central position parameters and when using the PAndAS sample. *Right panels*: Marginalized PDFs of the distance between the center of M31 and the one of the spatial distribution. While the favored distance of the center are shifted toward the MW, the center of the distribution is overall compatible with M31 center.

et al. (2013), we convolve the likelihood for a single value expressed in Equation VI.1 with the PDFs of distances of M31 satellites to the MW such that

$$\mathcal{L}(\mathcal{D}'_\Omega|\mathcal{P}') = \int_\Omega \mathcal{L}(\mathcal{D}'|\mathcal{P}')g(\mathcal{D}')d\mathcal{D}', \tag{VI.7}$$

with Ω the set of all combinaison of distances $\mathcal{D}'$ and $g(\mathcal{D}')$ the probability of a given combinaison. To compute this integral, we employ a Monte-Carlo method. We generate 50 satellite systems by drawing from the PDF of $D_{MW,gal}$ for each galaxy in our sample. The final distribution is obtained by summing the resulting chains.

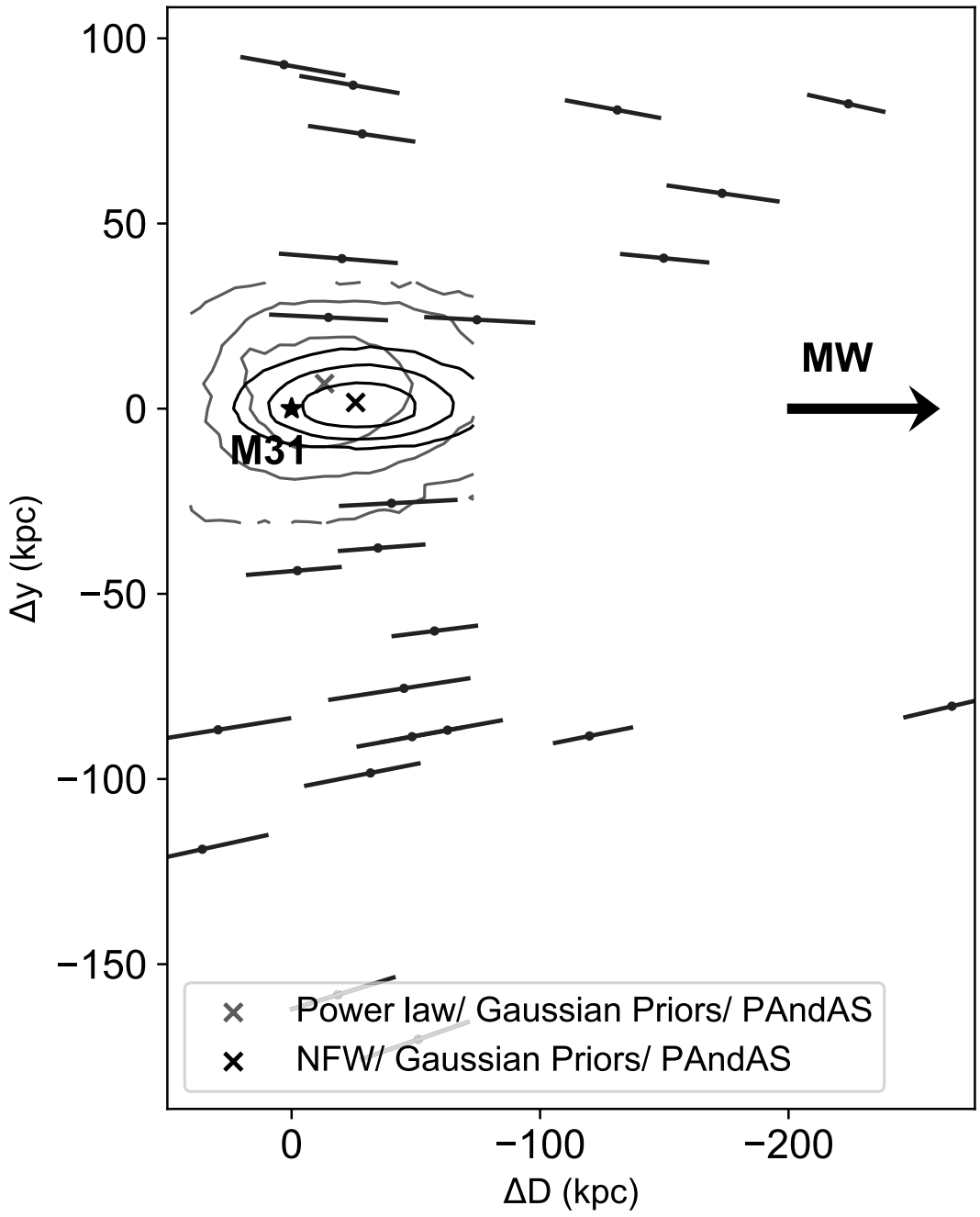

Figure VI.2: PDFs for the center's position in the y-z plane in the case of a power law and NFW spatial distribution. M31's position is marked by a star, known dwarf galaxies are represented by purple dots, and the inferred satellite distribution center positions are denoted by blue/black crosses, along with their associated confidence contours.. We infer that M31 center is compatible with the center of the distribution but the model favors a center shifted toward the MW.

VI.4 Results

For all spatial distribution models, Table VI.2 provides constraints on the center position and slope, where applicable. The equatorial coordinates of the distribution center are projected onto the tangential plane to the centre of M31 in order to present the parameters as the shift of the distribution center from M31. We refer to these sky coordinates as (Δx, Δy) and the shift in distance as ΔD. To determine the favored value, we consider the peak of the marginalized PDF, while the credible interval are bound by the parameter values whose PDF values are 0.61 of the maximum. However, to use these results effectively, we strongly recommend using the MCMC chains available at `https://github.com/dolivadolinsky`.

The left panels of Figure VI.1 show the correlation between parameters and the marginalized PDF for each parameter in the case of a power-law spatial distribution, incorporating a Gaussian prior on the position and using the PAndAS sample, and the right panels present the marginalized PDFs of the positional parameters of the center for each of the models tested. Although the three positional parameters are generally well constrained, the posteriors are rarely perfect Gaussians due to the non-trivial impact of the detection limits on the model.

In all cases with a power-law spatial distribution, we infer a favored slope of $\gamma = -2.0 \pm 0.1$. Although this agreement might suggest compatibility between the cases, since the favored slope is the lower bound of our uniform prior, it actually indicates that the limited number of dwarf galaxies is insufficient to adequately constrain this parameter.

We infer a marginal shift in sky coordinates ranging from $\Delta x = 2^{+7}_{-8}$ kpc to $\Delta x = 4^{+3}_{-3}$ kpc and from $\Delta y = 1 \pm 4$ kpc to $\Delta y = 8 \pm 12$ kpc.

When using a power-law spatial distribution, a uniform prior on the position of the center, and the PAndAS sample, we infer a shift in the heliocentric distance of $\Delta D = -46^{+35}_{-30}$ kpc. However, the distance difference decreases to $\Delta D = -14^{+21}_{-24}$ kpc when a Gaussian prior is imposed, considering the PAndAS sample alone, and to $\Delta D = -18^{+22}_{-27}$ kpc when both the PAndAS and SDSS samples are used. This increase in distance suggests that the available data are not robust enough to override our prior preference for the center to be in proximity to M31. However, when employing an NFW profile, which removes one degree of freedom, we infer a shift in the distance of $\Delta D = -27 \pm 14$ kpc.

VI.5 Discussion

In this paper, we use forward modeling to infer the center and, if applicable, the slope of the spatial distribution of M31 satellites, assuming an isotropic distribution. Our analysis incorporated the detection limits of the PAndAS and SDSS surveys.

We conclude that the sky coordinates of the distribution center (α_c, δ_c) are consistent with the position of M31. This suggests that any potential offset of M31 from its satellite system would primarily be along the axis pointing towards the MW. We infer that the shift

in the distance to the center of the satellite system compared to M31 is ranging between $\Delta D = -46^{+35}_{-30}$ to $\Delta D = -14^{+21}_{-24}$ kpc. While the favored value for M31 (Savino et al., 2022) is compatible in the case of a power-law distribution with the Gaussian prior, it fall outside the 1σ range when using the NFW profile (Figure VI.2). To establish a more robust constraint on the center and profile of this satellite distribution, it is crucial to increase the number of known dwarf galaxies, particularly beyond the coverage of the PAndAS footprint. Expanding the sample will provide a deeper understanding of this peculiar satellite distribution and enable more comprehensive insights on galaxy formation and on the cosmology.

We cannot confidently conclude that M31 is not at the center of its satellite distribution in any of the cases studied. The previous findings reported in Doliva-Dolinsky et al. (2023) indicated a rejection at a 99.9% confidence level of completeness as the sole explanation for the observed anisotropy, showing that it is a real feature of the satellite system. While these results may appear contradictory, it is important to note the differing approaches employed. In the previous study, the center of the distribution was fixed to the position of M31, allowing for the inference of the distribution's slope and subsequent derivation of the probability that our inferred model exhibits the same level of anisotropy as M31. Conversely, our current study focuses on investigating both the position of the center and, if applicable, the slope of the distribution. We find that, considering the limited number of known dwarf galaxies, the center of M31 remains compatible with the center of its satellite distribution. However, it is worth noting that the preferred center position still exhibits a slight shift towards the Milky Way. To conclude, as the models and questions are different, it is not unexpected that the conclusion differ slightly.

Finally, the inferred distance results in a shift of approximately 10 to 50 kpc between M31 and the center of the satellite distribution. This magnitude of shift is comparable to the effect caused by the Large Magellanic Cloud, where the outer halo (> 30 kpc) shifts from the center of mass (COM) of the disk by approximately 15 to 25 kpc (Garavito-Camargo et al., 2021). Similarly, the interaction of M31 with the now Giant stream, as described by Hammer et al. (2018) and D'Souza & Bell (2018), may have contributed to the observed shift between M31 and the center of the satellite distribution.

Claude Monet, Impression, soleil levant, 1872

Chapter VII

Conclusion

VII.1 Summary

Dwarf galaxies are important probes of the cosmology and the physics of galaxy formation & evolution. The 21th century witnessed a remarkable surge in the discovery of satellites, driven by the advent of large, homogeneous, photometric surveys, enabling rigorous statistical analyses to compare observations with models of cosmology and galaxy formation & evolution. While the majority of constraints stem from the analysis of the satellite system of our own galaxy as outlined in Chapter I, it is imperative to extend the study of dwarf galaxies to other host galaxies to ensure a comprehensive understanding, considering that the MW may not represent a typical system (Weisz et al., 2019).

Chapter II introduces M31 and its companions, which constitue the most accessible system beyond our own galaxy. The understanding of the M31 halo has been greatly enhanced by the PAndAS survey. This large, homogeneous, photometric program probed a region within a projected 150 kpc of M31, containing 26 known dwarf galaxies, with 19 of them being discovered through PAndAS. This survey has revealed numerous substructures in M31's halo, aligning with predictions from M31 modelization that indicate a recent significant merger (Hammer et al., 2018; D'Souza & Bell, 2018).

In Chapter III, the search algorithm developed by the PAndAS team (Martin et al., 2013a) is comprehensively detailed, encompassing the modifications tailored to precisely determine the detection limits for the PAndAS sample of dwarf galaxies.

Since detection limits are a key element in comparing observed satellite systems with simulated ones, in Chapter IV I determined the incompleteness of M31's satellite sample using the PAndAS survey. I obtain precise recovery fractions as a function of the magnitude, size, and position of a dwarf galaxy in the survey. I therefore generated $\sim$ 500000 artificial dwarf galaxies, inserted them into the survey, and tested their recovery using the search algorithm developed by the PAndAS team (Martin et al., 2013a). For most fields, the surface brightness detection threshold is between 29-30 mag arcsec^{-2}, but it depends strongly on the position

in the survey. Indeed, the detection of a satellite is affected by the contamination from the MW (in the north of the survey; b $> -20°$) and from the stellar halo of M31. Determining the completeness was the first step towards a global analysis of the M31 satellite system.

In Chapter V, I inferred the global properties of the M31 satellite system folding in the previously determined detection limits for the search for dwarf galaxies in the PAndAS survey. I designed a bayesian framework that allows for the determination of the luminosity function, the slope of the 2- or 3-dimensional density distribution, the size-luminosity relation, and the number of satellites. I conclude that M31 hosts from 92^{+19}_{-26} to 136^{+65}_{-35} within 300 kpc of M31 and with $M_V < -5.5$, while only ~ 40 satellites are known. The redetermination of the distance by Savino et al. (2022) highlighted the anisotropy of the M31 satellite distribution, as they are almost all located between the MW and M31. Using the derived global properties of the M31 satellite system, I tested whether the anisotropy could be explained by the detection limits alone. I rule this out with more than 99.9%, thus proving that this anisotropy is a real feature of the M31 dwarf galaxy system.

In Chapter VI I explore one of the possible explanations for the peculiar distribution of M31 dwarf galaxies. Indeed, following the predicted shift of the MW position due to the LMC, it seems natural that M31 could be similarly offset from its satellite distribution. I have derived the position of the center of M31's satellite distribution for an NFW and a power-law radial distribution model. In each case, the position of M31 is statistically compatible with the center of its dwarf distribution, but the position of the center is always shifted toward the MW by $\sim 10 - 50$ kpc.

Throughout my PhD, I have established a solid foundation for a rigorous examination of the M31 satellite system, encompassing the determination of its global properties through forward modeling while considering the detection limits of the PAndAS survey. The first outcome of this framework has been the investigation of the peculiar distribution of M31 satellites. With this essential groundwork accomplished, we are now well-equipped to undertake a comparative analysis of the satellite systems of M31 and the Milky Way.

VII.2 The MW and M31 satellite system : a comparative study

The sensitivity of dwarf galaxies to their environment and host merger history is widely acknowledged, though this has primarily been explored through simulations (Engler et al., 2021; Kanehisa et al., 2023; Van Nest et al., 2023) or through the detailed properties of individual MW or M31 dwarf galaxies (Weisz et al., 2019). In observations, only the impact on the brightest end of the satellite system has been studied (Mao et al., 2021; Carlsten et al., 2022), given the challenges of detecting faint satellites around more distant hosts. Nonetheless, in this thesis, I inferred the properties of the M31 satellite system for dwarf galaxies with $M_V < -5.5$, thereby paving the way for a comparative study between the properties of M31's satellite system and that of the MW.

Firstly, it is worth mentioning that the comparison of both satellite systems highlights

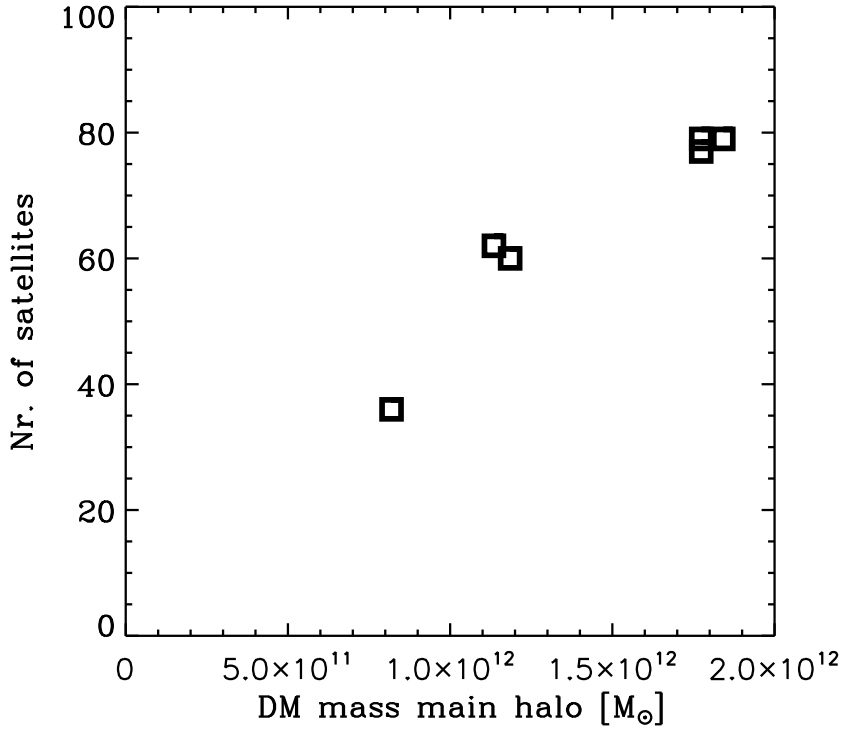

Figure VII.1: Number of satellites with $M_V < -5$ as a function of the virial masses of their host for 6 Aquaruis haloes. Credit : Starkenburg et al. (2013).

that dwarf galaxies in M31 stem from the same baryonic processes as those found in the MW. To first order, the global properties of the MW and M31 exhibit similarities. Specifically, the slope of the luminosity function falls within the same range. For the MW, $\beta = -1.9 \pm 0.2$ (Tollerud et al., 2008) or $\beta \sim -1.25$ (Koposov et al., 2008), while for M31, we infer a slope of $\beta = -1.5 \pm 0.1$. Furthermore, our results align with those of Brasseur et al. (2011) for the MW, illustrating that both systems of dwarf galaxies adhere to a similar size-luminosity relation.

VII.2.1 Is M31 more massive ?

It is well-established that M31 is expected to be more massive than the MW (Peñarrubia et al., 2016). Simulations consistently indicate a direct proportionality between the number of satellites and the mass of the host galaxy (Starkenburg et al., 2013; Engler et al., 2021), as depicted in Figure VII.1. Consequently, M31's halo is anticipated to contain more dwarf galaxies than the MW's. This prediction aligns with the expected number of dwarf galaxies for both the Milky Way and M31. Model predictions for the MW estimate ∼20 to 40 satellites with $M_V < -5.5$ and $r_{\rm MW} < 300$ kpc (Newton et al., 2018; Jethwa et al., 2018; Nadler et al., 2020; Manwadkar & Kravtsov, 2022; Drlica-Wagner et al., 2020). In contrast, for M31, our

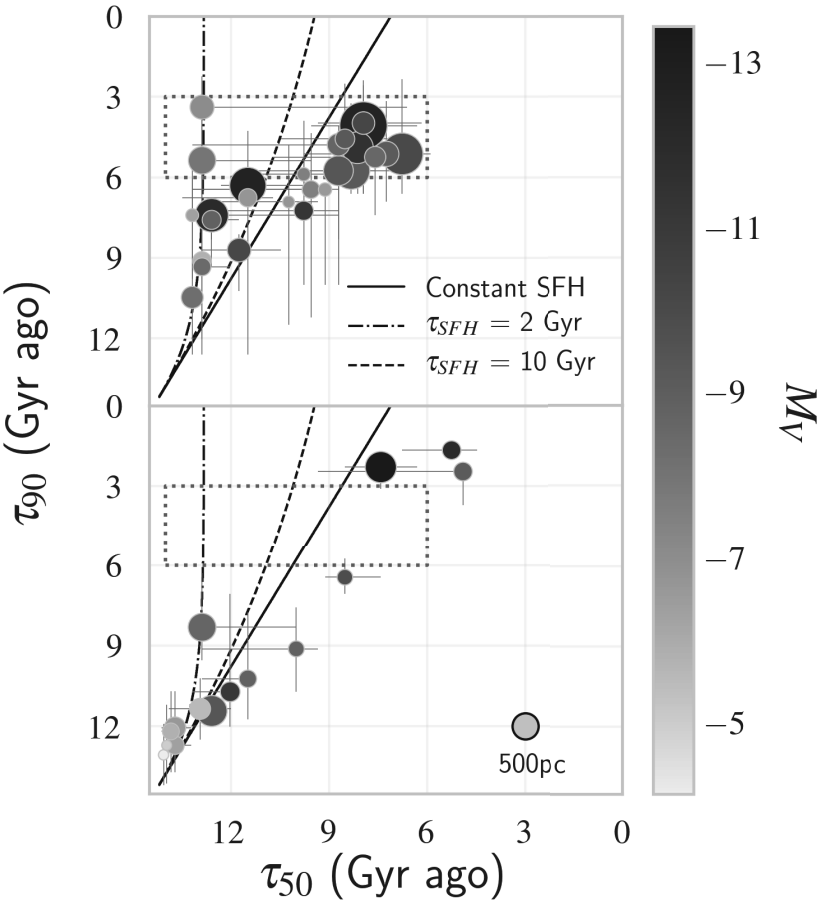

Figure VII.2: The top panel displays the lookback time at which 50% (τ_{50}) and 90% (τ_{90}) of the stellar mass was formed for M31 satellites, while the bottom panel illustrates the same for MW satellites. The colors of the dots indicate the luminosity of the dwarf galaxies, and their size scales with their half-light radii. In both panels, constant and exponentially declining SFHs are represented by black lines. Notably, half of M31 satellites are encompassed by the blue dotted rectangle, while the same region contains no MW satellites. Credit : Weisz et al. (2019).

inference reveals 2-3 times more satellites than for the MW, as we expect 92^{+19}_{-26} satellites with $M_V < -5.5$ and $r_{\rm MW} < 300$ kpc. Furthermore, M31 showcases a significantly higher abundance of globular clusters, with 92 globular clusters identified at projected distances between 25 and 150 kpc from M31 (Huxor et al., 2014; Mackey et al., 2019), this number is approximately seven times greater than the number of clusters found in a similar region for the MW. All of these tracers serve to reinforce the notion that M31 is indeed more massive than the MW.

VII.2.2 Did M31 have a more active accretion history?

The question of how typical the MW merger history is serves as a motivation for our work. Now, we direct our attention to the M31 halo to determine whether M31's accretion history is similar, reduced, or enhanced compared to the MW. Model predictions seem to suggest a more active history for M31 compared to the MW, as M31 is believed to have experienced a significant merger approximately $\sim 2-4$ Gyr ago, while the MW's last significant merger occurred around ~ 10 Gyr ago (D'Souza & Bell, 2018; Hammer et al., 2018; Helmi et al., 2018). However, it is important to note that the MW is presently undergoing a merger with the LMC (Besla et al., 2007; Vasiliev, 2023), and M31 is also experiencing a merger with M33, although the exact state of these mergers is still debated (Patel et al., 2017; Semczuk et al., 2018).

An initial observational clue lies in the number of bright substructures discovered in the PAndAS survey (McConnachie et al., 2018). Although an exact comparison is challenging due to the lack of detection limits for substructures, the halo of M31 appears to be more structured and contains a greater abundance of bright stellar substructures compared to the halo of the MW. Specifically, the presence of the Giant Stream is great evidence of a recent significant merger $\sim$ 2-4 Gyr ago (D'Souza & Bell, 2018; Hammer et al., 2018).

Another compelling clue resides in the Star Formation Histories (SFHs) of the M31 and MW dwarf galaxies, as they present different patterns highlighted in Figure VII.2. M31's dwarf galaxies exhibit extended SFHs, with the majority of satellites quenched between 3 to 6 Gyr ago. On the other hand, the MW's satellites show quenching that predominantly occurred around 9 Gyr ago, with only a few more recently quenched systems. These differences suggest a potential correlation between the satellites SFHs and the host merger history. One possible explanation for the surge of quenching of M31's dwarf galaxies between 3 to 6 Gyr ago is their environment, as simulations predict a major merger for M31 $\sim 2-4$ Gyr ago (Hammer et al., 2018; D'Souza & Bell, 2018). Indeed, these satellites may have been environmentally quenched or may have fell in M31 halo with the merger. This merger event could have played a significant role in shaping the SFHs of M31's satellites, and reenforce the idea of an active M31 merger history.

The presence of merging dwarf galaxies, along with their own satellite companions, is expected to impact the luminosity function. Simulations indicate that the signature of satellite enhancement is visible in the luminosity function for up to 2.25-4.25 Gyr (Joshi et al., 2023). Consequently, given the distinct merger histories of M31 and the MW, differences in their luminosity functions are expected to emerge. However, conducting a robust and quantified comparison of the slopes of the luminosity function is challenging due to the non-homogeneity of the methods used to derive these slopes and the fact that very faint satellites ($M_V \geq -5.5$) around M31 are currently undetectable.

A plausible explanation for the plane-like distribution of dwarf galaxies around the MW or M31 (Lynden-Bell, 1976; Kroupa et al., 2005; Ibata et al., 2013; Pawlowski et al., 2013)

is the activity of their host galaxies. However, according to Kanehisa et al. (2023), major mergers can enhance the phase-space correlation of satellites, with an observable signature lasting up to $2-5$ Gyr, but they may not create coherent and/or highly flattened planes of satellites. Even though the proper motion of M31's dwarf galaxies is currently unknown, this result suggests that the plane-like distribution of satellites around the MW and M31 may not be a signature of their merger history. However, the distribution of M31 dwarf galaxies display a strong anisotropy, as nearly all of them are between the MW and M31. This peculiar distribution may imply that the M31 satellites are not fully virialized, and the distribution could result from the sloshing of M31 due to a past merger event. While the constraints inferred in this study were compatible with M31 being at the center of its distribution, it also revealed a shift of approximately $\sim 10-50$ kpc towards the MW from the distribution center.

While there are indications that M31 is more active than the MW, a precise quantification of the impact of the host's merger history on the satellite system requires additional data on M31 dwarf galaxies. Increasing the sample of known M31 dwarf galaxy with fainter satellites or satellites outside of the PAndAS footprint is necessary to better understand the impact of the host environment and history.

VII.3 Future prospects

In this section, I will discuss some of the futur projects that will continue to explore the use of dwarf galaxies as a testbed for cosmology and galaxy formation & evolution.

Deepening our knowledge of M31 satellite system: While the advent of large, homogeneous surveys has significantly increased the number of known M31 satellites, the faintness regime still lags behind that of the MW's dwarf galaxies due to the challenges of detecting such faint objects at distances of $\sim 700-800$ kpc from the MW. The PAndAS survey has successfully discovered 19 dwarf galaxies through density maps or match-filter methods. However, the implementation of a Bayesian search algorithm, capable of modeling both the dwarf galaxy and the contamination, has revealed a number of potential dwarf galaxies that have yet to be confirmed. One of my objectives is to observe these candidate objects with deep photometry using the HST/ACS instrument to definitively ascertain whether they are indeed M31 satellites. By confirming their nature, we can further enhance our understanding of the M31 satellite system and shed light on the faint-end properties of dwarf galaxies.

The ultimate dwarf galaxy search algorithm: : The upcoming LSST and Euclid survey will be an incredible opportunity to increase the number of known MW dwarf galaxy as the scope to detect faint dwarf galaxies will go from our surrounding to the entire MW halo. This potential new dwarf galaxies are essential for better constraining the properties of dark matter particles, exploring the impact of baryonic physics, and resolving or confirming any tension between satellite observations and simulations. To capitalize on this opportunity, I wish to design the ultimate search algorithm that leverages the combination of photometric,

spectroscopic, and astrometric data to efficiently detect dwarf galaxies. By combining information from surveys such as the Sloan Digital Sky Survey (SDSS), the Panoramic Survey Telescope and Rapid Response System (Pan-STARR), Gaia, the Dark Energy Survey (DES), and the DESI Legacy survey, we can capitalize on their different footprints, depths, and photometric bands. Furthermore, with the anticipated depth of the future surveys, it becomes imperative to enhance the distinction between satellites, background galaxies, and globular clusters. Currently done manually, I plan to automate this step by utilizing spectrographic and astrometric information.

Dwarf galaxies as cosmological probes: The mass distribution of observed satellite systems holds significant power in constraining the mass of Dark Matter particles, but careful consideration of the completeness of observations is crucial for accurate results. Throughout my PhD, I have developed a robust statistical framework to infer precise constraints on the properties of Andromeda's satellites. The next step of my research involves comparing the expected Dark Matter subhalo mass distribution with the inferred luminosity function of Andromeda's satellite system, enabling the derivation of constraints on the mass of the Dark Matter particle from observations of Andromeda's satellites for the first time. Moreover, I will also utilize mock observations, similar to those in the PAndAS survey, derived from the Auriga simulations as presented in Thomas et al. (2021). By applying the framework developed in this thesis to these artificial satellite systems, I will determine their global properties and subsequently compare them to the observations. This comparative analysis aims to identify potential similarities and differences between the satellite systems from simulations and observations, shedding further light on the nature of Dark Matter and on the physics of galaxy formation & evolution.

Exploring the impact of the environment on satellite systems: The Milky Way's dwarf galaxies have been a primary reference for satellite systems. However, considering that the Milky Way may not be a typical system, it becomes imperative to investigate the properties of dwarf galaxies in other galactic environments. Detecting and characterizing faint galaxies at greater distances from us presents a challenge, but the forthcoming LSST and Euclid will provide unprecedented data on Local Volume galaxies as it is expected to resolve stars for systems within 5 Mpc of the MW. I propose utilizing the tools developed for Andromeda's system to search for and characterize new dwarf galaxies around these distant hosts. By employing this approach, we can assess the completeness and infer the properties of these satellite systems. Additionally, to build a more extensive sample of galaxies, I will also investigate unresolved dwarf galaxies around even more distant hosts. Dwarf galaxy systems exhibit diverse properties influenced by factors such as environment, and mergers with the main host. To quantify the impact of host properties and environment on dwarf galaxies, I will compare the properties of different satellite systems analyzed homogeneously, examining their mass distribution and spatial distribution.

In conclusion, characterizing the M31 satellite system marks the initial stride towards a comprehensive analysis of satellite systems. With the advent of revolutionary surveys

like LSST and Euclid, along with the expected discovery of numerous new satellites around diverse hosts, the future holds the promise of a deeper understanding of cosmology, galaxy formation & evolution.

Appendices

Appendix A Model parameters

Field	$M_{V,\mathrm{lim}}$	α	σ	$M_{V,\mathrm{lim},0}$	α_0
1	-5.51	-0.72	0.45	-5.17	-0.48
2	-5.27	-0.64	0.38	-4.93	-0.4
3	-5.29	-0.69	0.45	-4.95	-0.45
4	-5.34	-0.73	0.41	-5.0	-0.49
5	-5.42	-0.67	0.35	-5.08	-0.43
6	-5.14	-0.75	0.43	-4.8	-0.51
7	-5.27	-0.75	0.44	-4.93	-0.51
8	-5.35	-0.68	0.39	-5.01	-0.44
9	-5.17	-0.77	0.38	-4.83	-0.53
10	-5.33	-0.82	0.44	-4.99	-0.58
11	-5.17	-0.72	0.36	-4.83	-0.48
12	-5.16	-0.73	0.38	-4.82	-0.49
13	-5.41	-0.68	0.37	-5.07	-0.44
14	-5.79	-0.65	0.46	-5.45	-0.41
15	-5.23	-0.77	0.34	-4.89	-0.53
16	-5.14	-0.64	0.43	-4.8	-0.4
17	-5.34	-0.78	0.35	-5.0	-0.54
18	-5.47	-0.69	0.41	-5.13	-0.45
19	-5.26	-0.7	0.4	-4.92	-0.46
20	-5.26	-0.71	0.34	-4.92	-0.47
21	-5.2	-0.73	0.43	-4.86	-0.49
22	-5.3	-0.71	0.45	-4.96	-0.47
23	-5.15	-0.72	0.36	-4.81	-0.48
24	-5.3	-0.66	0.41	-4.96	-0.42
25	-5.32	-0.69	0.32	-4.98	-0.45
27	-5.29	-0.74	0.34	-4.95	-0.5
28	-5.37	-0.75	0.36	-5.03	-0.51
29	-5.24	-0.71	0.42	-4.9	-0.47
31	-5.24	-0.74	0.4	-4.9	-0.5

Field	$M_{V,\mathrm{lim}}$	α	σ	$M_{V,\mathrm{lim},0}$	α_0
32	-5.28	-0.78	0.41	-4.94	-0.54
33	-5.27	-0.68	0.34	-4.93	-0.44
34	-5.31	-0.73	0.37	-4.97	-0.49
35	-5.34	-0.81	0.44	-5.0	-0.57
36	-5.42	-0.66	0.4	-5.08	-0.42
37	-5.33	-0.75	0.36	-4.99	-0.51
38	-5.15	-0.61	0.39	-4.81	-0.37
39	-5.24	-0.72	0.36	-4.9	-0.48
40	-5.23	-0.71	0.38	-4.89	-0.47
41	-5.31	-0.68	0.35	-4.97	-0.44
42	-5.26	-0.64	0.38	-4.92	-0.4
43	-5.97	-0.64	1.0	-5.63	-0.4
44	-5.33	-0.86	0.4	-4.99	-0.62
45	-5.24	-0.73	0.36	-4.9	-0.49
46	-5.16	-0.65	0.33	-4.82	-0.41
47	-5.31	-0.76	0.34	-4.97	-0.52
48	-5.31	-0.75	0.36	-4.97	-0.51
49	-5.59	-0.76	0.46	-5.25	-0.52
50	-5.27	-0.72	0.29	-4.93	-0.48
51	-5.29	-0.76	0.29	-4.95	-0.52
52	-5.42	-0.82	0.43	-5.08	-0.58
53	-5.33	-0.73	0.37	-4.99	-0.49
54	-5.32	-0.74	0.37	-4.98	-0.5
55	-5.38	-0.64	0.34	-5.04	-0.4
56	-5.36	-0.66	0.37	-5.02	-0.42
57	-5.33	-0.71	0.4	-4.99	-0.47
58	-5.41	-0.75	0.43	-5.07	-0.51
59	-5.37	-0.73	0.4	-5.03	-0.49
60	-5.33	-0.73	0.38	-4.99	-0.49
61	-5.44	-0.74	0.37	-5.1	-0.5
62	-5.45	-0.72	0.37	-5.11	-0.48
63	-5.42	-0.74	0.39	-5.08	-0.5
64	-5.17	-0.68	0.4	-4.83	-0.44
65	-5.21	-0.8	0.35	-4.87	-0.56
66	-5.25	-0.72	0.4	-4.91	-0.48
67	-5.25	-0.67	0.37	-4.91	-0.43
68	-5.28	-0.65	0.35	-4.94	-0.41
69	-5.51	-0.79	0.43	-5.17	-0.55
70	-5.19	-0.74	0.42	-4.85	-0.5

Field	$M_{V,\mathrm{lim}}$	α	σ	$M_{V,\mathrm{lim},0}$	α_0
71	-5.3	-0.61	0.34	-4.96	-0.37
72	-5.33	-0.67	0.31	-4.99	-0.43
73	-5.28	-0.72	0.38	-4.94	-0.48
74	-5.21	-0.63	0.33	-4.87	-0.39
75	-5.15	-0.65	0.36	-4.81	-0.41
76	-5.3	-0.68	0.4	-4.96	-0.44
77	-5.39	-0.64	0.32	-5.05	-0.4
78	-5.39	-0.73	0.4	-5.05	-0.49
79	-5.25	-0.6	0.3	-4.91	-0.36
80	-5.22	-0.71	0.38	-4.88	-0.47
81	-5.28	-0.72	0.28	-4.94	-0.48
82	-5.39	-0.74	0.38	-5.05	-0.5
83	-5.33	-0.7	0.29	-4.99	-0.46
84	-5.18	-0.66	0.37	-4.84	-0.42
85	-5.3	-0.72	0.36	-4.96	-0.48
86	-5.23	-0.63	0.4	-4.89	-0.39
87	-5.3	-0.7	0.24	-4.96	-0.46
88	-5.38	-0.79	0.37	-5.04	-0.55
89	-5.32	-0.75	0.38	-4.98	-0.51
90	-5.47	-0.78	0.38	-5.13	-0.54
91	-5.37	-0.71	0.32	-5.03	-0.47
92	-5.43	-0.68	0.41	-5.09	-0.44
93	-5.41	-0.66	0.38	-5.07	-0.42
94	-5.46	-0.75	0.38	-5.12	-0.51
95	-5.35	-0.59	0.44	-5.01	-0.35
96	-5.39	-0.64	0.34	-5.05	-0.4
97	-5.31	-0.74	0.34	-4.97	-0.5
98	-5.26	-0.66	0.36	-4.92	-0.42
99	-5.39	-0.66	0.33	-5.05	-0.42
100	-5.44	-0.7	0.4	-5.1	-0.46
101	-5.37	-0.65	0.32	-5.03	-0.41
102	-5.37	-0.7	0.39	-5.03	-0.46
103	-5.47	-0.72	0.34	-5.13	-0.48
104	-5.35	-0.73	0.37	-5.01	-0.49
105	-5.36	-0.68	0.37	-5.02	-0.44
106	-5.25	-0.67	0.28	-4.91	-0.43
107	-5.46	-0.71	0.41	-5.12	-0.47
108	-5.36	-0.69	0.37	-5.02	-0.45
109	-5.37	-0.7	0.33	-5.03	-0.46

Field	$M_{V,\mathrm{lim}}$	α	σ	$M_{V,\mathrm{lim},0}$	α_0
110	-5.41	-0.79	0.32	-5.07	-0.55
111	-5.13	-0.6	0.32	-4.79	-0.36
112	-5.36	-0.67	0.38	-5.02	-0.43
113	-5.37	-0.71	0.36	-5.03	-0.47
114	-5.55	-0.7	0.38	-5.21	-0.46
115	-5.34	-0.68	0.36	-5.0	-0.44
116	-5.35	-0.69	0.41	-5.01	-0.45
117	-5.37	-0.61	0.27	-5.03	-0.37
118	-5.35	-0.59	0.37	-5.01	-0.35
119	-5.42	-0.66	0.31	-5.08	-0.42
120	-5.38	-0.72	0.37	-5.04	-0.48
121	-5.2	-0.65	0.37	-4.86	-0.41
122	-5.44	-0.75	0.38	-5.1	-0.51
123	-5.36	-0.65	0.38	-5.02	-0.41
124	-5.48	-0.76	0.38	-5.14	-0.52
125	-5.46	-0.76	0.36	-5.12	-0.52
126	-5.38	-0.74	0.34	-5.04	-0.5
127	-5.49	-0.81	0.44	-5.15	-0.57
128	-5.47	-0.72	0.37	-5.13	-0.48
129	-5.4	-0.67	0.3	-5.06	-0.43
130	-5.35	-0.69	0.4	-5.01	-0.45
131	-5.36	-0.66	0.35	-5.02	-0.42
132	-5.53	-0.71	0.28	-5.19	-0.47
133	-5.34	-0.68	0.42	-5.0	-0.44
134	-5.24	-0.6	0.31	-4.9	-0.36
135	-5.41	-0.7	0.36	-5.07	-0.46
136	-5.33	-0.65	0.4	-4.99	-0.41
137	-5.41	-0.65	0.36	-5.07	-0.41
138	-5.28	-0.72	0.41	-4.94	-0.48
139	-5.42	-0.66	0.38	-5.08	-0.42
140	-5.48	-0.68	0.39	-5.14	-0.44
141	-5.61	-0.72	0.38	-5.27	-0.48
142	-5.59	-0.71	0.28	-5.25	-0.47
143	-5.56	-0.79	0.4	-5.22	-0.55
144	-5.39	-0.59	0.36	-5.05	-0.35
145	-5.76	-0.91	0.42	-5.42	-0.67
146	-5.46	-0.6	0.4	-5.12	-0.36
147	-5.6	-0.91	0.41	-5.26	-0.67
148	-5.53	-0.83	0.35	-5.19	-0.59

Field	$M_{V,\mathrm{lim}}$	α	σ	$M_{V,\mathrm{lim},0}$	α_0
149	-5.38	-0.69	0.38	-5.04	-0.45
150	-5.52	-0.72	0.34	-5.18	-0.48
151	-5.41	-0.56	0.3	-5.07	-0.32
152	-5.35	-0.71	0.31	-5.01	-0.47
153	-5.35	-0.62	0.36	-5.01	-0.38
154	-5.48	-0.6	0.39	-5.14	-0.36
155	-5.34	-0.68	0.33	-5.0	-0.44
156	-5.59	-0.68	0.34	-5.25	-0.44
157	-5.49	-0.78	0.39	-5.15	-0.54
158	-5.59	-0.67	0.37	-5.25	-0.43
159	-5.58	-0.61	0.31	-5.24	-0.37
160	-5.32	-0.66	0.42	-4.98	-0.42
161	-5.58	-0.65	0.33	-5.24	-0.41
162	-5.48	-0.65	0.32	-5.14	-0.41
163	-5.51	-0.62	0.33	-5.17	-0.38
164	-5.72	-0.89	0.38	-5.38	-0.65
165	-5.56	-0.69	0.34	-5.22	-0.45
166	-6.28	-1.0	0.39	-5.94	-0.76
167	-5.79	-0.79	0.29	-5.45	-0.55
168	-5.89	-1.0	0.4	-5.55	-0.76
169	-5.54	-0.8	0.53	-5.2	-0.56
170	-5.39	-0.7	0.33	-5.05	-0.46
171	-5.26	-0.57	0.31	-4.92	-0.33
172	-5.58	-0.6	0.33	-5.24	-0.36
173	-5.38	-0.67	0.28	-5.04	-0.43
174	-5.61	-0.61	0.35	-5.27	-0.37
175	-5.43	-0.68	0.43	-5.09	-0.44
176	-5.43	-0.58	0.35	-5.09	-0.34
177	-5.36	-0.6	0.36	-5.02	-0.36
178	-5.6	-0.64	0.36	-5.26	-0.4
179	-5.59	-0.76	0.47	-5.25	-0.52
180	-5.7	-0.64	0.37	-5.36	-0.4
181	-5.58	-0.71	0.32	-5.24	-0.47
182	-5.52	-0.61	0.3	-5.18	-0.37
183	-5.81	-0.77	0.38	-5.47	-0.53
184	-5.69	-1.0	0.58	-5.35	-0.76
185	-5.81	-0.67	0.34	-5.47	-0.43
186	-6.13	-1.0	0.47	-5.79	-0.76
187	-5.6	-0.71	0.4	-5.26	-0.47

Field	$M_{V,\mathrm{lim}}$	α	σ	$M_{V,\mathrm{lim},0}$	α_0
188	-6.44	-1.0	0.61	-6.1	-0.76
189	-5.75	-0.74	0.36	-5.41	-0.5
190	-6.06	-0.99	0.42	-5.72	-0.75
191	-5.51	-0.67	0.24	-5.17	-0.43
192	-5.67	-0.56	0.29	-5.33	-0.32
193	-5.32	-0.59	0.32	-4.98	-0.35
194	-5.27	-0.57	0.27	-4.93	-0.33
195	-5.63	-0.56	0.36	-5.29	-0.32
196	-5.35	-0.61	0.25	-5.01	-0.37
197	-5.5	-0.54	0.35	-5.16	-0.3
198	-5.26	-0.57	0.35	-4.92	-0.33
199	-5.67	-0.62	0.37	-5.33	-0.38
200	-5.6	-0.66	0.37	-5.26	-0.42
201	-5.86	-0.68	0.3	-5.52	-0.44
202	-5.62	-0.68	0.2	-5.28	-0.44
203	-5.6	-0.59	0.34	-5.26	-0.35
204	-5.64	-0.74	0.36	-5.3	-0.5
205	-5.66	-0.8	0.35	-5.32	-0.56
206	-5.6	-0.65	0.36	-5.26	-0.41
207	-7.28	-0.78	0.32	-6.94	-0.54
208	-6.39	-1.0	0.49	-6.05	-0.76
209	-6.3	-0.98	0.53	-5.96	-0.74
210	-7.07	-0.75	0.33	-6.73	-0.51
211	-5.73	-0.84	0.42	-5.39	-0.6
213	-5.21	-0.55	0.27	-4.87	-0.31
215	-5.61	-0.53	0.3	-5.27	-0.29
216	-5.44	-0.59	0.37	-5.1	-0.35
217	-5.61	-0.7	0.36	-5.27	-0.46
218	-5.77	-0.6	0.29	-5.43	-0.36
219	-5.41	-0.61	0.25	-5.07	-0.37
220	-5.54	-0.56	0.35	-5.2	-0.32
221	-5.5	-0.55	0.3	-5.16	-0.31
222	-5.47	-0.6	0.32	-5.13	-0.36
223	-5.6	-0.68	0.4	-5.26	-0.44
224	-5.56	-0.56	0.28	-5.22	-0.32
225	-5.62	-0.71	0.46	-5.28	-0.47
226	-5.73	-0.72	0.36	-5.39	-0.48
227	-5.78	-0.66	0.3	-5.44	-0.42
229	-5.52	-0.65	0.39	-5.18	-0.41

Field	$M_{V,\mathrm{lim}}$	α	σ	$M_{V,\mathrm{lim},0}$	α_0
230	-5.86	-0.71	0.34	-5.52	-0.47
231	-7.24	-0.72	0.26	-6.9	-0.48
234	-5.69	-0.79	0.38	-5.35	-0.55
236	-5.39	-0.58	0.35	-5.05	-0.34
237	-5.51	-0.53	0.26	-5.17	-0.29
238	-5.48	-0.53	0.26	-5.14	-0.29
239	-5.44	-0.59	0.35	-5.1	-0.35
240	-5.67	-0.63	0.27	-5.33	-0.39
241	-5.56	-0.55	0.28	-5.22	-0.31
242	-5.39	-0.56	0.38	-5.05	-0.32
243	-5.56	-0.58	0.28	-5.22	-0.34
244	-5.56	-0.56	0.36	-5.22	-0.32
245	-5.53	-0.57	0.34	-5.19	-0.33
246	-5.68	-0.63	0.25	-5.34	-0.39
247	-5.66	-0.61	0.31	-5.32	-0.37
250	-5.62	-0.58	0.29	-5.28	-0.34
251	-5.65	-0.71	0.33	-5.31	-0.47
252	-5.64	-0.66	0.36	-5.3	-0.42
253	-5.8	-0.7	0.44	-5.46	-0.46
255	-5.69	-0.66	0.37	-5.35	-0.42
256	-5.88	-0.88	0.37	-5.54	-0.64
258	-5.44	-0.53	0.33	-5.1	-0.29
259	-5.53	-0.51	0.36	-5.19	-0.27
260	-5.44	-0.49	0.25	-5.1	-0.25
261	-5.52	-0.6	0.34	-5.18	-0.36
262	-5.51	-0.58	0.33	-5.17	-0.34
263	-5.64	-0.55	0.22	-5.3	-0.31
264	-5.57	-0.58	0.31	-5.23	-0.34
267	-5.61	-0.54	0.27	-5.27	-0.3
268	-5.45	-0.51	0.34	-5.11	-0.27
269	-5.6	-0.59	0.29	-5.26	-0.35
270	-5.56	-0.56	0.3	-5.22	-0.32
271	-5.55	-0.57	0.22	-5.21	-0.33
272	-5.6	-0.58	0.36	-5.26	-0.34
273	-5.63	-0.6	0.31	-5.29	-0.36
274	-6.1	-0.75	0.35	-5.76	-0.51
275	-5.95	-0.7	0.38	-5.61	-0.46
276	-5.87	-0.77	0.42	-5.53	-0.53
277	-5.75	-0.71	0.42	-5.41	-0.47

Field	$M_{V,\mathrm{lim}}$	α	σ	$M_{V,\mathrm{lim},0}$	α_0
278	-5.72	-0.6	0.31	-5.38	-0.36
280	-5.47	-0.52	0.3	-5.13	-0.28
281	-5.5	-0.5	0.24	-5.16	-0.26
282	-5.64	-0.6	0.35	-5.3	-0.36
283	-5.57	-0.57	0.35	-5.23	-0.33
284	-5.7	-0.53	0.26	-5.36	-0.29
286	-5.96	-0.63	0.33	-5.62	-0.39
287	-5.57	-0.58	0.29	-5.23	-0.34
288	-5.58	-0.5	0.31	-5.24	-0.26
289	-5.68	-0.56	0.31	-5.34	-0.32
290	-5.47	-0.51	0.33	-5.13	-0.27
291	-5.61	-0.53	0.25	-5.27	-0.29
292	-5.53	-0.53	0.26	-5.19	-0.29
293	-5.67	-0.62	0.37	-5.33	-0.38
294	-5.62	-0.51	0.28	-5.28	-0.27
295	-5.69	-0.53	0.28	-5.35	-0.29
296	-5.99	-0.59	0.38	-5.65	-0.35
297	-5.85	-0.66	0.36	-5.51	-0.42
298	-5.72	-0.67	0.34	-5.38	-0.43
299	-5.78	-0.77	0.37	-5.44	-0.53
300	-5.4	-0.51	0.33	-5.06	-0.27
301	-6.55	-0.61	0.3	-6.21	-0.37
302	-5.63	-0.47	0.27	-5.29	-0.23
303	-5.66	-0.55	0.23	-5.32	-0.31
304	-5.58	-0.53	0.32	-5.24	-0.29
305	-5.68	-0.48	0.25	-5.34	-0.24
306	-6.46	-0.67	0.28	-6.12	-0.43
307	-5.89	-0.59	0.33	-5.55	-0.35
308	-5.57	-0.52	0.41	-5.23	-0.28
309	-5.79	-0.53	0.29	-5.45	-0.29
310	-5.71	-0.51	0.3	-5.37	-0.27
311	-5.54	-0.52	0.21	-5.2	-0.28
312	-5.89	-0.55	0.24	-5.55	-0.31
313	-5.54	-0.52	0.33	-5.2	-0.28
314	-5.68	-0.59	0.32	-5.34	-0.35
315	-5.64	-0.56	0.28	-5.3	-0.32
316	-5.71	-0.57	0.21	-5.37	-0.33
317	-7.12	-0.62	0.2	-6.78	-0.38
318	-5.84	-0.66	0.32	-5.5	-0.42

Field	$M_{V,\mathrm{lim}}$	α	σ	$M_{V,\mathrm{lim},0}$	α_0
319	-5.84	-0.62	0.27	-5.5	-0.38
320	-5.71	-0.56	0.31	-5.37	-0.32
321	-5.66	-0.51	0.3	-5.32	-0.27
322	-6.29	-0.61	0.35	-5.95	-0.37
323	-5.74	-0.5	0.3	-5.4	-0.26
324	-5.56	-0.49	0.34	-5.22	-0.25
325	-5.69	-0.52	0.26	-5.35	-0.28
326	-5.73	-0.48	0.26	-5.39	-0.24
327	-5.78	-0.57	0.32	-5.44	-0.33
328	-5.82	-0.63	0.3	-5.48	-0.39
329	-5.65	-0.52	0.29	-5.31	-0.28
330	-5.62	-0.47	0.34	-5.28	-0.23
331	-5.46	-0.46	0.29	-5.12	-0.22
332	-5.55	-0.47	0.28	-5.21	-0.23
333	-5.65	-0.47	0.29	-5.31	-0.23
334	-5.61	-0.48	0.34	-5.27	-0.24
335	-5.74	-0.51	0.32	-5.4	-0.27
336	-5.57	-0.52	0.32	-5.23	-0.28
337	-5.59	-0.5	0.27	-5.25	-0.26
338	-5.76	-0.57	0.29	-5.42	-0.33
339	-5.78	-0.55	0.27	-5.44	-0.31
340	-5.8	-0.58	0.29	-5.46	-0.34
341	-5.68	-0.51	0.33	-5.34	-0.27
342	-5.57	-0.49	0.3	-5.23	-0.25
343	-5.81	-0.55	0.31	-5.47	-0.31
344	-5.78	-0.54	0.33	-5.44	-0.3
345	-5.66	-0.45	0.27	-5.32	-0.21
346	-5.68	-0.53	0.34	-5.34	-0.29
347	-5.76	-0.59	0.31	-5.42	-0.35
348	-5.67	-0.49	0.22	-5.33	-0.25
349	-5.87	-0.53	0.26	-5.53	-0.29
350	-5.64	-0.45	0.27	-5.3	-0.21
351	-5.56	-0.46	0.28	-5.22	-0.22
352	-5.84	-0.52	0.22	-5.5	-0.28
353	-5.7	-0.5	0.32	-5.36	-0.26
354	-5.94	-0.52	0.28	-5.6	-0.28
355	-5.79	-0.51	0.38	-5.45	-0.27
356	-5.61	-0.47	0.21	-5.27	-0.23
357	-5.8	-0.54	0.26	-5.46	-0.3

Field	$M_{V,\mathrm{lim}}$	α	σ	$M_{V,\mathrm{lim},0}$	α_0
358	-5.7	-0.53	0.31	-5.36	-0.29
359	-5.69	-0.49	0.34	-5.35	-0.25
360	-5.72	-0.49	0.31	-5.38	-0.25
361	-5.77	-0.53	0.29	-5.43	-0.29
362	-5.8	-0.51	0.34	-5.46	-0.27
363	-5.73	-0.44	0.23	-5.39	-0.2
364	-5.78	-0.52	0.26	-5.44	-0.28
365	-5.84	-0.56	0.32	-5.5	-0.32
366	-5.67	-0.45	0.31	-5.33	-0.21
367	-5.76	-0.45	0.28	-5.42	-0.21
368	-5.81	-0.46	0.23	-5.47	-0.22
369	-5.74	-0.46	0.3	-5.4	-0.22
370	-5.8	-0.45	0.24	-5.46	-0.21
371	-5.79	-0.48	0.28	-5.45	-0.24
372	-5.84	-0.46	0.26	-5.5	-0.22
373	-5.87	-0.51	0.24	-5.53	-0.27
374	-5.66	-0.48	0.26	-5.32	-0.24
375	-5.84	-0.51	0.3	-5.5	-0.27
376	-5.76	-0.47	0.23	-5.42	-0.23
377	-5.74	-0.46	0.28	-5.4	-0.22
378	-5.85	-0.46	0.25	-5.51	-0.22
379	-5.76	-0.49	0.29	-5.42	-0.25
380	-5.67	-0.46	0.31	-5.33	-0.22
381	-5.8	-0.48	0.28	-5.46	-0.24
382	-5.94	-0.5	0.36	-5.6	-0.26
383	-5.83	-0.49	0.25	-5.49	-0.25
384	-5.85	-0.46	0.3	-5.51	-0.22
385	-5.97	-0.49	0.25	-5.63	-0.25
386	-5.85	-0.48	0.28	-5.51	-0.24
387	-5.87	-0.47	0.28	-5.53	-0.23
388	-5.83	-0.49	0.32	-5.49	-0.25
389	-5.87	-0.47	0.27	-5.53	-0.23
390	-5.86	-0.45	0.27	-5.52	-0.21
391	-5.8	-0.47	0.33	-5.46	-0.23
392	-5.9	-0.49	0.28	-5.56	-0.25
393	-5.83	-0.48	0.22	-5.49	-0.24
394	-5.91	-0.48	0.27	-5.57	-0.24
395	-6.06	-0.48	0.36	-5.72	-0.24
396	-5.88	-0.48	0.32	-5.54	-0.24

Field	$M_{V,\mathrm{lim}}$	α	σ	$M_{V,\mathrm{lim},0}$	α_0
397	-5.86	-0.47	0.27	-5.52	-0.23
398	-6.15	-0.45	0.49	-5.81	-0.21
399	-5.86	-0.45	0.33	-5.52	-0.21
400	-5.99	-0.46	0.25	-5.65	-0.22
401	-5.85	-0.44	0.25	-5.51	-0.2
402	-6.11	-0.49	0.41	-5.77	-0.25
403	-5.82	-0.44	0.26	-5.48	-0.2
404	-6.11	-0.5	0.27	-5.77	-0.26
405	-6.01	-0.48	0.26	-5.67	-0.24
406	-5.93	-0.45	0.29	-5.59	-0.21

Appendix B Contraindre la cosmologie et la formation & l'évolution des galaxies grâce au système satellitaire de la Voie lactée

B.1 La recherche de galaxies naines de la Voie lactée

B.1.1 Premières découvertes

La première observation d'une galaxie naine remonte à l'observation des deux nuages de Magellan. Ces objets célestes ont été observés pour la première fois par le célèbre explorateur Amerigo Vespucci lors de ses voyages en 1503-1504. Toutefois, c'est l'expédition menée par Ferdinand Magellan en 1519 qui a attiré l'attention sur ces objets célestes. Les nuages de Magellan, nommés d'après Magellan lui-même, sont une paire de galaxies naines visibles depuis l'hémisphère sud et connues sous le nom de Grand nuage de Magellan et de Petit nuage de Magellan.

La découverte suivante d'une galaxie naine de la Voie lactée n'a eu lieu qu'en 1938, lorsque (Shapley, 1938a) a fait une observation révolutionnaire d'un "*grand amas riche avec des caractéristiques remarquables*" sur les plaques photographiques de l'observatoire de Boyden. Après l'identification de la galaxie naine du Sculptor, la découverte d'un second système dans la constellation de Fornax (Shapley, 1938b) a constitué une autre avancée majeure. Cette découverte a conduit l'auteur à suggérer la présence d'autres objets célestes similaires. Cette hypothèse a été confirmée une vingtaine d'années plus tard avec l'identification de Leo I, Leo II (Harrington & Wilson, 1950), Draco et Ursa Minor (Wilson, 1955) grâce à l'inspection visuelle des plaques photographiques du Palomar Sky Survey. Plus tard, Carina a été découverte grâce aux clichés du télescope britannique Schmidt (Cannon et al., 1977). La figure B.1 montre un exemple de plaque de Schmidt annotée centrée sur la galaxie naine Draco, soulignant la difficulté de détecter des objets peu lumineux et de creuser dans le bruit

avec des méthodes visuelles.

Alors que l'inspection visuelle des plaques photographiques existantes à la recherche de nouvelles découvertes semblait difficile, l'avènement des machines à mesurer a révolutionné le processus en permettant l'analyse au niveau du catalogue. Cette avancée sert de base aux techniques de recherche automatisées, comme le montre la découverte pionnière de Sextans (Irwin et al., 1990) dans les plaques photographiques Schmidt

Dernière découverte du vingtième siècle, la galaxie naine du Sagittaire est née de l'analyse de données spectroscopiques plutôt que photométriques. En effet, la détection de la galaxie naine du Sagittaire reposait sur la découverte d'un grand groupe étendu d'étoiles se déplaçant conjointement près du bulbe de la Voie Lactée ((Ibata et al., 1995)). De plus, des études ultérieures ont démontré que ce satellite subit une perturbation par effet de marée et qu'il est par conséquent intégré dans un courant (Ibata et al., 1997; Majewski et al., 2003). Cette détection est la première observation d'une fusion se produisant entre un satellite et son hôte, offrant une opportunité exceptionnelle d'étudier et d'analyser ces interactions. L'importance de cette découverte réside dans sa capacité à changer la perspective concernant l'état de notre propre galaxie, la Voie Lactée. Auparavant, la Voie lactée était considérée comme stable, statique et ayant déjà atteint sa forme finale. Or, le Sagittaire a démontré que notre galaxie est actuellement engagée dans une fusion, ce qui signifie qu'elle est toujours en train de changer.

B.1.2 Large photometric surveys

Au total, 11 satellites du MW ont été découverts au cours du vingtième siècle (Figure B.2) ; cependant, sur la base du modèle cosmologique privilégié, on s'attendait à ce qu'un nombre beaucoup plus important de sous-halo de matière noire existe au voisinage de la Voie Lactée (Klypin et al., 1999; Moore et al., 1999). Pour trouver les autres satellites potentiels, il était nécessaire de creuser plus profondément dans le bruit. Cela a été possible grâce à l'avènement de grands relevés photométriques homogènes. La mise en place des relevés CCD a grandement facilité l'étude des catalogues stellaires et renforcé l'utilisation des méthodes automatisées de détection des galaxies naines peu lumineuses. Ces techniques reposent sur l'identification de surdensités d'étoiles dans le diagramme couleur-magnitude (CMD) et/ou dans le ciel (Figure B.3). Les algorithmes automatisés sont décrits plus en détail dans le chapitre III.

Le premier de ces relevés a été le Sloan Digital Sky Survey (Abazajian et al., 2003). Sa première publication de données comprenait un catalogue photométrique complet avec cinq bandes (u, g, r, i, z), couvrant plus de 2099 deg^2 et atteignant une limite de complétude de 50% de $(u, g, r, i, z) = (22.5, 23.2, 22.6, 21.9, 20.8)$. Cette étude a conduit à une augmentation rapide et considérable du nombre de satellites de la Voie Lactée connus, puisque 16 nouveaux satellites ont été découverts en l'espace de ~ 7 ans (Figure B.2 ; Willman, 2005; Willman et al., 2005; Zucker et al., 2006; Belokurov et al., 2006, 2007; Irwin et al., 2007; Walsh

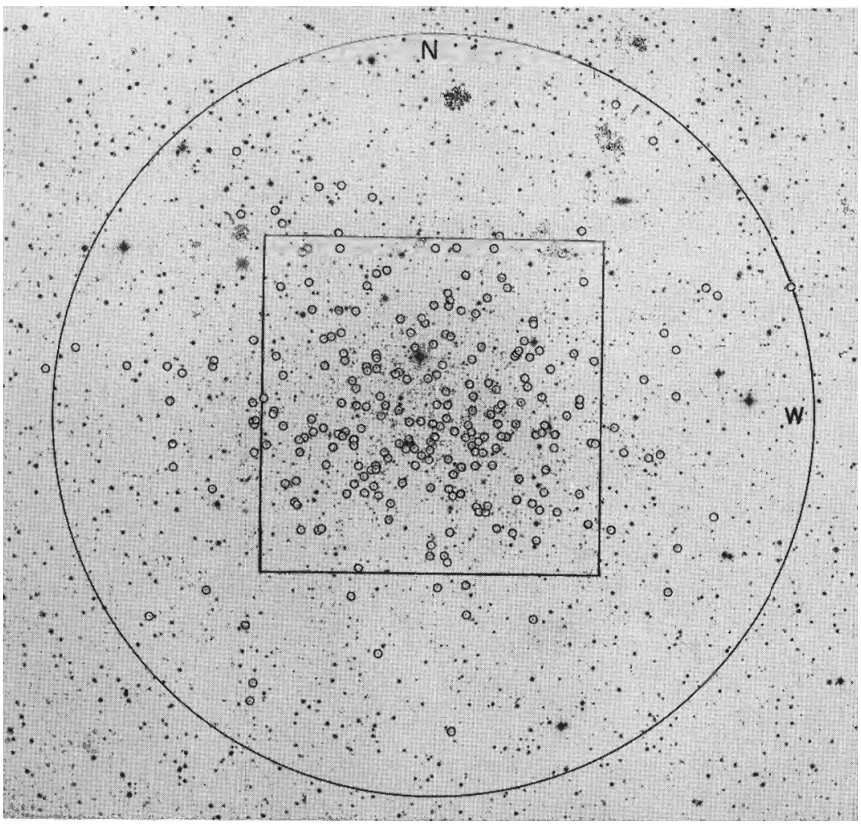

Figure B.1: Partie d'une plaque Schmidt de 48 pouces. L'anneau représente l'étendue de la galaxie naine Draco. Credit : Baade & Swope (1961).

et al., 2007; Grillmair, 2009; Belokurov et al., 2009, 2010). L'importance de ces nouvelles découvertes va au-delà de la simple expansion de la taille de l'échantillon de satellite ; elle introduit également une nouvelle gamme de magnitude, car presque toutes les galaxies naines nouvellement trouvées présentent $M_V > -8$ (Figure B.2) allant jusqu'à M_V=-1.5 (Segue 1 ; Belokurov et al., 2006).

La distinction entre galaxies naines et amas globulaires est devenue de plus en plus ambiguë avec l'avènement de l'étude SDSS, qui a permis la découverte d'objets moins lumineux. Auparavant, on pensait qu'à luminosité égale, les galaxies naines possédaient un rayon plus grand, ce qui créait un vide apparent servant de frontière entre les amas globulaires et les galaxies naines sur le graphe taille-luminosité (Figure B.4). Cependant, cette perspective a changé avec l'identification de satellites tels que William 1, Segue 1, Segue 2 et Bootes II, qui résident dans la région précédemment vide du graphe taille-luminosité, connue sous le nom de "vallée de l'ambiguïté" Gilmore et al. (2007).

En 2015, une augmentation notable du nombre de satellites de la Voie lactée s'est produite grâce au Dark Energy Survey (DES), qui a observé de manière extensive une zone

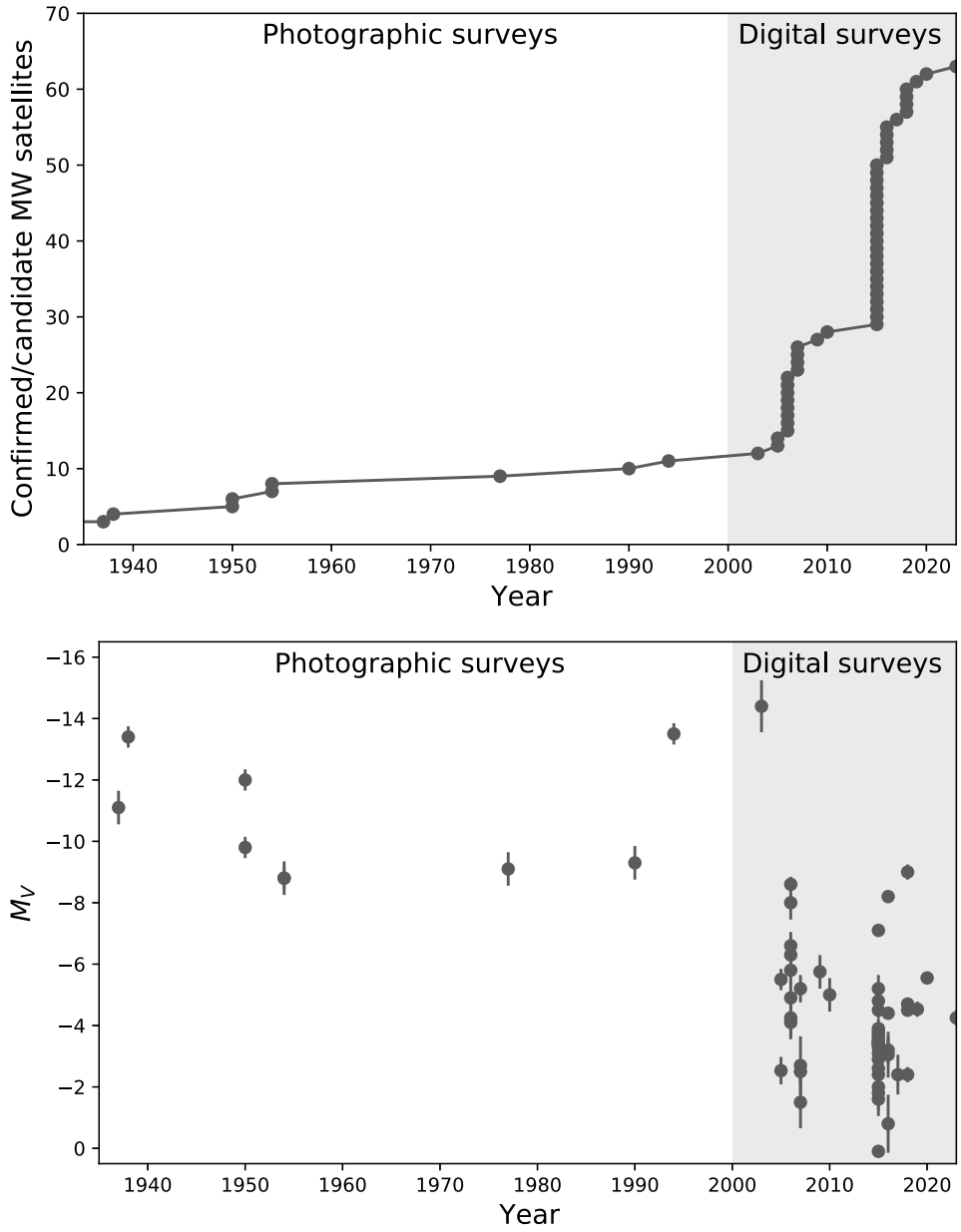

Figure B.2: *Panneau supérieur :* Nombre de galaxies naines de la Voie Lactée confirmées/candidates en fonction du temps. La taille de l'échantillon augmente considérablement avec l'avènement de grands relevés photométriques homogènes, passant de 11 à $\sim$ 60 en 2023. *Panneau du bas :* Magnitude des galaxies naines de la Voie Lactée confirmées/candidates en fonction du temps. L'introduction des relevés numériques au XXIe siècle a permis de détecter des objets moins lumineux en creusant plus profondément dans le bruit.

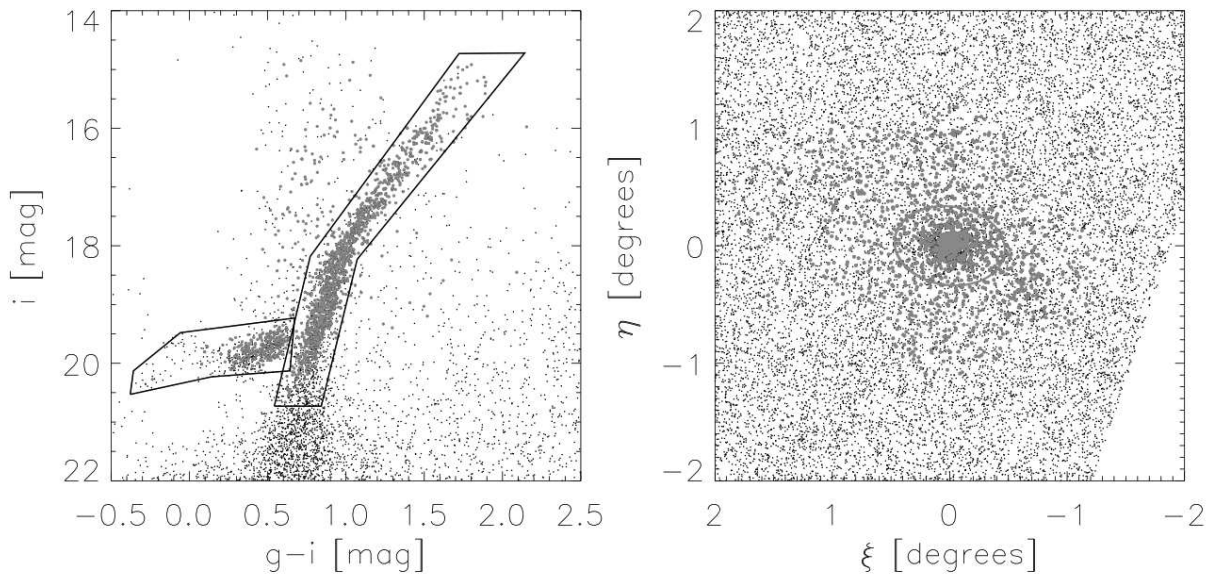

Figure B.3: *Panneau de gauche:* Diagramme couleur-magnitude des étoiles du catalogue photométrique du SDSS, à $\sim 10'$ du centre de Draco. *Panneau de droite:* Distribution spatiale des géantes rouges et des étoiles à branche horizontale du catalogue photométrique SDSS. Credit:Walker et al. (2015)

d'environ 5000 deg^2 dans le cap galactique sud en utilisant les bandes *grizY* et en atteignant une profondeur médiane de (g, r, i, z, Y)=(23,4,23,2,22,4,22,1,20,7). Ce relevé a conduit à la découverte de 17 pour les galaxies naines candidates (Drlica-Wagner et al., 2015; Koposov et al., 2015; Luque et al., 2016). Une fois de plus, un nombre important de ces candidates ont une nature ambiguë et pour certaines, la classification en tant que galaxies naines est encore débattue (Tucana V, Cetus II ; Conn et al., 2018a,b). Entre-temps, le Panoramic Survey Telescope And Rapid Response System (Pan-STARRS 1) a sondé les trois quarts du ciel avec des bandes *grizy* à une profondeur similaire à celle du SDSS et a conduit à la découverte de 3 nouveaux satellites (Laevens et al., 2015), tandis que l'étude VST ATLAS a observé 4500 deg^2 du ciel austral avec des bandes *ugrizy* à une profondeur similaire à celle du SDSS et a permis de découvrir 2 nouvelles galaxies naines (Torrealba et al., 2016a,b).

Comme on s'attend à ce que le Grand Nuage de Magellan possède ses propres galaxies naines, des efforts plus localisés ont été faits pour rechercher des objets de faible luminosité dans son voisinage (par exemple, SMASH, MagLites), ce qui a conduit à la découverte de 5 galaxies naines supplémentaires (Martin et al., 2015; Drlica-Wagner et al., 2016; Koposov et al., 2018). Il est important de noter que le véritable hôte de certains des satellites découverts dans le halo de la Voie lactée est débattu, étant donné que le Grand Nuage de Magellan possède son propre système de satellites (Battaglia et al., 2022).

Grâce au programme stratégique Subaru (SSP) de l'Hyper Suprime-Cam (HSC), trois

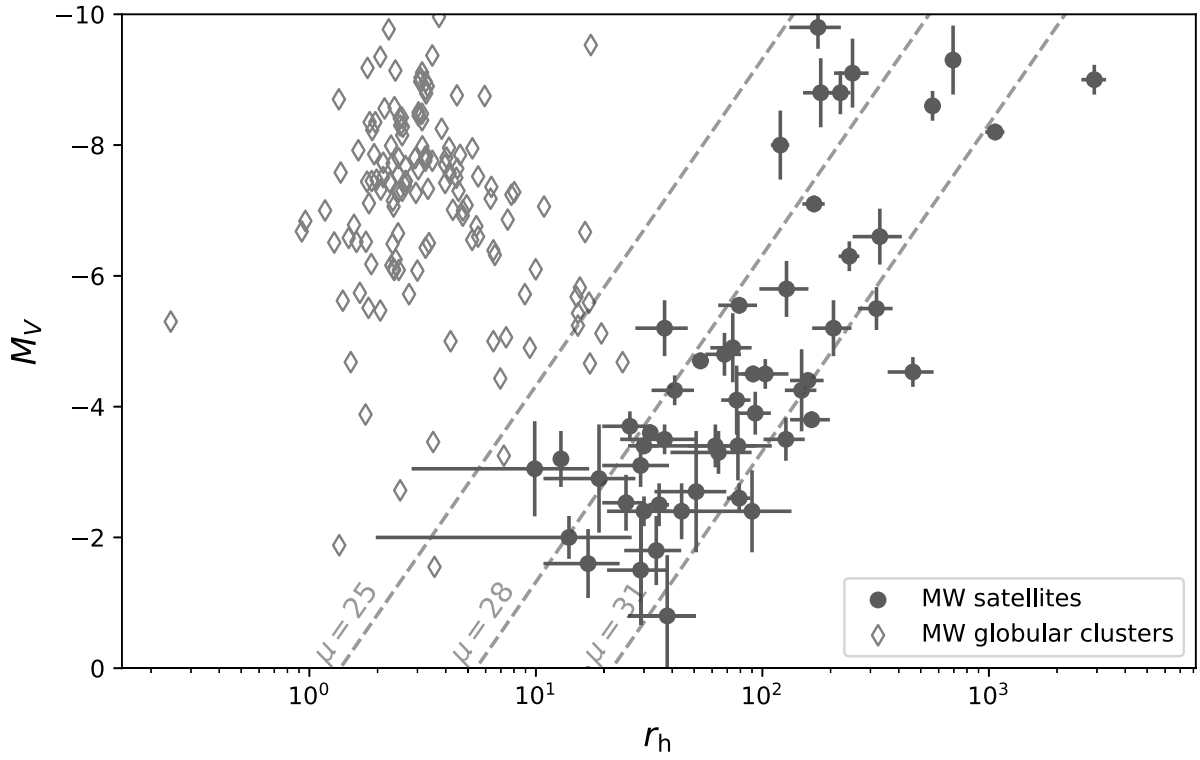

Figure B.4: Distribution des galaxies naines de la Voie lactée et de M31 dans l'espace taille-luminosité. A titre de comparaison, les amas globulaire (GC) de la Voie Lactée de Harris (1996) sont représentées par des losanges gris. Compte tenu de la gamme de magnitude des satellites de MW, la distinction entre GC et galaxie naine est ambiguë.

galaxies naines (Homma et al., 2018, 2019) ont été identifiées avec succès. Le HSC SSP est un relevé photométrique profond, atteignant des valeurs de profondeur de 5σ de (g, r, i, z, y)= (26,5, 26,1, 25,9, 25,1, 24,4) et conduisant à la découverte de Virgo I, la galaxie naine la moins lumineuse connue à ce jour, avec une magnitude de $M_V = -0,33^{+0,75}_{-0,87}$. Récemment, le DECam Local Volume Exploration Survey (DELVE) a permis de découvrir deux galaxies naines (Mau et al., 2020). DELVE utilise une approche globale en combinant les données d'archives du DECam (par exemple DES, DECals, DeROSITAS) avec de nouvelles observations utilisant le même instrument et englobant la Voie Lactée, les analogues des Nuages de Magellan, et le Volume Local.

B.1.3 Limites de détection et propriétés globales

L'avènement de grands relevés photométriques homogènes a considérablement élargi nos connaissances sur les galaxies naines de la Voie Lactée. La taille de l'échantillon de galaxies naines connues permet une analyse statistique complète du système de satellites,

ce qui permet de dériver des propriétés globales pour les comparer avec des simulations cosmologiques et des simulations de formation et d'évolution de galaxies. Cependant, étant donné que toutes les galaxies naines ne sont pas détectées, il est nécessaire de déterminer l'exhaustivité de l'échantillon afin de comparer de manière robuste les observations avec les prédictions des modèles de formation et d'évolution des galaxies. Cette étape fastidieuse est grandement facilitée par l'utilisation d'outils de détection automatique. Ces outils offrent des limites de détection quantifiables et définies de manière cohérente, dépassant la nature subjective des inspections visuelles. Néanmoins, l'implémentation de ces outils nécessite des ressources informatiques importantes.

La première analyse de ce type s'est concentrée sur la caractérisation des limites de détection de l'étude SDSS (Koposov et al., 2008). Pour ce faire, des galaxies naines simulées ont été injectées dans le catalogue du SDSS et leur détection a ensuite été identifiée à l'aide d'un algorithme de filtre de correspondance. L'exhaustivité de l'échantillon a ensuite été quantifiée en fonction de la luminosité et de la taille des galaxies naines sur différents intervalles de distance, allant d'une distance héliocentrique de 8 à 1024 kpc.

Depuis, des efforts ont été faits pour caractériser et publier les limites de détection des relevés conduisant à la découverte de nouveaux satellites (DES : Drlica-Wagner et al. 2020 ; Pan-STARRS : Laevens 2015), réduisant l'écart entre les observations et les modèles et permettant ainsi l'utilisation des systèmes satellitaires comme sondes cosmologiques et de formation et d'évolution des galaxies.

Nous disposons désormais d'un système de satellites bien peuplé et bien compris, ainsi que des limites de détection associées. Que pouvons-nous en apprendre ?

B.2 Les systèmes satellitaires comme sondes cosmologiques et d'évolution des galaxies

B.2.1 Formation des galaxies dans un contexte ΛCDM

La première indication de l'existence de "matière manquante" a été rapportée par Zwicky en 1933 (Zwicky, 1933). Cette découverte est née de l'observation que la dispersion des vitesses de l'amas de Coma dépassait le seuil à partir duquel il pouvait être lié gravitationnellement en tenant compte uniquement de la matière baryonique. Cependant, ce n'est que dans les années 1970 que le concept de matière noire a commencé à gagner du terrain, après la découverte de la masse manquante nécessaire pour expliquer les courbes de rotation des galaxies (Rubin et al., 1978). Entre-temps, la découverte du fond diffus cosmologique (CMB) (Penzias & Wilson, 1965) a renforcé l'idée d'un univers autrefois chaud et dense, qui s'est ensuite étendu au fil du temps. Par conséquent, en 1984, la théorie ΛCDM a émergé (Peebles, 1984; Turner et al., 1984), qui a été réaffirmée plus tard par la mesure des anisotropies dans le fond diffus cosmologique (CMB) (Smoot et al., 1991).

Actuellement, le modèle ΛCDM est le cadre cosmologique le plus largement accepté,

composé principalement de deux éléments clés. Premièrement, la constante cosmologique de la relativité générale (Λ) représente la présence de l'énergie noire (Peebles, 1984; Turner et al., 1984), qui est nécessaire pour rendre compte de l'expansion accélérée de l'univers établie par Riess et al. (1998) et Schmidt et al. (1998). Deuxièmement, la matière noire froide (CDM) joue un rôle essentiel dans la formation des galaxies, car on pense que les galaxies se forment dans des halos composés de matière noire (White & Rees, 1978). Une conséquence de la nature froide/massive des particules de matière noire est la formation potentielle de halos de matière noire de masse extrêmement faible (Bullock & Boylan-Kolchin, 2017). Ces halos ne peuvent pas être formés si les particules de matière noire étaient plus chaudes/légères. Cela souligne l'importance de l'hypothèse de la matière noire froide pour expliquer les structures et le comportement observés de l'univers à différentes échelles.

Dans le modèle ΛCDM, les structures de l'Univers sont la conséquence des fluctuations adiabatiques primordiales qui se produisent avant la recombinaison de l'hydrogène, lorsque les baryons et les photons sont dans un état de quasi-équilibre et sont distribués presque uniformément. Après la recombinaison ($\sim$ 380 000 ans après le Big Bang), les atomes d'hydrogène ne subissent plus de pression de radiation, ils se condensent gravitationnellement dans les puits de potentiel créés par les halos de matière noire (White & Rees, 1978) conduisant à la formation de nuages moléculaires. Ces processus conduisent à leur tour à l'apparition de la première génération d'étoiles et au début de l'ère de réionisation, qui s'est produite environ 100 millions d'années après le Big Bang. Les premières étoiles se caractérisent par leur masse élevée, leur faible métallicité et leur courte durée de vie. Par l'explosion de supernovae, elles initient l'enrichissement chimique de leur environnement immédiat. La réionisation est une étape cruciale dans la formation des galaxies ; à la fin de cette ère, les galaxies existantes continuent d'évoluer par la formation d'étoiles dans des halos de matière noire et par des fusions, ce qui correspond au concept de l'évolution hiérarchique des galaxies.

Le modèle ΛCDM a réussi à décrire la structure à grande échelle de notre Univers (Eisenstein et al., 2005), le CMB (Planck Collaboration et al., 2016), et la nucléosynthèse du Big Bang (Planck Collaboration et al., 2016). Cependant, des tensions apparentes apparaissent lorsque l'on compare les attentes du modèle cosmologique ΛCDM privilégié et les observations des propriétés des galaxies naines telles que leur nombre, leur distribution spatiale autour de leur hôte, leur taille, leurs courbes de rotation et l'extinction de leur formation stellaire (Bullock & Boylan-Kolchin, 2017; Sales et al., 2022). Alors que les prédictions cosmologiques reposent principalement sur des simulations de matière noire, les comparaisons avec les observations nécessitent l'incorporation de simulations de formation de galaxies. Par conséquent, ces comparaisons sont difficiles en raison de notre compréhension limitée de la physique baryonique qui régit la formation et l'évolution des galaxies. Le processus de formation des étoiles, par exemple, qui a un impact direct sur les propriétés des systèmes satellites, est influencé par divers phénomènes physiques, notamment la réionisation et le feedback stellaire (Bullock et al., 2000; Somerville, 2002; Mashchenko et al., 2008; Wheeler et al., 2015). Bien que la comparaison des données d'observation et de simulation pour les systèmes satel-

lites soit une entreprise complexe, elle constitue un test parfait pour contraindre et améliorer notre compréhension de la cosmologie et de la physique de l'évolution de la formation des galaxies.

B.2.2 Comparaison du système de satellites de la Voie Lactée avec les simulations

II.2.2.a Nombre de satellites

En 1999, les premières comparaisons entre le nombre observé de satellites et le nombre de sous-halo de matière noire ont été effectuées par Klypin et al. (1999) et Moore et al. (1999). Ces deux études ont mis en évidence une disparité significative entre les centaines de sous-halo trouvés dans les simulations de matière noire autour d'hôtes similaires à la Voie Lactée et les seulement ~ 10 satellites MW connus à l'époque (Figure B.5). Trois types de solutions ont été proposés :

- La première approche est de nature observationnelle, car il est essentiel de reconnaître les difficultés liées à la détection des galaxies naines. En effet, il convient de noter qu'une partie des galaxies satellites manquantes n'a probablement pas été détectée. Depuis 1999, environ 40 nouvelles galaxies naines de la Voie lactée ont été découvertes et d'autres devraient encore l'être (Koposov et al., 2008; Tollerud et al., 2008; Drlica-Wagner et al., 2020). Bien que cela ne comble pas le fossé entre le nombre de galaxies naines MW observées et le nombre simulé de sous-halo de matière noire, cela souligne la nécessité de prendre en compte les limites de détection lors de la comparaison.

- La seconde approche s'appuie sur la physique baryonique pour expliquer pourquoi une partie des sous-halo ne s'allume pas. La suppression de la formation d'étoiles est influencée par divers phénomènes, notamment la réionisation et la rétroaction stellaire (Bullock et al., 2000; Somerville, 2002; Mashchenko et al., 2008; Wheeler et al., 2015). Comme l'ampleur de ces processus reste incertaine, il est possible d'affiner l'impact de ces processus pour renforcer la suppression de la formation d'étoiles et, à son tour, augmenter le nombre de sous-halo de matière noire qui manquent à une galaxie naine.

- La dernière approche s'inscrit dans une perspective cosmologique, car elle implique une modification de la masse des particules de matière noire, influençant ainsi le nombre prévu de sous-halo de matière noire et, par conséquent, de galaxies naines, comme illustré dans la Figure B.6.

En combinant ces approches, des études ont démontré que le nombre observé de galaxies naines peut être compatible avec le nombre de sous-halo de matière noire identifiés dans les simulations(Koposov et al., 2009; Kim et al., 2018). Même en l'absence de contraintes sur les phénomènes physiques, le comptage des satellites reste un outil puissant pour étudier la masse des particules de matière noire. Pour ce faire, on considère diverses fonctions de masse

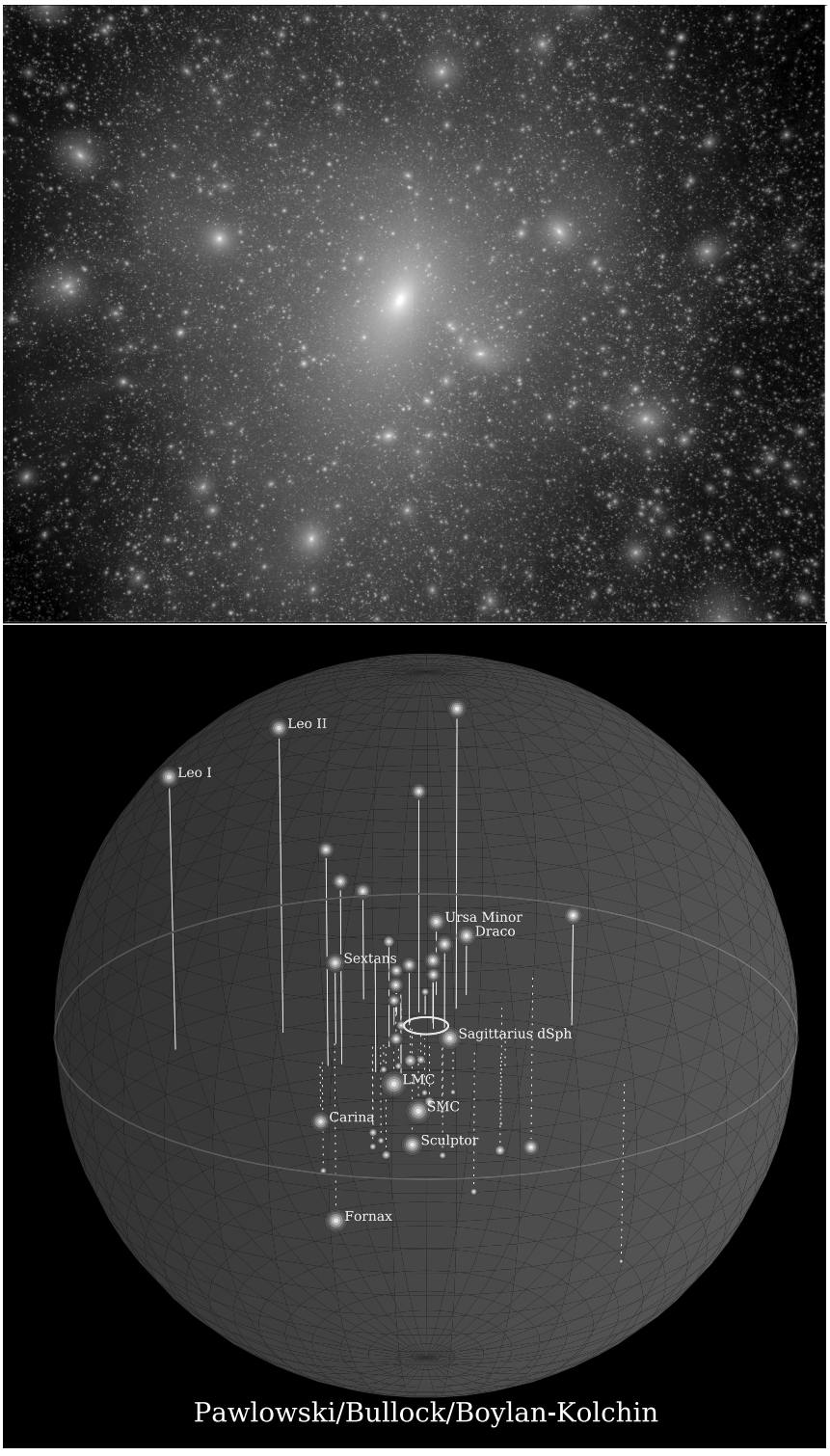

Figure B.5: *Panneau supérieur:* Distribution de la matière noire dans un halo de similaire à celui de la Voie Lactée issu de la simulation Aquarius à l'époque actuelle (z=0). Chaque point lumineux représente un sous-halo de matière noire. Crédit : Springel et al. (2008). *Panneau du bas:* Distribution des $\sim$ 60 satellites connus autour de la Voie Lactée. Credit: Bullock & Boylan-Kolchin (2017).

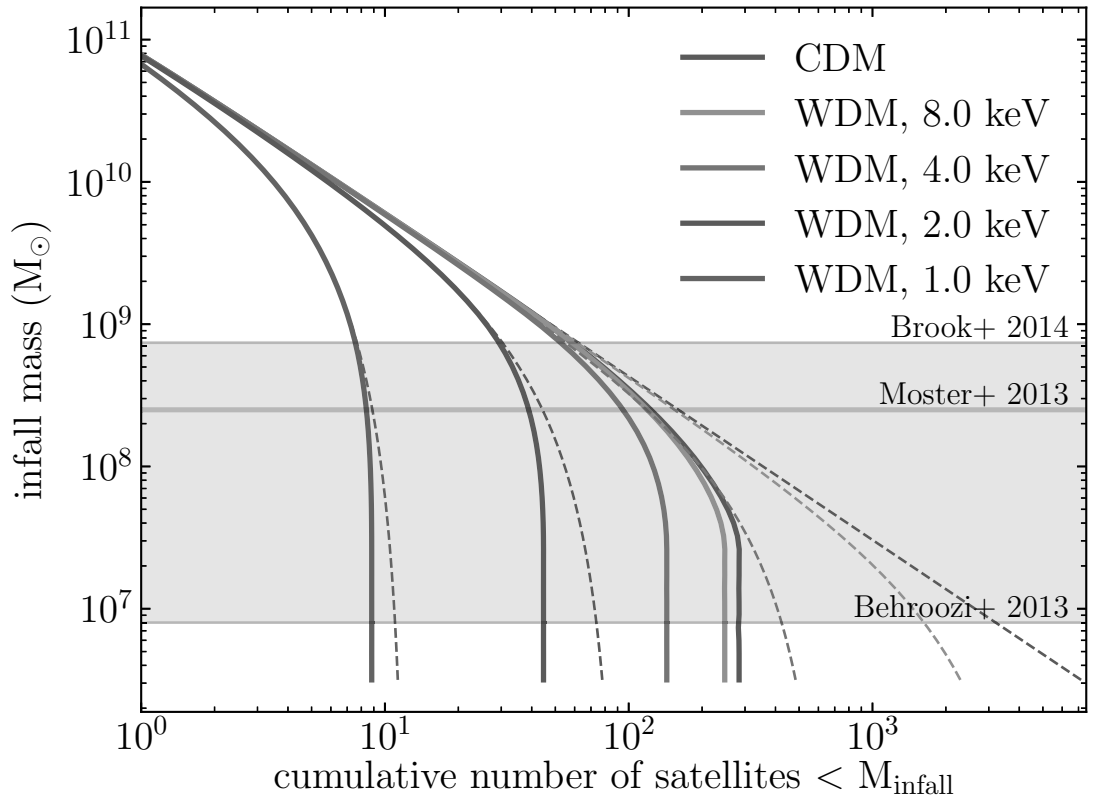

Figure B.6: La masse des sous-halo lumineux (lignes pleines) et de la totalité sous-halo (lignes pointillées) est présentée en fonction de leur nombre cumulé. Les différents types de matière noire sont distingués par un code couleur, montrant l'impact de la cosmologie sur le nombre attendu de satellites. Les lignes grises correspondent aux différentes masses prédites pour Segue I, soulignant l'importance de la physique baryonique sur les propriétés des satellites. Credit: Kim et al. (2018).

stellaire à masse du halo qui intègrent divers degrés de processus de feedback stellaire et de réionisation. Grâce à ces approches, des contraintes sur la masse de la particule de matière noire chaude (WDM) ont été obtenues ($m_{WDM} > 4$ keV : Kim et al. 2018 ; $m_{WDM} > 6,5$ keV : Nadler et al. 2021).Ceci est particulièrement prometteur avec l'avènement de grands relevés à venir tels que LSST et Euclid. Ces relevés offrent un grand potentiel pour la découverte d'une multitude de galaxies naines de la Voie Lactée, renforçant ainsi les contraintes sur les modèles cosmologiques.

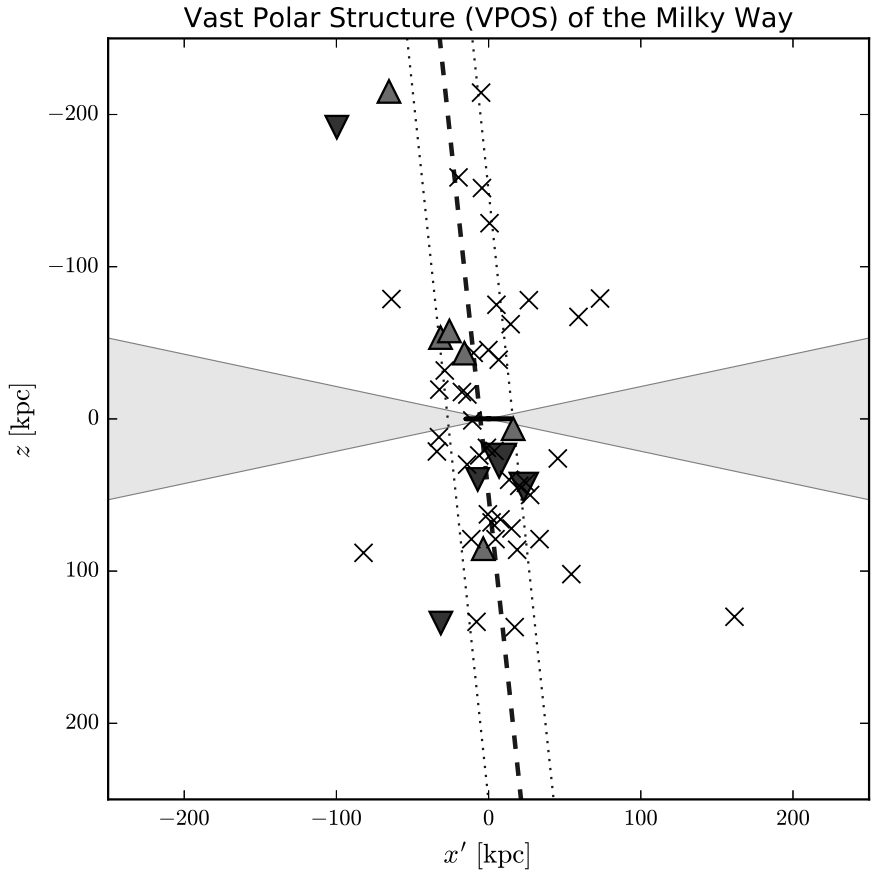

Figure B.7: Le plan des satellites dans la Voie lactée (observé sur le bord). Le plan privilégié est représenté par une ligne en pointillé indiquant son orientation, tandis que la ligne en pointillé indique sa largeur. Les satellites connus sont marqués par des triangles rouges s'ils s'approchent, des triangles bleus s'ils s'éloignent, et des croix si leur mouvement propre est inconnu. La région grise met en évidence une zone où la détection des galaxies naines est affectée par l'avant-plan galactique. Credit: Pawlowski (2018)

II.2.2.b Distribution spatiale

Les galaxies naines, nées dans les sous-halo de matière noire, offrent des informations précieuses sur la distribution spatiale de la matière noire. En conséquence, elles servent de référence importante pour les simulations cosmologiques et les simulations d'évolution de la formation des galaxies. Les comparaisons entre la distribution radiale des satellites classiques de la Voie Lactée ($M_V \lesssim -8$) et les simulations de matière noire seule ont révélé une divergence : les satellites les plus lumineux présentent une plus grande concentration

radiale par rapport aux sous-halo les plus grands (Kravtsov et al., 2004; Lux et al., 2010; Yniguez et al., 2014; Carlsten et al., 2020). Cette observation est encore renforcée par la concentration radiale globale de l'ensemble de la population de satellites de la Voie lactée, qui dépasse les prévisions des simulations en supposant une fonction de masse stellaire-halo raisonnable (Kim et al., 2018). Cette divergence peut avoir les causes suivantes :

- L'incomplétude du relevé affecte sans aucun doute la distribution radiale observée des satellites, cependant, il a été montré que les limites de détection ne peuvent pas expliquer à elles seules les disparités entre les observations et les simulations (Kim et al., 2018; Carlsten et al., 2020).
- La réionisation présente une autre solution potentielle, car elle arrête effectivement la formation d'étoiles et, par conséquent, conduit à ce que les halos les plus brillants soient formés plus tôt et situés plus près de l'hôte (Font et al., 2011; Starkenburg et al., 2013). Cependant, les simulations hydrodynamiques suggèrent que l'influence de la réionisation sur la formation d'étoiles ne devrait pas être significative dans la gamme de masse considérée pour les galaxies naines classiques (Ocvirk et al., 2016; Wheeler et al., 2019).
- Le mécanisme de perturbation par les marées des sous-halo par l'hôte n'est pas encore entièrement compris (Carlsten et al., 2020).

Il est important de reconnaître que ces comparaisons peuvent être influencées par une distribution spatiale déjà particulière des satellites. En fait, il est maintenant largement reconnu qu'une partie substantielle des galaxies naines MW présente une distribution planaire mince en co-rotation (Figure B.7 Lynden-Bell, 1976; Kroupa et al., 2005; Metz et al., 2008; Pawlowski et al., 2012) même si la nature préjudiciable de cette caractéristique pour le cadre ΛCDM est encore débattue (Pawlowski, 2021; Sales & Navarro, 2023; Sawala et al., 2023; Xu et al., 2023).

II.2.2.c Impact sur l'environnement

La plupart des contraintes sur la cosmologie et la physique de la formation et de l'évolution des galaxies ont été obtenues grâce à l'étude des galaxies naines de la Voie lactée, en raison de leur accessibilité. Mais ce système de satellites n'est peut-être pas typique.

La Voie Lactée est actuellement en train de fusionner avec le LMC (Battaglia et al., 2022), un processus qui a une influence notable sur les propriétés de son système de satellites. La présence de galaxies satellites apportées par la galaxie en fusion conduit en effet à une augmentation du nombre de satellites pour la galaxie hôte (Nadler et al., 2020; Joshi et al., 2023). Cet effet peut expliquer la bosse observée à l'extrémité faible ($M_V > -5$) de la fonction de luminosité de la Voie Lactée, telle que présentée par l'équipe DES (voir Figure B.8 Drlica-Wagner et al., 2020). En outre, cette augmentation des satellites a également un impact sur

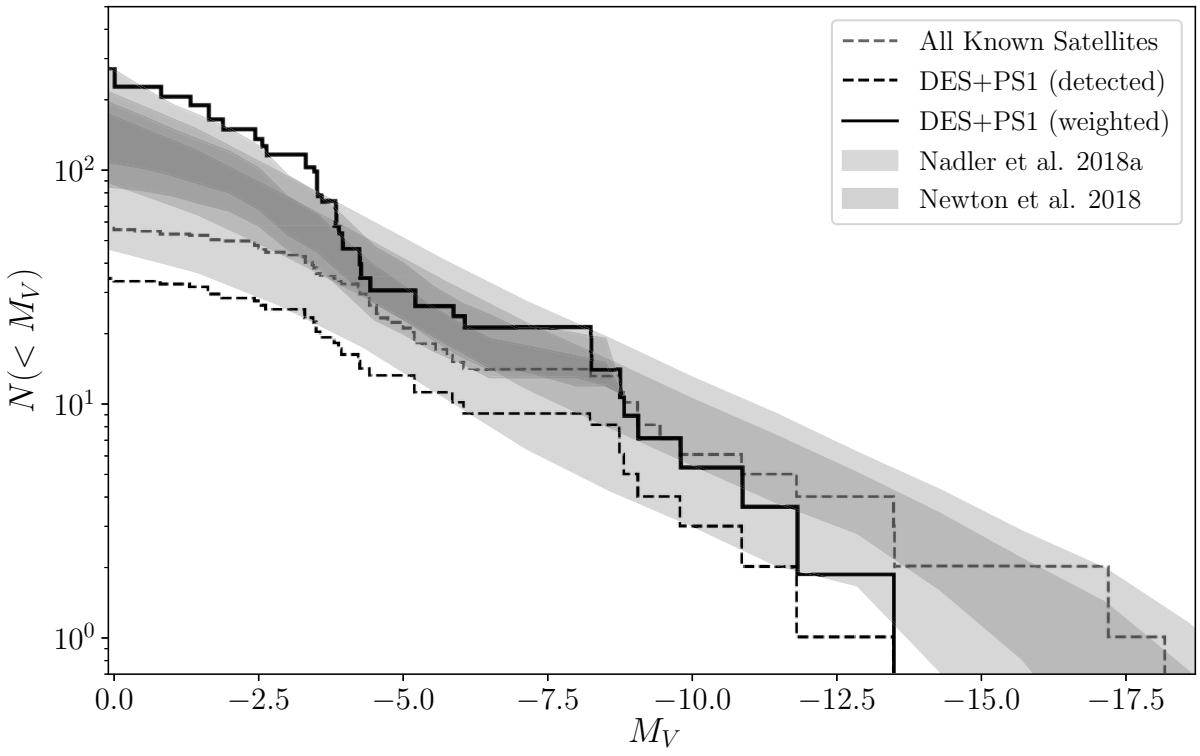

Figure B.8: Fonction de luminosité cumulée des satellites de la Voie Lactée. Les satellites connus sont représentés par la ligne grise en pointillés. Les satellites détectés dans le cadre de l'étude DES sont représentés par la ligne noire en pointillés. La fonction de luminosité corrigée pour le volume observable est représentée par la ligne noire pleine. Credit: Drlica-Wagner et al. (2020)

la distribution radiale observée des satellites, comme l'a démontré Carlsten et al. (2020), qui a montré que les systèmes avec une galaxie naine de type LMC présentent une concentration radiale légèrement plus prononcée.

Tout au long de cette section, nous avons exploré l'impact significatif de la suppression de la formation d'étoiles sur les propriétés d'une population de satellites. En examinant les temps d'extinction des galaxies naines de la Voie Lactée, Weisz et al. (2019) a montré que tous les satellites peu lumineux ont été éteints il y a 12 Gyr, tandis que les plus lumineux ont connu des événements d'extinction récents. En revanche, l'histoire de l'extinction des galaxies naines de M31 montre une histoire de formation d'étoiles plus longue Savino et al. (2023). Cette différence dans les schémas d'extinction conduit Weisz et al. (2019) à proposer que l'histoire de l'accrétion de la galaxie hôte joue un rôle central dans la détermination des propriétés de ses galaxies naines.

Par conséquent, les propriétés d'un système satellite sont fortement influencées par

l'environnement et l'histoire de la fusion de sa galaxie hôte. Si l'on considère que la Voie lactée n'est peut-être pas représentative d'un système typique, il est crucial d'explorer divers systèmes satellites. L'un des systèmes les plus accessibles pour une étude détaillée est notre voisin cosmique, M31, qui se trouve à une distance de moins de 800 kpc de la Voie Lactée. Cette proximité nous permet de résoudre les galaxies naines de M31 en étoiles individuelles, ce qui constitue un excellent second laboratoire pour tester la cosmologie et la physique de la formation et de l'évolution des galaxies.

Appendix C Le système satellitaire de M31: un second test pour la cosmologie et la formation et l'évolution des galaxies

C.1 La recherche des satellites de M31 : de l'inspection visuelle à SDSS

La première observation d'une galaxie naine en dehors de la Voie Lactée a été faite en 1654 par Hodierna. (Hodierna, 1654) rapporte un objet ressemblant à un nuage près de la constellation du Triangle, qui fut plus tard redécouvert par Messier en 1764 (Messier, 1781). Cet objet est aujourd'hui connu sous le nom de M33 et est considéré comme le satellite le plus brillant de M31. Au 18e siècle, trois autres satellites de M31 ont également été détectés. NGC 221, initialement découverte par Guillaume Le Gentil en 1749, a été classée comme M32 dans le catalogue de Messier en 1781. Un autre satellite, NGC 205, a été découvert par Caroline Herschel et rapporté par William Herschel en 1785 Herschel (1785). Bien que Messier n'ait pas classé cette galaxie naine au départ, car elle était présente dans son dessin de la nébuleuse d'Andromède, elle a été ajoutée plus tard à la liste sous le nom de M101. Enfin, NGC 185 a été découverte par Herschel en 1787, suivie au 19e siècle par la découverte de NGC 147 par John Herschel et la découverte de IC10 par Lewis Swift.

Les découvertes suivantes de galaxies naines M31 n'ont eu lieu qu'à la fin du 20e siècle, grâce à l'introduction des plaques photographiques. Bien que la recherche de galaxies naines de M31 dans le Palomar Sky Survey se soit avérée infructueuse en raison de la distance et de la faible luminosité de ces objets, suite aux découvertes autour de la Voie Lactée, on s'attendait à ce que de nouvelles galaxies naines soient présentes autour de M31. De nouvelles observations ont donc été effectuées à l'aide d'un ensemble de neuf plaques très sensibles, ce qui a permis de détecter trois nouveaux satellites : And I, And II et And III (van den Bergh,

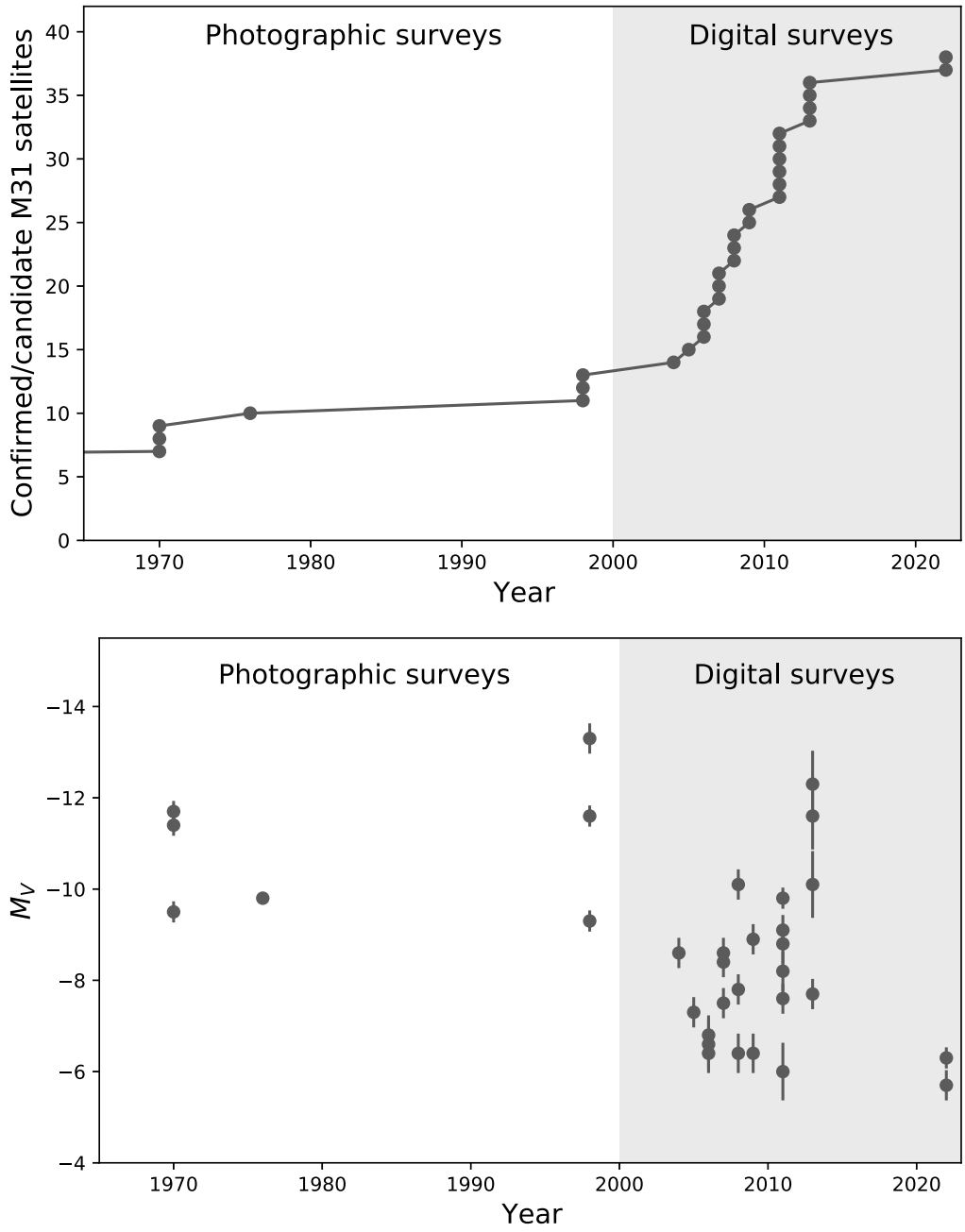

Figure C.1: *Panneau supérieur:* Nombre de galaxies naines de M31 confirmées/candidates en fonction du temps. La taille de l'échantillon augmente considérablement avec l'avènement des relevés numériques, passant de 11 à $\sim$ 40 en 2023. *Panneau du bas:* Magnitude des galaxies naines de M31 confirmées/candidates en fonction du temps.

1972). Une autre découverte importante a été l'identification de LGS 3, qui a été reconnue plus tard comme la galaxie naine Pisces par (Karachentseva, 1976).

Après ces découvertes, il s'est écoulé 20 ans avant que de nouvelles galaxies naines ne soient découvertes grâce à la deuxième version du relevé du ciel de l'observatoire de Palomar (POSS II). En utilisant la version numérisée de l'étude et en employant une technique de filtre de correspondance, (Armandroff et al., 1999) a réussi à identifier deux galaxies naines inconnues jusqu'alors, à savoir And V et And VI. Pendant ce temps, Karachentsev & Karachentseva (1999) a utilisé un critère morphologique sur le POSS II, ce qui a conduit à la découverte de And VI et And VII. Ces découvertes significatives ont porté le nombre total de galaxies naines de M31 à 11, ce qui est comparable au nombre de galaxies naines observées dans la Voie Lactée à cette époque. La première analyse comparative des systèmes satellites de la Voie Lactée et de M31, réalisée en 1994, a révélé des similitudes dans les propriétés de leurs galaxies naines. Notamment, ces galaxies suivent les mêmes relations taille-luminosité et luminosité-métallicité. Par conséquent, l'auteur a suggéré que malgré les masses différentes des deux hôtes, elles offraient toutes deux un environnement assez similaire pour la formation et l'évolution des satellites.

De même que pour la recherche de galaxies naines autour de la Voie Lactée, l'avènement de grand relevés photométriques homogènes a conduit à une augmentation significative du nombre de satellites connus de M31 (Figure C.1). En l'espace de ~ 10 ans, le relevé SDSS a conduit à la découverte de 4 nouvelles galaxies naines aussi faibles en luminosité que $M_V = -8.1 \pm 0.5$ (Et IX, Et X, Et XXVIII, Et XXIX ; Zucker et al., 2004a, 2007; Bell et al., 2011; Slater et al., 2011). Entre-temps, deux autres découvertes fortuites ont été faites par Irwin et al. (2008) et Majewski et al. (2007). Néanmoins, l'avancée la plus substantielle dans notre compréhension du système de satellites de M31, et plus généralement du halo de M31, est apparue grâce au Pan-Andromeda Archaeological Survey (PAndAS).

C.2 Explorer le halo de M31 grâce à PAndAS

C.2.1 Un bref aperçu technique

En 2001, Ibata et al. (2001) a mené une étude à l'aide du télescope Isaac Newton (INT) de 2,5 m dans le but d'étudier une région située jusqu'à environ 55 kpc de M31. Cette étude a abouti à la découverte du Giant Stellar Stream (Ibata et al., 2001; Ferguson et al., 2002). À peu près à la même époque, l'étude des courants de gaz et d'étoiles dans la Voie lactée a progressé de manière significative (Ibata et al., 1997), révélant une évolution active par le biais de fusions avec des galaxies satellites. La découverte du Giant Stream dans M31 a confirmé cette perspective sur l'évolution des galaxies et a suscité un suivi minutieux en utilisant le télescope Canada-France-Hawaii (CFHT) de 3,6 m avec MegaCam pour cartographier l'ensemble du courant Ibata et al. (2007). En raison de l'abondance des sous-structures révélées au cours de cette étude, celle-ci a finalement été transformée officiellement en relevé

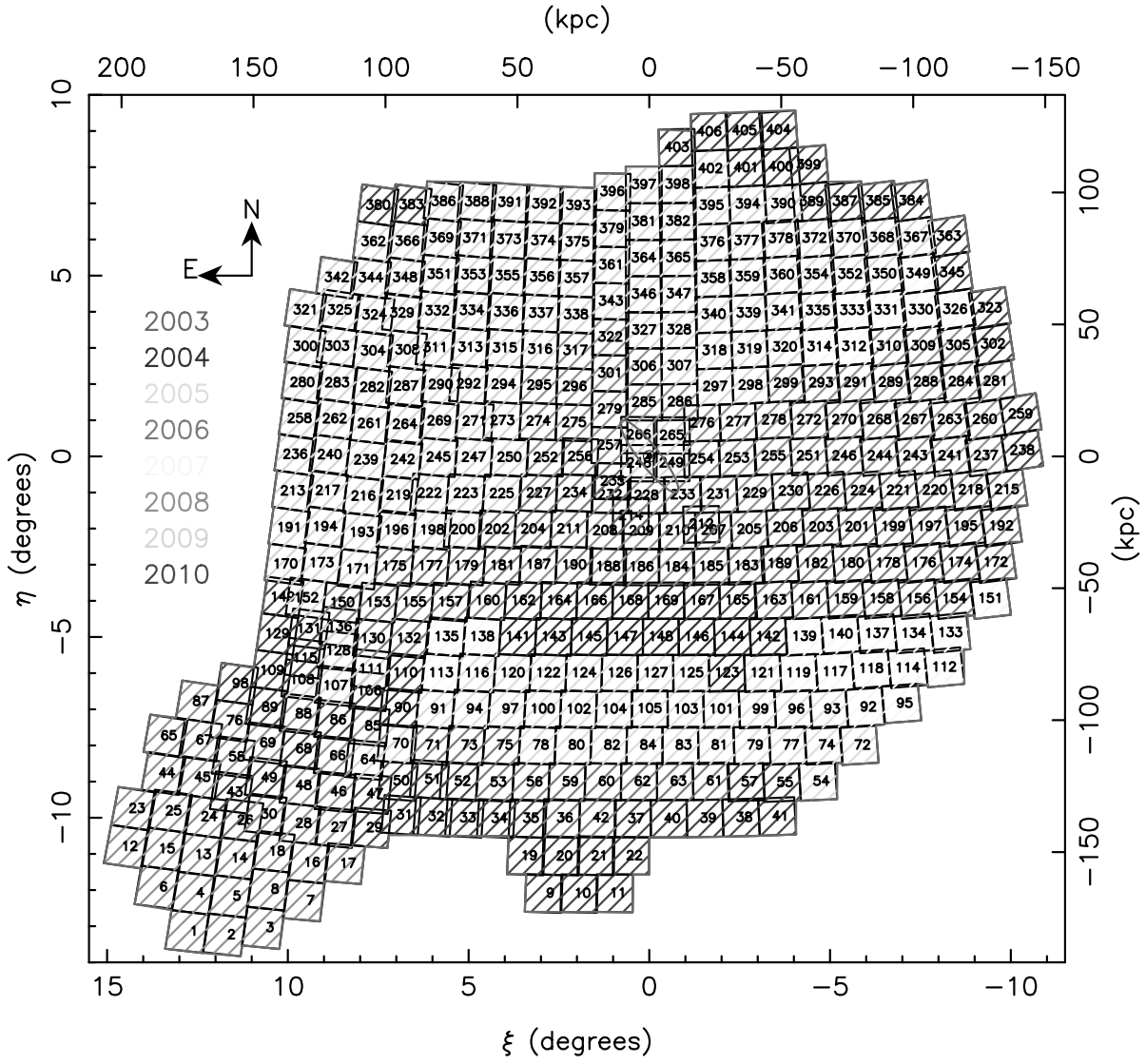

Figure C.2: Empreinte de PAndAS en fonction du temps pour l'imagerie en bande i. Chaque carré correspond à un champ du relevé. L'empreinte et l'agenda d'observation pour la bande g sont presque identiques. L'ellipse rouge représente le disque de M31. Le relevé couvre plus de 400 deg^2, stratégiquement centrés sur M31 et son compagnon M33, ce qui permet une exploration complète de leur environnement. Credit: Ibata et al. (2014).

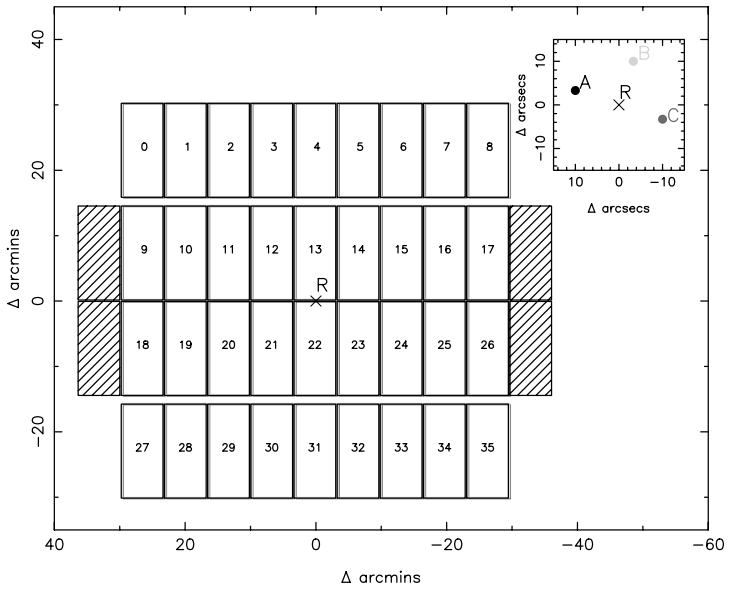

Figure C.3: Disposition des 36 CCDs de l'instrument CFHT/MegaCam. Chaque champ de l'étude a fait l'objet de trois expositions, et les empreintes résultantes sont représentées par les couleurs associées à leurs centres (A, B, C) qui sont représentés dans le panneau supérieur droit. Alors que les petits écarts à l'intérieur d'un rang de CCDs sont comblés par les différentes expositions, l'écart entre deux rangs de CCDs est toujours présent. Credit: McConnachie et al. (2018).

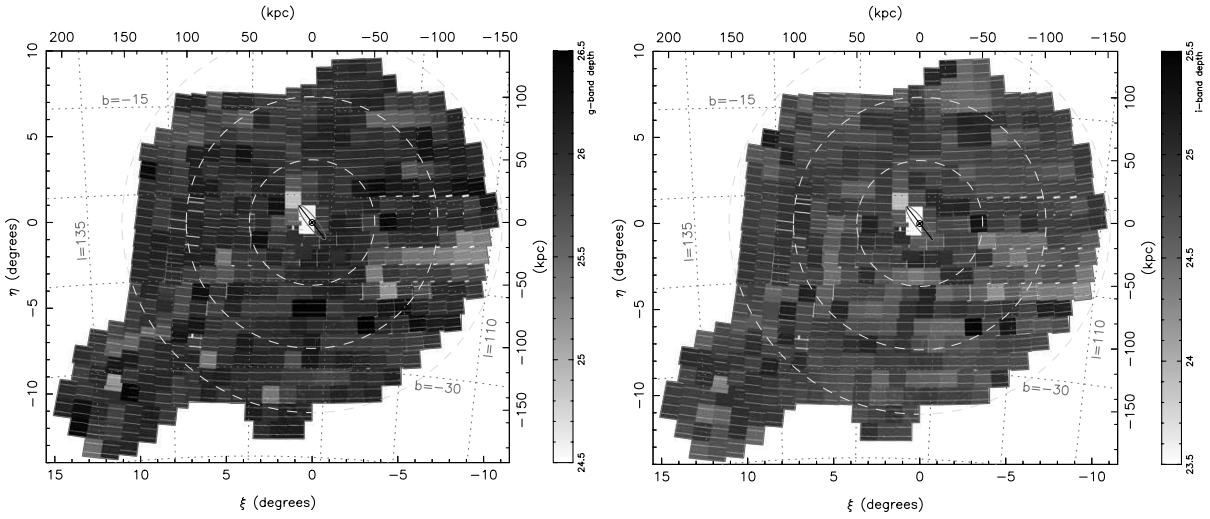

Figure C.4: *Panneau gauche* : Carte de la profondeur photométrique de 5σ pour la bande g. *Panneau droit* : Carte de la profondeur photométrique de 5σ pour la bande i. Dans les deux panneaux, l'ellipse rouge représente le disque de M31 et le cercle bleu en pointillé délimite les régions situées à 50, 100 et 150 kpc de M31. Il est intéressant de noter que les profondeurs sont assez homogènes sur l'ensemble de l'étude malgré de faibles variations.Credit: Ibata et al. (2014).

PAndAS. De nouvelles observations ont été faites avec le CFHT/MegaCam pour cartographier une région située jusqu'à $\sim$ 150 kpc de M31 et $\sim$ 50 kpc de M33. L'empreinte de l'étude est représentée dans la Figure C.2.

Bien qu'une description plus approfondie de l'étude puisse être trouvée dans Ibata et al. (2014) et McConnachie et al. (2018), je vais donner ici un aperçu rapide de sa conception. PAndAS a observé plus de 400 champs de ~ 1 deg^2 dans les bandes g et i avec l'instrument MegaCam. La disposition de MegaCam et de ses 36 CCDs est illustrée dans la Figure C.3. Chaque champ du grand programme a été observé pendant 3 expositions de 450 secondes prises à 3 positions légèrement différentes. Comme le montre la figure C.3, ce changement de position est suffisant pour couvrir les écarts à l'intérieur d'un rang de CCD, mais pas entre les rangées.

La photométrie a été corrigée pour l'extinction en utilisant les cartes de Schlegel et al. (1998) et affinée par Schlafly & Finkbeiner (2011). PAndAS a réalisé une photométrie profonde dans les bandes g et i, bénéficiant d'excellentes conditions (seeing médian de $0.67''$ pour la bande g et de $0.60''$ pour la bande i). Il en résulte une profondeur de 5σ de 26,0 pour la bande g et de 24,7 pour la bande i. La Figure C.4 présente une carte de la complétude pour les sources ponctuelles, illustrant une profondeur d'étude homogène malgré des variations mineures.

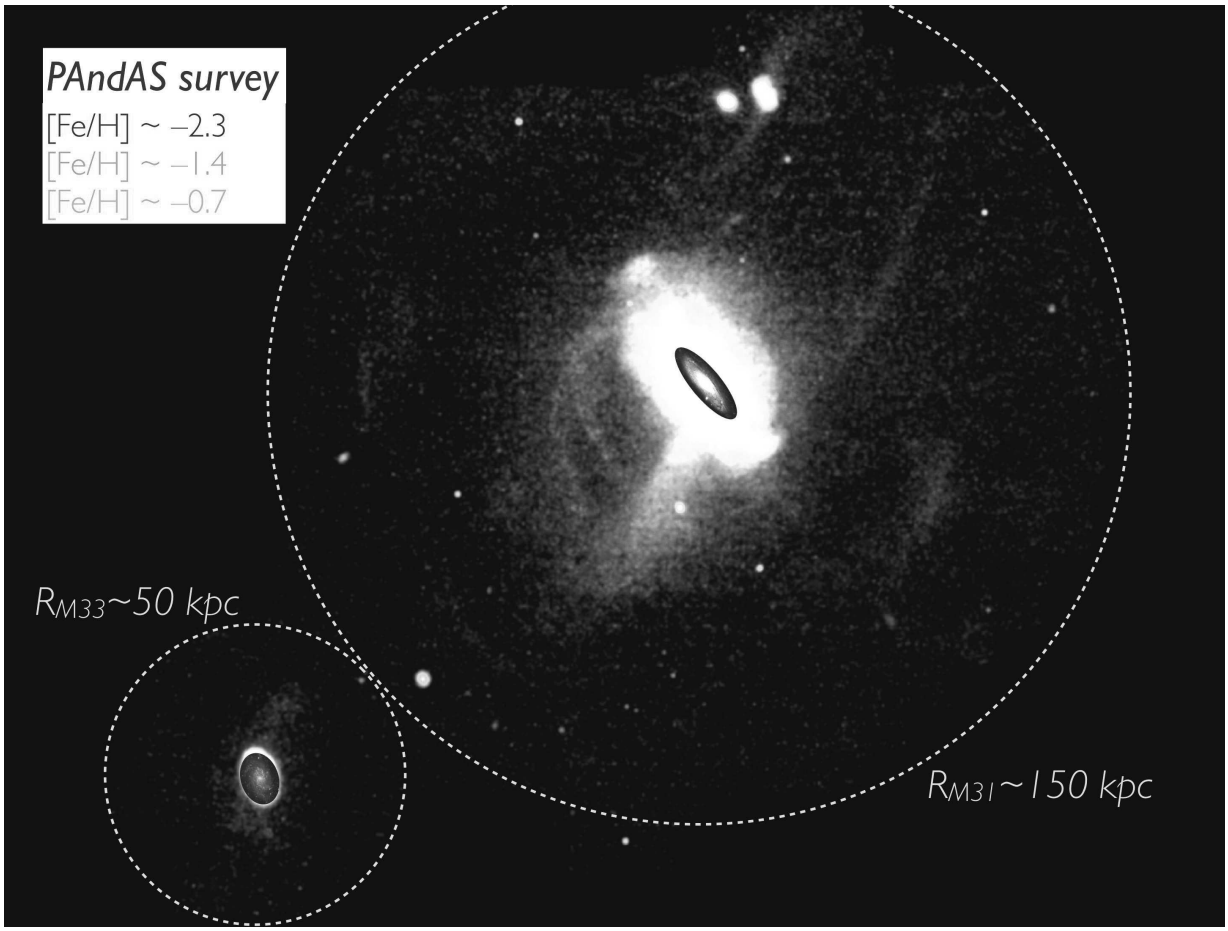

Figure C.5: Distribution des étoiles RGB dans le relevé PAndAS. Les populations stellaires avec une métallicité de -0.7, -1.4 et -2.3 sont respectivement en rouge, vert et bleu. L'intensité de la couleur varie en fonction de la densité. Credit: Martin et al. (2013a).

C.2.2 La vision actuelle des structures du halo de M31

La figure C.5 présente une image composite comprenant des cartes rouges, vertes et bleues d'étoiles RGB, qui correspondent individuellement à des populations stellaires avec des valeurs [Fe/H] ; de -0.7, -1.4 et -2.3, respectivement. Les nombreuses et diverses structures du halo sont visuellement renforcées par le gradient de métallicité de l'image. Par conséquent, des courants deviennent apparents, le plus proéminent étant le Giant Stream (couleur rouge). De plus, la plupart des galaxies naines connues sont également identifiables sous forme de points verts et bleus.

La richesse du halo de M31 en structure est résumée dans la Figure C.6. Au total, 13 sous-structures stellaires ont été identifiées dans des études précédentes (Ibata et al., 2001; Ferguson et al., 2002; Zucker et al., 2004b; Ibata et al., 2007; McConnachie et al.,

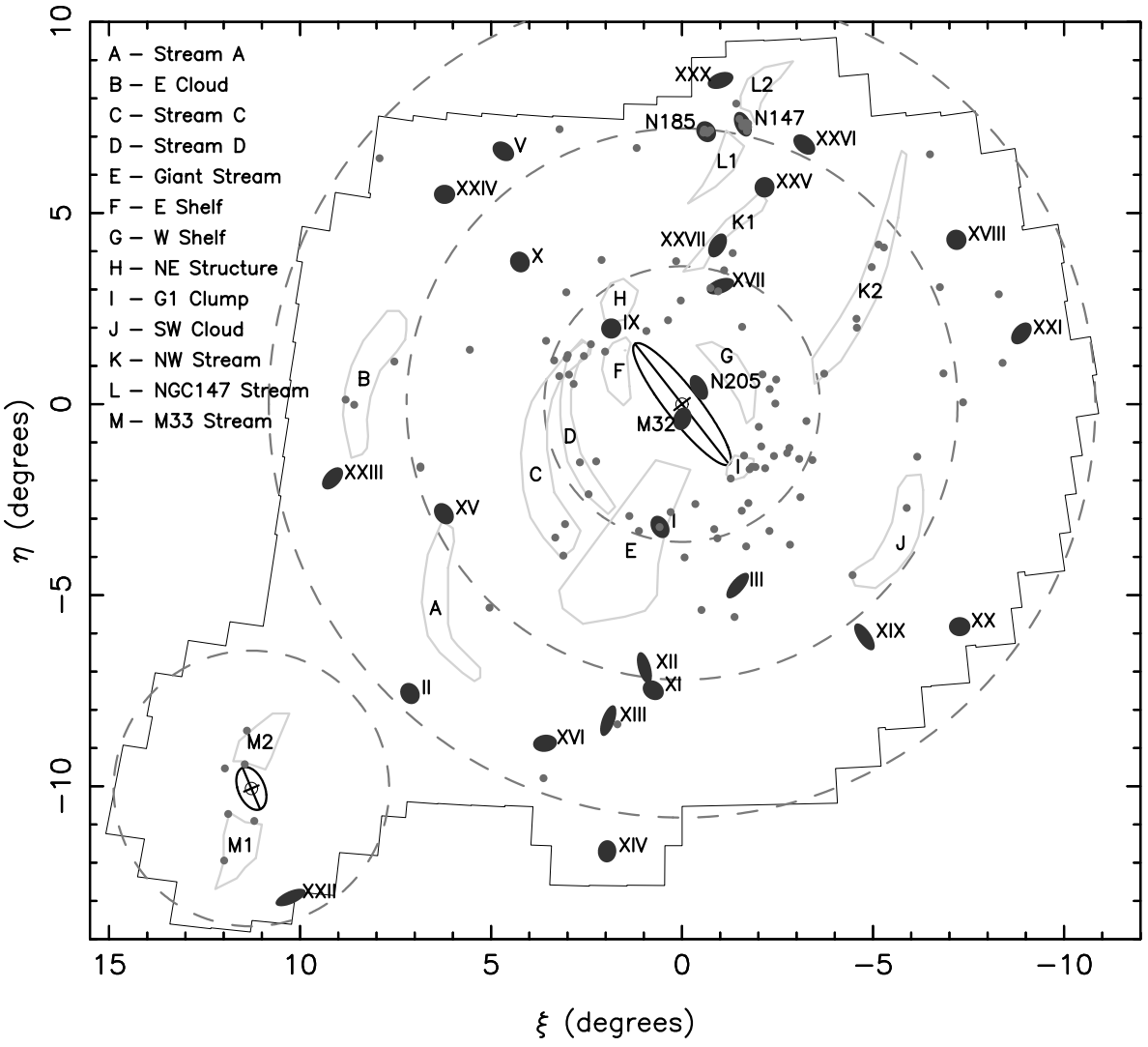

Figure C.6: Schéma des sous-structures les plus importantes dans le halo de M31 vu par PAndAS. Les ellipses bleues correspondent aux galaxies naines, les polygones verts représentent les sous-structures stellaires, et les points rouges indiquent les amas globulaires. Les cercles roses pointillés délimitent les régions situées à 50, 100 et 150 kpc de M31 et à 50 kpc de M33. Credit: McConnachie et al. (2018).

2009). Des études ultérieures menées par Ferguson et al. (2005), Richardson et al. (2008) et Bernard et al. (2015) ont révélé que le Giant Stream, le Western Shelf et le Eastern Shelf sont potentiellement liés au même événement d'accrétion, ce qui est confirmé par leurs populations stellaires similaires à celles du Giant Stellar Stream. D'autre part, Andromada North-East et l'amas G1 présentent une population stellaire semblable à celle du disque, ce qui suggère qu'ils

pourraient s'être formés en raison du chauffage ou de la perturbation du disque résultant de l'interaction entre M31 et un satellite (McConnachie et al., 2018). Par conséquent, ces cinq sous-structures proviennent probablement du même événement. Notamment, (McConnachie et al., 2018) a proposé qu'un minimum de cinq événements, y compris l'interaction entre M33 et NGC147/185, l'événement GSS, K1, et K2, sont nécessaires pour expliquer la vue observée du halo de M31 par PAndAS.

Le relevé PAndAS a également contribué de manière significative à l'élargissement de nos connaissances sur les amas globulaires (GC) dans le halo de M31 (Huxor et al., 2004, 2008, 2014). En effet, dans Mackey et al. (2019), le nombre d'amas connus a été rapporté comme atteignant 92 et une partie significative, allant de 35% à 60%, de ces amas présentait une corrélation spatiale avec des sous-structures stellaires et semble donc avoir été accrétée par des fusions récentes. De plus, selon McConnachie et al. (2018), l'abondance des amas globulaires observés dans le relevé PAndAS implique deux possibilités : soit une série de fusions multiples impliquant des progéniteurs plus massifs que ce que les luminosités de leurs restes indiquent, soit une fusion avec un seul grand progéniteur.

Le relevé PAndAS a joué un rôle essentiel dans l'élargissement de notre compréhension de la population de galaxies naines de M31, doublant effectivement le nombre de satellites connus en permettant la découverte de 19 compagnons précédemment non identifiés grâce à des inspections visuelles et à des techniques de match-filter (Martin et al., 2006; Ibata et al., 2007; McConnachie et al., 2008; Martin et al., 2009; Richardson et al., 2011). Ces découvertes ont considérablement élargi notre compréhension des satellites de M31 car PAndAS a permis la détection de satellites peu lumineux, le moins lumineux étant And XXVI, avec une magnitude absolue de $M_V = -6.0^{+0.7}_{-0.5}$ (Richardson et al., 2009; Martin et al., 2016; Savino et al., 2022). Cependant, en raison de la distance de M31 et ses satellite, il est difficile de détecter des satellites aussi peu lumineux que ceux de la Voie Lactée. Par conséquent, dans le cas de M31, il existe toujours une distinction claire entre les galaxies naines et les GC, comme le montre la figure B.4. Pour approfondir le bruit, l'équipe du PAndAS a développé un algorithme de recherche bayésien automatique, qui a été présenté dans Martin et al. (2013a) et dans le chapitre **??**, ainsi que les galaxies naines candidates qui en résultent.

La distribution spatiale des galaxies naines de M31, telle que trouvée dan PAndAS, a soulevé quelques questions car la densité de surface des satellites sur le ciel semble être plate McConnachie et al. (2009). De plus, comme pour la Voie Lactée, Ibata et al. (2013) a révélé une distribution plane pour 15 galaxies naines autour de M31 (Figure C.7). Parmi cet échantillon de satellites, 13 présentent une co-rotation. Pawlowski et al. (2013) a également identifié une distribution plane comparable, composée de 19 galaxies naines, qu'il a appelée le Grand Plan d'Andromède (GPoA). En outre, Santos-Santos et al. (2020) a découvert un plan perpendiculaire au GPoA, englobant 18 satellites. Cependant, l'analyse de l'aspect transitoire de ces distributions s'avère difficile en raison de l'absence de mesures du mouvement propre de la plupart des satellites. Néanmoins, Sohn et al. (2020) suggère que le système peut présenter une cohérence dynamique, comme indiqué par la détermination du mouvement

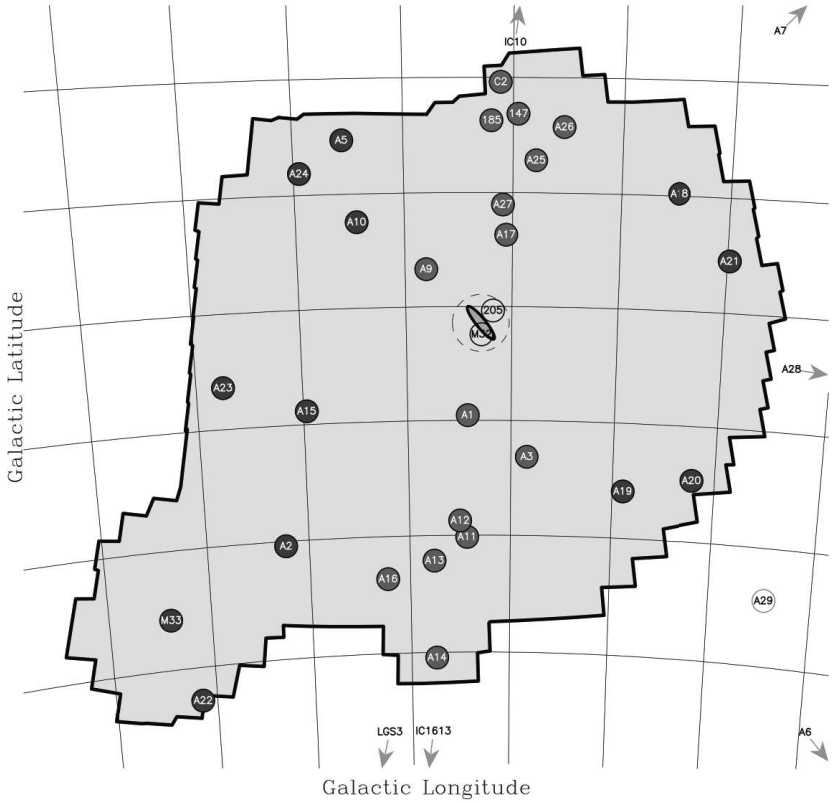

Figure C.7: Carte de la position des galaxies naines de M31 (cercle plein) dans le relevé PAndAS. Les satellites en rouge ont une distribution spatiale plane. Credit: Ibata et al. (2013).

propre de NGC 147 et NGC 185. En tout état de cause, la présence de ces plans de satellites dans Andromède renforce l'idée que la distribution des galaxies naines autour de leur hôte peut ne pas être isotrope.

Un autre aspect particulier de la distribution des satellites de M31 est mis en évidence par McConnachie & Irwin (2006). Remarquablement, la majorité des compagnons de M31 sont situés entre M31 et le MW. Ce modèle anisotrope a été confirmé par Conn et al. (2012) via la détermination des distances TRGB et Savino et al. (2022), qui a réévalué les distances aux galaxies naines en utilisant des étoiles RR-Lyrae, en tirant parti des observations profondes du télescope spatial Hubble (HST). La figure C.8 montre la distribution spatiale anisotrope des satellites de M31 telle qu'elle a été trouvée avec les nouvelles distances. La nature particulière de cette distribution soulève des questions non seulement sur la cosmologie, puisqu'elle s'écarte des attentes typiques du modèle ΛCDM, mais aussi sur la physique de la formation et de l'évolution des galaxies. Elle pourrait potentiellement indiquer que M31 n'est pas au centre de son système de satellites, comme le décalage de position attendu dans

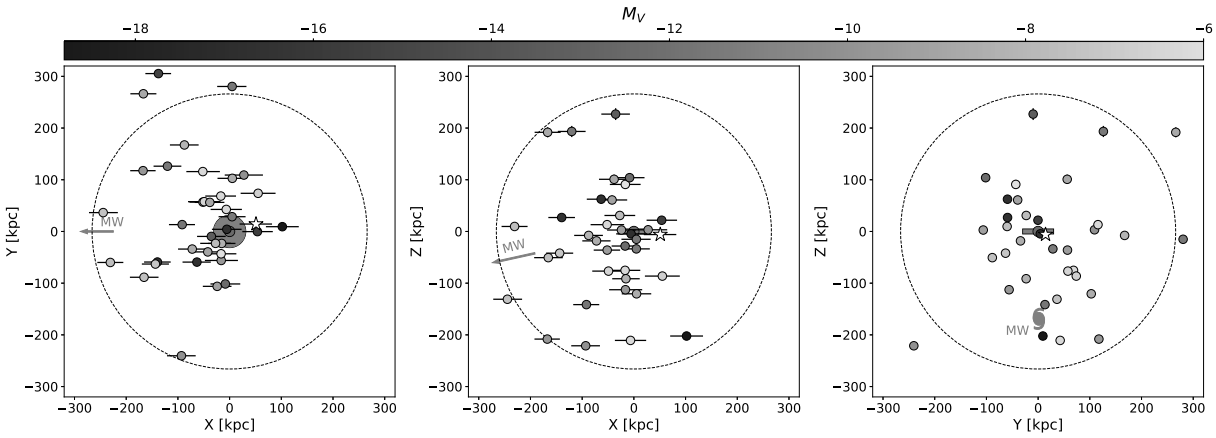

Figure C.8: Distribution spatiale des galaxies naines de M31 dans un système de coordonnées cartésiennes où le plan XY correspond au disque de M31 et l'axe Z pointe vers le pôle galactique nord de M31. Les couleurs codent la magnitude des satellites. Le cercle en pointillé délimite une région située dans un rayon de 266 kpc autour de M31. Il est à noter que la plupart des galaxies naines de M31 sont situées dans l'hémisphère entre le MW et M31. Credit: Savino et al. (2022).

la Voie Lactée en raison de la présence du LMC, ou qu'une partie significative des satellites de M31 a été récemment accrétée, ce qui fait qu'ils ne sont pas en phase.

On s'attendait à découvrir de nombreuses galaxies naines peu lumineuses dans le voisinage de M33, à l'instar de ce qui est observé autour du LMC. Cependant, le seul satellite candidat trouvé autour de M33 est And XXII. Cette observation s'aligne sur un scénario impliquant une rencontre passée entre M31 et M33, car la plupart des satellites de M33 ont pu être éliminés. Néanmoins, l'occurrence d'une telle interaction est sujette à débat. D'une part, certains éléments suggèrent qu'une interaction étroite a déjà eu lieu, laissant une signature distincte dans la distribution des étoiles et du gaz de M33 (McConnachie et al., 2009; Putman et al., 2009; Semczuk et al., 2018). D'autre part, la cinématique de M33 et de M31 semble soutenir un scénario dans lequel M33 et M31 n'ont pas encore interagi ou ont eu une interaction il y a environ 6 milliards d'années, avec une distance minimale de 100 kpc (Patel et al., 2017; van der Marel et al., 2019). Néanmoins, les recherches menées par (Patel et al., 2018) ont démontré que, compte tenu de la couverture et des limites de détection de l'étude PAndAS, le nombre limité de satellites de M33 n'est pas incompatible avec les attentes dérivées de ΛCDM.

L'étude PAndAS a permis de faire une multitude de découvertes concernant la composition du halo M31, offrant une opportunité exceptionnelle d'explorer l'histoire de sa formation. Suite à ces découvertes, divers scénarios de fusion ont été proposés pour élucider les caractéristiques observées au sein du halo M31. Hammer et al. (2018) rapporte que le disque de M31 est compatible avec un événement de fusion 4:1 survenu il y a environ 1,8-3 Gyr ans.

Parallèlement, D'Souza & Bell (2018) propose un événement de fusion unique prédominant il y a environ 2 milliards d'années impliquant un satellite avec une masse stellaire d'environ $2{,}5\times10^{10}$ M$\odot$, M32 étant le vestige de la galaxie naine qui a fusionné. Cette fusion permet d'expliquer la rotation interne de M31, la présence du Giant Stream et l'explosion de la formation d'étoiles dans M31 il y a environ 2 Gyr.

C.3 Vers une caractérisation du système satellitaire de M31

Comme indiqué précédemment, les systèmes satellites sont des outils puissants pour étudier la cosmologie et la physique de la formation et de l'évolution des galaxies. Cependant, l'étude détaillée des systèmes de galaxies naines autour d'hôtes ayant des environnements et des histoires de fusion variés est un défi en raison de la difficulté à détecter ces objets. Heureusement, l'émergence de grands relevés photométriques homogènes comme le SDSS et particulièrement le PAndAS a considérablement augmenté le nombre de galaxies naines connues autour de M31, nous permettant de mener une étude statistique rigoureuse de ce système satellite. Etant donné l'histoire apparemment active de M31, de telles études ont le potentiel d'améliorer notre compréhension de l'impact de l'histoire d'accrétion de l'hôte sur les galaxies naines, mais aussi de mieux contraindre l'impact des processus baryoniques et les propriétés de la Matière Noire. La motivation de mon travail provient de la nécessité de déterminer les propriétés du système satellite de M31 tout en prenant en compte le caractère incomplet de l'échantillon de galaxies naines. Il s'agit d'une étape cruciale pour comparer les galaxies naines observées et simulées, ainsi que pour permettre des comparaisons entre différents systèmes de satellites.

Chapitre III décrit l'algorithme de recherche développé par Martin et al. (2013a) pour identifier les satellites peu lumineux dans PAndAS, ainsi que les modifications que j'ai mises en uvre pour déterminer la complétude de l'échantillon de galaxies naines de PAndAS.

Chapitre IV présente la détermination de limites de détection précises pour la recherche de galaxies naines dans l'étude PAndAS.

Chapitre V fournit un compte-rendu détaillé du cadre statistique conçu pour dériver les propriétés globales du système de satellites M31, tout en incorporant efficacement les limites de détection. En outre, cette analyse présente et discute les diverses propriétés dérivées de l'étude, y compris le nombre de galaxies naines, leur distribution radiale, leur fonction de luminosité et leur relation taille-luminosité. Enfin, j'étudie l'impact des limites de détection sur l'anisotropie observée des satellites de M31.

Dans *Chapitre VI*, étant donné la possibilité d'un déplacement positionnel de M31 comme explication potentielle de la distribution particulière de ses galaxies naines, je déduis la position du centre de la distribution des satellites pour tester sa compatibilité avec le centre de M31.

Je présente un résumé complet de mon travail dans *Chapitre VII*. Ensuite, je présente une analyse comparative des systèmes de satellites de M31 et du MW, en soulignant leurs

similitudes et leurs différences. Enfin, je suggère des pistes de recherche pour l'avenir.

Appendix D Conclusion

D.1 Résumé

Les galaxies naines sont des sondes importantes de la cosmologie et de la physique de la formation et de l'évolution des galaxies. Le 21ème siècle a été témoin d'une augmentation remarquable de la découverte de satellites, grâce à l'avènement de grands relevés photométriques homogènes, permettant des analyses statistiques rigoureuses pour comparer les observations avec les modèles de la cosmologie, de la formation et de l'évolution des galaxies. Bien que la majorité des contraintes proviennent de l'analyse du système satellite de notre propre galaxie, comme indiqué dans le chapitre I, il est impératif d'étendre l'étude des galaxies naines à d'autres galaxies hôtes pour assurer une compréhension complète, compte tenu du fait que la Voie Lactée peut ne pas représenter un système typique (Weisz et al., 2019).

Le chapitre II présente M31 et ses compagnons, qui constituent le système le plus accessible au-delà de notre propre galaxie. La compréhension du halo de M31 a été grandement améliorée par l'étude PAndAS. Ce vaste programme photométrique homogène a sondé une région située dans un rayon de 150 kpc autour de M31, contenant 26 galaxies naines connues, dont 19 ont été découvertes par PAndAS. Cette étude a révélé de nombreuses sous-structures dans le halo de M31, s'alignant sur les prédictions de la modélisation de M31 qui indiquent une récente fusion majeur (Hammer et al., 2018; D'Souza & Bell, 2018).

Dans le chapitre III, l'algorithme de recherche développé par l'équipe de PAndAS (Martin et al., 2013a) est détaillé, ainqi que les modifications apportée pour déterminer précisément les limites de détection pour l'échantillon de galaxies naines de PAndAS.

Comme les limites de détection sont un élément clé dans la comparaison des systèmes de satellites observés avec ceux simulés, dans le Chapitre IV j'ai déterminé l'incomplétude de l'échantillon de satellites de M31 en utilisant l'étude PAndAS. J'ai obtenu des fractions de détection précises en fonction de la magnitude, de la taille et de la position d'une galaxie naine dans la relevé. J'ai donc généré $\sim$ 500000 galaxies naines artificielles, je les ai insérées dans le relevé, et j'ai testé leur récupération en utilisant l'algorithme de recherche développé par l'équipe PAndAS (Martin et al., 2013a). Pour la plupart des champs, le seuil de détection de la luminosité de surface se situe entre 29-30 mag arcsec^{-2}, mais il dépend fortement de la position dans le relevé. En effet, la détection d'un satellite est affectée par la contamination de la Voie Lactée (au nord du relevé ; b > -20°) et du halo stellaire de M31. La détermination

de la complétude a été la première étape vers une analyse globale du système de satellites de M31.

Dans le chapitre V, j'ai déduit les propriétés globales du système de satellites de M31 en tenant compte des limites de détection précédemment déterminées pour la recherche de galaxies naines dans le cadre de l'étude PAndAS. J'ai conçu un cadre bayésien qui permet de déterminer la fonction de luminosité, la pente de la distribution spatiale en 2 ou 3D, la relation taille-luminosité et le nombre de satellites. Je conclus que M31 héberge de 92^{+19}_{-26} à 136^{+65}_{-35} satellites dans un rayon de 300 kpc et avec $M_V < -5.5$, alors que seulement ~ 40 satellites sont connus. La redétermination de leurs distances par Savino et al. (2022) a mis en évidence l'anisotropie de la distribution des satellites de M31, car ils sont presque tous situés entre la Voie Lactée et M31. En utilisant les propriétés globales dérivées du système de satellites de M31, j'ai testé si l'anisotropie pouvait être expliquée par les seules limites de détection. J'ai exclu cette possibilité avec plus de 99.9%, prouvant ainsi que cette anisotropie est une caractéristique réelle du système de galaxies naines de M31.

Dans le chapitre VI, j'explore l'une des explications possibles de la distribution particulière des galaxies naines de M31. En effet, suite au décalage prédit de la position de la Voie Lactée dû au LMC, il semble naturel que M31 puisse être décalé de la même façon par rapport à sa distribution de galaxies satellites. J'ai dérivé la position du centre de la distribution des satellites de M31 pour un modèle de distribution radiale de type NFW et de type loi de puissance. Dans chaque cas, la position de M31 est statistiquement compatible avec le centre de sa distribution de galaxies naines, mais la position du centre est toujours décalée vers la Voie Lactée de $\sim 10 - 50$ kpc.

Tout au long de mon doctorat, j'ai établi une base solide pour un examen rigoureux du système de satellites de M31, englobant la détermination de ses propriétés globales par la modélisation bayésienne tout en considérant les limites de détection de l'étude PAndAS. Le premier résultat a été l'étude de la distribution particulière des satellites de M31. Avec ce travail accompli, nous sommes maintenant bien équipés pour entreprendre une analyse comparative des systèmes de satellites de M31 et de la Voie Lactée.

D.2 Le système de satellites de la Voie Lactée et de M31 : une étude comparative

La sensibilité des galaxies naines à leur environnement et à l'histoire d'accrétion de leur hôte est largement reconnue, bien qu'elle ait été principalement explorée par des simulations (Engler et al., 2021; Kanehisa et al., 2023; Van Nest et al., 2023) ou par les propriétés détaillées de galaxies naines individuelles de la Voie Lactée ou de M31 (Weisz et al., 2019). Dans les observations, seul l'impact sur l'extrémité la plus brillante du système de satellites a été étudié (Mao et al., 2021; Carlsten et al., 2022), compte tenu des difficultés à détecter des satellites peu lumineux autour d'hôtes plus éloignés. Néanmoins, dans cette thèse, j'ai

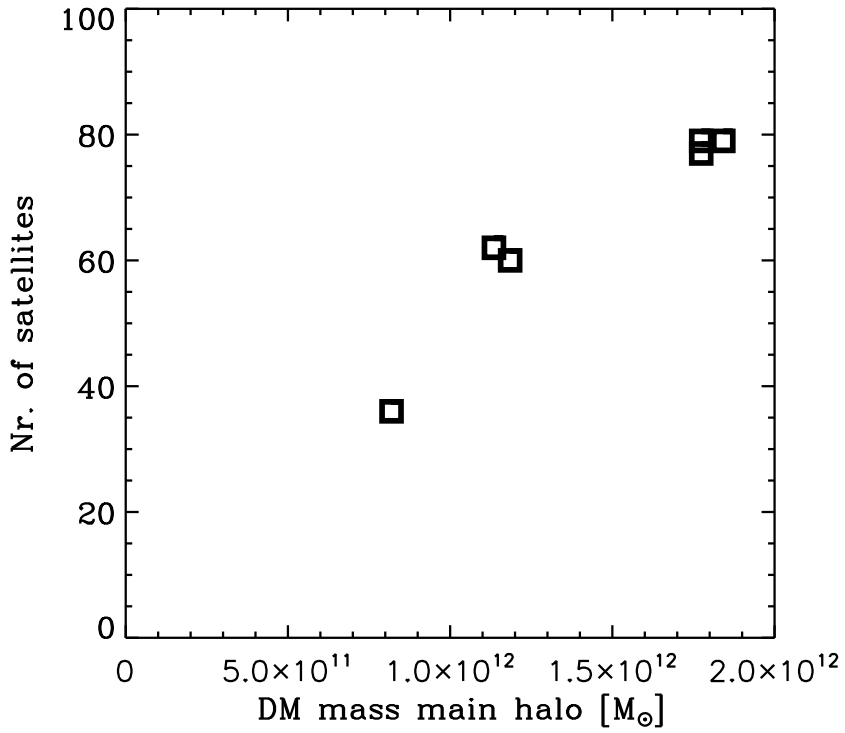

Figure D.1: Nombre de satellites avec $M_V < -5$ en fonction de la masse virale de leur hôte pour 6 halos Aquaruis. Credit : Starkenburg et al. (2013).

déduit les propriétés du système de satellites de M31 pour les galaxies naines avec $M_V < -5.5$, ouvrant ainsi la voie à une étude comparative entre les propriétés du système de satellites de M31 et celles de la Voie Lactée.

Tout d'abord, il convient de mentionner que la comparaison des deux systèmes de satellites met en évidence le fait que les galaxies naines de M31 sont issues des mêmes processus baryoniques que ceux observés dans la Voie Lactée. Au premier abord, les propriétés globales de M31 présentent des similitudes avec celles de la Voie Lactée . En particulier, la pente de la fonction de luminosité se situe dans la même fourchette. Pour la Voie Lactée, β = -1.9 $\pm$ 0.2 (Tollerud et al., 2008) ou $\beta \sim$ -1.25 (Koposov et al., 2008), alors que pour M31, nous déduisons une pente de β = -1.5 $\pm$0.1. De plus, nos résultats s'alignent avec ceux de Brasseur et al. (2011) pour la Voie Lactée, illustrant que les deux systèmes de galaxies naines adhèrent à une relation taille-luminosité similaire.

D.2.1 M31 est-elle plus massive ?

Il est bien établi que M31 devrait être plus massive que la Voie Lactée (Peñarrubia et al., 2016). Les simulations indiquent systématiquement une proportionnalité directe entre le nombre de satellites et la masse de la galaxie hôte (Starkenburg et al., 2013; Engler et al.,

2021), comme le montre la Figure D.1. Par conséquent, le halo de M31 devrait contenir plus de galaxies naines que celui du MW. Cette prédiction est en accord avec le nombre attendu de galaxies naines pour la Voie Lactée et M31. Les prédictions du modèle pour la Voie Lactée estiment ~ 20 à 40 satellites avec $M_V < -5.5$ et $r_{\rm MW} < 300$ kpc (Newton et al., 2018; Jethwa et al., 2018; Nadler et al., 2020; Manwadkar & Kravtsov, 2022; Drlica-Wagner et al., 2020). En revanche, pour M31, notre inférence révèle 2 à 3 fois plus de satellites que pour la Voie Lactée, car nous nous attendons à 92^{+19}_{-26} satellites avec $M_V < -5.5$ et $r_{\rm MW} < 300$ kpc.

De plus, M31 présente une abondance significativement plus élevée d'amas globulaires, avec 92 amas globulaires identifiés à des distances projetées entre 25 et 150 kpc de M31 (Huxor et al., 2014; Mackey et al., 2019), ce nombre est environ sept fois plus élevé que le nombre d'amas trouvés dans une région similaire pour la Voie Lactée.

D.2.2 M31 a-t-elle eu une histoire d'accrétion plus active ?

La question de savoir dans quelle mesure l'histoire d'accrétion de la Voie Lactée est typique est une motivation ce travail. Nous portons maintenant notre attention sur le halo de M31 afin de déterminer si l'histoire de l'accrétion de M31 est similaire, réduite ou intensifiée par rapport à celle de la Voie Lactée. Les prédictions des modèles semblent suggérer une histoire plus active pour M31 par rapport à la Voie Lactée, car M31 aurait connu une fusion importante il y a environ $\sim 2-4$ Gyr, alors que la dernière accrétion majeure de la Voie Lactée s'est produite il y a environ ~ 10 Gyr (D'Souza & Bell, 2018; Hammer et al., 2018; Helmi et al., 2018). Cependant, il est important de noter que la Voie Lactée est actuellement en train de fusionner avec le LMC (Battaglia et al., 2022), et que M31 est également en train de fusionner avec M33, bien que l'état exact de ces accrétions soit encore débattu (Patel et al., 2017; Semczuk et al., 2018).

Un premier indice observationnel réside dans le nombre de sous-structures brillantes découvertes dans le relevé PAndAS (McConnachie et al., 2018). Bien qu'une comparaison exacte soit difficile en raison de l'absence de limites de détection pour les sous-structures, le halo de M31 semble être plus structuré et contient une plus grande abondance de sous-structures stellaires brillantes par rapport au halo du MW. Plus précisément, la présence du Giant Stream est une preuve importante d'une fusion récente et significative $\sim$ 2-4 Gyr ago (D'Souza & Bell, 2018; Hammer et al., 2018).

Un autre indice convaincant réside dans les historiques de formation d'étoiles (SFH) des galaxies naines de M31 et de la Voie Lactée, qui présentent des schémas différents mis en évidence dans la Figure D.2. Les galaxies naines de M31 présentent des SFH étendues, avec la majorité des satellites éteints il y a 3 à 6 Gyr. D'un autre côté, les satellites de la Voie Lactée montrent une extinction qui s'est produite principalement il y a environ 9 Gyr, avec seulement quelques systèmes plus récemment éteints. Ces différences suggèrent une corrélation potentielle entre les SFHs des satellites et l'histoire d'accrétion de l'hôte. L'une

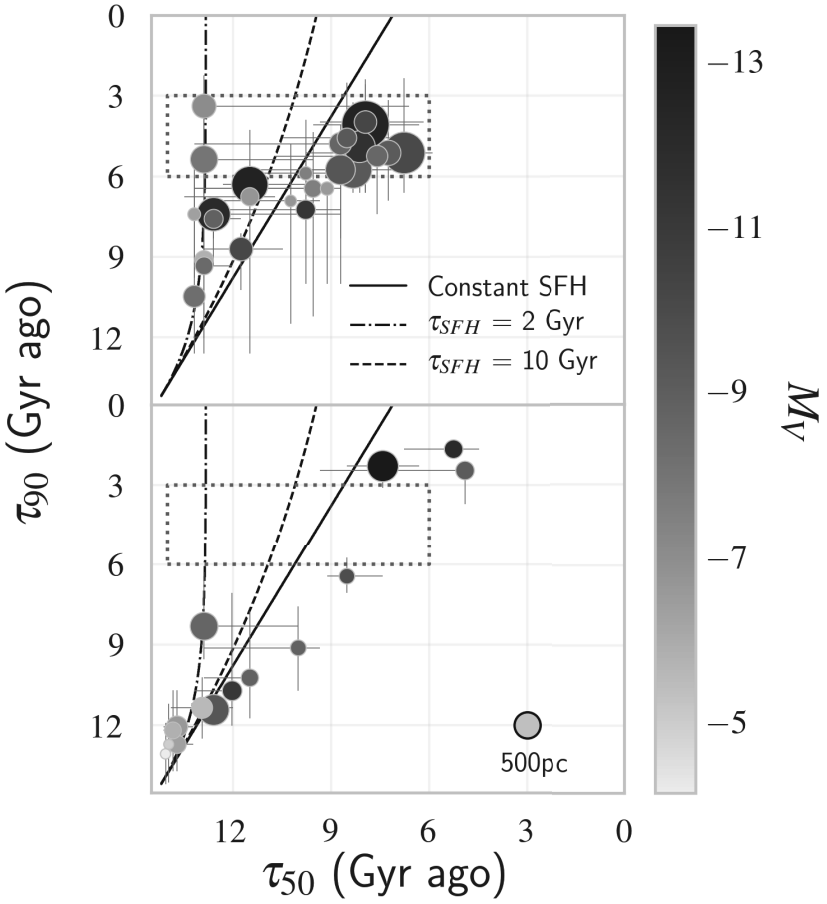

Figure D.2: Le panneau supérieur affiche le temps auquel 50% (τ_{50}) et 90% (τ_{90}) de la masse stellaire ont été formés pour les satellites de M31, tandis que le panneau inférieur illustre la même chose pour les satellites de la Voie Lactée. Les couleurs des points indiquent la luminosité des galaxies naines, et leur taille correspond à leur rayon de demi-lumière. Dans les deux panneaux, les SFH constants et à décroissance exponentielle sont représentés par des lignes noires. Notamment, la moitié des satellites de M31 sont compris dans le rectangle bleu pointillé, alors que la même région ne contient aucun satellite de MW.Credit : Weisz et al. (2019).

des explications possibles pour la vague d'extinction des galaxies naines de M31 entre 3 et 6 Gyr est leur environnement, car les simulations prédisent une fusion majeure pour M31 il y a $\sim 2-4$ Gyr (Hammer et al., 2018; D'Souza & Bell, 2018). En effet, ces satellites peuvent avoir été éteints par l'environnement ou être tombés dans le halo de M31 lors de l'accrétion. Cet événement d'accrétion pourrait avoir eu un impact important sur les SFHs des satellites de M31, et renforcer l'idée d'une histoire active d'accrétion pour M31.

L'accrétion de galaxies naines, ainsi que de leurs propres satellites, devrait avoir un im-

pact sur la fonction de luminosité. Les simulations indiquent que la signature du renforcement des satellites est visible dans la fonction de luminosité jusqu'à 2,25-4,25 Gyr (Joshi et al., 2023). Par conséquent, étant donné les histoires d'accrétion distinctes de M31 et de la Voie Lactée, des différences dans leurs fonctions de luminosité devraient apparaître. Cependant, mener une comparaison robuste et quantifiée des pentes de la fonction de luminosité est un défi en raison de la non-homogénéité des méthodes utilisées pour dériver ces pentes et du fait que les satellites très faibles ($M_V \geq -5.5$) autour de M31 sont actuellement indétectables.

Une explication plausible de la distribution plane des galaxies naines autour de la Voie Lactée ou de M31 (Lynden-Bell, 1976; Kroupa et al., 2005; Ibata et al., 2013; Pawlowski et al., 2013) est l'activité de leurs galaxies hôtes. Cependant, selon Kanehisa et al. (2023), les fusions majeures peuvent améliorer la corrélation espace-phase des satellites, avec une signature observable qui dure jusqu'à $2-5$ Gyr, mais elles ne peuvent pas créer des plans de satellites cohérents et/ou très aplatis. Même si le mouvement propre des galaxies naines de M31 est actuellement inconnu, ce résultat suggère que la distribution plane des satellites autour de la Voie Lactée et de M31 n'est peut-être pas une signature de leur histoire d'accrétion. Cependant, la distribution des galaxies naines de M31 montre une forte anisotropie, car presque toutes se trouvent entre la Voie Lactée et M31. Cette distribution particulière peut impliquer que les satellites de M31 ne sont pas complètement viralisés, et la distribution pourrait résulter du ballottement de M31 dû à une fusion passée. Bien que les contraintes déduites dans cette étude soient compatibles avec le fait que M31 soit au centre de sa distribution, elles ont également révélé un décalage d'environ $\sim 10-50$ kpc vers la Voie Lactée par rapport au centre de la distribution.

Bien qu'il y ait des indications que M31 est plus actif que la Voie Lactée, une quantification précise de l'impact de l'histoire de la fusion de l'hôte sur le système de satellites nécessite des données supplémentaires sur les galaxies naines de M31. L'augmentation de l'échantillon de galaxies naines de M31 connues avec des satellites plus faibles ou des satellites en dehors de l'empreinte du PAndAS est nécessaire pour mieux comprendre l'impact de l'environnement et de l'histoire de l'hôte.

D.3 Perspectives

Dans cette section, j'aborderai certains des projets futurs qui continueront à explorer l'utilisation des galaxies naines comme test pour la cosmologie, la formation et l'évolution des galaxies.

Approfondir notre connaissance du système de satellites M31 : Bien que l'avènement de grands relevés homogènes ait considérablement augmenté le nombre de satellites connus de M31, le régime de faible luminosité est encore atteint pour les satellites de la Voie Lactée reste encore inconnu en raison des défis que pose la détection d'objets aussi faibles en luminosité à des distances de $700-800$ kpc de la Voie Lactée. Le relevé PAndAS a permis de découvrir 19 galaxies naines grâce à des cartes de densité ou à des méthodes de

match-filter. Cependant, la mise en uvre d'un algorithme de recherche bayésien, capable de modéliser à la fois la galaxie naine et la contamination, a révélé un certain nombre de galaxies naines potentielles qui doivent encore être confirmées. L'un de mes objectifs est d'observer ces objets candidats avec une photométrie profonde à l'aide de l'instrument HST/ACS afin de vérifier définitivement s'il s'agit bien de satellites de M31. En confirmant leur nature, nous pourrons améliorer notre compréhension du système de satellites de M31 et faire la lumière sur les propriétés des galaxies naines.

L'algorithme ultime de recherche de galaxies naines: : Les prochains relevés LSST et Euclid seront une occasion incroyable d'augmenter le nombre de galaxies naines de la Voie Lactée connues, car le champ de détection des galaxies naines peu lumineuses s'étendra de notre environnement à l'ensemble du halo de la Voie Lactée. Ces nouvelles galaxies naines potentielles sont essentielles pour mieux contraindre les propriétés des particules de matière noire, explorer l'impact de la physique baryonique et résoudre ou confirmer toute tension entre les observations de satellites et les simulations. Pour tirer parti de cette opportunité, je souhaite concevoir l'algorithme de recherche ultime qui exploite la combinaison des données photométriques, spectroscopiques et astrométriques pour détecter efficacement les galaxies naines. En combinant les informations provenant d'études telles que le Sloan Digital Sky Survey (SDSS), le Panoramic Survey Telescope and Rapid Response System (Pan-STARR), Gaia, le Dark Energy Survey (DES) et l'étude DESI Legacy, nous pouvons tirer parti de leurs différentes empreintes, profondeurs et bandes photométriques. De plus, avec la profondeur anticipée des futurs relevés, il devient impératif d'améliorer la distinction entre les satellites, les galaxies d'arrière-plan et les amas globulaires. Actuellement réalisée manuellement, je prévois d'automatiser cette étape en utilisant les informations spectrographiques et astrométriques.

Les galaxies naines comme sondes cosmologiques : La distribution de la masse des systèmes de satellites observés permet de contraindre la masse des particules de matière noire, mais il est essentiel de tenir compte de la complétude des observations pour obtenir des résultats précis. Tout au long de mon doctorat, j'ai développé un cadre statistique robuste pour déduire des contraintes précises sur les propriétés des satellites d'Andromède. La prochaine étape de ma recherche consiste à comparer la distribution de masse attendue des sous-halos de matière noire avec la fonction de luminosité déduite du système de satellites d'Andromède, ce qui permettra pour la première fois de déduire des contraintes sur la masse de la particule de matière noire à partir des observations des satellites d'Andromède. De plus, j'utiliserai également des observations artificielles, similaires à celles de l'étude PAndAS, dérivées des simulations Auriga telles que présentées dans Thomas et al. (2021). En appliquant le cadre développé dans cette thèse à ces systèmes de satellites artificiels, je déterminerai leurs propriétés globales et les comparerai ensuite aux observations. Cette analyse comparative vise à identifier les similitudes et les différences potentielles entre les systèmes de satellites issus des simulations et des observations, ce qui permettra de mieux comprendre la nature de la matière noire et la physique de la formation et de l'évolution des galaxies.

Explorer l'impact de l'environnement sur les systèmes satellitaires: Les galaxies naines de la Voie lactée ont été la principale référence pour les systèmes satellites. Cependant, si l'on considère que la Voie lactée n'est peut-être pas un système typique, il devient impératif d'étudier les propriétés des galaxies naines dans d'autres environnements galactiques. La détection et la caractérisation de galaxies peu lumineuses à de plus grandes distances de nous représentent un défi, mais prochainement LSST et Euclid fourniront des données sans précédent sur les galaxies du Volume Local, car il est prévu de résoudre les étoiles pour les systèmes situés dans un rayon de 5 Mpc de la Voie Lactée. Je propose d'utiliser les outils développés pour le système d'Andromède pour rechercher et caractériser de nouvelles galaxies naines autour de ces hôtes lointains. En employant cette approche, nous pouvons évaluer la complétude et déduire les propriétés de ces systèmes satellites. De plus, afin de constituer un échantillon de galaxies plus étendu, j'étudierai également les galaxies naines non résolues autour d'hôtes encore plus lointains. Les systèmes de galaxies naines présentent diverses propriétés influencées par des facteurs tels que l'environnement et les fusions avec l'hôte principal. Pour quantifier l'impact des propriétés de l'hôte et de l'environnement sur les galaxies naines, je comparerai les propriétés de différents systèmes satellites analysés de manière homogène, en examinant leur distribution de masse et leur distribution spatiale.

En conclusion, la caractérisation du système de satellites M31 marque le premier pas vers une analyse complète des systèmes de satellites. Avec l'avènement de relevés révolutionnaires telles que LSST et Euclid, ainsi que la découverte attendue de nombreux nouveaux satellites autour d'hôtes divers, l'avenir promet une compréhension plus approfondie de la cosmologie, de la formation et de l'évolution des galaxies.

Bibliography

Abazajian, K., et al. 2003, AJ, 126, 2081

Abbott, T. M. C., et al. 2018, ApJS, 239, 18

Abel, T., Bryan, G. L., & Norman, M. L. 2002, Science, 295, 93

Armandroff, T. E. 1994, in European Southern Observatory Conference and Workshop Proceedings, Vol. 49, European Southern Observatory Conference and Workshop Proceedings, 211

Armandroff, T. E., Davies, J. E., & Jacoby, G. H. 1999, in Astronomical Society of the Pacific Conference Series, Vol. 170, The Low Surface Brightness Universe, ed. J. I. Davies, C. Impey, & S. Phillipps, 111

Baade, W., & Swope, H. H. 1961, AJ, 66, 300

Battaglia, G., Taibi, S., Thomas, G. F., & Fritz, T. K. 2022, A&A, 657, A54

Bayes, M., & Price, M. 1763, Philosophical Transactions of the Royal Society of London Series I, 53, 370

Bechtol, K., et al. 2015, ApJ, 807, 50

Bell, E. F., Slater, C. T., & Martin, N. F. 2011, ApJL, 742, L15

Belokurov, V., et al. 2010, ApJL, 712, L103

Belokurov, V., et al. 2009, MNRAS, 397, 1748

Belokurov, V., et al. 2007, ApJ, 654, 897

Belokurov, V., et al. 2006, ApJL, 647, L111

Bennet, P., Sand, D. J., Crnojević, D., Spekkens, K., Karunakaran, A., Zaritsky, D., & Mutlu-Pakdil, B. 2019, ApJ, 885, 153

Bernard, E. J., et al. 2015, MNRAS, 446, 2789

Besla, G., Kallivayalil, N., Hernquist, L., Robertson, B., Cox, T. J., van der Marel, R. P., & Alcock, C. 2007, ApJ, 668, 949

Bode, P., Ostriker, J. P., & Turok, N. 2001, ApJ, 556, 93

Boylan-Kolchin, M., Weisz, D. R., Johnson, B. D., Bullock, J. S., Conroy, C., & Fitts, A. 2015, MNRAS, 453, 1503

Brasseur, C. M., Martin, N. F., Macciò, A. V., Rix, H.-W., & Kang, X. 2011, ApJ, 743, 179

Brown, T. M., et al. 2014, ApJ, 796, 91

Bullock, J. S., & Boylan-Kolchin, M. 2017, ARA&A, 55, 343

Bullock, J. S., Kravtsov, A. V., & Weinberg, D. H. 2000, ApJ, 539, 517

Cannon, R. D., Hawarden, T. G., & Tritton, S. B. 1977, MNRAS, 180, 81P

Carlsten, S. G., Greene, J. E., Beaton, R. L., Danieli, S., & Greco, J. P. 2022, ApJ, 933, 47

Carlsten, S. G., Greene, J. E., Peter, A. H. G., Greco, J. P., & Beaton, R. L. 2020, ApJ, 902, 124

Chambers, K. C., et al. 2016, arXiv e-prints, arXiv:1612.05560

Chapman, S. C., et al. 2013, MNRAS, 430, 37

Chiboucas, K., Jacobs, B. A., Tully, R. B., & Karachentsev, I. D. 2013, AJ, 146, 126

Chiboucas, K., Karachentsev, I. D., & Tully, R. B. 2009, AJ, 137, 3009

Collins, M. L. M., et al. 2013, ApJ, 768, 172

Collins, M. L. M., Charles, E. J. E., Martínez-Delgado, D., Monelli, M., Karim, N., Donatiello, G., Tollerud, E. J., & Boschin, W. 2022, MNRAS, 515, L72

Collins, M. L. M., et al. 2023, arXiv e-prints, arXiv:2305.13966

Conn, A. R., et al. 2012, ApJ, 758, 11

Conn, A. R., et al. 2013, ApJ, 766, 120

Conn, B. C., Jerjen, H., Kim, D., & Schirmer, M. 2018a, ApJ, 852, 68

Conn, B. C., Jerjen, H., Kim, D., & Schirmer, M. 2018b, ApJ, 857, 70

Crnojević, D., et al. 2014, MNRAS, 445, 3862

Crnojević, D., et al. 2019, ApJ, 872, 80

Danieli, S., Greene, J. E., Carlsten, S., Jiang, F., Beaton, R., & Goulding, A. D. 2022, arXiv e-prints, arXiv:2210.14233

Diemer, B., & Joyce, M. 2019, ApJ, 871, 168

Doliva-Dolinsky, A., et al. 2022, ApJ, 933, 135

Doliva-Dolinsky, A., et al. 2023, arXiv e-prints, arXiv:2303.01528

D'Onghia, E., Springel, V., Hernquist, L., & Keres, D. 2010, ApJ, 709, 1138

Dooley, G. A., Peter, A. H. G., Yang, T., Willman, B., Griffen, B. F., & Frebel, A. 2017, MNRAS, 471, 4894

Drlica-Wagner, A., et al. 2016, ApJL, 833, L5

Drlica-Wagner, A., et al. 2020, ApJ, 893, 47

Drlica-Wagner, A., et al. 2015, ApJ, 813, 109

D'Souza, R., & Bell, E. F. 2018, Nature Astronomy, 2, 737

Eisenstein, D. J., et al. 2005, ApJ, 633, 560

Engler, C., et al. 2021, MNRAS, 507, 4211

Evans, T. A., Fattahi, A., Deason, A. J., & Frenk, C. S. 2020, MNRAS, 497, 4311

Ferguson, A. M. N., Irwin, M. J., Ibata, R. A., Lewis, G. F., & Tanvir, N. R. 2002, AJ, 124, 1452

Ferguson, A. M. N., Johnson, R. A., Faria, D. C., Irwin, M. J., Ibata, R. A., Johnston, K. V., Lewis, G. F., & Tanvir, N. R. 2005, ApJL, 622, L109

Font, A. S., et al. 2011, MNRAS, 417, 1260

Garavito-Camargo, N., Besla, G., Laporte, C. F. P., Price-Whelan, A. M., Cunningham, E. C., Johnston, K. V., Weinberg, M., & Gómez, F. A. 2021, ApJ, 919, 109

Garling, C. T., Peter, A. H. G., Kochanek, C. S., Sand, D. J., & Crnojević, D. 2021, arXiv e-prints, arXiv:2105.01082

Garrison-Kimmel, S., et al. 2019, MNRAS, 487, 1380

Garrison-Kimmel, S., et al. 2017, MNRAS, 471, 1709

Geha, M., et al. 2017, ApJ, 847, 4

Gilmore, G., Wilkinson, M. I., Wyse, R. F. G., Kleyna, J. T., Koch, A., Evans, N. W., & Grebel, E. K. 2007, ApJ, 663, 948

Grillmair, C. J. 2006, ApJL, 645, L37

Grillmair, C. J. 2009, ApJ, 693, 1118

Guo, Q., Cole, S., Eke, V., Frenk, C., & Helly, J. 2013, MNRAS, 434, 1838

Hammer, F., Yang, Y. B., Wang, J. L., Ibata, R., Flores, H., & Puech, M. 2018, MNRAS, 475, 2754

Harrington, R. G., & Wilson, A. G. 1950, PASP, 62, 118

Harris, W. E. 1996, VizieR Online Data Catalog, VII/195

Hastings, W. K. 1970, Biometrika, 57, 97

Helmi, A., Babusiaux, C., Koppelman, H. H., Massari, D., Veljanoski, J., & Brown, A. G. A. 2018, Nature, 563, 85

Herschel, W. 1785, Philosophical Transactions of the Royal Society of London Series I, 75, 213

Herschel, W. 1789, Philosophical Transactions of the Royal Society of London Series I, 79, 212

Hodierna, G. B. 1654, De systemate orbis cometici deque admirandis coeli characteribus explicantur, necnon vie Com etarum, per orbem cometicum multiplices opuscula duo, in quorum primo cometarum causae disquiruntur, & indicantur. In secundo vero quid, quales, quotue sint stellae luminosae, nebulae, necnon, & occultae, manifestantur & rerum caelestium studiosis commendantur

Homma, D., et al. 2019, PASJ, 71, 94

Homma, D., et al. 2016, ApJ, 832, 21

Homma, D., et al. 2018, PASJ, 70, S18

Huxor, A., Tanvir, N. R., Irwin, M., Ferguson, A., Ibata, R., Lewis, G., & Bridges, T. 2004, in Astronomical Society of the Pacific Conference Series, Vol. 327, Satellites and Tidal Streams, ed. F. Prada, D. Martinez Delgado, & T. J. Mahoney, 118

Huxor, A. P., et al. 2014, MNRAS, 442, 2165

Huxor, A. P., Tanvir, N. R., Ferguson, A. M. N., Irwin, M. J., Ibata, R., Bridges, T., & Lewis, G. F. 2008, MNRAS, 385, 1989

Ibata, R., Irwin, M., Lewis, G., Ferguson, A. M. N., & Tanvir, N. 2001, Nature, 412, 49

Ibata, R., Martin, N. F., Irwin, M., Chapman, S., Ferguson, A. M. N., Lewis, G. F., & McConnachie, A. W. 2007, ApJ, 671, 1591

Ibata, R. A., Gilmore, G., & Irwin, M. J. 1995, MNRAS, 277, 781

Ibata, R. A., et al. 2013, Nature, 493, 62

Ibata, R. A., et al. 2014, ApJ, 780, 128

Ibata, R. A., Wyse, R. F. G., Gilmore, G., Irwin, M. J., & Suntzeff, N. B. 1997, AJ, 113, 634

Irwin, M. J., et al. 2007, ApJL, 656, L13

Irwin, M. J., Bunclark, P. S., Bridgeland, M. T., & McMahon, R. G. 1990, MNRAS, 244, 16P

Irwin, M. J., Ferguson, A. M. N., Huxor, A. P., Tanvir, N. R., Ibata, R. A., & Lewis, G. F. 2008, ApJL, 676, L17

Ivezić, Ž., et al. 2019, ApJ, 873, 111

Jerjen, H., Conn, B., Kim, D., & Schirmer, M. 2018, arXiv e-prints, arXiv:1809.02259

Jethwa, P., Erkal, D., & Belokurov, V. 2018, MNRAS, 473, 2060

Joshi, G. D., Pontzen, A., Agertz, O., Rey, M. P., Read, J., & Renaud, F. 2023, arXiv e-prints, arXiv:2307.02206

Kanehisa, K. J., Pawlowski, M. S., & Müller, O. 2023, MNRAS, 524, 952

Karachentsev, I. D., & Karachentseva, V. E. 1999, A&A, 341, 355

Karachentseva, V. E. 1976, Soobshcheniya Spetsial'noj Astrofizicheskoj Observatorii, 18, 42

Kelley, T., Bullock, J. S., Garrison-Kimmel, S., Boylan-Kolchin, M., Pawlowski, M. S., & Graus, A. S. 2019, MNRAS, 487, 4409

Kepner, J., Fan, X., Bahcall, N., Gunn, J., Lupton, R., & Xu, G. 1999, ApJ, 517, 78

Kim, D., & Jerjen, H. 2015, ApJL, 808, L39

Kim, S. Y., Peter, A. H. G., & Hargis, J. R. 2018, PhRvL, 121, 211302

Klypin, A., Kravtsov, A. V., Valenzuela, O., & Prada, F. 1999, ApJ, 522, 82

Koposov, S., et al. 2008, ApJ, 686, 279

Koposov, S. E., Belokurov, V., Torrealba, G., & Evans, N. W. 2015, ApJ, 805, 130

Koposov, S. E., et al. 2018, MNRAS, 479, 5343

Koposov, S. E., Yoo, J., Rix, H.-W., Weinberg, D. H., Macciò, A. V., & Escudé, J. M. 2009, ApJ, 696, 2179

Kravtsov, A. V., Berlind, A. A., Wechsler, R. H., Klypin, A. A., Gottlöber, S., Allgood, B., & Primack, J. R. 2004, ApJ, 609, 35

Kroupa, P. 2001, MNRAS, 322, 231

Kroupa, P., Theis, C., & Boily, C. M. 2005, A&A, 431, 517

Laevens, B. 2015, Ph.D. thesis, 2015STRAE024

Laevens, B. P. M., et al. 2015, ApJ, 813, 44

Loeb, A., & Zaldarriaga, M. 2005, PhRvD, 71, 103520

Loveday, J., et al. 2012, MNRAS, 420, 1239

Luque, E., et al. 2016, MNRAS, 458, 603

Lux, H., Read, J. I., & Lake, G. 2010, MNRAS, 406, 2312

Lynden-Bell, D. 1976, MNRAS, 174, 695

Mackey, A. D., et al. 2019, MNRAS, 484, 1756

Majewski, S. R., et al. 2007, ApJL, 670, L9

Majewski, S. R., et al. 2004, in American Astronomical Society Meeting Abstracts, Vol. 205, American Astronomical Society Meeting Abstracts, 141.13

Majewski, S. R., Skrutskie, M. F., Weinberg, M. D., & Ostheimer, J. C. 2003, ApJ, 599, 1082

Manwadkar, V., & Kravtsov, A. V. 2022, MNRAS, 516, 3944

Mao, Y.-Y., Geha, M., Wechsler, R. H., Weiner, B., Tollerud, E. J., Nadler, E. O., & Kallivayalil, N. 2021, ApJ, 907, 85

Marigo, P., Girardi, L., Bressan, A., Groenewegen, M. A. T., Silva, L., & Granato, G. L. 2008, A&A, 482, 883

Marigo, P., et al. 2017, ApJ, 835, 77

Marquis de Laplace, P.-S. 1812, Theorie analytique des probabilites

Martin, N. F., Ibata, R. A., Irwin, M. J., Chapman, S., Lewis, G. F., Ferguson, A. M. N., Tanvir, N., & McConnachie, A. W. 2006, MNRAS, 371, 1983

Martin, N. F., et al. 2016, ApJ, 833, 167

Martin, N. F., Ibata, R. A., McConnachie, A. W., Mackey, A. D., Ferguson, A. M. N., Irwin, M. J., Lewis, G. F., & Fardal, M. A. 2013a, ApJ, 776, 80

Martin, N. F., et al. 2009, ApJ, 705, 758

Martin, N. F., et al. 2015, ApJL, 804, L5

Martin, N. F., et al. 2013b, ApJL, 779, L10

Martin, N. F., et al. 2013c, ApJ, 772, 15

Martin, N. F., et al. 2017, ApJ, 850, 16

Martínez-Delgado, D., Karim, N., Charles, E. J. E., Boschin, W., Monelli, M., Collins, M. L. M., Donatiello, G., & Alfaro, E. J. 2022, MNRAS, 509, 16

Mashchenko, S., Wadsley, J., & Couchman, H. M. P. 2008, Science, 319, 174

Mateo, M. L. 1998, ARA&A, 36, 435

Mau, S., et al. 2020, ApJ, 890, 136

McConnachie, A. W. 2012, AJ, 144, 4

McConnachie, A. W., et al. 2008, ApJ, 688, 1009

McConnachie, A. W., et al. 2018, ApJ, 868, 55

McConnachie, A. W., & Irwin, M. J. 2006, MNRAS, 365, 902

McConnachie, A. W., Irwin, M. J., Ferguson, A. M. N., Ibata, R. A., Lewis, G. F., & Tanvir, N. 2005, MNRAS, 356, 979

McConnachie, A. W., et al. 2009, Nature, 461, 66

McDonough, B., & Brainerd, T. G. 2022, ApJ, 933, 161

Messier, C. 1781, Catalogue des Nébuleuses et des Amas d'Étoiles (Catalog of Nebulae and Star Clusters), Connoissance des Temps ou des Mouvements Célestes, for 1784, p. 227-267

Metropolis, N., Rosenbluth, A. W., Rosenbluth, M. N., Teller, A. H., & Teller, E. 1953, Journal of Chemical Physics, 21, 1087

Metz, M., Kroupa, P., & Jerjen, H. 2007, MNRAS, 374, 1125

Metz, M., Kroupa, P., & Libeskind, N. I. 2008, ApJ, 680, 287

Moore, B., Ghigna, S., Governato, F., Lake, G., Quinn, T., Stadel, J., & Tozzi, P. 1999, ApJL, 524, L19

Müller, O., Pawlowski, M. S., Jerjen, H., & Lelli, F. 2018, Science, 359, 534

Mutlu-Pakdil, B., et al. 2018, ApJ, 863, 25

Mutlu-Pakdil, B., et al. 2021, ApJ, 918, 88

Nadler, E. O., et al. 2021, PhRvL, 126, 091101

Nadler, E. O., Gluscevic, V., Boddy, K. K., & Wechsler, R. H. 2019, ApJL, 878, L32

Nadler, E. O., et al. 2020, ApJ, 893, 48

Nashimoto, M., Tanaka, M., Chiba, M., Hayashi, K., Komiyama, Y., & Okamoto, T. 2022, arXiv e-prints, arXiv:2207.11992

Navarro, J. F., Frenk, C. S., & White, S. D. M. 1996, ApJ, 462, 563

Newton, O., Cautun, M., Jenkins, A., Frenk, C. S., & Helly, J. C. 2018, MNRAS, 479, 2853

Ocvirk, P., & Aubert, D. 2011, MNRAS, 417, L93

Ocvirk, P., et al. 2016, MNRAS, 463, 1462

Okamoto, S., Arimoto, N., Ferguson, A. M. N., Irwin, M. J., Bernard, E. J., & Utsumi, Y. 2019, ApJ, 884, 128

Patel, E., Besla, G., & Sohn, S. T. 2017, MNRAS, 464, 3825

Patel, E., Carlin, J. L., Tollerud, E. J., Collins, M. L. M., & Dooley, G. A. 2018, MNRAS, 480, 1883

Pawlowski, M. S. 2018, Modern Physics Letters A, 33, 1830004

Pawlowski, M. S. 2021, Nature Astronomy, 5, 1185

Pawlowski, M. S., Ibata, R. A., & Bullock, J. S. 2017, ApJ, 850, 132

Pawlowski, M. S., Kroupa, P., & Jerjen, H. 2013, MNRAS, 435, 1928

Pawlowski, M. S., Pflamm-Altenburg, J., & Kroupa, P. 2012, MNRAS, 423, 1109

Peñarrubia, J., Gómez, F. A., Besla, G., Erkal, D., & Ma, Y.-Z. 2016, MNRAS, 456, L54

Peebles, P. J. E. 1984, ApJ, 284, 439

Penzias, A. A., & Wilson, R. W. 1965, ApJ, 142, 419

Planck Collaboration, et al. 2016, A&A, 594, A13

Preston, J., et al. 2019, MNRAS, 490, 2905

Putman, M. E., et al. 2009, ApJ, 703, 1486

Richardson, J. C., et al. 2008, AJ, 135, 1998

Richardson, J. C., et al. 2009, MNRAS, 396, 1842

Richardson, J. C., et al. 2011, ApJ, 732, 76

Riess, A. G., et al. 1998, AJ, 116, 1009

Rockosi, C. M., et al. 2002, AJ, 124, 349

Rubin, V. C., Ford, J., W. K., & Thonnard, N. 1978, ApJL, 225, L107

Rykoff, E. S., et al. 2012, ApJ, 746, 178

Sales, L. V., & Navarro, J. F. 2023, Nature Astronomy, 7, 376

Sales, L. V., Wetzel, A., & Fattahi, A. 2022, Nature Astronomy, 6, 897

Salomon, J.-B., Libeskind, N., & Hoffman, Y. 2023, MNRAS, 523, 2759

Samuel, J., et al. 2020, MNRAS, 491, 1471

Santos-Santos, I. M., Domínguez-Tenreiro, R., & Pawlowski, M. S. 2020, MNRAS, 499, 3755

Savino, A., et al. 2023, arXiv e-prints, arXiv:2305.13360

Savino, A., et al. 2022, arXiv e-prints, arXiv:2206.02801

Sawala, T., et al. 2023, Nature Astronomy, 7, 481

Sawala, T., Pihajoki, P., Johansson, P. H., Frenk, C. S., Navarro, J. F., Oman, K. A., & White, S. D. M. 2017, MNRAS, 467, 4383

Schlafly, E. F., & Finkbeiner, D. P. 2011, ApJ, 737, 103

Schlegel, D. J., Finkbeiner, D. P., & Davis, M. 1998, ApJ, 500, 525

Schmidt, B. P., et al. 1998, ApJ, 507, 46

Semczuk, M., Łokas, E. L., Salomon, J.-B., Athanassoula, E., & D'Onghia, E. 2018, ApJ, 864, 34

Shapley, H. 1938a, Harvard College Observatory Bulletin, 908, 1

Shapley, H. 1938b, Nature, 142, 715

Shen, S., Mo, H. J., White, S. D. M., Blanton, M. R., Kauffmann, G., Voges, W., Brinkmann, J., & Csabai, I. 2003, MNRAS, 343, 978

Slater, C. T., Bell, E. F., & Martin, N. F. 2011, ApJL, 742, L14

Smoot, G. F., et al. 1991, ApJL, 371, L1

Sohn, S. T., Patel, E., Fardal, M. A., Besla, G., van der Marel, R. P., Geha, M., & Guhathakurta, P. 2020, ApJ, 901, 43

Somerville, R. S. 2002, ApJL, 572, L23

Spergel, D. N., & Steinhardt, P. J. 2000, PhRvL, 84, 3760

Springel, V., et al. 2008, MNRAS, 391, 1685

Starkenburg, E., et al. 2013, MNRAS, 429, 725

Thomas, G. F., Famaey, B., Ibata, R., Renaud, F., Martin, N. F., & Kroupa, P. 2018, A&A, 609, A44

Thomas, G. F., et al. 2021, ApJ, 910, 92

Tollerud, E. J., et al. 2012, ApJ, 752, 45

Tollerud, E. J., Bullock, J. S., Strigari, L. E., & Willman, B. 2008, ApJ, 688, 277

Torrealba, G., Koposov, S. E., Belokurov, V., & Irwin, M. 2016a, MNRAS, 459, 2370

Torrealba, G., et al. 2016b, MNRAS, 463, 712

Turner, M. S., Steigman, G., & Krauss, L. M. 1984, PhRvL, 52, 2090

van den Bergh, S. 1972, ApJL, 171, L31

van der Marel, R. P., Fardal, M. A., Sohn, S. T., Patel, E., Besla, G., del Pino, A., Sahlmann, J., & Watkins, L. L. 2019, ApJ, 872, 24

Van Nest, J., Munshi, F., Christensen, C., Brooks, A. M., Tremmel, M., & Quinn, T. R. 2023, arXiv e-prints, arXiv:2304.02007

Vasiliev, E. 2023, Galaxies, 11, 59

Walker, M. G., Olszewski, E. W., & Mateo, M. 2015, MNRAS, 448, 2717

Walsh, S. M., Jerjen, H., & Willman, B. 2007, ApJL, 662, L83

Walsh, S. M., Willman, B., & Jerjen, H. 2009, AJ, 137, 450

Wan, Z., Oliver, W. H., Lewis, G. F., Read, J. I., & Collins, M. L. M. 2020, MNRAS, 492, 456

Weisz, D. R., & Boylan-Kolchin, M. 2017, MNRAS, 469, L83

Weisz, D. R., Dolphin, A. E., Skillman, E. D., Holtzman, J., Gilbert, K. M., Dalcanton, J. J., & Williams, B. F. 2014, ApJ, 789, 148

Weisz, D. R., et al. 2019, ApJL, 885, L8

Wheeler, C., et al. 2019, MNRAS, 490, 4447

Wheeler, C., Oñorbe, J., Bullock, J. S., Boylan-Kolchin, M., Elbert, O. D., Garrison-Kimmel, S., Hopkins, P. F., & Kereš, D. 2015, MNRAS, 453, 1305

White, S. D. M., & Rees, M. J. 1978, MNRAS, 183, 341

Whiting, A. B., Hau, G. K. T., Irwin, M., & Verdugo, M. 2007, AJ, 133, 715

Willman, B. 2005, arXiv e-prints, astro

Willman, B., et al. 2005, ApJL, 626, L85

Wilson, A. G. 1955, PASP, 67, 27

Xu, Y., Kang, X., & Libeskind, N. I. 2023, arXiv e-prints, arXiv:2303.00441

Yniguez, B., Garrison-Kimmel, S., Boylan-Kolchin, M., & Bullock, J. S. 2014, MNRAS, 439, 73

Zucker, D. B., et al. 2006, ApJL, 650, L41

Zucker, D. B., et al. 2004a, ApJL, 612, L121

Zucker, D. B., et al. 2004b, ApJL, 612, L117

Zucker, D. B., et al. 2007, ApJL, 659, L21

Zwicky, F. 1933, Helvetica Physica Acta, 6, 110

UNIVERSITÉ DE STRASBOURG

Amandine DOLIVA-DOLINSKY

Les galaxies naines du Groupe Local comme sonde cosmologique

Observatoire astronomique de Strasbourg

Les galaxies naines agissent comme des capsules temporelles et ont des masses stellaires très faibles, ce qui en fait le laboratoire idéal pour explorer la physique de la formation et de l'évolution des galaxies et la cosmologie. La plupart des contraintes sont dérivées du système satellitaire de la Voie Lactée, mais comme il n'est pas forcément typique, il est important d'étudier les galaxies naines autour d'autres hôtes. Le but de ce travail est donc de caractériser le système satellitaire de notre voisine cosmique, M31. La première partie de ce travail est consacrée à l'obtention des limites de détection des galaxies naines de M31 en fonction de leur luminosité, de leur taille, de leur distance et de leur position. Dans la deuxième partie de cette thèse, je déduis les propriétés globales de ce système de satellites, en intégrant les limites de détection, créant ainsi une base solide pour une comparaison future entre les observations et les simulations des satellites M31.

Mots clés : Galaxies naines, Groupe Local, M31

Dwarf galaxies are primitive objects that are essential to understanding the universe around us. They act like time capsules and have very low stellar masses, making them the perfect laboratory to explore the physics of galaxy formation & evolution and cosmology. Most of the constraints are derived from the satellite system of our own galaxy, the Milky Way, but as it may not be typical, it is important to study dwarf galaxies around other hosts. Therefore, the aim of this work is to characterize the satellite system of our cosmic neighbor, M31. The first part of this work is dedicated to obtaining the completeness of the search for M31 dwarf galaxies as a function of their luminosity, size, distance and position. In the second part of this thesis, I infer the global properties of this satellite system, folding in the detection limits, creating a solid foundation for future comparison between M31 satellite observations and simulations.

Key words: Dwarf galaxies, Local Group, M31